UNIVERSITAT DE BARCELONA

Forces and flows in cells and tissues

Blebs, active gels, and collective cell migration

Ricard Alert Zenón

Forces and flows in cells and tissues

Blebs, active gels, and collective cell migration

Ricard Alert Zenón

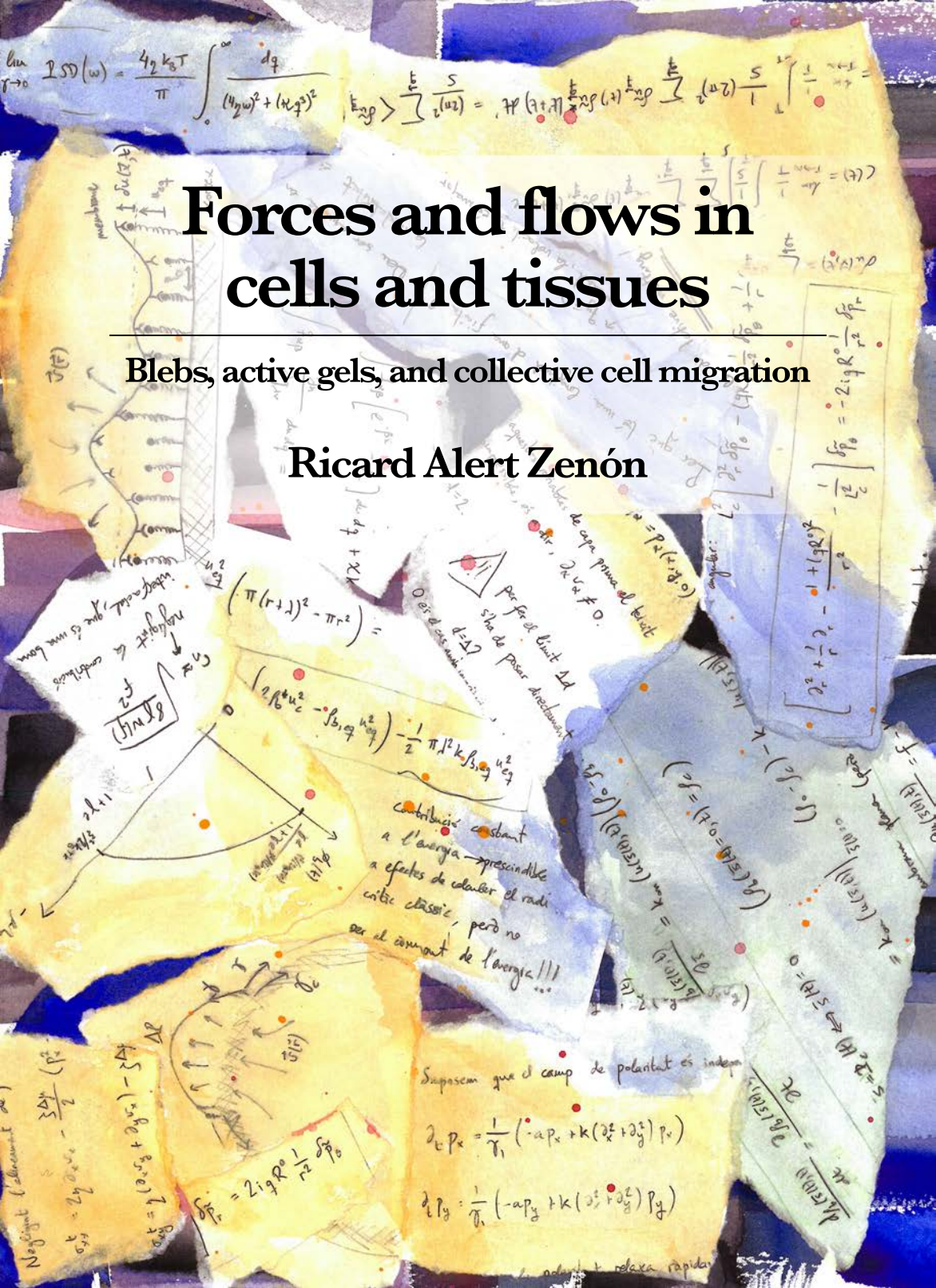

Forces and flows in cells and tissues

Blebs, active gels, and collective cell migration

RICARD ALERT ZENÓN

– Ph.D. Thesis –

Ph.D. advisor:

JAUME CASADEMUNT VIADER

Tutor:

GIANCARLO FRANZESE

Barcelona, October 2017

Programa de Doctorat en Física
Departament de Física de la Matèria Condensada
Facultat de Física

UNIVERSITAT DE BARCELONA

Ricard Alert Zenón
Departament de Física de la Matèria Condensada
Facultat de Física
Universitat de Barcelona
Barcelona, E-08028 (Spain)
ricard.alert@fmc.ub.edu
http://www.ecm.ub.edu/~ricardaz

Forces and flows in cells and tissues.
Blebs, active gels, and collective cell migration
Ph.D. Thesis
Programa de Doctorat en Física
Línia de recerca en Física de la matèria condensada
Memòria presentada per a optar al grau de Doctor per la Universitat de Barcelona
Barcelona, October 2017

About the cover

Artwork by Mariona Esquerda Ciutat and Josep Enric Esquerda Colell
Watercolour-painted collage of handwritten notes from my PhD research

The work described in this thesis was funded by a PhD fellowship granted by Fundació "La Caixa".

Research stays in Paris were funded by a short-term fellowship (ASTF 365-2015) by the European Molecular Biology Organization (EMBO), a Travelling Fellowship (DEVTF-151206) by the journal Development, from The Company of Biologists, and a complementary fellowship by Fundació Universitària Agustí Pedro i Pons.

The work had also financial support from Ministerio de Economía y Competitividad under projects FIS2010-21924-C02-02, FIS2013-41144-P and FIS2016-78507-C2-2-P, and from Generalitat de Catalunya under projects 2009-SGR-00014 and 2014-SGR-878.

I propose to develop first what you might call ‘a naive physicist’s ideas about organisms’, that is, the ideas which might arise in the mind of a physicist who, after having learnt his physics and, more especially, the statistical foundation of his science, begins to think about organisms and about the way they behave and function and who comes to ask himself conscientiously whether he, from what he has learnt, from the point of view of his comparatively simple and clear and humble science, can make any relevant contributions to the question.
It will turn out that he can. The next step must be to compare his theoretical anticipations with the biological facts. It will then turn out that — though on the whole his ideas seem quite sensible — they need to be appreciably amended.

Erwin Schrödinger
What is Life? The Physical Aspect of the Living Cell (1994)

A la Mariona

Acknowledgements

It is my pleasure to thank many people who have contributed in many different ways to this thesis. A few words fall short to express how thankful I am to all of you, but I hope that the feeling that part of this work is yours is a much better acknowledgement of your contribution.

L'agraïment més important és pel Jaume, que va obrir-me les portes al món de la recerca i em va encaminar a fer una tesi que m'ha apassionat. T'agraeixo la teva confiança en mi des de l'època de la carrera i, sobretot, la teva insistència i flexibilitat quan estava en un mar de dubtes per escollir treball de màster i doctorat. No podria haver escollit millor. Durant la tesi, t'agraeixo la diversitat temàtica que m'has ofert, la llibertat que m'has donat a l'hora de treballar, i l'amistat en la relació diària — sabàtic inclòs. En conjunt, has fet que aquests anys fossin un repte científic excitant, en què he gaudit molt discutint i aprenent física de tu en un entorn distès, amable, i fins i tot divertit. També valoro molt que m'hagis transmès la teva honestedat, ètica, i filosofia científica. Et tindré com a referent també en això. Finalment, t'agraeixo la teva preocupació constant pel meu futur. Espero que, d'una manera o altra, puguem seguir fent la mena de física que ens apassiona a tots dos. De fet, tenim un llibre a mitges!

En segon lloc, vull donar les gràcies al Pietro Tierno per donar-me una oportunitat clau per treballar en un tema de física estadística. La col·laboració en les transicions de fase dels teus cristalls col·loïdals ha estat molt enriquidora. Gràcies per ajudar-me sobretot ben al principi i durant tot el doctorat.

Un agraïment important també és pel Carlos Pérez i el Xavier Trepat, amb qui hem establert una magnífica col·laboració sobre teixits epitelials. Agraeixo al Xavi que m'obrís les portes del seu laboratori i que mostrés tota la predisposició a escoltar el que un teòric hi pugués aportar. Poder participar a les trobades del teu grup m'ha permès aprendre sobre mecanobiologia de teixits i establir una col·laboració molt motivadora. Gràcies també per aconsellar-me i donar-me suport pel futur de la meva carrera. Al Carlos li agraeixo la seva amplitud de mires i el seu continu interès per les prediccions teòriques que jo feia. T'agraeixo la valentia d'involucrar-te en una recerca de caire molt físic malgrat la teva formació biomèdica. Com pocs, has tingut l'atreviment fer experiments motivats per la teoria. La teva voluntat d'aprendre i entendre conceptes físics o matemàtics han fet que el projecte que tenim en comú hagi estat, per mi, una col·laboració molt estimulant i agraïda. Gràcies també a tots els membres dels grups del Xavier Trepat i el Pere Roca-Cusachs, que m'han integrat com un membre més dels seus grups en els seminaris i trobades.

Durant el doctorat he tingut la sort de compartir grup amb companys com el

Carles Blanch, el David Oriola, o el Javier G. Orlandi. A tots ells, els agraeixo l'ajuda que m'han donat en diferents moments del doctorat. A més, he tingut el privilegi de treballar directament tant amb el Carles com amb el David. Carles, gràcies per tot el que m'has ensenyat, per les moltes discussions i l'ajuda amb els teixits. Pràcticament m'has supervisat aquesta part de la tesi; sense tu no haguéssim arribat pas tan lluny. I gràcies per les moltes estones que vam passar junts diàriament a París. Allà et vaig conèixer de veritat. David, gràcies per haver engegat els càlculs dels gels actius. Vaig gaudir molt amb les discussions i amb tot el que finalment ha suposat aquest projecte inesperat. Tenim coses pendents per continuar! I gràcies també pels consells!

I also want to thank Bart Smeets, Romaric Vincent, Ignasi Pagonabarraga, and the rest of collaborators for the work on cell colonies. It's a nice illustration of how different perspectives about a common interest can be combined into a nice collaboration.

From my time in Paris, I thank Jacques Prost for supervising my stays at Institut Curie. Although we could not put in the time that we would have liked to work together, it was a pleasure to discuss with you, and I appreciate very much your ideas as well as your pedagogic and friendly style. I also thank Pierre Sens and Jean-François Joanny for welcoming me in the theory group and for the discussions we had. Similarly, I thank all the members of group, with whom I shared lunch, discussions, and even Eurocup matches. Thanks Philippe, Pierre, Thomas, Françoise, Michele, Marco, Quentin, Vincent, Sabya, Matej, Jean-François, and all the rest.

Mención aparte merece la gente del Colegio de España en París. Sois una panda terrible! Fue una suerte vivir con vosotros durante los seis meses que pasé en París. Hecho de menos las cenas, las salidas y las charlas!

També vull agrair als professors de la facultat que m'han ensenyat física i que m'han transmès passió per qualsevol dels seus temes. Sou més importants del que sembla. En especial, al José María Sancho i a la Marta Ibañes, que s'han interessat contínuament per mi durant la tesi. Gràcies també a tots els membres dels grups de física no lineal i del Consolider. I no em vull deixar la gent dels Encontres amb el Tercer Cicle. Que segueixin a tota màquina!

També els toca a la gent amb qui he compartit dinar durant tota la tesi. Aquí el protagonisme se l'enduen el Joan i el Xavi, amb qui hem compartit cada dinar que hem pogut. Sou... com ho diria... especials. No us oblidaré. Thanks as well to Fabien. The year we spent together was so funny! Moreover, I learnt a lot from you in many senses — also physics, entropic issues in particular, I'd say. I miss the conversations. A lot. Thank you Ido, as well. Your arrival enlivened the group this last year. Good luck with your thesis!

També vull agrair a la gent amb qui vaig compartir el màster, la carrera, o la vida a la facultat. Només per fer-ne una petita selecció, mencionaré l'Òscar, el Jordi, el Genís, l'Artemi, l'Alejandro, la Laia, la Clàudia, el Francesc, el Rubén, el Valentí, l'Ignasi, l'Edu, el Dani, el Joan, la Marina, el Lluís, l'Albert i el Pau. La vostra bogeria particular va fer que la carrera fos l'època més divertida i alhora més intel·lectualment estimulant que he viscut fins ara.

Per altra banda, gràcies a la gent del ping-pong per oferir-me un excel·lent contrapès a la meva feina. I gràcies als amics, especialment al Bernat, per escoltar-me i per donar-me tota la confiança del món.

Finalment, vull agrair a tota la família, i en particular a la mare, haver-me cuidat en tot moment.

I a tu, Mariona, per fer-me gaudir de la vida que voldria amb tu. Gràcies per venir-me a veure a París i per marxar amb mi cap als Estats Units. Sé el que significa. Valoro molt tot el que has fet per mi, i especialment com m'has ajudat aquest últim parell de mesos. Aquesta tesi és per tu.

Preface

This thesis presents my PhD research in biophysics, performed under the supervision of Jaume Casademunt at the University of Barcelona between November 2013 and October 2017. It covers three main topics related to mechanical aspects of cellular behaviour, both in single cells and in tissues, for which we develop theoretical physical models. However, to give it a well-defined scope, this thesis does not include all the work that I have performed during my PhD. Here, I briefly comment on the inception and development of the different research projects that I have pursued during my PhD, giving a minimal account of some of the ones that have not been included in this thesis.

What is in this thesis

The first topic of this thesis concerns the mechanics of the adhesion between the plasma membrane and the actin cortex in eukaryotic cells. This research stems from my Master thesis, which arose as an extension of one of the topics of Jan Brugués' PhD thesis. This work is summarized in Chapter 2, which was published in 2015 [Alert 2015]. Then, as a first project of the thesis, we used the model for membrane-cortex adhesion to study bleb nucleation. This work is summarized in Chapter 3, which we published in 2016 [Alert 2016a], thus completing the research line on membrane-cortex adhesion and blebs.

The second topic concerns the theory of active gels. Although I was using this theory in the context of tissues, specific research on the theory itself was not in the initial plan, but it rather arose spontaneously during my PhD. Motivated by the interest of David Oriola in the theory of active gels, and upon preliminary discussions on friction forces, we derived the constitutive equations of active gels from a mesoscopic description. This work is presented in Chapter 4, and we published it in early 2017 [Oriola 2017], in a paper with shared first authorship with David.

Finally, the third topic of my thesis concerns collective cell migration in epithelial tissues. This research line was planned as a natural continuation of the last topic of Carles Blanch-Mercader's thesis, and it was one of the core elements of my PhD proposal. However, I only focused on it during the second half of my PhD. The specific research questions were largely influenced by the interaction with the members of the lab of Xavier Trepat. In fact, results from the Master thesis and early stages of the PhD of Carlos Pérez-González motivated me to develop the

model for tissue wetting. This fact sparked a close collaboration with Carlos that has spanned the last few years. The results are presented in Chapters 6 and 7, and they are currently being prepared for publication. In parallel, the interaction with Bart Smeets and Romaric Vincent, respectively a visitor and a postdoc in Xavier's lab, led to the collaboration on the collective behaviour of cell colonies. The results of this collaborative work are presented in Chapter 5, and they were published in late 2016 [Smeets 2016].

What is not in this thesis

Motivated by the experimental results obtained by Raimon Sunyer [Sunyer 2016], a researcher in Xavier Trepat's lab, I also modeled the phenomenon of collective durotaxis. The results of this research are not presented in this thesis.

During my PhD, I enjoyed two 3-month stays at Institut Curie under the supervision of Jacques Prost. There, I started an ongoing collaboration with him on modeling cell-cell adhesion. In addition, during my second stay, in collaboration with Jean-François Joanny and coinciding with Jaume's sabbatical period at Institut Curie, I started working on simulations of complex spontaneous flows in active liquid crystal layers, with the aim of exploring regimes of active turbulence. The results of these two ongoing projects are still very preliminary, and they are not included in this thesis.

Moreover, starting in my Master and continuing throughout my PhD, I pursued my interest in statistical physics by working on fundamental aspects of phase transitions. This research was done in collaboration with Pietro Tierno, who conducted experiments in magnetic colloidal crystals, which we used as an experimental model system. I outline the main findings below.

By means of a mean-field model and Brownian dynamics simulations, we predicted two structural phase transitions in the crystal [Alert 2014]. The theory allowed us to discover that one of them does not proceed via the usual mechanism of first-order phase transitions, but that it is due to a complete inversion of the energy landscape of the system. This mechanism opens a new scenario in the traditional field of phase transitions, thus adding new phenomena and possibilities to the well-known textbook scenarios. Most strikingly, we have recently proven that the transition is indeed of a mixed order, exhibiting critical phenomena due to the divergence of the correlation length like second-order transitions, yet being discontinuous like first-order transitions. The paper reporting the latter result is currently under review at PNAS.

We also studied the kinetics of the so-called "Landscape-Inversion Phase Transition" [Alert 2016b], which revealed surprising phenomena. For example, we showed, both experimentally and by means of a dynamical field model, that domains of a metastable phase are formed by spinodal decomposition and subsequently eliminated by front propagation. This phenomenon is but an illustration of how the new scenario allows for unexpected relations between classical concepts of phase-ordering kinetics.

Finally, during my PhD I have also started writing a textbook on cellular biophysics together with Jaume. In addition, with Marta Ibañes and Jordi Soriano, we prepared and gave a course on biophysics in the fourth year of the physics degree at the University of Barcelona. Altogether, these two experiences combined my pedagogic interests with the opportunity to continue learning different aspects of biological physics.

Publications

The work in this thesis has been published in the following articles:

- R. Alert, J. Casademunt, J. Brugués, and P. Sens. *Model for Probing Membrane-Cortex Adhesion by Micropipette Aspiration and Fluctuation Spectroscopy*. Biophys. J. **108**, 1878 (2015) — Chapter 2
- R. Alert, and J. Casademunt. *Bleb Nucleation through Membrane Peeling*. Phys. Rev. Lett. **116**, 068101 (2016) — Chapter 3
- D. Oriola*, R. Alert*, and J. Casademunt. *Fluidization and Active Thinning by Molecular Kinetics in Active Gels*. Phys. Rev. Lett. **118**, 088002 (2017) — Chapter 4
- B. Smeets, R. Alert, J. Pešek, I. Pagonabarraga, H. Ramon, and R. Vincent. *Emergent structures and dynamics of cell colonies by contact inhibition of locomotion*. Proc. Natl. Acad. Sci. U. S. A. **113**, 14621 (2016) — Chapter 5

Two more are in preparation, with the following tentative titles

- C. Pérez-González*, R. Alert*, C. Blanch-Mercader, M. Gómez-González, T. Kolodziek, E. Bazellières, J. Casademunt, and X. Trepat. *Active wetting of epithelial tissues*. — Chapters 6 and 7
- R. Alert, C. Blanch-Mercader, and J. Casademunt. *Active fingering: Morphological instability during epithelial spreading*. — Chapter 7

* Equal contributions

In addition, the research on phase transitions, not included in this thesis, has been published in the following articles:

- R. Alert, J. Casademunt, and P. Tierno. *Landscape-Inversion Phase Transition in Dipolar Colloids: Tuning the Structure and Dynamics of 2D Crystals*. Phys. Rev. Lett. **113**, 198301 (2014)
- R. Alert, P. Tierno, and J. Casademunt. *Formation of metastable phases by spinodal decomposition*. Nat. Commun. **7**, 13067 (2016)
- R. Alert, P. Tierno, and J. Casademunt. *Mixed-order phase transition in a colloidal crystal*. Under review at Proc. Natl. Acad. U. S. A.

Contents

1 General introduction

1.1 Context and overview of the thesis

In the last few decades, research at the interface between physics and biology has flourished. On the one hand, biology has become an increasingly quantitative discipline, progressively drifting from observation to measurement. On the other hand, physics has embraced the challenge to expand its borders towards areas of knowledge traditionally belonging to biology. This interdisciplinary enterprise has two-way benefits: physics provides quantitative approaches, tools, and concepts to biology, and biological phenomena inspire whole new areas of research for physics.

In this context, biological physics emerged as a field that aims at applying physical principles to understand biological phenomena. This endeavour often leads to new concepts, methods, theories, and experiments that do not only advance our biological knowledge but also expand the frontiers of physics. In fact, in my opinion, biological physics should ultimately address whether new physical principles are required to build physical theories of biological systems. In the path towards such a grand challenge, unraveling the physical laws that govern specific biological processes has the prospect of gaining predictibility over the behaviour of biological systems.

The scope of biological physics is very broad by definition: with approaches rooted in different fields of physics, including statistical physics, condensed matter physics, and the mechanics of continuum media, it addresses questions in several fields of biology, spanning from the molecular to the population scale. At somehow intermediate scales, one area that has rapidly expanded is the biological physics of cells and tissues. Particularly, because of the ability of cells to exert forces to move, change shape, and divide, physicists have been interested in mechanical aspects of

cellular behaviour, often addressed from the point of view of soft matter physics. The present thesis belongs to this area of research, and focuses on developing theoretical models of the forces and flows involved in some specific biological processes at the cellular and multicellular scales.

The thesis is structured in three parts. Part I is devoted to the adhesion between the plasma membrane and the actin cortex of a cell, which are two of the main structural elements of eukaryotic cells. In Chapter 2, we propose a continuum model that couples the mechanics and hydrodynamics of membranes to the force-dependent binding kinetics of proteins that link the membrane to the cortex. Then, we use concepts and methods of statistical physics to study the fluctuations of an adhered membrane. In Chapter 3, the model is employed to study the physics of a specific cellular process: blebbing. Blebs are cellular protrusions arising from local detachments of the membrane from the cortex, and they have specific roles in some physiological cellular functions such as cell motility. In particular, we apply concepts of statistical physics and stochastic simulations methods to study the nucleation of blebs.

Part II deals with the physics of active gels. Active gels are soft, transiently crosslinked materials, usually based on polymer networks, that are maintained out of equilibrium by internal energy-transduction processes that locally break detailed balance. In addition, the constituents of the gel, e.g. protein filaments, are usually polar, and hence they can form orientationally ordered phases such as liquid crystals. Thus, active gels are a member of the larger family of active matter systems, which are currently the subject of intensive research by part of the statistical physics community. In Chapter 4, we provide a derivation of the constitutive equations of active polar gels from a stochastic model of their constituents, in an effort to bridge the mesoscopic and macroscopic scales of description. Our approach is largely based on the statistical physics of polymeric networks and of liquid crystals, with the aim of combining them and extending them to active systems. Thus, this part of the thesis takes a more fundamental perspective, in the sense that it does not intend to model a specific biological process. Yet, the development of the physics of active gels was originally inspired by the behaviour of the cell cytoskeleton. Recently, other biological systems, such as the mitotic spindle or tissues, have also been described as active gel materials. In this sense, our work is both inspired by, and has implications for the physics of cells and tissues. In fact, we discuss how our predictions could explain experimental results on the rheological properties of several biological systems.

Finally, Part III is devoted to cell colonies and tissues, focused on collective cell migration and tissue morphology. In Chapter 5, following an active matter approach, we model cell colonies as collections of self-propelled particles with interactions meant to capture generic cellular behaviours. Then, we employ concepts of nonequilibrium statistical physics to interpret the results of simulations, predict phase transitions, and hence build a phase diagram of the model. In the biological context, we discuss how the different phases in our diagram could be related to existing types of tissues, encompassing distinct morphologies and collective behaviours. In turn, in Chapters 6 and 7 we study the spreading of cohesive

monolayers of collectively migrating epithelial cells. In both chapters, using the framework provided by active gel theory, we model a cell monolayer as an active polar fluid continuum medium with specific properties, such as featuring active contact forces. Specifically, Chapter 6 focuses on the "active" wetting transition of such a medium, which separates the spreading of epithelial monolayers from their retraction into droplet-like aggregates. Respectively, Chapter 7 concentrates on the "active" fingering instability that occurs during epithelial spreading, whereby the propagating front of the cell monolayer develops finger-like protrusions. Therefore, these last two chapters illustrate the application of active gel theory to modeling the spreading of epithelial monolayers.

In the following, we briefly review the context and background of the topics of this thesis. First, we discuss the different modes of cell motility, emphasizing the role of the membrane and its adhesion to the cortex. Then, we discuss the collective migration of cells in tissues, particularly in cell monolayers. Finally, we present a brief overview of active gel theory as an overarching theoretical approach to the modeling of mechanical aspects of cells and tissues. More focused introductions to the specific questions addressed by our research are provided at the beginning of each chapter.

1.2 The plasma membrane in cell motility

Cell membranes are ~ 5 nm-thick phospholipid bilayers self-assembled by the interactions between the amphiphilic lipid molecules and the surrounding water. In addition to the basic lipid bilayer structure, cell membranes include other molecules such as cholesterol, as well as a number of inserted proteins involved in a myriad of cell functions (Fig. 1.1). Despite their complex molecular architecture, from the materials perspective, membranes are extremely thin sheets with striking mechanical properties. On the one hand, lipids can almost freely move within each layer of the membrane. Hence, in the bilayer plane, lipid membranes are essentially fluid, opposing no resistance to shear. On the other hand, both in-plane stretching and out-of-plane bending deformations of the bilayer expose the apolar tails of the lipid molecules to water. Consequently, stretching and bending have a free energy cost that generates elastic restoring forces, respectively defining bulk and bending moduli. Thus, lipid membranes are complex materials featuring distinct mechanical responses to different types of deformation. In fact, the unique combination of fluid and elastic properties enables membranes to flow and change shape yet preserve their integrity as a physical barrier.

Lipid bilayer membranes are ubiquitous within the cell. From the plasma membrane that encloses the cell to the endoplasmatic reticulum through the Golgi apparatus and the mitocondrial and nuclear envelopes, lipid membranes are key structural and functional components of the cell. On the one hand, membranes are structures that physically separate the cell interior from the external medium, and that isolate cellular organelles from the rest of the cytosol. On the other hand, membranes have many nonstructural functions. They not only mediate the

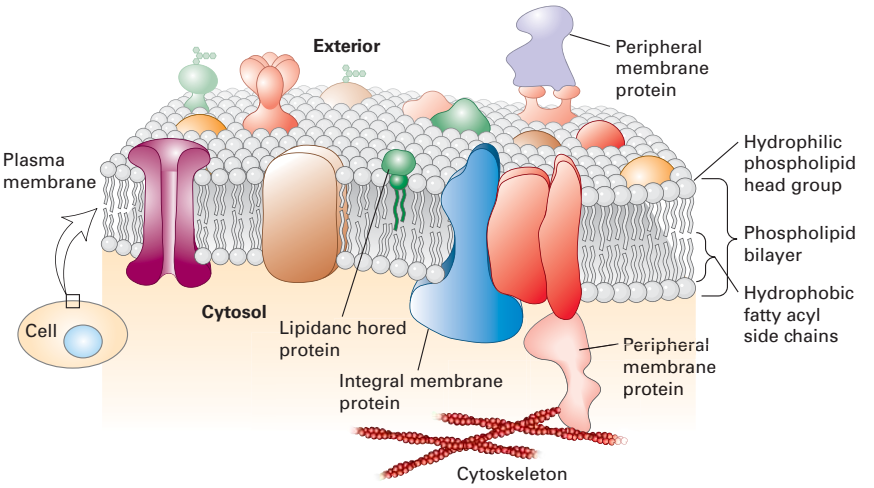

Figure 1.1 | Sketch of the cell membrane. A phospholipid bilayer provides the basic architecture, and membrane proteins endow each specific cellular membrane with its unique set of functions, in what is known as the fluid mosaic membrane model. In particular, the plasma membrane that encloses the cell is attached to the cytoskeleton via specific proteins. From [Lodish 2016].

communication between the cell and other cells or the extracellular medium, but they are also instrumental in many intracellular processes such as molecular transport, as well as in processes at the whole cell scale such as cell motility [Phillips 2012].

In particular, through its interaction with the underlying cytoskeletal structures, the cell membrane is directly involved in cell migration. Eukaryotic cell motility mainly relies on the actin cytoskeleton, a dynamic network of actin filaments that is found throughout the cytoplasm. In addition to passive crosslinker proteins, actin filaments are crosslinked by myosin motor proteins that transduce the chemical energy of ATP hydrolisis into forces exerted on the polymer network. In general, a coordinated combination of the forces generated by active actin polymerization and by myosin motors powers cell shape changes and motility. However, there are different modes of cell motility [Mierke 2015], based on distinct types of cellular protrusions, such as lamellipodia, filopodia, and blebs (Fig. 1.2), which involve different patterns of force transmission to the extracellular medium.

The so-called mesenchymal motility mode is based on the extension of lamellipodia, which are wide, actin-rich protrusions at the cell's leading edge. At the front of the lamellipodium, actin polymerization pushes the membrane forward, and gives rise to a retrograde flow of actin monomers. Behind the leading edge, the lamellipodium attaches to the extracellular matrix by means of focal adhesion complexes based on integrin proteins. By engaging the retrograde flow of actin, focal adhesions exert traction forces on the extracellular matrix, thus propelling the lamellipodium forward. Inside the cell, focal adhesions at the front

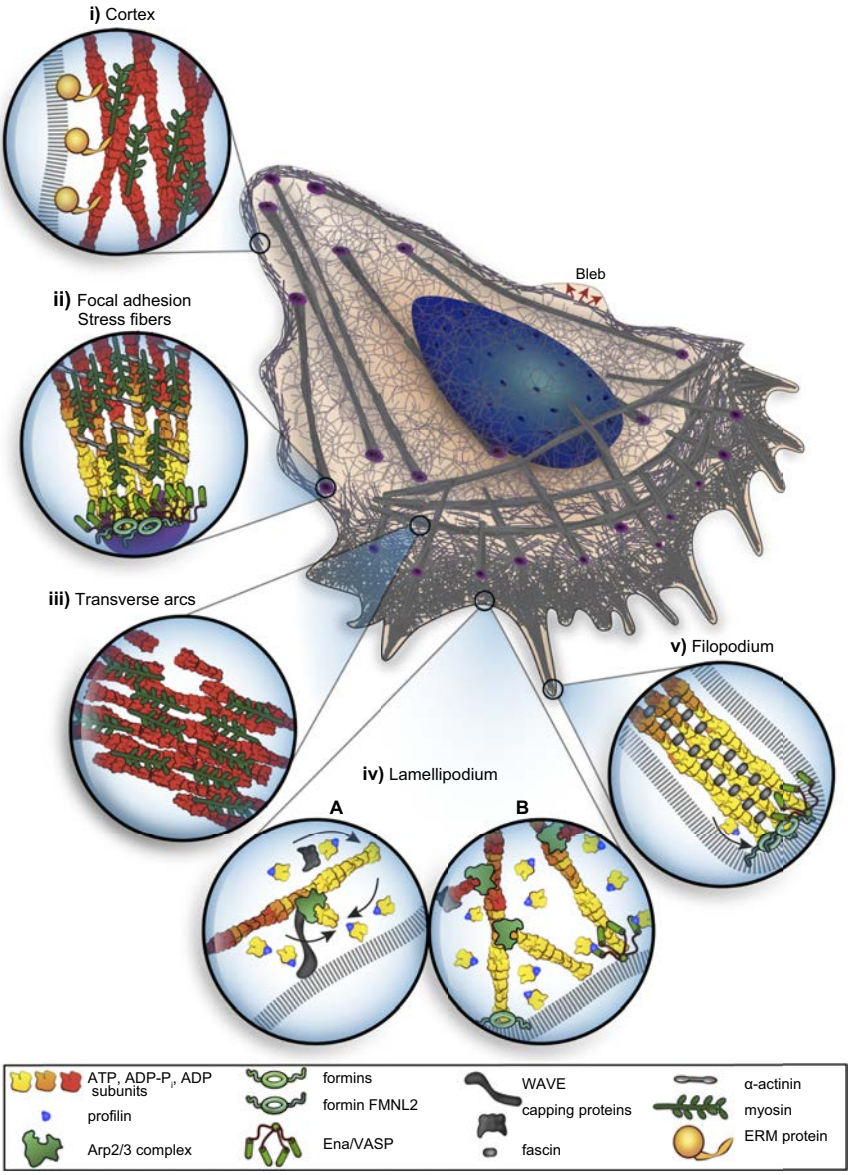

Figure 1.2 | Sketch of different actin structures in a migrating cell. From [Blanchoin 2014].

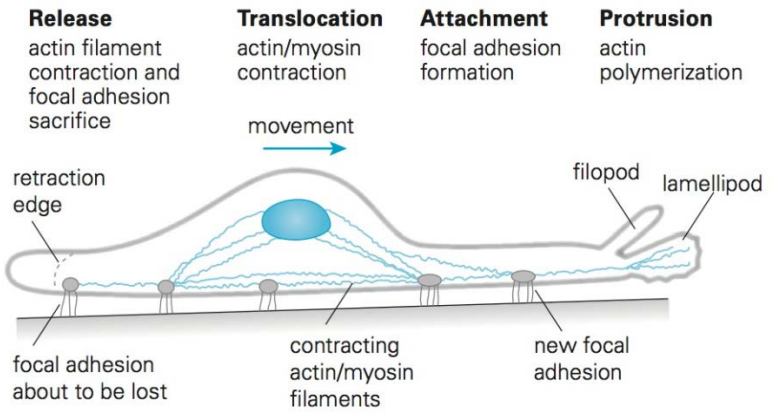

Figure 1.3 | Major steps of mesenchymal cell motility. From [Jacobs 2013].

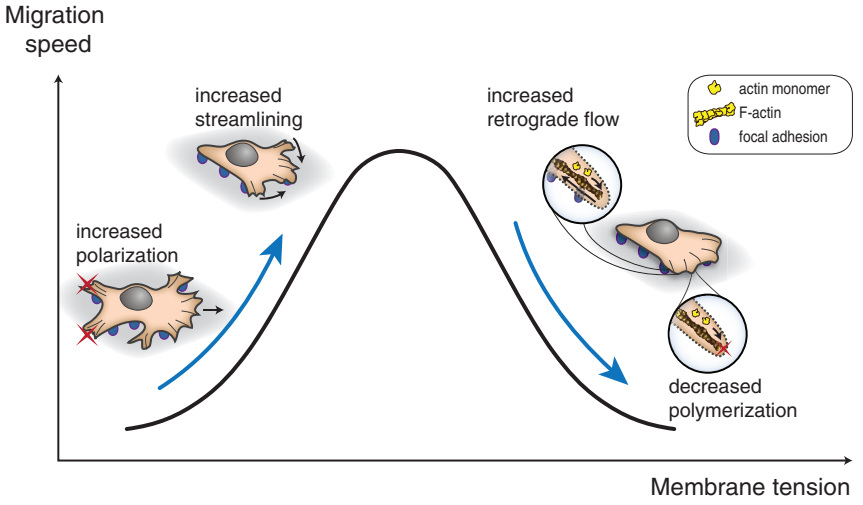

Figure 1.4 | Effects of membrane tension on mesenchymal cell motility. Membrane tension can concentrate and confine lamellipodial protrusions at the cell front, hence increasing migration speed and persistence. However, large membrane tensions can also hinder actin polymerization and promote the retrograde flow of the lamellipodium, thus decreasing cell migration speed. From [Sens 2015].

and the back of the cell are connected through bundles of actin filaments called stress fibers. These fibers sustain myosin-generated tension that couples the lamellipodium extension with the detachment and retraction of the cell's trailing edge (Figs. 1.2 and 1.3) [Ananthakrishnan 2007, Jacobs 2013, Blanchoin 2014]. Thus, traction forces on the extracellular matrix point inwards both at the front and at the back of the cell, forming an asymmetric force dipole in the migration direction [Fournier 2010, Tanimoto 2014].

During mesenchymal cell migration, the membrane remains generally attached to the underlying actin cytoskeleton, adapting to cell shape as a glove. However, the membrane does not simply act as a passive participant in cell motility. In fact, through its interplay with cytoskeletal dynamics, membrane mechanics is a key regulator of mesenchymal migration [Diz-Muñoz 2013, Sens 2015]. For example, membrane tension can confine protrusions at the cell front, thereby favouring cell polarization and directed motion, but also oppose actin polymerization, thus hindering lamellipodial extension (Fig. 1.4) [Sens 2015]. Even front-back gradients in membrane tension and in membrane-cortex adhesion have been proposed to be implicated in the directed migration of some cell types [Sens 2015, Lieber 2015].

The membrane is even more instrumental in the other major mode of cell motility. The so-called amoeboid motility does not necessarily rely on polymerization-driven protrusions, but it often uses membrane blebs. Blebs are balloon-like protrusions arising from a local detachment of the cell membrane from the underlying actin cortex. The cell cortex is a thin dense layer of the actin cytoskeleton located underneath the membrane, bound to it by specific linker proteins, and maintained under tension by myosin-generated forces (Fig. 1.2). Consequently, membrane detachment can be induced by a local myosin-generated contraction of the cortex, which gives rise to a local increase in intracellular pressure that breaks membrane-cortex bonds. Alternatively, the membrane can detach because of a local decrease in the concentration of membrane-cortex linker proteins. Moreover, a bleb can also form because of a local rupture of the cortex. Cortical rupture can be due either to a local dissassembly of actin or to a local increase in cortical tension sufficient to tear the cortex (Fig. 3.2) [Charras 2008c].

As in mesenchymal motility, membrane mechanics has a major influence on bleb-based motility. First, membrane-cortex adhesion is locally regulated to polarize blebbing in the migration direction. In addition, membrane tension and bending rigidity limit the pressure-driven expansion of the bleb. Finally, the mechanical properties of the membrane were also thought to play an essential role in bleb nucleation [Sens 2015] — a view that we challenge in Chapter 3.

Upon bleb expansion, a new actin cortex reassembles beneath the unbound membrane. Then, to translocate the cell body, traction forces must be exerted on the extracellular matrix. However, the mechanisms of traction force transmission in bleb-based motility are less well known than in its lamellipodial counterpart. In nonconfined environments, the bleb must adhere to the extracellular matrix to move the cell body forward, similarly to the lamellipodium in mesenchymal migration. However, in confined environments, a blebbing cell can move even in the absence of specific cell-matrix adhesions, relying only on nonuniform friction forces of

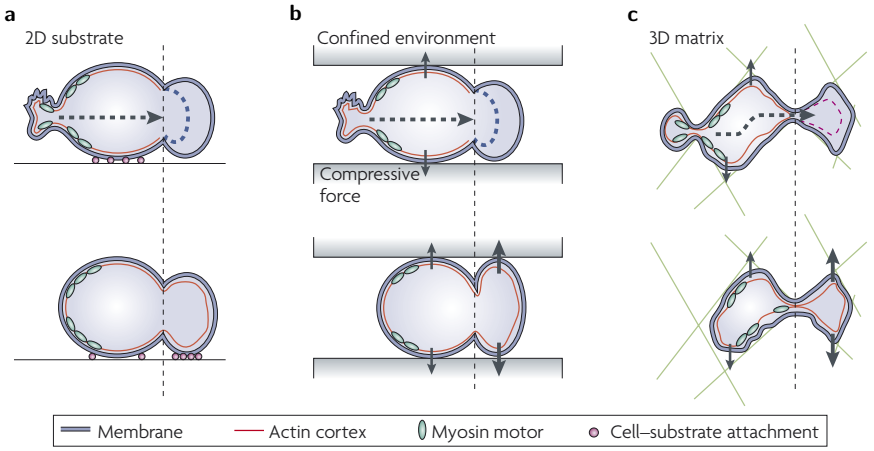

Figure 1.5 | Force transmission mechanisms in bleb-based motility. a, In nonconfined environments, the bleb must form specific adhesions to the substrate to allow the cell body to stream forward (dashed arrows). **b,** In contrast, in confined environments, cells can move by exerting normal forces on the environment (solid arrows), which generates nonuniform friction forces that enable cell body translocation even in the absence of specific adhesions. **c,** When migrating through extracellular matrices, cells can combine both mechanisms of force transmission. Thin dashed lines indicate the position of the leading edge before bleb formation. From [Charras 2008c].

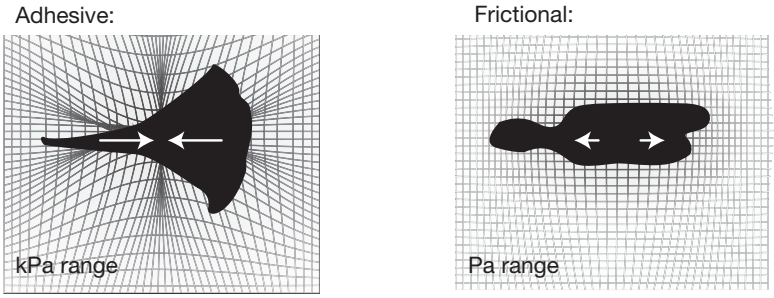

Figure 1.6 | Traction patterns in adhesive versus frictional force transmission. Adhesive cells exert large, inward-pointing traction forces that cause contractile dipolar deformations on the environment. In contrast, nonadhesive cells exert weaker, outwards-pointing traction forces that cause extensile dipolar deformations. From [Bergert 2015].

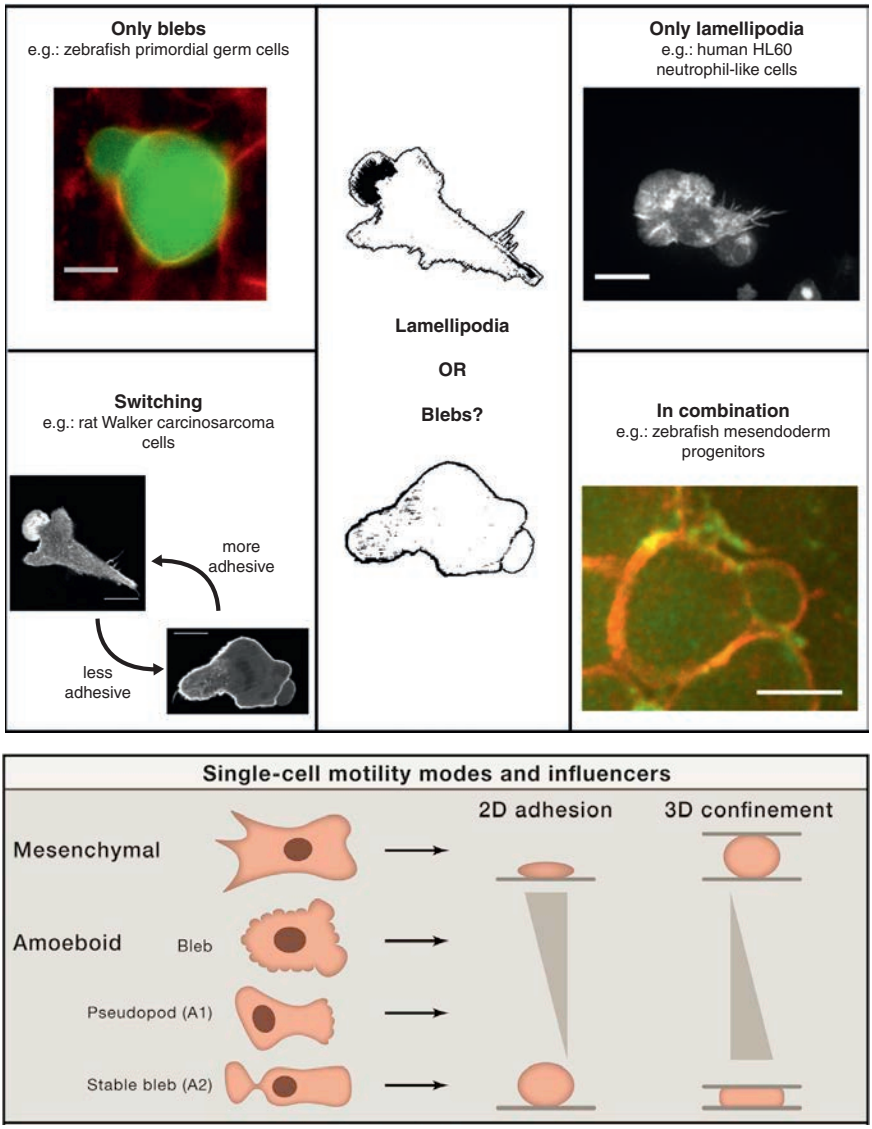

Figure 1.7 | Cell motility modes, their interplay, and the influence of external parameters. (Top) Examples of migrating cells forming exclusively blebs, exclusively lamellipodia, switching between protrusion types or forming both protrusion types in combination. From [Paluch 2013]. (Bottom) Influence of cell-substrate adhesion and confinement on the mode of cell motility. From [Welch 2015].

nonspecific origin. In this case, the cell can push on the extracellular environment perpendicularly to the direction of motion and squeeze the cell body forward — a force-transmission mechanism known as chimneying (Fig. 1.5) [Charras 2008c, Paluch 2013, Paluch 2016]. With respect to adhesion-based migration, traction forces exerted by chimneying cells are much weaker and point outwards (Fig. 1.6) [Bergert 2015].

The mesenchymal motility mode is used by cell types such as fibroblasts and some cancer cells, whereas the different variants of amoeboid motility are primarily employed by cell types such as amoeba or embryonic cells. However, both motility modes can coexist in most cell types, which rely on either mode under different environmental conditions. For example, confined and/or poorly adhesive environments favour amoeboid motility, including blebbing. In fact, to adapt to changing environmental conditions, cells can rapidly switch motility modes or even combine different kinds of protrusions, such as lamellipodia and blebs (Fig. 1.7) [Paluch 2006, Yoshida 2006, Lämmermann 2009, Diz-Muñoz 2010, Bergert 2012, Paluch 2013, Tozluoğlu 2013, Tyson 2014, Liu 2015, Ruprecht 2015, Welch 2015, Mierke 2015, Diz-Muñoz 2016, Ibo 2016]. Therefore, rather than acting as independent migration strategies, the different motility modes can cooperate to endow cells with versatile migration abilities.

1.3 Collective cell migration

In many biological settings, eukaryotic cells do not move individually but rather in groups. Migration of cell groups is key to many physiological and pathological processes in different contexts, such as embryonic development, tissue morphogenesis and renewal, wound healing, angiogenesis, and tumor spreading [Friedl 2009, Rørth 2009, Weijer 2009, Scarpa 2016, Mayor 2016, Hakim 2017]. In all these processes, groups of cells migrate in a coordinated manner. In addition to coordinating their migratory behaviour, collectively migrating cells move more efficiently than if they migrated individually. Therefore, collective cell migration is cooperative, implying that, rather than simply being a response of many cells to an externally imposed signal, coordinated migration emerges from intercellular communication. Such a communication is generally based on a combination of biochemical signaling and direct mechanical interactions [Mayor 2016, Rørth 2012, Rørth 2009].

Different cell types exhibit distinct modes of collective migration, with different degrees of coordination and involving from a few cells to whole tissues [Friedl 2012, Rørth 2012, Theveneau 2013]. For example, cells of the so-called mesenchymal phenotype, such as neural crest cells, fibroblasts, embryonic, and immune-system cells, are generally motile and they do not form stable intercellular adhesions. Nonetheless, they can migrate directionally as a group, coordinating their migration both by means of transient cell-cell contacts and via extracellular biochemical signaling (Fig. 1.8) [Weijer 2009, Theveneau 2013, Scarpa 2016, Hakim 2017].

In contrast, epithelial cells establish stable cell-cell adhesions based on cadherin proteins, thus assembling into cohesive tissues. In vivo, epithelial cells usually

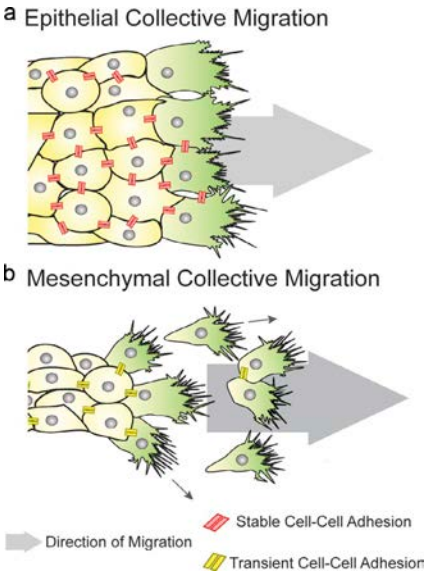

Figure 1.8 | Epithelial and mesenchymal collective migration. a, Epithelial cells move as cohesive groups, maintaining cell-cell adhesions. **b,** Mesenchymal cells can migrate directionally as a noncohesive group. Transient cell-cell contacts and intercellular signaling coordinate the directed migration. From [Scarpa 2016].

form cell monolayers that cover organs, acting as protective physical barriers. On the so-called basal side, epithelial monolayers are adhered to the underlying connective tissue via a basement membrane of extracellular matrix, to which they attach via integrin-based adhesions. In turn, the outer part of the epithelial layer, called the apical side, is exposed to the external environment, which is often a fluid-filled luminal space, such as the interior of the digestive and respiratory tracts, excretory ducts, blood vessels, lymph glands, etc. As a consequence of these different environments, epithelial cells feature an apico-basal polarity, which directs transport of nutrients and other substances across the epithelial layer. Therefore, in mature epithelia, cells do not normally exhibit any polarity along the plane of the basement membrane (planar polarity), and hence they remain mostly nonmotile (Fig. 1.9) [Alberts 2008].

Similar to motility modes, cell migratory phenotypes are plastic, and many cell types can exhibit more mesenchymal or more epithelial traits under different conditions. In fact, in development and in metastatic invasion, cells undergo the so-called epithelial-mesenchymal transition (EMT), whereby epithelial cells lose their apico-basal polarity and intercellular junctions to gain a planar polarity and become migratory (Fig. 5.15) [Thiery 2009, Lim 2012b, Nieto 2013]. Rather than being a sharp transition, the EMT is currently seen as a multistep phenotypic evolution that encompasses several collective behaviours of tissues. For example, when exposed to lateral free space, epithelial cells can migrate collectively as cohesive groups (Fig. 1.8). Recent investigations of the molecular programs governing the collective migration of epithelial monolayers have led to propose that it constitutes an intermediate state in the complex spectrum of epithelial-mesenchymal behaviours [Revenu 2009, Friedl 2012, Nieto 2016, Hakim 2017].

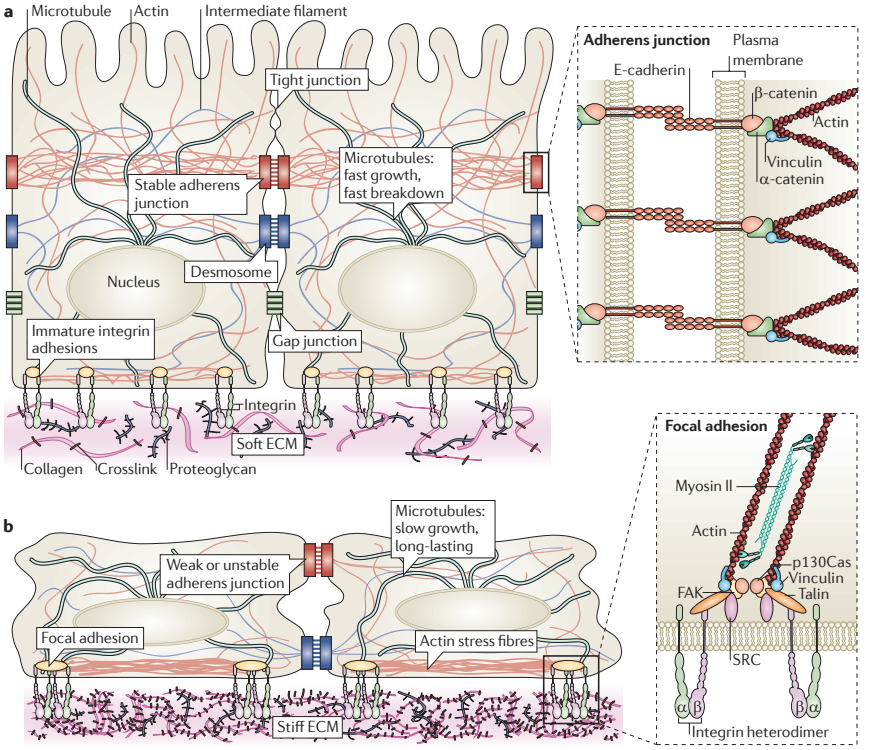

Figure 1.9 | Cell-cell and cell-matrix adhesions in epithelial monolayers. Epithelial monolayers are cohesive tissues in which cells are tightly adhered by different adhesions complexes, mainly adherens junctions based on cadherin proteins. Cells are also attached to the underlying extracellular matrix by integrin-based adhesion complexes. Inside the cell, the actin cytoskeleton connects to both adhesion systems, thus allowing cells to exert cell-cell and cell-substrate forces, and to sense the mechanical properties of the environment. In particular, mechanosensing feeds back on the architecture of the cytoskeleton and adhesions themselves. **a,** On softer matrices, epithelial cells are generally taller, and they feature actomyosin belts connected to stable adherens junctions on their apical sides. **b,** In contrast, in stiffer matrices, epithelial cells are shorter and exhibit stronger focal adhesions connected by stress fibers on their basal side. From [DuFort 2011].

Epithelial migration is constrained by the maintenance of cell-cell adhesion, which ensures the physical integrity of the epithelium. Consequently, unlike mesenchymal migration, the collective migration of epithelial cells involves force transmission not only to the extracellular matrix but also among cells through cell-cell junctions (Fig. 1.10) [Trepat 2011, Vedula 2013, Saw 2014]. Thereby, active forces generated by the actomyosin cytoskeleton propagate through the tissue, making it a mechanically coherent structure. Moreover, the actin cytoskeleton also mediates a mechanical crosstalk between cell-cell and cell-matrix adhesions

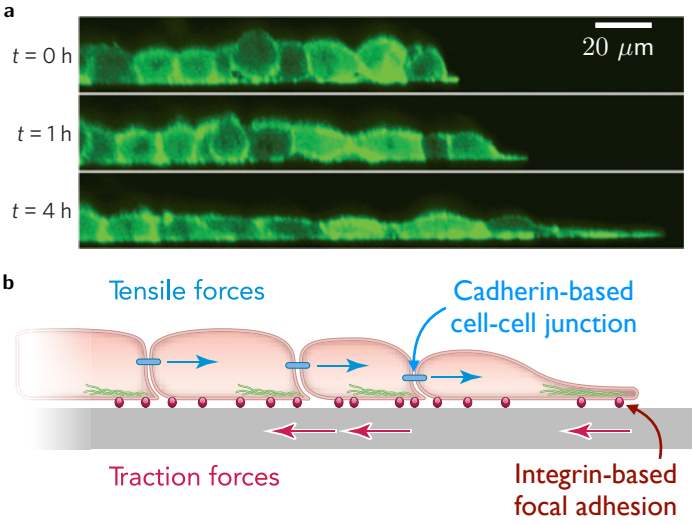

Figure 1.10 | Collective polarization in epithelial migration. a, Transversal view of an in vitro monolayer of LifeAct MDCK cells that is exposed to free space at $t = 0$ h. Adapted from [Serra-Picamal 2012]. **b,** Sketch of cell shape, as well as traction and intercellular forces during the collective cell migration of an epithelial monolayer. Adapted from [Vedula 2013].

that is involved in the transduction of mechanical signals from the environment (Fig. 1.9). Hence, the interplay between both adhesion systems has a major role in the regulation of the collective migration of epithelial cell groups [Collins 2015].

To start migrating, epithelial cells must acquire a planar polarity. At a free edge of an epithelial monolayer, the lateral asymmetry of cadherin-based intercellular junctions acts as a cue for the loss of the so-called contact inhibition of locomotion (Fig. 6.13). Thereby, the cells at the border of the monolayer polarize, developing lamellipodia that exert traction forces to migrate towards free space. As a consequence, cells immediately behind the leading edge are pulled through cell-cell junctions, and hence they also polarize and start migrating by extending so-called cryptic lamellipodia underneath the cells in front. This collective polarization process continues to involve further rows of cells, finally leading to the coordinated migration of the entire monolayer (Figs. 1.10 and 6.13) [Theveneau 2013, Vedula 2013, Ladoux 2016, Hakim 2017].

The last decade has seen a great advance in the understanding of the mechanics of collective cell migration, mainly due to the possibility to measure the traction and intercellular force fields during the spreading of epithelial monolayers in vitro. Such measurements are often performed using the so-called traction-force microscopy, which infers the traction forces by measuring the cell-induced deformations of an artifical substrate of controlled elastic properties [Serra-Picamal 2015]. In addition, the stress field in the cell monolayer can be obtained from the force balance condition with the traction forces, in what is known as monolayer stress

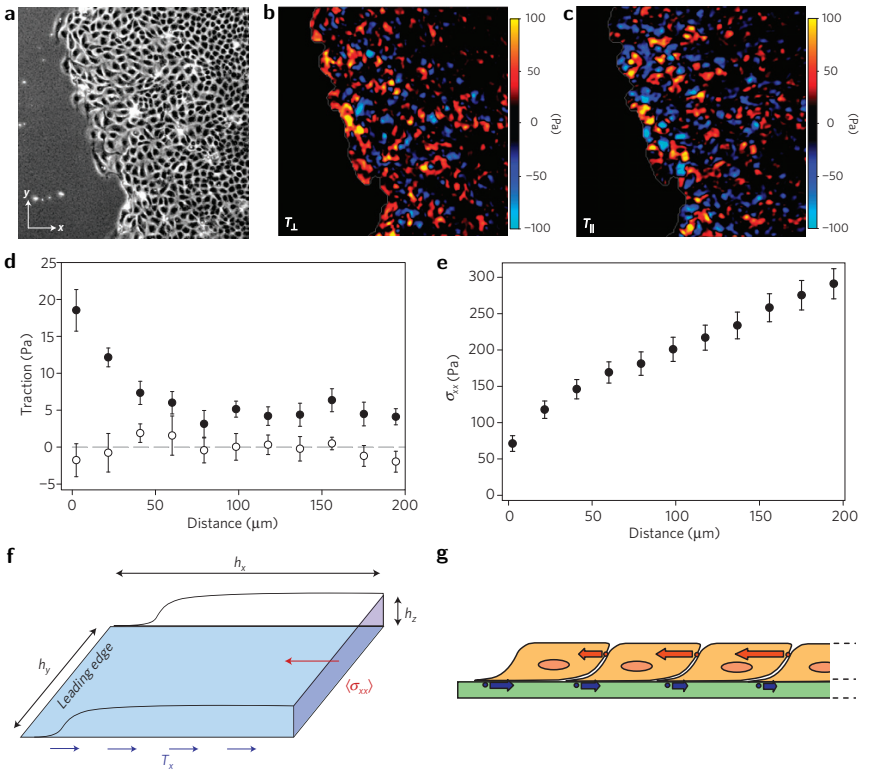

Figure 1.11 | Mechanics of epithelial collective cell migration. **a,** Phase-contrast image of a collectively migrating monolayer of MDCK cells. **b, c,** Components of the traction force normal and parallel to the monolayer edge. The field of view is 750 μm $\times$ 750 μm. **d,** Profiles of the components of the traction force, averaged along the direction parallel to the edge. The average normal component (filled symbols) decays from the edge towards the interior of the monolayer, whereas the average parallel component (open symbols) vanishes all across the tissue. **e,** Profile of the average xx-component of the stress tensor in the cell monolayer, obtained by integrating the x-component of the tractions. **f,** Sketch of the computation of the stress component from the traction forces. **g,** Sketch of the traction (blue) and intercellular stress (red) profiles in the cell monolayer. Adapted from [Trepat 2009].

microscopy[1]. These measurements revealed that, during collective cell migration, traction forces are mainly directed along the direction of expansion, and that their magnitude is the largest at the monolayer edge, decaying towards the bulk of the tissue. As a consequence, stress builds up in the monolayer, increasing from the

[1] In general, solving the force balance condition to infer the stress field requires some assumptions on the rheology of the monolayer [Tambe 2011, Tambe 2013, Zimmermann 2014b]. To overcome this issue, an inference method based on Bayesian inversion has been recently proposed to obtain the stress field without explicit rheological assumptions [Nier 2016].

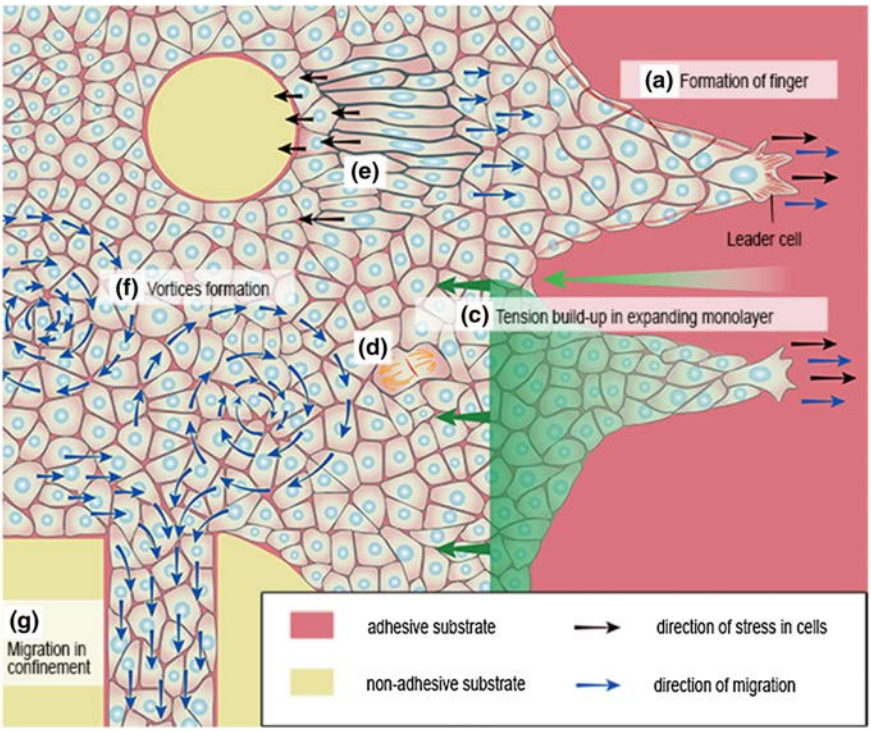

Figure 1.12 | Emergent dynamical phenomena in spreading epithelial monolayers. From [Saw 2014].

edge towards the interior (Fig. 1.11, see also Fig. 6.15) [Trepat 2009, Hakim 2017].

Complementarily to the measurement of forces, flow fields during epithelial spreading have also been characterized. These measurements reveal flow fields with spatial correlations over distances much larger than cell size, implying that collective motion occurs in the monolayer. In fact, a number of emergent dynamical phenomena have been found in spreading epithelial monolayers, including swirl-like motion, multicellular protrusions at the leading edge, mechanical waves, velocity oscillations, etc. (Fig. 1.12) [Hakim 2017, Vedula 2013, Saw 2014].

All these phenomena require cell-cell adhesion to allow for stress transmission through the tissue, and occur on timescales at which the monolayer should exhibit a fluid rheology. The elastic stress built by tissue deformations relaxes through several processes occurring at different timescales, including the turnover of cytoskeletal and adhesive structures, cell shape changes, cell rearrangements, cell extrusion, and cell division and death (Fig. 1.13) [Guillot 2013, Wyatt 2016, Khalilgharibi 2016]. Clear illustrations of the fluid behaviour of tissues on appropriate timescales include cell sorting or the fusion of cell aggregates (Fig. 1.14), for which both surface tension and viscosity have been measured [Gonzalez-

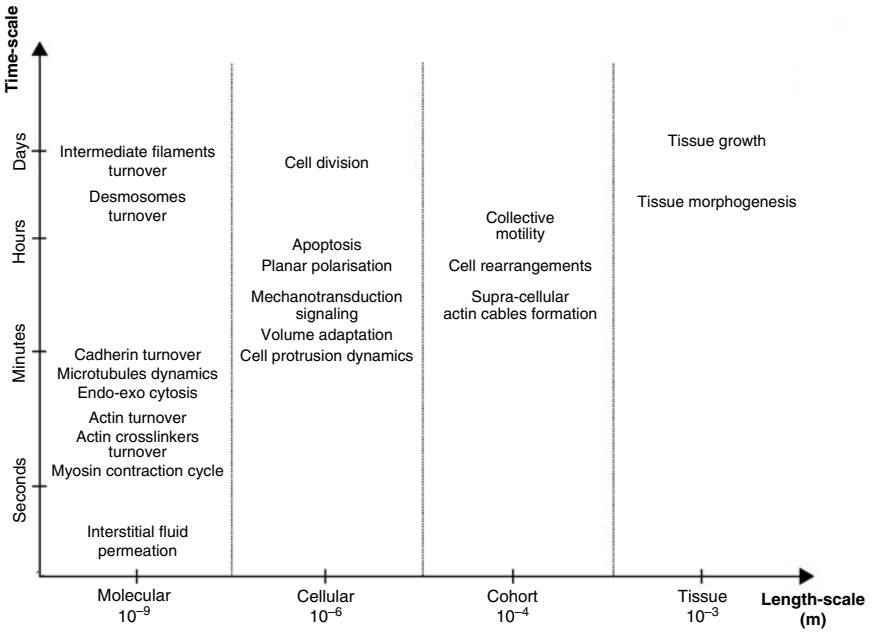

Figure 1.13 | Processes contributing to tissue rheology, classified by length-scale and timescale. Adapted from [Khalilgharibi 2016].

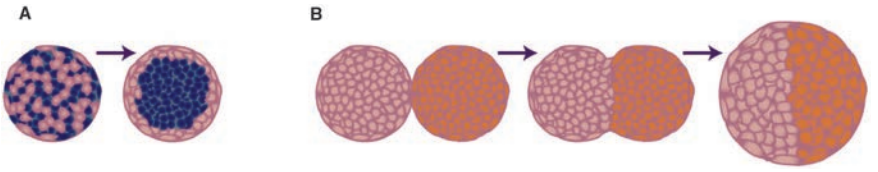

Figure 1.14 | Fluid behaviour of cell aggregates. a, Two different cell populations sort out according to their interfacial tensions. **b,** When brought into contact, two aggregates of the same cell line fuse into a larger spherical aggregate. From [Gonzalez-Rodriguez 2012].

Rodriguez 2012]. Furthermore, cell aggregates also spread into cell monolayers and viceversa, in the equivalent of the wetting and dewetting processes of conventional fluids. Both the wetting transition and the spreading dynamics are strongly influenced by cell-cell and cell-substrate adhesion, which in turn depends on both the chemical and mechanical properties of the substrate (Figs. 6.1 to 6.3) [Gonzalez-Rodriguez 2012, Hakim 2017].

Finally, collective cell migration in epithelial monolayers is mainly driven by oriented active forces, such as traction or anisotropic cellular contractility. Thus, at least mechanically, epithelial monolayers exhibit an in-plane orientational order that

arises from the planar polarity of individual cells. Therefore, collectively migrating cell monolayers can be thought of as nematic liquid crystal phases. Indeed, continuum models of epithelial monolayers as active liquid crystals have been proposed [Lee 2011b, Lee 2011a, Doostmohammadi 2015, Lee 2016, Notbohm 2016, Blanch-Mercader 2017b, Saw 2017, Kawaguchi 2017, Hirst 2017, Morita 2017, Blanch-Mercader 2017a, Yabunaka 2017b, Hakim 2017] — an approach that we follow in our models in Chapters 6 and 7.

1.4 Active polar gels in cell and tissue biology

In this section, we introduce some of the main concepts underpinning the theory of active polar gels. This theory provides a general framework to describe the hydrodynamics of several biological systems in the context of cells and tissues. Examples include mixtures of cytoskeletal filaments and molecular motors, the mitotic spindle, the lamellipodium, the cell cortex, and epithelial monolayers [Joanny 2011, Prost 2015]. In this thesis, the theory of active gels plays two different roles. On the one hand, in Chapter 4, we contribute to the theory itself by deriving the constitutive equations from a mesoscopic model inspired by some biological systems. On the other hand, in Chapters 6 and 7, we employ the formalism of active gel theory to model the spreading of epithelial monolayers, focusing on the wetting transition and on the stability of the monolayer front.

Active polar gels are soft materials made out of polar microscopic constituents that are transiently crosslinked and maintained out of equilibrium by internal processes that continuously transduce energy. The development of hydrodynamic equations that describe the large-scale and long-time dynamics of such materials was motivated by the behaviour of the actin cytoskeleton [Kruse 2004, Kruse 2005, Jülicher 2007, Joanny 2009, Prost 2015]. Thus, as an illustration, here we detail the features that make the actin cortex (see Fig. 1.2) one of the most promiment examples of a biological active polar gel.

- Physical gel: Actin filaments in the cortex are crosslinked by a variety of proteins like fascin, actinin, and filamin. These proteins bind to actin filaments mainly via dipolar interactions or ionic bonds. Therefore, the links between actin filaments have binding energies comparable to the thermal energy k_BT, much smaller than typical energies of covalent bonds[2]. Hence, actin crosslinks are relatively short-lived, lasting hundreds of seconds at most, which makes it a physical gel[3]. As a consequence, the actin cortex exhibits the mechanical response of a viscoelastic fluid with a relatively short relaxation time.

[2] The fact that the energy scale of the interactions between the constituents of a system is comparable to the thermal energy is one of the defining features of soft materials.

[3] The term physical gel refers to polymeric materials with transient crosslinks due to weak interactions, as opposed to the term chemical gel, which denotes a material with almost permanent crosslinks due to strong covalent bonds [Jones 2002].

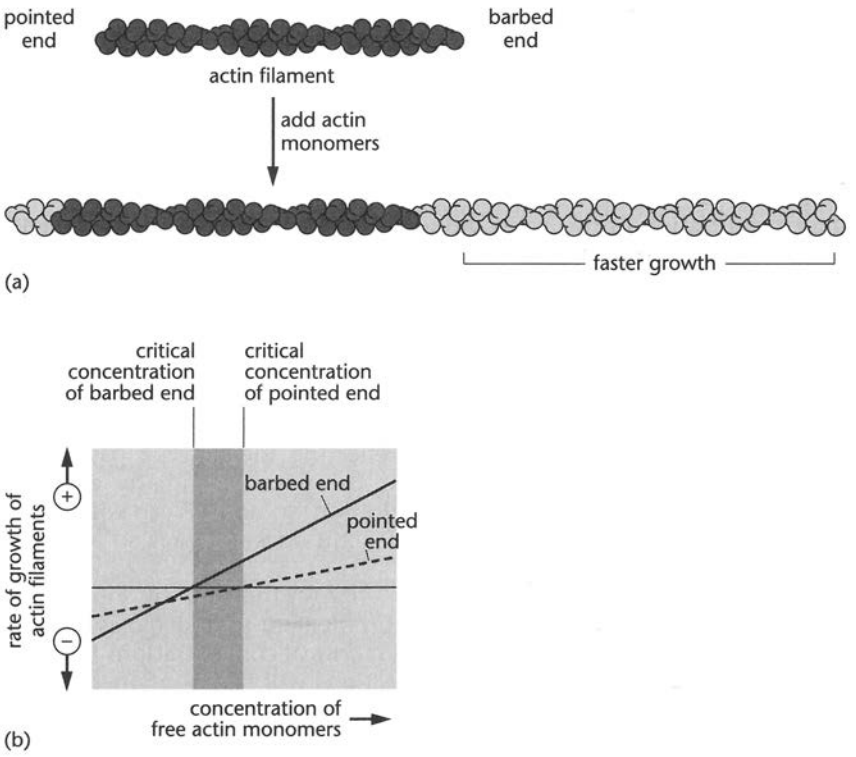

Figure 1.15 | Polar nature of actin filaments. a, An actin filament is a right-handed helix of actin monomers, which makes both ends distinct. As a consequence, actin polymerizes faster at the barbed end than at the pointed end. **b,** Polymerization rates of each end of actin filaments as a function of the concentration of free actin monomers. The darker region indicates the regime in which the filament grows at the barbed end and shrinks at the pointed end, generating a net flux of polymerized actin known as treadmilling. From [Bray 2001].

- Polar material: Due to both excluded-volume interactions and crosslinking, cortical actin filaments typically feature an average alignment (see Fig. 1.2). Thus, the cell cortex can form a nematic liquid crystal of actin filaments. In addition to their tendency to align, individual actin filaments are polar, meaning that their head and tail are distinct. Such asymmetry stems from the properties of actin monomers, which assemble into right-handed helicoidal filaments. Hence, the two ends of an actin filament are different, being termed barbed and pointed ends. As a consequence of their structural polarity, actin filaments generally polymerize at different rates at each end (Fig. 1.15a). Under physiological conditions, monomers are typically added at the barbed end and lost at the pointed end. This fact generates a net flux of polymerized actin towards the direction of the barbed end, which is known as actin

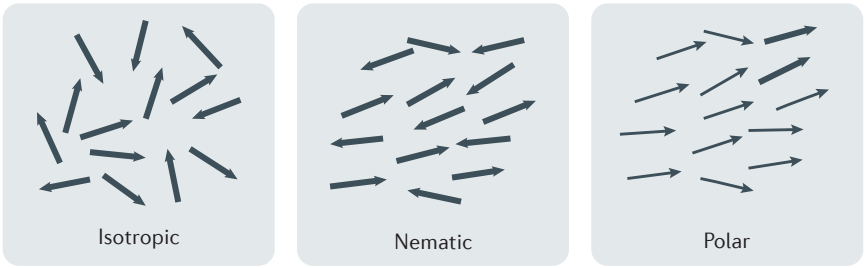

Figure 1.16 | Orientational order in polar materials. Polar constituents (arrows), such as cytoskeletal filaments or polarized cells, may form isotropic phases lacking orientational order. Otherwise, the constituents align to form either a nematic phase, if they point in either direction along a given axis, or a polar phase, if they point in a common direction. From [Needleman 2017].

treadmilling (Fig. 1.15b). When actin polymerization is locally induced, such as at the leading edge of a lamellipodium (Fig. 1.2), the ensuing treadmilling is directed towards the cell interior, thus yielding the cytoskeletal network globally polar. In contrast, the cortex or other actin structures such as stress fibers need not form a polar phase, but they can form a nematic phase as well (see Fig. 1.16).

- Active material: Actin polymerization requires the hydrolysis of ATP, so that this chemical reaction must be maintained out of equilibrium for polymerization to proceed. Therefore, this process is active, allowing for the chemical energy of ATP hydrolysis to be transduced into mechanical work if polymerization acts against some load. In addition, cortical actin filaments are not only crosslinked by passive proteins but also by aggregates (mini-filaments) of myosin molecular motors. These proteins transduce the chemical energy of ATP hydrolisis into mechanical work employed to pull on the filaments they are bound to. These active pulling forces drive relative slidings between the filaments, which finally gives rise to the contractile behaviour of the cortex (Fig. 2.2). In all, the cell cortex is an active material.

Beyond the specificities of each particular system, the hydrodynamic theory of active polar gels provides a general description of the long-time, large-scale behaviour of any system having the symmetries of an active polar gel. As a hydrodynamic theory, it gives the evolution of slow variables[4] describing macroscopic observables, whereas the system-specific microscopic details are encoded in the values of a set of phenomenological transport coefficients. Slow or hydrodynamic variables are generally either densities of conserved quantities, or order-parameter fields arising from broken continuous symmetries [Chaikin 1995, Forster 1990, Re-

[4] Slow variables are those featuring a slow evolution at long wavelengths, meaning vanishing relaxation rates at short wave-vectors, $\lim_{q\to 0} \omega(q) = 0$.

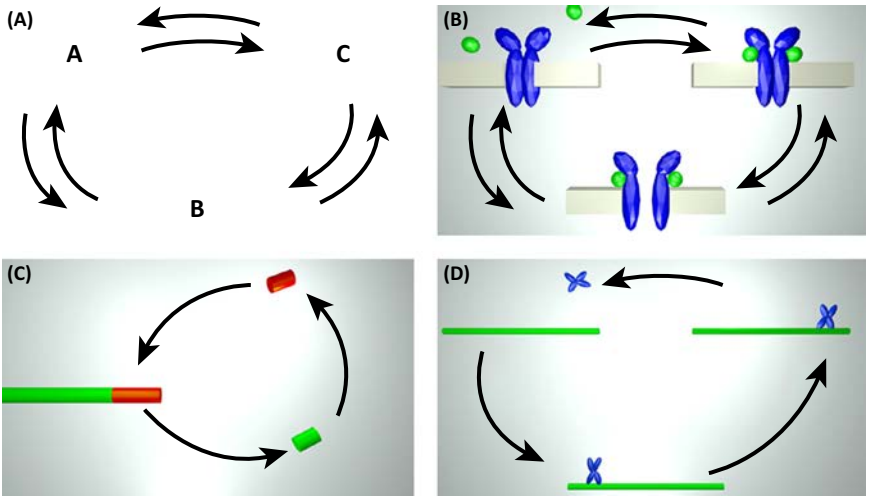

Figure 1.17 | Detailed balance and its violation. a, In equilibrium, all microscopic processes obey detailed balance: the rate of any of them equals the rate of its reverse, so that no net cycles through series of states (A, B, and C) are possible. **b,** Example of an equilibrium situation for a transmembrane receptor exhibiting three states: closed, closed-bound to a ligand, and open-bound to a ligand. **c,** Energy transduction by a hydrolysis reaction allows detailed balance to be violated during active polymerization. Thus, a net cycle occurs from monomer-reactant (red), to monomer incorporated in the polymer (red tip), to monomer-product (green). **d,** Similarly, the action of molecular motors violates detailed balance. In this case, a net cycle occurs from the free motor, to motor bound to a cytoskeletal filament, to motor bound at a different position along the filament. From [Needleman 2015].

ichl 1998, Mazenko 2006]. For example, in a simple fluid, mass, energy, and linear momentum are conserved quantities. Consequently, their respective densities are slow variables described by hydrodynamic theories. A polar medium features two additional slow variables associated to its orientational degrees of freedom. Indeed, orientational order stems from a broken continuous symmetry, namely rotational invariance. Thus, the rotational degrees of freedom of the macroscopic director or polarity field experience no restoring force, and hence they are slow variables. For the same reason, the modulus of the director or polarity vector is also a slow variable in the vicinity of the isotropic-nematic/polar transition[5]. Finally, an active medium features yet another broken symmetry, namely time reversal. This symmetry is broken by microscopic processes that are favoured over their time-reverse (absence of detailed balance, Fig. 1.17), which is enabled by the continuous transduction of energy at the molecular level. In turn, continuous energy transduction requires

[5] In most applications, the system under consideration is far from the transition, for example deep in the ordered phase. Therefore, the modulus of the polarity is often considered a fast variable, and hence is taken as fixed. However, in our model of epithelial spreading in Chapters 6 and 7, the modulus of the polarity is a slow variable.

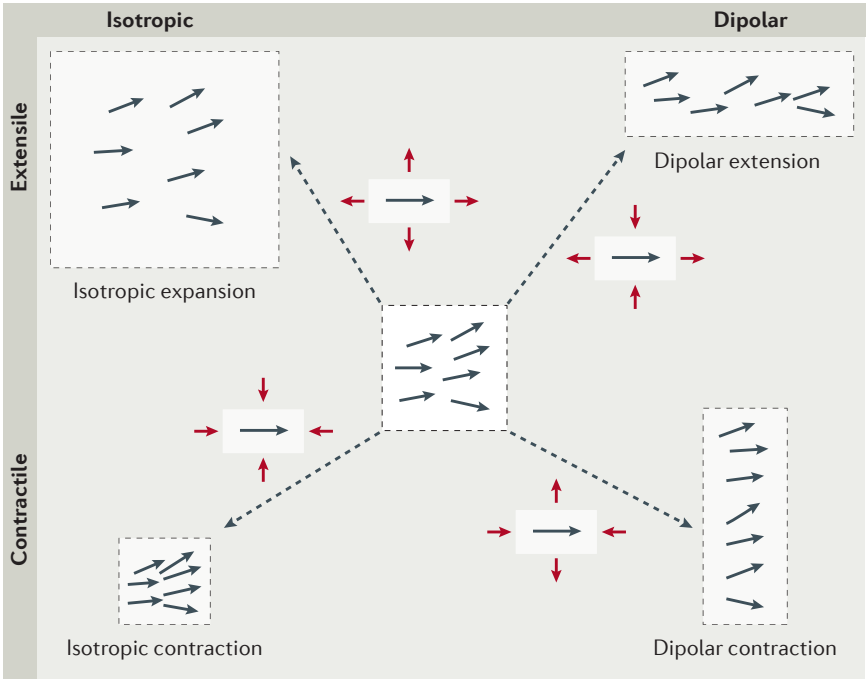

Figure 1.18 | Symmetries and signs of active stresses. In an active polar gel, active stresses (red arrows) can either be isotropic or dipolar, and either contractile or extensile. The schematic depicts the deformations produced by each type of active stress on a volume element with a given polarity. Grey arrows stand for the microscopic polar constituents of the system. From [Needleman 2017].

maintaining the corresponding chemical reaction, such as ATP hydrolisis, out of equilibrium. Hence, the number of reactant molecules is a conserved quantity, and therefore its density is also a slow variable.

Once all slow variables have been identified, the framework of linear irreversible thermodynamics [de Groot 1984, Le Bellac 2004, Balian 2007] provides a systematic procedure to derive the hydrodynamic equations [Kruse 2004, Kruse 2005, Jülicher 2011, Marchetti 2013]. First, one writes a coarse-grained free energy of the system in terms of the slow variables. For example, for an active polar medium, the free energy includes the kinetic energy associated to flows, the energy of the distortions of the orientational order, and the energy of the chemical reaction. Then, one must identify generalized fluxes and forces, which are thermodynamically conjugated pairs of variables. Next, one establishes constitutive equations that phenomenologically give the generalized fluxes as linear combinations of the generalized forces, which are valid in the linear response regime. The matrix of coefficients of these linear combinations is known as the Onsager matrix, and its coefficients are directly related to transport coefficients. The constitutive equations

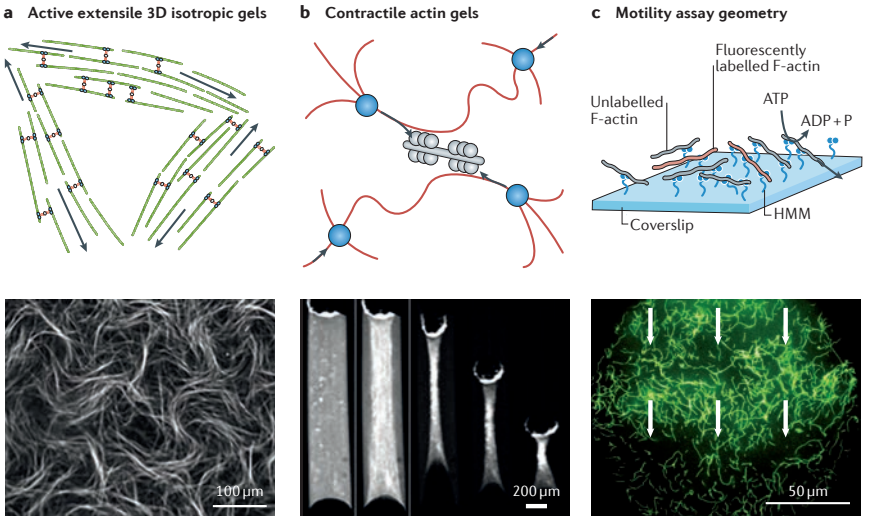

Figure 1.19 | Examples of synthetic realizations of active gels from cytoskeletal components. a, At intermediate densities, a mixture of microtubule bundles (green) and clusters of kinesin motors (red and blue) forms an active fluid. The extensile active stresses generated by the motors induce spontaneous turbulent-like flows. **b,** Myosin molecular motors (grey) generate contractile active stress in actin filament networks (red), which may result in a global contraction of the network. The sequence of images shows the spontaneous contraction of an actomyosin network attached to two oil droplets. **c,** In the so-called motility assay, a carpet of myosin molecular motors (blue) attached to a surface propels actin filaments on top (grey and red). At high densities, filaments form an active polar liquid that can exhibit travelling density waves (white arrows). From [Needleman 2017].

must respect the symmetries of the system. For instance, in an isotropic system such as a simple liquid, forces of a given tensorial rank can only contribute to a flux of the same rank. In contrast, anisotropic systems such as liquid crystals feature a vectorial or tensorial field — the polarity vector or the nematic tensor — that allows fluxes and forces of different tensorial rank to be coupled. These symmetry restrictions are generically known as the Curie principle. Similarly, the time-reversal symmetry of the microscopic dynamics (microscopic reversibility) yields specific relations between the Onsager coefficients, which are known as Onsager reciprocity relations. Finally, the complete hydrodynamic equations of the system are obtained by combining the constitutive equations with the continuity equations that encode the corresponding conservation laws.

In an active gel, the activity, namely the maintenance of a nonvanishing chemical potential difference of the energy-transducing reaction, enables the generation of active stresses. If the system has orientational order, either nematic or polar, both isotropic and dipolar active stresses may be generated[6] (Fig. 1.18). The sign of the

[6]The dipolar active stress term can be obtained as the average force density in a collection of

active stress coefficients is not dictated by symmetries or thermodynamic stability, but rather by the interactions between the microscopic constituents. Accordingly, active stresses can be either contractile or extensile (Fig. 1.18). Both cases are observed in different biological active gels (see Fig. 1.19). The generation of active stresses is the most important new feature of active gels as compared to passive systems. In fact, active stresses generally lead to spontaneous flows (see Fig. 1.19a), in one of the most striking consequences of activity [Simha 2002, Voituriez 2005, Jülicher 2007, Jülicher 2011, Marchetti 2013].

The ability of such a general theory, only based on symmetries and conservation laws, to capture collective behaviours in cells and tissues can be limited by several factors [Jülicher 2007, Prost 2015]. First, in a given biological system, the long-wavelength limit of a hydrodynamic description may not be sufficient due to strong spatiotemporal variations. Second, nonlinear effects are relevant in many biological systems, so that restricting to the linear response regime may not be sufficient to account for some specific phenomena. Finally, couplings to other fields such as biochemical regulators, the surrounding flow, etc. may be required. However, despite these limitations, active gel theory has been applied to many biological systems, in which it has successfully predicted and captured a number of striking effects. Hence, it stands out as a powerful theoretical framework to build hydrodynamic models that provide insight into a broad range of biological phenomena.

noninteracting microscopic force dipoles [Simha 2002].

Part I

Membrane-cortex adhesion and bleb nucleation

2

Membrane-cortex adhesion

Contents

Abstract

Controlling the adhesion between the cell membrane and the cytoskeletal cortex is crucial for many cellular processes, such as cytokinesis or blebbing. In this chapter, we present a model for membrane-cortex adhesion that couples the binding kinetics of linker proteins to membrane motion. Considering a flat membrane, we explicitly predict the critical pressure difference for membrane-cortex detachment, as well as the adhesion energy. Both quantities depend on the myosin-generated cortical tension. With these predictions, we discuss micropipette suction experiments that induce membrane-cortex detachment, from which we estimate the cortical tension of *Dictyostelium discoideum* cells. Then, we extend the model to include membrane

undulations, accounting for hydrodynamic interactions. Under the approximation of fast linker kinetics, we predict the spatiotemporal correlations of membrane undulations. Using these predictions, we suggest how fluctuation spectroscopy experiments could probe membrane-cortex adhesion.

2.1 Introduction

Eukaryotic cells are enclosed by the plasma membrane, which mediates communication with the extracellular environment. Beneath it, there is a thin layer of cytoskeleton called cortex (Fig. 2.1), which is a dynamic network of crosslinked actin filaments and myosin molecular motors that provides rigidity to the cell and drives cell shape changes (Fig. 2.2). The membrane and the cortex are attached by means of specific linker proteins (Fig. 2.3) [Sheetz 2001] such as talin [Tsujioka 2012], the ezrin/radixin/moesin (ERM) family [Tsukita 1999, Fritzsche 2014, Rouven Brückner 2015], or even myosin I molecular motors [Dai 1999b, Nambiar 2009]. Together, the membrane-cortex composite constitutes the main structural component of the cellular interface. Therefore, the control of membrane-cortex adhesion is crucial for many cellular processes, such as cell division or cell motility. In fact, membrane-cortex detachments, which often give rise to balloon-like protrusions of unbound membrane called blebs, are often a sign of apoptosis [Mills 1998, Coleman 2001]. However, blebs also appear during cytokinesis [Sedzinski 2011], and they are specifically used for cell motility [Fackler 2008, Charras 2008c, Paluch 2013].

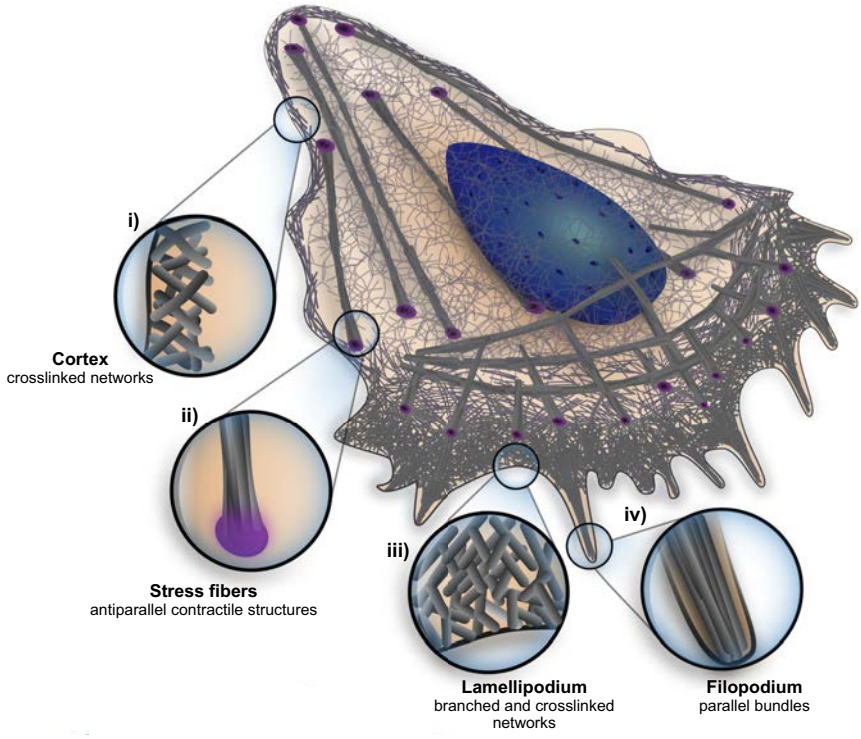

Figure 2.1 | Sketch of the actin cytoskeleton of a migrating cell. Insets show the architecture of the major structures. From [Blanchoin 2014].

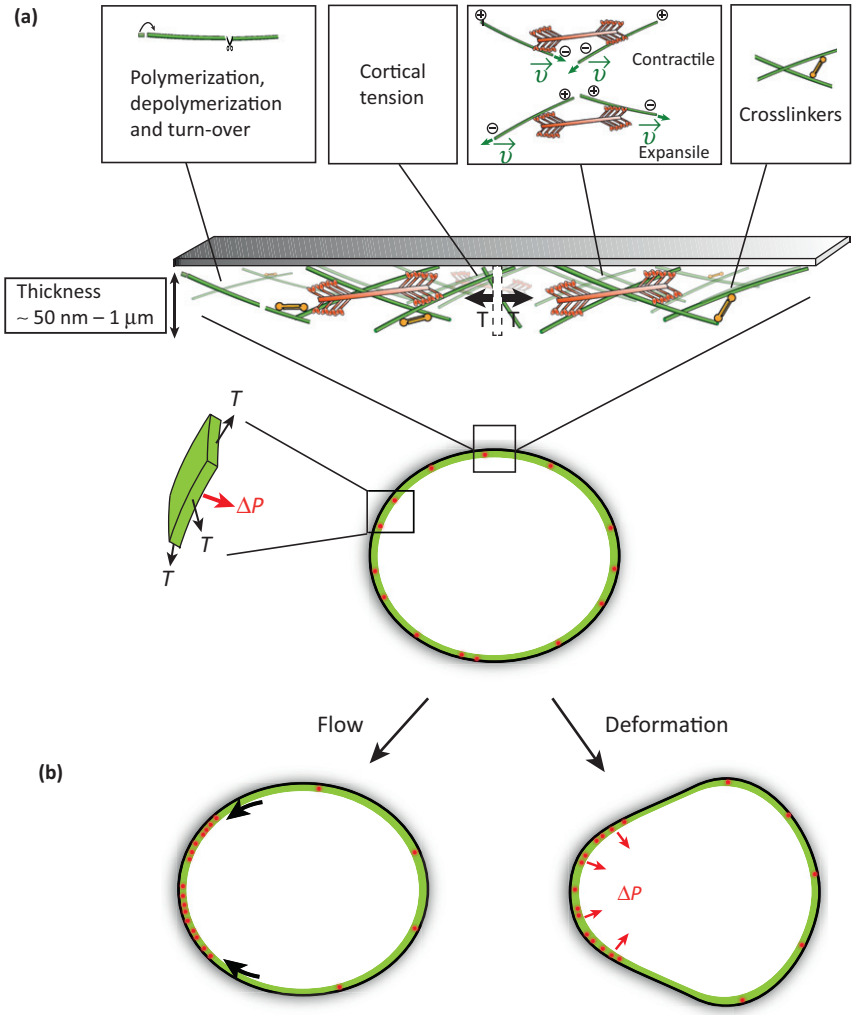

Figure 2.2 | Cortical tension and cell shape. **a,** The cortex is a layer of crosslinked actin filaments (green) undergoing continuous turnover. Myosin II motors assembled in mini-filaments (red) exert sliding forces on the filaments, giving rise to cortical tension. Under curvature, cortical tension gives rise to hydrostatic pressure in the cytoplasm. **b,** Gradients of myosin-generated cortical tension may generate flows of cortical material and polarize the cell. Then, pressure gradients can drive cell shape changes and motion. From [Salbreux 2012].

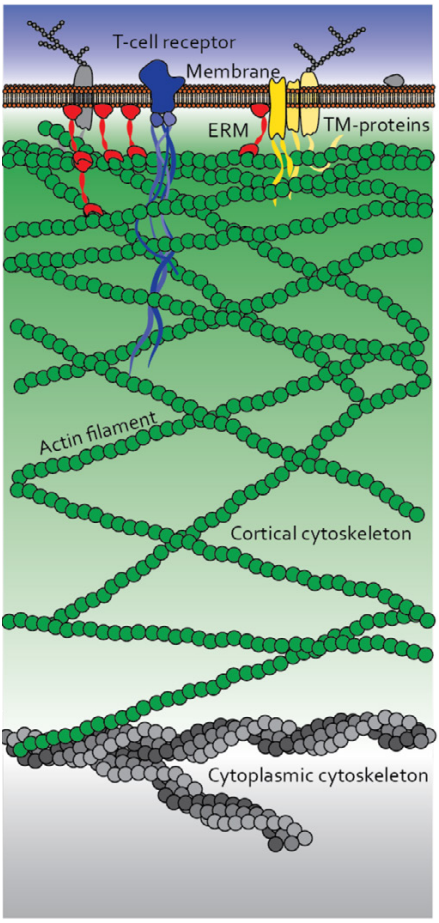

Figure 2.3 | Sketch of the membrane-cortex interface. The lipid bilayer membrane (orange) is attached to cortical actin filaments (green) via ERM proteins (red). The actin cortex extends into the cytoplasm and is further interconnected with the cytoplasmic cytoskeleton (grey). The maximal density of actin cortical filaments could as well be at the center of the cortical layer, instead of at its outer border as depicted. Ligand receptors in the membrane, e.g. a T-cell receptor (blue), bind to cytoplasmic protein partners, such as their signaling domains, that span into the cortex. Other transmembrane (TM) proteins (yellow) associate with ERM proteins, forming obstacles and barriers in the membrane. From [Clausen 2017].

Membrane-cortex detachment can be triggered internally by an increase of myosin-generated cortical tension [Charras 2008b, Tinevez 2009, Loiseau 2016]. Alternatively, it can be externally induced by micropipette suction [Merkel 2000, Rentsch 2000, Brugués 2010, Campillo 2012, Sliogeryte 2014] or osmotic shocks [Sliogeryte 2014]. These studies show that a sufficiently large pressure difference across the cell interface induces membrane detachment. Thus, membrane-cortex bonds constantly bear stress due both to osmotic pressure and to cortical tension (Fig. 2.4). Therefore, whether the membrane remains adhered or detaches from the cortex is determined by the interplay between molecular kinetics of the linker proteins and mechanical forces at the cell interface. Inspired by cell adhesion, previous theoretical work considered the lifetime of linker-mediated adhesions under force [Erdmann 2004a, Erdmann 2004b, Schwarz 2013]. Futher research studied the adhesion of an elastic membrane to a substrate via ligand-receptor complexes. Mainly by means of simulations, different studies focused on several facets of this problem, such as the formation of adhesion domains, the role of active

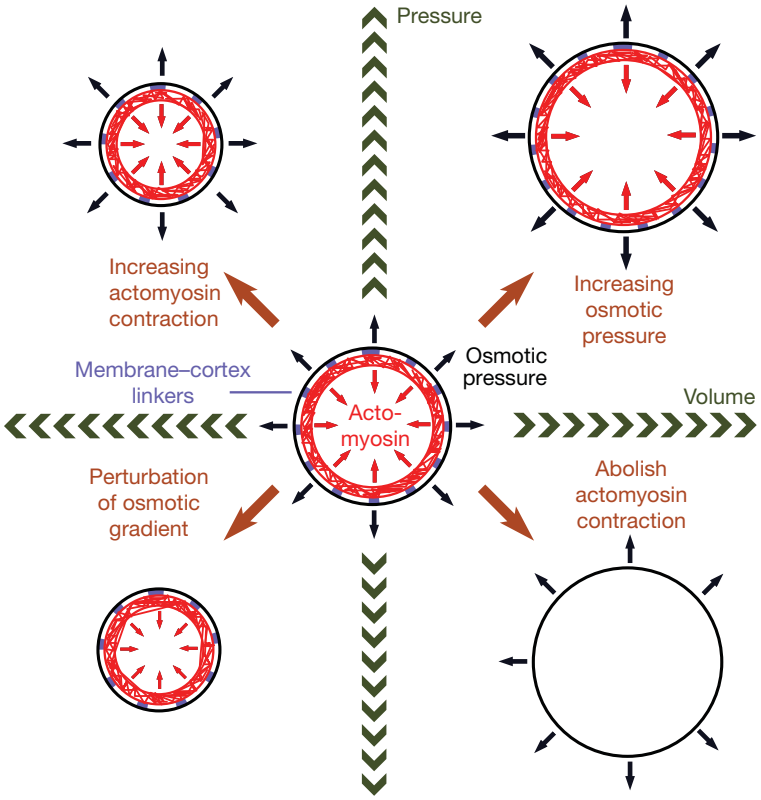

Figure 2.4 | Osmotic pressure and cortical tension set cell pressure and volume. Membrane-cortex bonds (purple) resist the outwards osmotic pressure on the membrane (black) and the inwards myosin-generated cortical tension (red). Changes in osmotic equilibria and/or actomyosin contractility modify cell pressure and volume. From [Stewart 2011].

processes, the role of membrane undulations on linker binding cooperativity and, hence, on the unbinding transition, etc [Weikl 2009]. However, the linker-mediated adhesion of a membrane under pressure, as in membrane-cortex adhesion, has been less studied. Thus, this chapter addresses this problem, with the goal to investigate the role of cortical tension and intracellular pressure on membrane-cortex adhesion.

In Section 2.2, we present a model for adhesion based on the force-dependent binding kinetics of membrane-cortex linker molecules. The coupling between linker kinetics and membrane motion leads to a membrane-cortex unbinding transition at a critical pressure difference across the membrane. By means of a force balance at the cell interface, we predict how the critical pressure and the membrane-cortex adhesion energy depend on cortical tension. In Section 2.3, we discuss micropipette aspiration experiments that estimate the critical suction pressure, which, by means of our model, allows estimating the cortical tension. Then, in Section 2.4 we generalize

the model to include membrane undulations. To this end, we couple linker kinetics to membrane mechanics and hydrodynamics. Under the approximation of fast linker kinetics, we study the fluctuations of an adhered membrane, giving explicit predictions for the structure factor and the power spectrum in different limits. Finally, we suggest fluctuation spectroscopy experiments to probe membrane-cortex adhesion by measuring the statistical properties of membrane undulations.

2.2 Kinetic model for membrane-cortex adhesion

We propose a model that considers a nearly flat membrane subject to a pressure difference f and attached to an underlying flat cortex by a uniform surface density of bonds ρ_b, smaller than the total density of molecular linkers ρ_0 (Fig. 2.5a). These linkers are modeled as Hookean springs of elastic constant k that form membrane-cortex bonds at a rate k_{on} and unbind at a rate k_{off}. Thus, the dynamics of the density of bonds is given by

$$\frac{d\rho_b}{dt} = k_{\text{on}}\left[\rho_0 - \rho_b\right] - k_{\text{off}}\rho_b, \tag{2.1}$$

where $\rho_0 - \rho_b$ is the surface density of unbound linkers. Linker unbinding is likely to be a thermally activated process, for which we assume a Bell force-dependent rate [Bell 1978, Evans 2007]

$$k_{\text{off}}(u) = k_{\text{off}}^0 e^{\beta k u \delta}, \tag{2.2}$$

where u is the stretching of the linker, δ is a characteristic length of the binding energy landscape, and $\beta = (k_B T)^{-1}$ (Fig. 2.5b). In contrast, the binding process is likely active, for example induced by ATP hydrolysis. Hence, we assume a force-independent[1] binding rate k_{on}. Note that these rates do not obey the detailed balance condition, implying that the binding kinetics is not in thermodynamic equilibrium.

Now, the linker stretching u is coupled to the motion of the membrane, which is pushed outwards by the pressure difference f and pulled inwards by membrane-cortex bonds. Thus, the dynamics of the linker stretching is given by

$$\mu\frac{du}{dt} = f - ku\rho_b, \tag{2.3}$$

where μ is a friction coefficient per unit area. The dissipation associated to small membrane displacements is dominated by the contribution of the flow of cytosol through the cortical meshwork (Appendix 2.A). Thus, the friction coefficient is estimated by $\mu \sim \eta h/\xi^2$, where $\eta \sim 0.003 - 0.2$ Pa·s is the cytosol viscosity [Charras 2008b], $h \sim 0.1 - 1$ μm is the cortex thickness [Salbreux 2012, Clark 2013, Clausen 2017, Chugh 2017], and $\xi \sim 10 - 50$ nm is the cortex mesh size [Charras 2008b, Charras 2009, Moeendarbary 2013, Bovellan 2014] (Table 2.1). We

[1] Assuming a Bell force-dependent binding rate gives no qualitative change of the results.

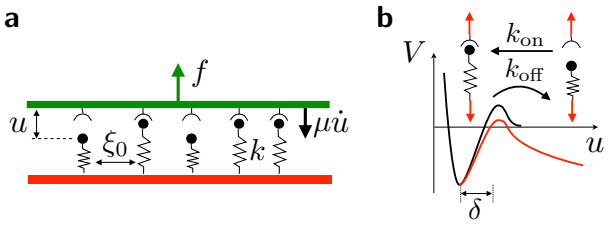

Figure 2.5 | Kinetic model for membrane-cortex adhesion. a, Linker molecules (black) at an average spacing $\xi_0 = \rho_0^{-1/2}$ bind the membrane (green) to the cortex (red). The membrane is pushed outwards by the pressure difference f, and pulled back by the elastic force of the bound linkers. Membrane motion is damped by an effective viscous friction, Eq. (2.3). **b,** Sketch of the binding energy landscape of the linkers V along the stretching direction [Evans 2007]. Linkers bind at a force-independent rate $k_{\rm on}$, and unbind at a force-dependent rate $k_{\rm off}$. Stretching the linker (red arrows) decreases the energy barrier between the bound and unbound states (red curve), hence increasing the unbinding rate, Eq. (2.2).

assume that linker kinetics is faster than membrane displacements, so that the free membrane between bonds does not have time to inflate between linker binding events. In this limit, the membrane features a nearly flat shape, and membrane-mediated spatial correlations between linkers are negligible.

The equilibrium solutions to the coupled Eqs. (2.1) to (2.3) are implicitly given by

$$f = k u_{\rm eq} \rho_b^{\rm eq}(u_{\rm eq}), \qquad \rho_b^{\rm eq}(u) = \frac{\rho_0}{1 + k_{\rm off}^0/k_{\rm on}\, e^{\beta k u \delta}}. \tag{2.4}$$

To identify the combinations of parameters that determine the stability of the system, we define dimensionless variables:

$$\bar{\rho}_b \equiv \frac{\rho_b}{\rho_0}, \qquad \bar{u} \equiv \frac{u}{u_0}, \tag{2.5}$$

where $u_0 \equiv k_B T/(k\delta)$ is the characteristic amplitude of stretching fluctuations of bound linkers. In terms of these dimensionless variables, the equilibrium solutions read

$$\bar{\rho}_b^{\rm eq} = \frac{\alpha}{\bar{u}_{\rm eq}}, \qquad \bar{u}_{\rm eq} = \alpha\left(1 + \chi e^{\bar{u}_{\rm eq}}\right), \tag{2.6}$$

where we have defined the dimensionless parameters

$$\chi \equiv \frac{k_{\rm off}^0}{k_{\rm on}}, \qquad \alpha \equiv \frac{f}{\rho_0 k_B T/\delta}. \tag{2.7}$$

The function $\bar{u}_{\rm eq} - \alpha\left(1 + \chi e^{\bar{u}_{\rm eq}}\right)$ has a maximum at $\bar{u}_{\rm eq} = \bar{u}_m$. Hence, the equilibrium solution Eq. (2.6) can only exist if the maximum is positive, $\bar{u}_m - \alpha\left(1 + \chi e^{\bar{u}_m}\right) > 0$, which implies $\alpha < \alpha^*$, where α^* is the solution of

$$\alpha^* e^{1+\alpha^*} = \chi^{-1}. \tag{2.8}$$

Symbol	Description	Estimate	Reference
η	cytosol viscosity	0.01 Pa·s	[Charras 2008b]
ξ	cortex mesh size	30 nm	[Bovellan 2014]
h	cortex thickness	0.2 μm	[Clausen 2017]
μ	membrane friction coefficient	20 Pa·s/μm	this work
k_{on}	linker binding rate	10^4 s^{-1}	[Rognoni 2012]
k_{off}^0	free linker unbinding rate	10 s^{-1}	[Rognoni 2012]
δ	characteristic bond length	1 nm	[Evans 2001]
k	linker stiffness	0.1 pN/nm	
ξ_0	average linker spacing	0.1 μm	
ρ_0	surface density of linkers	100 μm^{-2}	$\rho_0 = \xi_0^{-2}$
R	cell radius	10 μm	[Merkel 2000]
γ	membrane tension	$5 \cdot 10^{-5}$ N/m	[Tinevez 2009]
κ	membrane bending ridigity	10^{-19} J	[Dai 1999a]
γ_c	cortical tension	5 mN/m	this work
ρ_t/ρ_0	fraction of talin bonds	$5 - 40\%$	this work

Table 2.1 | Estimates of model parameters. Parameter values are expected to vary significantly for different cell types and experimental conditions. Typical ranges of parameter values are given in the text and the references. Therefore, the values shown in this table must be taken as illustrative estimates. Nevertheless, the cortical tension and the fraction of talin bonds in *Dictyostelium discoideum* do not depend on the parameter estimates, but are directly estimated by applying Eq. (2.17) to the experimental data in [Merkel 2000].

Therefore, an equilibrium solution exists only for pressures

$$f < f^* = \alpha^* \rho_0 \frac{k_B T}{\delta}, \tag{2.9}$$

so that f^* is the critical pressure for membrane-cortex detachment. In conclusion, we have predicted a membrane-cortex unbinding transition that is independent of the mechanical properties of the membrane and of the linkers, but rather fully specified by the linker binding kinetics. For example, taking $\chi \sim 10^{-3}$ [Rognoni 2012] (Table 2.1), we estimate $\alpha^* \sim 4.5$, namely that the critical force per link is ~ 4.5 times the thermal force per link $k_B T/\delta$. Then, taking $\delta \sim 1$ nm [Evans 2001, Evans 2007] (Table 2.1), we estimate a critical force per link $f^*/\rho_0 \sim 18$ pN, which, for an average linker spacing $\xi_0 = \rho_0^{-1/2} \sim 0.1$ μm [Lieber 2015], gives a critical pressure $f^* \sim 2$ kPa. Moreover, we may also estimate the critical bond density, ρ^*. Solving $\bar{u}^* = \alpha^* \left(1 + \chi e^{\bar{u}^*}\right)$, we get $\bar{u}^* \sim 5.2$, which yields $\bar{\rho}_b^* = \alpha^*/\bar{u}^* \sim 0.85$. We emphasize that parameter values may vary significantly for different linker proteins [Fritzsche 2014], cell types, and experimental conditions. Consequently, these estimates serve illustration purposes rather than providing robust parameter values.

Finally, we define the membrane-cortex adhesion energy as the reversible work required to stretch the linkers from their equilibrium stretching up to their critical

stretching u^*. Under quasistatic conditions, the bond density follows the stretching at equilibrium, $\rho_b^{\text{eq}}(u)$, as given by Eq. (2.4), so that

$$w(u_{\text{eq}}) = \int_{u_{\text{eq}}}^{u^*} \rho_b^{\text{eq}}(u)\, ku\, du = \rho_0 k \int_{u_{\text{eq}}}^{u^*} \frac{u}{1+\chi e^{\beta k u \delta}} du. \tag{2.10}$$

Equation (2.10) shows that the adhesion energy depends on the equilibrium stretching of the linkers u_{eq}, which does not only depend on linker kinetics but also on the actual force balance at the membrane-cortex interface. Thus, in particular, the equilibrium linker stretching, and hence the adhesion energy, will depend on the cortical tension.

2.3 Discussion of micropipette experiments

Micropipette aspiration allows combining pressure perturbations of controlled intensity and section (Fig. 2.6), with biochemical or genetic perturbations of myosin activity, linker density, or cortex architecture. Consequently, among other techniques such as tether pulling (Fig. 2.6) [Sens 2015], micropipette aspiration has been widely used to study the mechanics of membrane-cortex adhesion [Dai 1999b, Rentsch 2000, Merkel 2000, Brugués 2010, Campillo 2012, Sliogeryte 2014]. In this section, we apply our model to micropipette experiments, employing it to probe cortical activity from measurements of the critical suction pressure for membrane-cortex detachment.

In a curved membrane, the stress f on the membrane includes the normal contribution of the membrane tension γ (Fig. 2.6). Thus, for a spherical cell of radius R, the force balance on the membrane at mechanical equilibrium reads

$$\Delta P - \frac{2\gamma}{R} = f_{\text{cell}} = k u_{\text{cell}} \rho_b^{\text{eq}}(u_{\text{cell}}), \tag{2.11}$$

where $\Delta P = P_{\text{cell}} - P_{\text{ext}}$, and $\rho_b^{\text{eq}}(u)$ is given by Eq. (2.4). In turn, on the cortex, the elastic force of the linkers balances the normal component of the cortical tension γ_c (Fig. 2.6):

$$f_{\text{cell}} = \frac{2\gamma_c}{R}. \tag{2.12}$$

Hence, the total force balance at the cell interface reads

$$\Delta P = \frac{2}{R}(\gamma + \gamma_c) \equiv \frac{2\gamma_{\text{cell}}}{R}, \tag{2.13}$$

where we have defined a cell surface tension $\gamma_{\text{cell}} = \gamma + \gamma_c$ that adds membrane and cortical tensions.

Now, suctioning with a micropipette at pressure P_p locally alters the force balance at the aspirated region of radius R_p (Fig. 2.6):

$$P_{\text{cell}} - P_p = \frac{2\gamma}{R_p} + f_p, \tag{2.14}$$

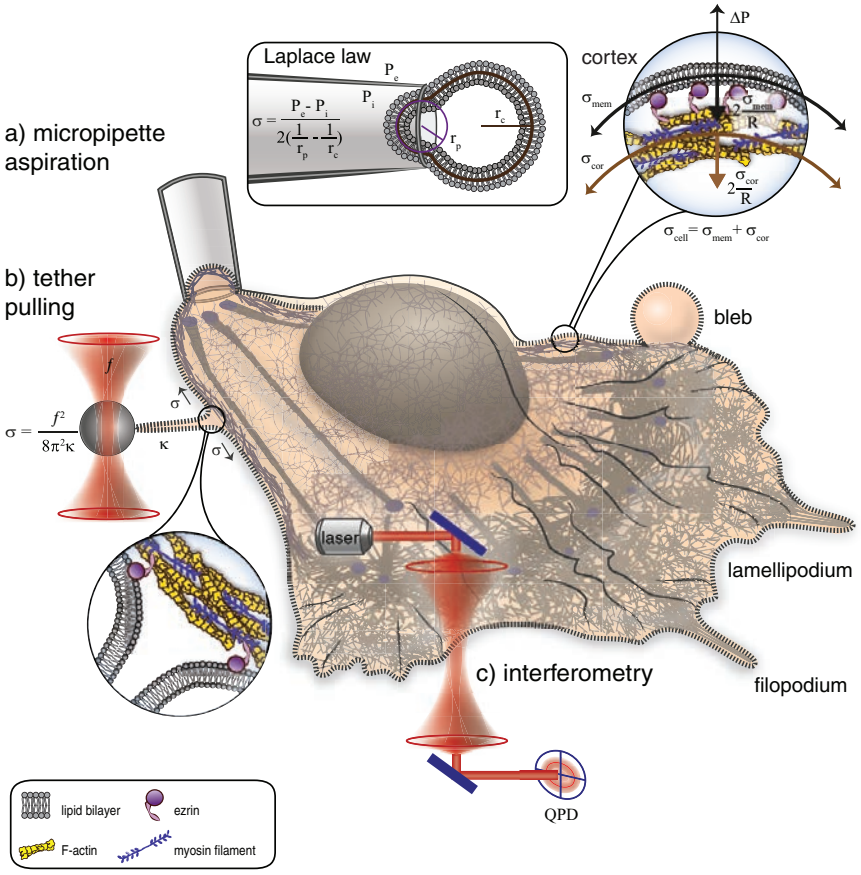

Figure 2.6 | Probing the cell membrane. Sketch of the main experimental techniques to study membrane and membrane-cortex adhesion mechanics. Notation is different than in the text. From [Sens 2015].

where $f_p = k u_p \rho_b^{\mathrm{eq}}(u_p)$ is the value of the stress on the membrane and, therefore, on the linkers, at the aspirated region. Then, combining Eqs. (2.11), (2.12) and (2.14), we obtain the micropipette suction pressure difference:

$$\Delta P_p = P_{\mathrm{ext}} - P_p = 2\gamma\left(\frac{1}{R_p} - \frac{1}{R}\right) + f_p - \frac{2\gamma_c}{R}. \tag{2.15}$$

For typical values of membrane tension $\gamma \lesssim 0.1$ mN/m, cell radius $R \sim 10$ μm, and micropipette radius $R_p \sim 5$ μm, the normal contribution of membrane tension is $\lesssim 20$ Pa, which is small compared with the range of aspiration pressures $\Delta P_p \sim 0.1 - 1$ kPa. Therefore, we approximate

$$\Delta P_p \approx f_p - \frac{2\gamma_c}{R}. \tag{2.16}$$

ΔP_p^* (kPa)	Talin normal	Talin-null	
Myosin-II normal	0.20	0.20	leading edge
	0.33	0.23	trailing edge
Myosin-II-null	0.95	0.93	leading edge
	1.50	0.90	trailing edge

Table 2.2 | Critical suction pressure for membrane-cortex detachment in *Dictyostelium discoideum*. Estimates are presented for four mutants, showing that the critical pressure is higher in the absence of myosin and in the presence of talin, in agreement with the predictions of our model. In addition, the critical pressure is lower when measured on the side corresponding to the leading edge as compared to the trailing edge of cell migration, which suggests that membrane-cortex linkers such as talin are enriched in the back compared to the front of the cell. Data from [Merkel 2000].

Hence, since membrane-cortex unbinding occurs when the stress f on the linkers surpasses the threshold f^* (Eq. (2.9)), the critical suction pressure for membrane-cortex unbinding reads

$$\Delta P_p^* \approx \alpha^* \rho_0 \frac{k_B T}{\delta} - \frac{2\gamma_c}{R}. \tag{2.17}$$

Next, we assess our predictions by analyzing estimates of the critical suction pressure ΔP_p^* from micropipette experiments on different mutants of the amoeba *Dictyostelium discoideum* [Merkel 2000] (Table 2.2). First, the myosin-null mutant should feature a strongly reduced cortical tension. Hence,

$$\Delta P_p^{*,m^-} \approx \alpha^* \rho_0 \frac{k_B T}{\delta}. \tag{2.18}$$

The data confirm that, in the absence of myosin-generated cortical tension, a much higher suction pressure is required to detach the membrane from the cortex (Table 2.2). Therefore, comparing the myosin-null mutant to the wild type, we can estimate the cortical tension of the amoeba:

$$\Delta P_p^{*,m^-} - \Delta P_p^{*,wt} \approx \frac{2\gamma_c}{R}, \tag{2.19}$$

which gives $\gamma_c \sim 5$ mN/m, in agreement with direct measurements [Dai 1999b]. Second, the critical suction pressure of myosin-null mutants depends only on the density of linkers (Eq. (2.18)). Therefore, we can infer the relative abundance of talin among membrane-cortex linker molecules by comparing the double mutant to the myosin-null mutant:

$$\frac{\Delta P_p^{*,m^-} - \Delta P_p^{*,m^-,t^-}}{\Delta P_p^{*,m^-}} \approx \frac{\rho_t}{\rho_0}, \tag{2.20}$$

where ρ_t is the surface density of talin. This way, we estimate a $\sim 5\%$ fraction of talin bonds in the leading edge and up to $\sim 40\%$ in the trailing edge of *Dictyostelium*

discoideum. This front-back difference in talin distribution seems to be enough to drive the directed migration of *D. discoideum*. Similar observations were reported for zebrafish germ layer progenitor cells [Diz-Muñoz 2010]. Finally, assuming $\rho_0 \sim 100$ linkers/μm^2 and $\delta \sim 1$ nm, we estimate $\alpha^* \sim 3.6$ or, in other words, a critical force per link $f^*/\rho_0 \sim 15$ pN. Since this value is similar to the initial estimate $f^*/\rho_0 \sim 18$ pN, we conclude that $\chi \sim 10^{-3}$.

2.4 Adhesion of an undulated membrane

In this section, we extend the model to include membrane undulations. In addition to the adhesion force and the pressure difference, an undulated membrane is subject to elastic forces due to surface tension and bending rigidity. Membrane deformations induce flows of the surrounding fluid, which then mediate long-range hydrodynamic interactions along the membrane.

Thus, to derive an equation of motion for the membrane, we consider an undulated membrane patch that moves in a fluid of viscosity η that does not flow through it [Seifert 1997, Brown 2008]. Using the Monge gauge, we describe the position of the membrane by means of the height field $u(\vec{x}, t)$, where $\vec{x}$ is the two-dimensional position vector along the membrane. Membrane height evolves as dictated by the surrounding fluid flow $\vec{v}(\vec{r}, t)$, where $\vec{r} = (\vec{x}, z)$ is the three-dimensional position vector:

$$\partial_t u(\vec{x}, t) = \vec{v} \cdot \hat{n}|_{z=\delta u(\vec{x},t)} . \tag{2.21}$$

Here, $\hat{n}$ is the normal vector of the membrane, and z is the coordinate along the direction perpendicular to the membrane plane, with the origin $z = 0$ at the average membrane plane. Therefore, at the lowest order in membrane shape perturbations $\delta u(\vec{x}, t) = u(\vec{x}, t) - \langle u(\vec{x}, t)\rangle_{\vec{x}}$,

$$\partial_t u(\vec{x}, t) \approx v_z(\vec{r}, t)|_{z=0} . \tag{2.22}$$

Thus, to specify membrane dynamics, we need to obtain the flow field of the surrounding fluid by solving Stokes' equation for an incompressible fluid:

$$\vec{\nabla} P - \eta \nabla^2 \vec{v} = \vec{T}, \qquad \vec{\nabla} \cdot \vec{v} = 0, \tag{2.23}$$

where P is the fluid pressure and $\vec{T}$ is the density of extenal forces acting on the fluid, such as those exerted by the membrane. The general solution to Stokes' equation in the incompressible regime is given by [Doi 1986]

$$v_\alpha(\vec{r}) = \int_{\mathcal{V}} H_{\alpha\beta}(\vec{r}, \vec{r}\,') T_\beta(\vec{r}\,') \, d^3\vec{r}\,', \tag{2.24}$$

where

$$H_{\alpha\beta}(\vec{r}, \vec{r}\,') = \frac{1}{8\pi\eta |\vec{r} - \vec{r}\,'|} \left[\delta_{\alpha\beta} + \frac{(r_\alpha - r'_\alpha)(r_\beta - r'_\beta)}{|\vec{r} - \vec{r}\,'|^2} \right] \tag{2.25}$$

is the Oseen tensor, namely the Green's function of Stokes' equation. Therefore, the surrounding fluid gives rise to long-range hydrodynamic interactions that yield non-local membrane dynamics, which are better dealt with in Fourier space. Introducing the planar Fourier components

$$\tilde{u}_{\alpha,\vec{q}}(z) = \int_{\mathcal{S}} u_\alpha(\vec{r})\, e^{-i\vec{q}\cdot\vec{x}}\, d^2\vec{x} \tag{2.26a}$$

$$\tilde{v}_{\alpha,\vec{q}}(z) = \int_{\mathcal{S}} v_\alpha(\vec{r})\, e^{-i\vec{q}\cdot\vec{x}}\, d^2\vec{x}, \tag{2.26b}$$

$$\tilde{T}_{\alpha,\vec{q}}(z) = \int_{\mathcal{S}} T_\alpha(\vec{r})\, e^{-i\vec{q}\cdot\vec{x}}\, d^2\vec{x}, \tag{2.26c}$$

and using Eqs. (2.22), (2.24) and (2.25), the hydrodynamics of membrane undulations reads [Seifert 1997, Brown 2008] (Appendix 2.B)

$$\partial_t \delta\tilde{u}_{\vec{q}} \approx \tilde{v}_{z,\vec{q}}(0) \approx \frac{1}{4\eta q}\tilde{F}_{z,\vec{q}}, \tag{2.27}$$

where $q \equiv |\vec{q}|$, and $\tilde{F}_{z,\vec{q}}$ are the Fourier components of the normal force exerted by the membrane on the fluid, namely the lowest-order contribution of the force density, $\tilde{T}_{z,\vec{q}} \approx \tilde{F}_{z,\vec{q}}\,\delta(z)$.

Now, a uniform, non-constant velocity $v_\alpha^0(\vec{r})$ can be added to the solution of Stokes' equation Eq. (2.24), which accounts for the motion of the average membrane position $\langle u(\vec{x},t)\rangle_{\vec{x}}$. The dynamics of uniform membrane motion follows from the balance between the total force exerted by the membrane on the fluid and the friction force exerted by the fluid on the membrane, which is dominated by cytosol flow through the cortex (Appendix 2.A). In Fourier space,

$$\mu\tilde{v}_{z,\vec{0}}(0) = \tilde{T}_{z,\vec{0}}(0), \tag{2.28}$$

where

$$\tilde{v}_{\alpha,\vec{0}}(z) = \int_{\mathcal{S}} v_\alpha^0(\vec{r})\, d^2\vec{x}. \tag{2.29}$$

Thus,

$$\partial_t \delta\tilde{u}_{\vec{0}} = \frac{1}{\mu}\tilde{F}_{z,\vec{0}}. \tag{2.30}$$

Note that we account for the effect of the porous cortex on the uniform motion of the membrane, Eq. (2.30), but not on the hydrodynamics of membrane undulations, Eq. (2.27), which we assume to be governed by a Stokes' flow without permeation effects. This approximation is valid if the cortex is sufficiently porous and/or sufficiently far from the membrane. Otherwise, corrections due to fluid permeation into the cortex must be included [Gov 2003, Gov 2004b] (Appendix 2.C).

To close the equations for membrane hydrodynamics, we must specify the forces exerted by the membrane on the fluid, which follow from the coarse-grained Hamiltonian of the membrane:

$$\mathcal{H} = \int_{\mathcal{S}} \left[\frac{\kappa}{2}\left[\nabla^2 u(\vec{x})\right]^2 + \frac{\gamma}{2}\left[\vec{\nabla} u(\vec{x})\right]^2 + \frac{k}{2}\rho_b(\vec{x})\, u^2(\vec{x}) - f u(\vec{x})\right] d^2\vec{x}. \tag{2.31}$$

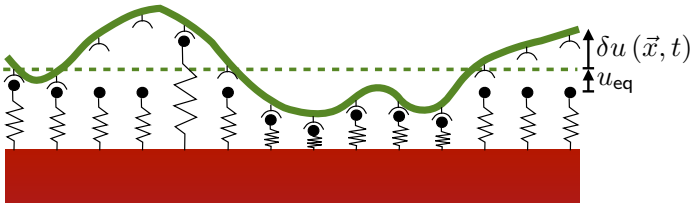

Figure 2.7 | Sketch of an undulated membrane adhered to the cortex. The membrane (green) is attached to the cortex (red) via linker molecules (black). The spatiotemporal average position of the membrane, $\langle u\,(\vec{x},t)\rangle_{\vec{x},t}$, is given by the equilibrium stretching of the linkers in the flat membrane model, u_{eq} (Eq. (2.4)). Thus, perturbations around this state allow both for uniform and non-uniform membrane displacements.

This Hamiltonian includes the classical Canham-Helfrich contributions accounting for elastic forces due to membrane bending, with bending rigidity κ, and to apparent area changes, with membrane tension γ [Helfrich 1990, Safran 1994, Boal 2002]. Then, we add terms accounting for the elastic force due to linker-mediated adhesion to the cortex, and for the pressure difference on the membrane. The continuum description of membrane elasticity was shown to hold down to length scales of a few nanometers [Goetz 1999], much below the scope of our approach. However, the tension γ of a membrane coupled to an elastic network such as the cortex was shown to experience a jump at length scales below the network mesh size [Fournier 2004]. Here, we neglect this effect because our continuum description of membrane-cortex adhesion is restricted to length scales larger than the average linker spacing $\xi_0 \sim 0.1$ μm, which is, in turn, larger than the cortex mesh size $\xi \sim 30$ nm (Table 2.1).

Now, we introduce small-amplitude perturbations around the mechanical equilibrium state given by Eq. (2.4) (Fig. 2.7):

$$u\,(\vec{x},t) = u_{\mathrm{eq}} + \delta u\,(\vec{x},t)\,, \qquad \rho_b\,(\vec{x},t) = \rho_b^{\mathrm{eq}} + \delta\rho_b\,(\vec{x},t)\,. \tag{2.32}$$

Note that the equilibrium values of linker stretching and bond density correspond to the spatiotemporal averages of the corresponding fields:

$$u_{\mathrm{eq}} = \langle\langle u\,(\vec{x},t)\rangle_{\vec{x}}\rangle_t\,, \qquad \rho_b^{\mathrm{eq}} = \langle\langle \rho_b\,(\vec{x},t)\rangle_{\vec{x}}\rangle_t\,. \tag{2.33}$$

Thus, the perturbation fields $\delta u\,(\vec{x},t)$ and $\delta\rho_b\,(\vec{x},t)$ include both uniform ($\vec{q}=\vec{0}$) and non-uniform ($\vec{q}\neq\vec{0}$) displacements from the equilibrium state. Next, we decompose the perturbations in their Fourier modes,

$$\delta u\,(\vec{x},t) = \sum_{\vec{q}} \delta\tilde{u}_{\vec{q}}\,(t)\,e^{i\vec{q}\cdot\vec{x}}, \qquad \delta\rho_b\,(\vec{x},t) = \sum_{\vec{q}} \delta\tilde{\rho}_{b,\vec{q}}\,(t)\,e^{i\vec{q}\cdot\vec{x}}, \tag{2.34}$$

and introduce them into the Hamiltonian. To the lowest order in perturbations, we obtain

$$\mathcal{H} \approx \sum_{\vec{q}} H_{\vec{q}} = \sum_{\vec{q}} \left[\frac{1}{2}\left(\kappa q^4 + \gamma q^2 + k\rho_b^{\mathrm{eq}}\right)\left|\delta\tilde{u}_{\vec{q}}\right|^2 + k u_{\mathrm{eq}}\,\delta\tilde{\rho}_{b,\vec{q}}\,\delta\tilde{u}_{-\vec{q}}\right]. \tag{2.35}$$

Then, the normal force exerted by the membrane is computed as [Seifert 1997]

$$\tilde{F}_{z,\vec{q}} = -\frac{\partial H_{\vec{q}}}{\partial \delta \tilde{u}^*_{\vec{q}}}, \tag{2.36}$$

so that the dynamics of small-amplitude membrane undulations finally reads

$$\partial_t \delta\tilde{u}_{\vec{0}} = -\frac{1}{\mu}\left[k\rho_b^{\mathrm{eq}}\,\delta\tilde{u}_{\vec{0}} + k u_{\mathrm{eq}}\,\delta\tilde{\rho}_{b,\vec{0}}\right], \tag{2.37a}$$

$$\partial_t \delta\tilde{u}_{\vec{q}} = -\frac{1}{4\eta q}\left[\left(\kappa q^4 + \gamma q^2 + k\rho_b^{\mathrm{eq}}\right)\delta\tilde{u}_{\vec{q}} + k u_{\mathrm{eq}}\,\delta\tilde{\rho}_{b,\vec{q}}\right], \tag{2.37b}$$

where we have used Eqs. (2.27) and (2.30). We also recall that $\rho_b^{\mathrm{eq}} k u_{\mathrm{eq}} = f$. In real space, the nonlocal character of the dynamics of membrane undulations becomes apparent:

$$\partial_t \left\langle \delta u\left(\vec{x},t\right)\right\rangle_{\vec{x}} = -\frac{1}{\mu}\left[k\rho_b^{\mathrm{eq}}\left\langle \delta u\left(\vec{x},t\right)\right\rangle_{\vec{x}} + k u_{\mathrm{eq}}\left\langle \delta\rho_b\left(\vec{x},t\right)\right\rangle_{\vec{x}}\right], \tag{2.38a}$$

$$\partial_t \delta u\left(\vec{x},t\right) = \int_{\mathcal{S}} \frac{1}{8\pi\eta\left|\vec{x}-\vec{x}\,'\right|} F_z\left(\vec{x}\,'\right) d^2\vec{x}\,', \tag{2.38b}$$

where

$$F_z\left(\vec{x}\right) = -\frac{\delta\mathcal{H}}{\delta\delta u\left(\vec{x}\right)} = -\left[\kappa\nabla^4 - \gamma\nabla^2 + k\rho_b^{\mathrm{eq}}\right]\delta u\left(\vec{x},t\right) - k u_{\mathrm{eq}}\delta\rho_b\left(\vec{x}\right) \tag{2.39}$$

is the normal force exerted by the membrane.

Finally, unlike membrane motion, linkers feature local dynamics. Introducing Eq. (2.32) into Eqs. (2.1) and (2.2), we obtain, to linear order in the perturbations,

$$\partial_t \delta\rho_b\left(\vec{x},t\right) = -\rho_b^{\mathrm{eq}}\beta k\delta k_{\mathrm{off}}^0 e^{\beta k u_{\mathrm{eq}}\delta}\delta u\left(\vec{x},t\right) - \left[k_{\mathrm{on}} + k_{\mathrm{off}}^0 e^{\beta k u_{\mathrm{eq}}\delta}\right]\delta\rho_b\left(\vec{x},t\right). \tag{2.40}$$

In total, Eqs. (2.37) and (2.40) constitute the extension of our membrane-cortex adhesion model to include spatiotemporal small-amplitude perturbations around the mechanical equilibrium state.

2.5 Fluctuations of an adhered membrane

In this section, we employ our model to study the fluctuations of a membrane attached to the cortex. Equations (2.37) and (2.40) give the coupled linear dynamics of the membrane position and bond density fields. However, in the long-wavelength limit, membrane motion is notably slower than the linker binding kinetics. Such a separation of time scales is supported by estimates based on the flat membrane model in Section 2.2. Introducing the dimensionless variables in Eq. (2.5) plus the dimensionless time $\bar{t} = k_{\mathrm{on}} t$, Eq. (2.3) reads

$$\zeta\frac{d\bar{u}}{d\bar{t}} = \alpha - \bar{u}\bar{\rho}_b, \tag{2.41}$$

where α is defined in Eq. (2.7), and we have identified the dimensionless parameter

$$\zeta \equiv \frac{\mu k_{\text{on}}}{\rho_0 k} = \frac{\tau_u}{\tau_b}; \qquad \tau_u = \frac{\mu}{\rho_0 k}, \quad \tau_b = k_{\text{on}}^{-1} \tag{2.42}$$

that compares the time scales of membrane displacements, τ_u, and of linker kinetics, τ_b. Using the estimates in Table 2.1, we obtain $\tau_u \sim 2$ ms, $\tau_b \sim 0.1$ ms, and hence $\zeta \sim 20$. Therefore, we expect linker kinetics to be typically faster than uniform membrane displacements.

In general, membrane undulation dynamics depends on the wavevector and is coupled to the bond density field. In the following, we perform an adiabatic approximation for the linker kinetics, considering that the bond density field adiabatically follows the membrane position field. Under this approximation, the dynamics of the system reduces to that of the slow variable:

$$\partial_t \delta\tilde{u}_{\vec{q}} \approx -\frac{\kappa q^4 + \gamma q^2 + k\rho_b^{\text{eq}}}{4\eta q}\delta\tilde{u}_{\vec{q}}, \tag{2.43}$$

from where we identify the growth rate of membrane undulations:

$$\omega_q = -\frac{\kappa q^4 + \gamma q^2 + k\rho_b^{\text{eq}}}{4\eta q}. \tag{2.44}$$

This result shows that, in contrast to a free membrane, an adhered membrane exhibits a nonmonotonous growth rate[2] (Fig. 2.8). Therefore, membrane-cortex adhesion gives rise to a characteristic wavelength

$$\lambda_c = 2\pi \left[\frac{6\kappa/\gamma}{\left(1 + 12\kappa k \rho_b^{\text{eq}}/\gamma^2\right)^{1/2} - 1} \right]^{1/2} \tag{2.45}$$

at which membrane undulations decay the slowest. Note that this characteristic wavelength depends on the pressure f via the equilibrium density of bonds ρ_b^{eq}. A pressure-independent estimate of the characteristic wavelength is $\lambda^* \equiv \lambda_c\left(\rho_b^{\text{eq}} \to \rho_0\right) \sim 0.6$ μm, which is used to scale wave vectors hereafter. The adhesion-induced peak of the growth rate should fall in the range of wave vectors accessible to fluctuation spectroscopy experiments [Betz 2012] (shaded area in Fig. 2.8), in which membrane fluctuations are tracked via, for example, interferometric techniques (Fig. 2.6) [Monzel 2016]. Therefore, performing such experiments on adhered membranes, using either live cells or reconstituted systems, would allow testing our predictions and inferring adhesion parameters such as the density of membrane-cortex bonds.

To compare with spectroscopy experiments, we compute the spatiotemporal correlations of membrane undulations which, in Fourier space, are given by the

[2] Including the hydrodynamic effect of the cortex makes the relaxation rate of long-wavelength undulations ($q \to 0$) finite, tending to the limit $\omega_0 = -k\rho_b^{\text{eq}}/\mu$ that follows from Eq. (2.37) in the adiabatic approximation. Therefore, the growth rate may even be monotonous for low cortex porosity and short membrane-cortex distances (Appendix 2.C).

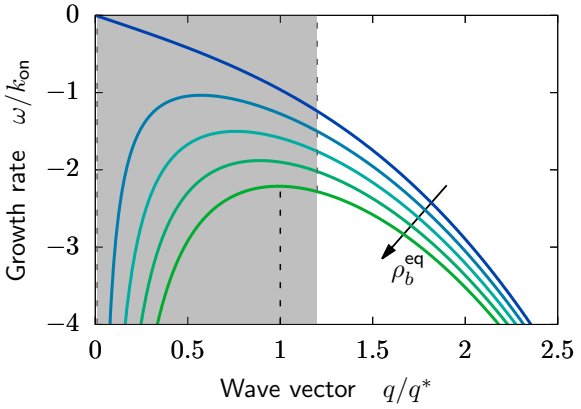

Figure 2.8 | Growth rate of undulations of an adhered membrane. Membrane-cortex adhesion is responsible for the nonmonotonous behaviour of the growth rate (Eq. (2.44)), thereby defining a characteristic wavelength of membrane undulations, λ_c (Eq. (2.45)), namely the peak of the growth rate. The peak falls within the range of wave vectors accessible to fluctuation spectroscopy experiments (shaded area), $1/R < q < 2\pi/d$, where $R \sim 10$ μm is the cell radius and $d \sim 0.5$ μm is the focal diameter of the laser used for interferometry (Fig. 2.6) [Betz 2012]. For the completely adhered case $\rho_b^{eq} = \rho_0$, the characteristic wavelength is $\lambda_c\,(\rho_b^{eq} = \rho_0) \equiv \lambda^* = 2\pi/q^*$ (dashed line), with which we scale the wave vector. Parameter values are those in Table 2.1, and $\rho_b^{eq}/\rho_0 = n/4$; $n = 0, \ldots, 4$.

dynamic structure factor

$$S_{\vec{q}}(t) \equiv \frac{1}{\mathcal{S}} \left\langle \delta\tilde{u}_{\vec{q}}(t)\, \delta\tilde{u}^*_{\vec{q}}(0) \right\rangle = S_{\vec{q}}\, e^{\omega_q t}, \tag{2.46}$$

where $\mathcal{S}$ is the area of the membrane plane, and the average is an ensemble (thermal) average. $S_{\vec{q}}$ is the static structure factor

$$S_{\vec{q}} = \frac{1}{\mathcal{S}} \left\langle \delta\tilde{u}_{\vec{q}}(t)\, \delta\tilde{u}^*_{\vec{q}}(t) \right\rangle, \tag{2.47}$$

which characterizes spatial correlations along the membrane. At thermal equilibrium, the structure factor can be determined via the energy equipartition theorem for the quadratic degrees of freedom of the Hamiltonian Eq. (2.35). Under the adiabatic approximation, namely considering only the slow variable δu, we obtain

$$S_q = \frac{k_B T}{\kappa q^4 + \gamma q^2 + k\rho_b^{eq}}. \tag{2.48}$$

The same functional form of the structure factor was obtained for a membrane under a harmonic potential[3] [Gov 2003, Fournier 2004, Merath 2006]. Therefore,

[3] A harmonic confining potential was found to stem from other fluctuating membranes in a stack [de

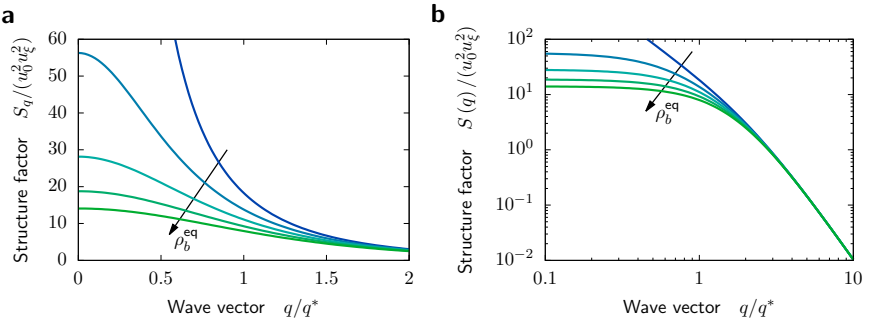

Figure 2.9 | Structure factor of an adhered membrane. **a,** Linear, and **b,** logarithmic scales. Long-wavelength fluctuations are much more pronounced than short-wavelength fluctuations, with a cross-over at $q \sim q^*$. Membrane-cortex adhesion limits long-wavelength fluctuations. The wave vector is scaled with the characteristic wavelength $2\pi/q^* = \lambda^* = \lambda_c\,(\rho_b^{\mathrm{eq}} = \rho_0)$ (Eq. (2.45)), and the structure factor is scaled with $u_0 \equiv k_B T/(k\delta)$ and $u_\xi \equiv k_B T/(k\xi)$. Parameter values are those in Table 2.1, and $\rho_b^{\mathrm{eq}}/\rho_0 = n/4$; $n = 0, \ldots, 4$.

our result indicates that, in the adiabatic approximation, membrane-cortex adhesion constrains membrane fluctuations as an effective harmonic potential of stiffness $k\rho_b^{\mathrm{eq}}$, which depends on the linker properties and on the pressure on the membrane. Thus, in principle, Eq. (2.48) allows determining the stiffness $k\rho_b^{\mathrm{eq}}$ of the effective adhesion potential under different experimental conditions from measurements of the static structure factor of the cell membrane [Popescu 2006]. Specifically, the long-wavelength limit $q \to 0$ of the structure factor[4] should be measured to determine $k\rho_b^{\mathrm{eq}}$ from Eq. (2.48) (Fig. 2.9). Moreover, the density of membrane-cortex bonds ρ_b^{eq} could be estimated provided that the stiffness of individual linkers, k, were known. Alternatively, the same information can also be inferred from the growth rate, Eq. (2.44) (Fig. 2.8), obtained from measurements of the dynamic structure factor Eq. (2.46).

Next, we compute the mean-square amplitude of membrane undulations:

$$\left\langle \delta u^2 \right\rangle = \left\langle \left\langle \delta u^2\,(\vec{x}, t) \right\rangle_{\vec{x}} \right\rangle = \sum_{\vec{q}} S_q \approx \frac{1}{2\pi} \int_{q_{\min}}^{q_{\max}} S_q\, q\, dq. \tag{2.49}$$

Taking $q_{\min} = \pi/L$, with $L = \sqrt{\mathcal{S}}$, and $q_{\max} = \pi/\xi_0$, where the linker spacing ξ_0

Gennes 1982], and from the presence of a nearby wall [Gov 2004b] or sparse harmonic anchors [Gov 2004a].

[4] The accurate measurement of the long-wavelength response is difficult due to finite-size effects.

sets the microscopic cutoff, we obtain

$$\left\langle \delta u^2 \right\rangle = \frac{k_B T}{2\pi} \frac{1}{\sqrt{4\kappa\rho_b^{\mathrm{eq}} k - \gamma^2}} \left[\arctan\left(\frac{2\pi^2 \kappa \rho_0 + \gamma}{\sqrt{4\kappa\rho_b^{\mathrm{eq}} k - \gamma^2}} \right) - \arctan\left(\frac{2\kappa \left(\pi/L\right)^2 + \gamma}{\sqrt{4\kappa\rho_b^{\mathrm{eq}} k - \gamma^2}} \right) \right], \tag{2.50a}$$

$$\left\langle \delta u^2 \right\rangle = \frac{k_B T}{4\pi} \frac{1}{\sqrt{\gamma^2 - 4\kappa\rho_b^{\mathrm{eq}} k}} \left[\ln\left(\frac{2\pi^2 \kappa \rho_0 + \gamma - \sqrt{\gamma^2 - 4\kappa\rho_b^{\mathrm{eq}} k}}{2\pi^2 \kappa \rho_0 + \gamma + \sqrt{\gamma^2 - 4\kappa\rho_b^{\mathrm{eq}} k}} \right) - \ln\left(\frac{2\kappa \left(\pi/L\right)^2 + \gamma - \sqrt{\gamma^2 - 4\kappa\rho_b^{\mathrm{eq}} k}}{2\kappa \left(\pi/L\right)^2 + \gamma + \sqrt{\gamma^2 - 4\kappa\rho_b^{\mathrm{eq}} k}} \right) \right], \tag{2.50b}$$

for $\gamma^2 < 4\kappa\rho_b^{\mathrm{eq}} k$ and for $\gamma^2 > 4\kappa\rho_b^{\mathrm{eq}} k$, respectively. Using the parameter values in Table 2.1, we estimate $\left\langle \delta u^2 \right\rangle^{1/2} \sim 3$ nm. Such a small amplitude of membrane undulations suggests that restricting to the linear elasticity regime of membrane-cortex linkers might be a good approximation.

Finally, we compute the power spectral density

$$S(\omega) = \sum_{\vec{q}} \int_{-\infty}^{\infty} S_{\vec{q}}(t)\, e^{-i\omega t}\, dt = -\sum_{\vec{q}} \frac{2 S_{\vec{q}}\, \omega_q}{\omega^2 + \omega_q^2} \approx -\frac{1}{\pi} \int_{q_{\mathrm{min}}}^{q_{\mathrm{max}}} \frac{S_q\, \omega_q}{\omega^2 + \omega_q^2} q\, dq, \tag{2.51}$$

which characterizes temporal correlations of membrane undulations. Introducing Eqs. (2.44) and (2.48), we obtain

$$S(\omega) = \frac{4\eta k_B T}{\pi} \int_{q_{\mathrm{min}}}^{q_{\mathrm{max}}} \frac{dq}{\left(4\eta\omega\right)^2 + \left(\kappa q^3 + \gamma q + \rho_b^{\mathrm{eq}} k/q\right)^2}, \tag{2.52}$$

which can not be analytically integrated in general. In the following, we discuss the role of membrane-cortex adhesion in the fluctuation spectrum, and obtain approximate analytical expressions in some limits.

Specifically, in a free membrane, fast relaxations take place at short wavelengths, and hence are dominated by bending forces, $\omega_q \approx -\kappa q^3/(4\eta)$. However, an adhered membrane may feature a nonmonotonous growth rate, so that high-frequency responses may occur both at long and at short wavelengths (Fig. 2.8). Consequently, high-frequency membrane fluctuations may be dominated by either adhesion or bending forces, respectively. If bending dominates the high-frequency response, the power spectral density should decay as[5] [Helfer 2001, Betz 2009, Betz 2012]

$$\lim_{\gamma, \rho_b^{\mathrm{eq}} \to 0} S(\omega) \approx \frac{k_B T}{6 \left(2\kappa\eta^2\right)^{1/3} \omega^{5/3}}, \tag{2.53}$$

[5] If the flow-confining effect of the cortex on membrane hydrodynamics is relevant, as in red blood cells, then an intermediate regime with scaling $S(\omega) \propto \omega^{-4/3}$ is expected [Brochard 1975, Gov 2003].

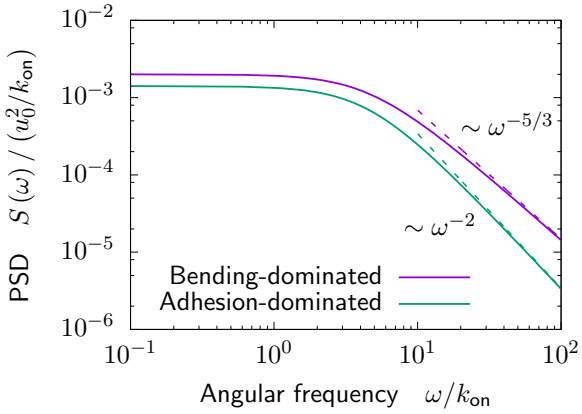

Figure 2.10 | Power spectral density (PSD) of an adhered membrane. Equation (2.52) in the bending-dominated limit, $\gamma, \rho_b^{\mathrm{eq}} \to 0$, and in the adhesion-dominated limit, $\kappa, \gamma \to 0$. The corresponding power-law decays (dashed lines), Eqs. (2.53) and (2.54), respectively, allow distinguishing both cases. The numerical integration of Eq. (2.52) is performed from $q_{\mathrm{min}} = 1/R$, with $R \sim 10$ μm the cell radius, to $q_{\mathrm{max}} = 2\pi/d$, with $d = 0.5$ μm the focal diameter of the optical trap used for interferometric measurements [Betz 2012]. The rescaling length is $u_0 \equiv k_B T/(k\delta)$. Parameter values are those in Table 2.1, and $\rho_b^{\mathrm{eq}} = \rho_0$.

where we have taken the limits $q_{\mathrm{min}} \to 0$ and $q_{\mathrm{max}} \to \infty$. In contrast, if the high-frequency response is dominated by membrane-cortex adhesion, we predict

$$\lim_{\kappa,\gamma\to 0} S(\omega) = \frac{k_B T}{4\pi\eta\omega^2}\left[q_{\mathrm{max}} - q_{\mathrm{min}} + \frac{\rho_b^{\mathrm{eq}} k}{4\eta\omega}\left[\arctan\left(\frac{4\eta q_{\mathrm{min}}\omega}{\rho_b^{\mathrm{eq}} k}\right) - \arctan\left(\frac{4\eta q_{\mathrm{max}}\omega}{\rho_b^{\mathrm{eq}} k}\right)\right]\right]. \quad (2.54)$$

In this case, the power spectral density decays as $S(\omega) \propto \omega^{-2}$ at high frequencies. Therefore, the exponent of the power-law decay of the fluctuation spectrum could allow distinguishing whether bending or membrane-cortex adhesion dominate the high-frequency response of a cell membrane[6] (Fig. 2.10). In general, adhesion

[6] At the highest frequencies, the power spectral density always decays as

$$\lim_{\omega\to\infty} S(\omega) = \frac{k_B T\,(q_{\mathrm{max}} - q_{\mathrm{min}})}{4\pi\eta\omega^2}. \quad (2.55)$$

This very-high-frequency regime is insensitive to any membrane property because it simply reveals the Brownian motion of the membrane, which only depends on the viscosity of the surrounding fluid. Therefore, when analyzing experimental spectra, it may be challenging to distinguish between a true adhesion-dominated behaviour, Eq. (2.54), or simply a crossover between the bending-dominated scaling $S(\omega) \propto \omega^{-5/3}$ and the universal Brownian-motion regime. Nevertheless, even if a clear scaling is not apparent, the full expression Eq. (2.52) can be numerically fit to the experimental data to infer the parameters of the model.

dominates membrane undulations over bending at wavelengths much larger than $\left(\rho_b^{\mathrm{eq}} k/\kappa\right)^{-1/4}$. Therefore, we expect an adhesion-dominated high-frequency regime of the power spectrum if $q_{\max} \ll \left(\rho_b^{\mathrm{eq}} k/\kappa\right)^{1/4}$. In this case, the stiffness $k\rho_b^{\mathrm{eq}}$ of the effective adhesion potential could be inferred by fitting Eq. (2.54) to the experimental power spectral density. Moreover, if the linker stiffness k were known, the density of membrane-cortex bonds ρ_b^{eq} could be estimated.

Finally, we have only considered thermally excited membrane undulations. However, active processes in cells also produce nonthermal membrane undulations, which are most pronounced at low frequencies [Levin 1991, Betz 2009, Turlier 2016]. At high-frequencies, activity can be accounted for by an increased effective temperature [Prost 1998, Manneville 1999, Manneville 2001, Gov 2003, Gov 2004c, Betz 2009, Park 2010, Ben-Isaac 2011, Turlier 2016]. Therefore, our predictions for the high-frequency part of the fluctuation spectrum should allow probing membrane-cortex adhesion regardless of activity (Fig. 2.10). In contrast, active fluctuations could significantly contribute to the low wave vector part of the structure factor [Prost 1996, El Alaoui Faris 2009], thus hampering the inference of information about membrane-cortex adhesion from the measurement of spatial correlations (Fig. 2.9).

2.6 Discussion and conclusions

In this chapter, we have proposed a model for membrane-cortex adhesion based on the binding kinetics of linker molecules. The force dependence of the linkers' unbinding rate gives rise to a membrane-cortex unbinding transition. We predicted the critical suction pressure required to detach the membrane in micropipette aspiration experiments, which depends on the cell's cortical tension. We tested our predictions against published experimental data [Merkel 2000], which allowed us to estimate the cortical tension in *Dictyostelium discoideum* cells. However, further experiments are needed to fully assess the validity of the model.

Then, we generalized the model to include membrane undulations. Considering the hydrodynamics of an impermeable membrane, we derived the coupled dynamics of small-amplitude perturbations of the membrane position and bond density fields. In the limit of fast linker kinetics, we showed that membrane-cortex adhesion yields a fast relaxation of long-wavelength perturbations when the hydrodynamic influence of the underlying cortex is not too large. The validity of such approximations should be checked in each particular experimental situation, and the model predictions adapted accordingly.

Further, we predicted the structure factor and the power spectrum of an adhered membrane. We proposed that our predictions could be employed to probe membrane-cortex adhesion from the statistics of membrane fluctuations, which can be measured by means of a number of techniques [Monzel 2016]. Detailed measurements of the structure factor and power spectrum of membrane fluctuations have been obtained in vesicles, red blood cells, and even blebs [Peukes 2014]. However, measurements of the fluctuations of the strongly adhered membrane of

nucleated cells are still scarce [Zidovska 2006, Monzel 2015, Monzel 2016]. Measuring membrane fluctuations at different pressures on the membrane would allow testing our model, as well as emplyoing the predictions to infer membrane-cortex adhesion properties such as the density of bonds.

Altogether, our model provides a theoretical framework to probe membrane-cortex adhesion both via micropipette aspiration and in fluctuation spectroscopy experiments. Both approaches are complementary, so that their combination could give access to quantitative information about membrane-cortex adhesion, such as the cortical tension and the density of bonds.

Contributions and acknowledgements

The work described in this chapter was done in collaboration with Jan Brugués (MPI-CBG & MPI-PKS, Dresden) and Pierre Sens (ESPCI, Paris, and then Institut Curie, Paris). They had formulated the kinetic model for membrane-cortex adhesion, and applied it to micropipette experiments. I extended the model to include membrane undulations, and computed their spatiotemporal correlations.

I thank Cornelia Monzel, as well as Marco Ribezzi-Crivellari, Fèlix Ritort, and Marta Gironella for discussions about measuring membrane fluctuation spectra in living cells.

Appendices

2.A Dissipation by membrane displacements

In this appendix, we estimate the energy dissipation associated to small membrane displacements. We consider two main dissipation sources, namely the lateral flow of the membrane, and the flow of cytosol through the cortex (Fig. 2.A.1). The latter is found to be the dominant contribution, defining an effective viscosity of membrane displacements.

First, we consider the flow of the membrane over the cortex towards an inflating membrane patch (bleb) of projected radius a. Assuming that no membrane is added, the increase of membrane area per unit time in this patch is given by mass conservation: $\dot{S}_b = 2\pi r\dot{r}$, where r is the distance from the center of the basis of the patch, and $\dot{r}$ is the radial speed of the membrane flow (Fig. 2.A.2a). Membrane flow vanishes at the points at which the membrane is anchored to the cortex by linker molecules. Therefore, velocity gradients of order $\dot{r}/\xi_0 = \dot{S}_b/\left(2\pi r\xi_0\right)$ appear between anchoring points, where $\xi_0 \sim \rho_0^{-1/2}$ is the typical distance between them. In addition to these local velocity gradients, the velocity gradient of the overall membrane flow towards the inflating patch is of order $\dot{r}/r = \dot{S}_b/\left(2\pi r^2\right)$. Then, the dissipation associated to membrane flows includes the contributions of the local and global velocity gradients: $\dot{E}_m = \dot{E}_m^{\text{links}} + \dot{E}_m^{\text{global}}$.

Now, the energy dissipation in a viscous flow is given by [Guyon 2001]

$$\dot{E} = 2\eta_f \int_{\mathcal{V}} v_{\alpha\beta} v_{\beta\alpha}\, d^3\vec{r}, \tag{2.A.1}$$

where η_f is the fluid viscosity and $v_{\alpha\beta} = 1/2\left(\partial_\alpha v_\beta + \partial_\beta v_\alpha\right)$. Thus, the two

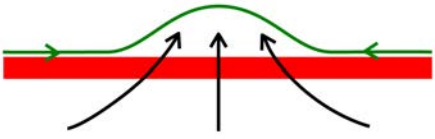

Figure 2.A.1 | Membrane and cytosol flows generated by a membrane displacement. To locally modify the membrane-cortex distance, the membrane (green) needs to flow over the cortex (red), and the cytosol needs to flow through it (black arrows). From [Brugués 2008].

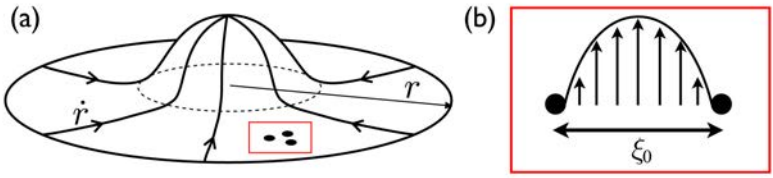

Figure 2.A.2 | Membrane flow dissipation. a, Sketch of the membrane flow towards an inflating patch (dotted line). **b,** Flow gradients between membrane-cortex bonds (black dots). From [Brugués 2008].

contributions to membrane flow dissipation are estimated by

$$\dot{E}_m^{\text{links}} \sim 4\pi\eta_m g \int_a^R \left(\frac{\dot{S}_b}{2\pi r \xi_0}\right)^2 r dr = \frac{\eta_m g \dot{S}_b^2}{\pi \xi_0^2} \ln\left(\frac{R}{a}\right) \approx \frac{\eta_m g \dot{S}_b^2}{2\pi \xi_0^2} \ln\left(\frac{S}{4A_b}\right), \tag{2.A.2}$$

$$\dot{E}_m^{\text{global}} \sim 4\pi\eta_m g \int_a^R \left(\frac{\dot{S}_b}{2\pi r^2}\right)^2 r dr \approx \frac{\eta_m g \dot{S}_b^2}{2\pi a^2} = \frac{\eta_m g \dot{S}_b^2}{2A_b}. \tag{2.A.3}$$

Here, η_m is the viscosity of the membrane, g its thickness, and $R \gg a$ is the cell radius. Accordingly, $S = 4\pi R^2$ is the total visible area of the cell membrane, and $A_b = \pi a^2$ is the projected area of the circular inflating patch. The continuum model in this chapter describes membrane displacements at length scales larger than ξ_0^2. Therefore, $A_b > \pi\xi_0^2$ and, hence, the dissipation of local velocity gradients between linkers, $\dot{E}_m^{\text{links}}$, is expected to dominate membrane flow dissipation.

Next, we consider the flow of cytosol towards the inflating membrane patch (bleb). For incompressible flow, and assuming cytosol mass conservation, the increase of volume of the inflating patch per unit time is given by $\dot{V}_b = 4\pi\varrho^2 v_\varrho$, where ϱ is the distance from the tip of the inflating patch, and v_ϱ is the cytosol velocity towards it. As for the membrane flow, there are global and local velocity gradients. First, the cytosol flows through the cortex, which generates velocity gradients of order $v_\varrho/\xi = \dot{V}_b/\left(4\pi\varrho^2\xi\right)$, where ξ is the cortex mesh size. Second, there is a global flow of cytosol across the cytoplasm, with velocity gradients of order $v_\varrho/\varrho = \dot{V}_b/\left(4\pi\varrho^3\right)$. Thus, we must estimate both contributions to the energy dissipation, $\dot{E}_c = \dot{E}_c^{\text{cortex}} + \dot{E}_c^{\text{global}}$.

To compute the dissipation of the flow of cytosol through the cortex, we consider the cortex as a porous material, which we model as an array of parallel straight capillary tubes of diameter ξ and length h [Guyon 2001, Beran 1968]. We also consider that the flow of cytosol through the cortex is purely transversal and restricted to the circular area of radius a under the inflating patch (Fig. 2.A.1). Thus, we estimate that $\sim a^2/\xi^2$ of capillary tubes are involved in the cytosol flow through the cortex. In addition, we consider the inflating membrane to be at a distance $\sim a$ of the underlying cortex. Therefore, the cortex is located at $a < z < a + h$, where z is the vertical distance from the inflated membrane. Then,

using Eq. (2.A.1),

$$\dot{E}_c^{\text{cortex}} \sim \frac{a^2}{\xi^2} 4\pi\eta \int_a^{a+h} dz \int_0^{\xi} r dr \left(\frac{\dot{V}_b}{4\pi z^2 \xi} \right)^2 \approx \frac{\eta h \dot{V}_b^2}{4\pi \xi^2 a^2} = \frac{\eta h \dot{V}_b^2}{4\xi^2 A_b}, \quad (2.A.4)$$

where we have used $h < a$ to obtain an approximate expression valid for the motion of the nearly flat membrane that our model considers. In turn, the dissipation of the global cytosol flow is estimated as

$$\dot{E}_c^{\text{global}} \sim 8\pi\eta \int_a^{R} \varrho^2 d\varrho \left(\frac{\dot{V}_b}{4\pi \varrho^3} \right)^2 \approx \frac{\eta \dot{V}_b^2}{6\pi a^3} = \frac{\sqrt{\pi}\, \eta \dot{V}_b^2}{6 A_b^{3/2}}. \quad (2.A.5)$$

Similar to the case of the membrane dissipation, since $A_b > \pi\xi^2$, the contribution of the permeation through the cortex is expected to dominate the dissipation associated to cytosol flow.

In conclusion, an estimate for the rate of energy dissipation due to the flows involved in large-scale membrane displacements is given by

$$\dot{E} \sim \dot{E}_m^{\text{links}} + \dot{E}_c^{\text{cortex}} \sim \frac{\eta_m g \dot{S}_b^2}{2\pi\xi_0^2} \ln\left(\frac{S}{4A_b} \right) + \frac{\eta h \dot{V}_b^2}{4\xi^2 A_b}, \quad (2.A.6)$$

where we have included only the dominant contribution of the membrane and cytosol flows. Now, $\dot{S}_b$ and $\dot{V}_b$ must be estimated in terms of membrane displacement u and speed $\dot{u}$. To this end, we consider the inflating patch, an incipient bleb, to be a spherical cap of radius R_b, polar radius a, and height u. Thus,

$$S_b \sim 2\pi R_b u, \qquad V_b \sim \pi R_b u^2; \qquad R_b = \frac{1}{2}\left(\frac{a^2}{u} + u \right). \quad (2.A.7)$$

We assume that the polar radius a remains constant during the inflation, while both u and R_b change. Then, to the lowest order in u,

$$S_b \sim \pi\left(a^2 + u^2\right), \qquad V_b \sim \frac{\pi a^2}{2} u, \quad (2.A.8)$$

so that

$$\dot{S}_b \sim 2\pi u \dot{u}, \qquad \dot{V}_b \sim \frac{\pi a^2}{2} \dot{u}. \quad (2.A.9)$$

Introducing these estimates into Eq. (2.A.6) shows that the contribution of cytosol flow through the cortex dominates for small membrane displacements u. Hence,

$$\dot{E} \sim \frac{\eta h A_b}{4\xi^2} \dot{u}^2. \quad (2.A.10)$$

Finally, we can identify an effective friction coefficient μ_{eff} for the motion of the membrane above the cortex. The drag force is $F_f = \mu_{\text{eff}} \dot{u}$, which entails a dissipation $\dot{E} = F_f \dot{u} = \mu_{\text{eff}} \dot{u}^2$. Hence, $\mu_{\text{eff}} \sim \eta h A_b / \xi^2$, so that the friction coefficient of membrane displacements per unit area is $\mu \equiv \mu_{\text{eff}} / A_b \sim \eta h / \xi^2$.

2.B Hydrodynamic interactions in a nearly flat membrane

In this section, we derive the shape dynamics of a membrane under generic membrane forces, accounting for the hydrodynamic interactions mediated by the surrounding fluid [Seifert 1997]. For a nearly flat membrane, the height function $u(\vec{x},t)$ follows Eq. (2.22):

$$\partial_t u(\vec{x},t) \approx v_z(\vec{r},t)|_{z=0}\,. \tag{2.B.1}$$

Here, $\vec{v}(\vec{r},t)$ is the flow field of the surrounding fluid, which is the solution of Stokes' equation in the incompressible regime, Eq. (2.23):

$$\vec{\nabla}P - \eta\nabla^2\vec{v} = \vec{T}, \qquad \vec{\nabla}\cdot\vec{v} = 0. \tag{2.B.2}$$

To solve it, we introduce the Fourier components

$$\tilde{v}_{\alpha,\vec{k}} = \int_{\mathcal{V}} v_\alpha(\vec{r})\, e^{-i\vec{k}\cdot\vec{r}}\, d^3\vec{r}, \qquad \tilde{T}_{\alpha,\vec{k}} = \int_{\mathcal{V}} T_\alpha(\vec{r})\, e^{-i\vec{k}\cdot\vec{r}}\, d^3\vec{r}. \tag{2.B.3}$$

In Fourier space, the general solution to Stokes' equation reads [Doi 1986]

$$\tilde{v}_{\alpha,\vec{k}} = \frac{1}{\eta k^2}\left[\delta_{\alpha\beta} - \frac{k_\alpha k_\beta}{k^2}\right]\tilde{T}_{\beta,\vec{k}}, \tag{2.B.4}$$

where the pressure field $P(\vec{r},t)$ has been eliminated via the incompressibility condition.

Now, since we need to compute the flow field at the membrane plane $z=0$, we introduce the planar Fourier components

$$\tilde{v}_{\alpha,\vec{q}}(z) = \int_{\mathcal{S}} v_\alpha(\vec{r})\, e^{-i\vec{q}\cdot\vec{x}}\, d^2\vec{x}, \qquad \tilde{T}_{\alpha,\vec{q}}(z) = \int_{\mathcal{S}} T_\alpha(\vec{r})\, e^{-i\vec{q}\cdot\vec{x}}\, d^2\vec{x}, \tag{2.B.5}$$

where $\vec{q}$ is the in-plane wavevector, so that $\vec{k} = (\vec{q}, k_z)$. Then, introducing the inverse of Eq. (2.B.3), we rewrite

$$\tilde{v}_{\alpha,\vec{q}}(z) = \frac{1}{2\pi}\int_{-\infty}^{\infty} \tilde{v}_{\alpha,\vec{k}}\, e^{ik_z z}\, dk_z, \qquad \tilde{T}_{\alpha,\vec{q}}(z) = \frac{1}{2\pi}\int_{-\infty}^{\infty} \tilde{T}_{\alpha,\vec{k}}\, e^{ik_z z}\, dk_z. \tag{2.B.6}$$

To relate $\tilde{v}_{\alpha,\vec{q}}(z)$ to $\tilde{T}_{\alpha,\vec{q}}(z)$, we introduce the Oseen solution Eq. (2.B.4):

$$\begin{aligned}\tilde{v}_{\alpha,\vec{q}}(z) &= \frac{1}{2\pi\eta}\int_{-\infty}^{\infty}\frac{1}{q^2+k_z^2}\left[\delta_{\alpha\beta} - \hat{k}_\alpha\hat{k}_\beta\right]\tilde{T}_{\beta,\vec{k}}\, e^{ik_z z}\, dk_z \\ &= \frac{1}{2\pi\eta}\int_{-\infty}^{\infty}\int_{-\infty}^{\infty}\frac{1}{q^2+k_z^2}\left[\delta_{\alpha\beta} - \hat{k}_\alpha\hat{k}_\beta\right]\tilde{T}_{\beta,\vec{q}}(z')\, e^{ik_z(z-z')}\, dk_z\, dz',\end{aligned} \tag{2.B.7}$$

where we have used that $k^2 = q^2 + k_z^2$, and we have introduced the inverse of Eq. (2.B.6) for $\tilde{T}_{\beta,\vec{k}}$. At this point, to compute the integrals, we must use the

specific components of the tensor $\hat{k}_\alpha \hat{k}_\beta$, where $\hat{k} = (\vec{q}, k_z)/\sqrt{q^2 + k_z^2}$. To this end, we express the velocity and force fields in a vector base comprising $\hat{z}$, $\hat{q}$, and the normal in-plane vector $\hat{t}$:

$$\tilde{\vec{v}}_{\vec{q}}(z) = \tilde{v}_{z,\vec{q}}(z)\,\hat{z} + \tilde{v}_{\ell,\vec{q}}(z)\,\hat{q} + \tilde{v}_{t,\vec{q}}(z)\,\hat{t}, \tag{2.B.8a}$$

$$\tilde{\vec{T}}_{\vec{q}}(z) = \tilde{T}_{z,\vec{q}}(z)\,\hat{z} + \tilde{T}_{\ell,\vec{q}}(z)\,\hat{q} + \tilde{T}_{t,\vec{q}}(z)\,\hat{t}. \tag{2.B.8b}$$

Thus, the flow field Fourier components read

$$\tilde{v}_{z,\vec{q}}(z) = \frac{1}{2\pi\eta}\int_{-\infty}^{\infty}\int_{-\infty}^{\infty}\frac{1}{q^2+k_z^2}\left[\left[1-\frac{k_z^2}{q^2+k_z^2}\right]\tilde{T}_{z,\vec{q}}(z') - \frac{|k_z|q}{q^2+k_z^2}\tilde{T}_{\ell,\vec{q}}(z')\right]e^{ik_z(z-z')}\,dk_z\,dz', \tag{2.B.9a}$$

$$\tilde{v}_{\ell,\vec{q}}(z) = \frac{1}{2\pi\eta}\int_{-\infty}^{\infty}\int_{-\infty}^{\infty}\frac{1}{q^2+k_z^2}\left[\left[1-\frac{q^2}{q^2+k_z^2}\right]\tilde{T}_{\ell,\vec{q}}(z') - \frac{q|k_z|}{q^2+k_z^2}\tilde{T}_{z,\vec{q}}(z')\right]e^{ik_z(z-z')}\,dk_z\,dz', \tag{2.B.9b}$$

$$\tilde{v}_{t,\vec{q}}(z) = \frac{1}{2\pi\eta}\int_{-\infty}^{\infty}\int_{-\infty}^{\infty}\frac{1}{q^2+k_z^2}\tilde{T}_{t,\vec{q}}(z')\,e^{ik_z(z-z')}\,dk_z\,dz'. \tag{2.B.9c}$$

Then, performing the Fourier transforms over k_z,

$$\tilde{v}_{z,\vec{q}}(z) = \frac{1}{4\eta q}\int_{-\infty}^{\infty}\Big[[1+q|z-z'|]\,\tilde{T}_{z,\vec{q}}(z') - iq(z-z')\tilde{T}_{\ell,\vec{q}}(z')\Big]\,e^{-q|z-z'|}\,dz', \tag{2.B.10a}$$

$$\tilde{v}_{\ell,\vec{q}}(z) = \frac{1}{4\eta q}\int_{-\infty}^{\infty}\Big[[1-q|z-z'|]\,\tilde{T}_{\ell,\vec{q}}(z') - iq(z-z')\tilde{T}_{z,\vec{q}}(z')\Big]\,e^{-q|z-z'|}\,dz', \tag{2.B.10b}$$

$$\tilde{v}_{z,\vec{q}}(z) = \frac{1}{2\eta q}\int_{-\infty}^{\infty}\tilde{T}_{t,\vec{q}}(z')\,e^{-q|z-z'|}\,dz'. \tag{2.B.10c}$$

Now, at the lowest order in $\delta u\,(\vec{x}, t)$, the force density is simply evaluted at the plane $z = 0$:

$$\tilde{T}_{\alpha,\vec{q}}(z) \approx \tilde{F}_{\alpha,\vec{q}}\,\delta\,(z)\,, \tag{2.B.11}$$

which yields

$$\tilde{v}_{z,\vec{q}}(z) \approx \frac{1}{4\eta q}\Big[[1+q|z|]\,\tilde{F}_{z,\vec{q}} - iqz\tilde{F}_{\ell,\vec{q}}\Big]\,e^{-q|z|}, \tag{2.B.12a}$$

$$\tilde{v}_{\ell,\vec{q}}(z) \approx \frac{1}{4\eta q}\Big[[1-q|z|]\,\tilde{F}_{\ell,\vec{q}} - iqz\tilde{F}_{z,\vec{q}}\Big]\,e^{-q|z|} \tag{2.B.12b}$$

$$\tilde{v}_{z,\vec{q}}(z) \approx \frac{1}{2\eta q}\tilde{F}_{t,\vec{q}}\,e^{-q|z|}. \tag{2.B.12c}$$

Hence, the hydrodynamics of membrane undulations in Fourier space reads

$$\partial_t \delta\tilde{u}_{\vec{q}} = \tilde{v}_{z,\vec{q}}(0) = \frac{1}{4\eta q}\tilde{F}_{z,\vec{q}} \tag{2.B.13}$$

in terms of the Fourier components $\tilde{F}_{z,\vec{q}}$ of generic normal forces exerted by the membrane on the fluid. Thus, the factor $1/(4\eta q)$ in Eq. (2.B.13) accounts for the long-range hydrodynamic interactions along the membrane for any local forces that the membrane may exert on the fluid.

2.C Membrane hydrodynamics over a porous cortex

In this section, we comment on the effects of the cortex on membrane hydrodynamics. In general, the presence of confinement or some kind of boundary conditions modifies the flow field of the fluid surrounding the membrane (Eqs. (2.24) and (2.25), and hence impacts the growth rate of membrane undulations [Seifert 1997]. In our model, under the adiabatic approximation for linker kinetics, membrane-cortex adhesion acts as an effective harmonic potential of stiffness $k\rho_b^{\mathrm{eq}}$ on the membrane (Section 2.5). For a membrane in a harmonic potential, the presence of a nearby porous wall with permeation length L_p at a distance D was shown to modify the growth rate by a mode-dependent factor [Gov 2004b]:

$$\omega_q = \omega_q^0 e^{-2Dq} \frac{e^{2Dq}\left(1+4L_pq\right) - 1 - 2Dq - 2\left(Dq\right)^2\left(1+2L_pq\right)}{1+4L_pq}, \qquad (2.C.1)$$

where ω_q^0 is the growth rate in the absence of hydrodynamic effects of the cortex (Eq. (2.44)). The cortical permeation length, which indicates the typical length of flow penetration into the cortex, is defined as $L_p = \sqrt{\eta\left(1-\phi_v\right)K_p}$, where η is the cytosol viscosity, ϕ_v is the cortex volume fraction, and K_p is its volume permeability [Ranft 2012].

If the cortex is sufficiently porous (large L_p), its sole qualitative effect on membrane hydrodynamics is to limit the relaxation rate of the large-wavelength modes to a finite value (Fig. 2.C.1). In addition, the characteristic wavelength with the slowest relaxation rate is slightly increased. However, if the cortex is too dense (small L_p), or too close to the membrane (small D), the growth rate may feature two local maxima or even become monotonous (Fig. 2.C.1). The membrane-cortex distance has been recently estimated to be $D \sim 100$ nm [Clausen 2017]. In turn, detailed experimental measurements of cortex porosity and permeability are lacking. Thus, a rough estimate for the permeation length L_p is simply the pore size of the cortical meshwork, $L_p \sim \xi \sim 10-50$ nm [Charras 2008b, Charras 2009, Moeendarbary 2013, Bovellan 2014]. Alternatively, we may estimate the cortex permeation length from the mechanical properties of the whole cytoplasm considered as a poroelastic medium [Charras 2005, Charras 2008b, Charras 2009, Moeendarbary 2013], which was estimated to feature a viscosity $\eta \sim 0.003 - 0.2$ Pa·s and a volume permeability $K_p \sim 0.004-0.025\ \mu\mathrm{m}^2/(\mathrm{Pa}\cdot\mathrm{s})$ [Charras 2008c]. Hence, we estimate $L_p \sim 5 - 50$ nm. Similar results are obtained from cortex permeability estimates inferred from simulations of bleb formation [Strychalski 2013].

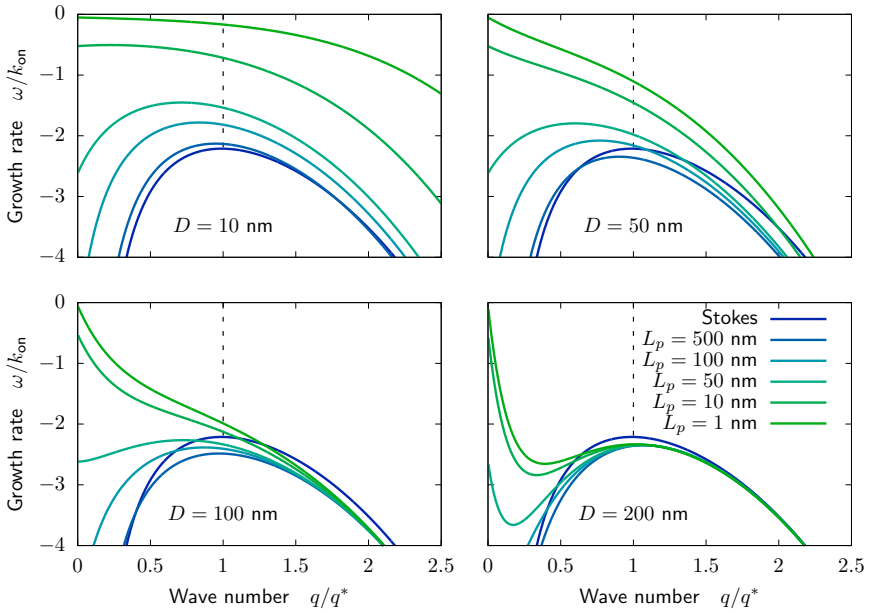

Figure 2.C.1 | Growth rate of undulations of a membrane adhered to a porous cortex. Curves are shown for different values of the membrane-cortex distance D and the cortical permeation length L_p. The curve in the absence of cortical influence on membrane hydrodynamics (Stokes) is shown for comparison. The wave vector is scaled with the characteristic wavelength $2\pi/q^* = \lambda^* = \lambda_c\,(\rho_b^{\mathrm{eq}} = \rho_0)$ (Eq. (2.45)).

3 Bleb nucleation

Contents

Abstract

Blebs are cellular protrusions arising from a local detachment of the cell membrane from the underlying actin cortex. In this chapter, we study the nucleation of blebs by means of the kinetic model of membrane-cortex adhesion introduced in Chapter 2. The model shows that bleb nucleation is governed by membrane peeling, namely the fracture propagation process whereby adjacent membrane-cortex bonds sequentially break. By this mechanism, the growth or shrinkage of a detached membrane patch is completely determined by the linkers' binding kinetics, regardless of the energetic cost of the local detachment. We predict the critical nucleation radius for membrane peeling and the corresponding effective energy barrier. We estimate that these quantities are typically smaller than those predicted by classical nucleation theory, implying a much faster nucleation. Then, by means of numerical simulations of a fluctuating adhered membrane, we obtain the statistics of bleb nucleation times as

a function of the pressure difference across the membrane. The determinant role of membrane peeling changes our understanding of bleb nucleation, opening new directions in the study of blebs.

3.1 Introduction

The cell membrane is adhered to the underlying actin cortex via a number of specific linker molecules [Sheetz 2001] (Fig. 2.3). These linkers continuously bind and unbind, and they are under stress due both to osmotic pressure on the membrane and to myosin-generated cortical tension (Fig. 2.4). Consequently, a fluctuation may locally unbind the membrane from the cortex. Upon detachment, intracellular pressure inflates the unbound membrane, which acquires the shape of a spherical cap. The ensuing balloon-like membrane protrusion is known as a cellular bleb (Fig. 3.1a). Eventually, a new cortical layer starts to assemble beneath the detached membrane and retracts the bleb. Therefore, the life cycle of a bleb can be divided into three stages: nucleation, growth, and retraction (Figs. 3.1b and 3.1c) [Charras 2008b, Charras 2008a, Charras 2008c, Charras 2006].

Blebbing occurs during several processes of cellular physiology [Charras 2008a, Charras 2008c], such as apoptosis [Mills 1998, Coleman 2001], cytokinesis [Sedzinski 2011], and cell spreading [Norman 2010, Norman 2011], and it is specifically employed for cell motility [Charras 2008c, Fackler 2008, Paluch 2013]. The so-called bleb-based motility proceeds in cycles of bleb extension at the leading edge followed by retraction of the cell rear (Fig. 3.2). This motility mode is primarily used by cell types such as amoebae [Langridge 2006, Maugis 2010, Zatulovskiy 2014], embryonic cells [Blaser 2006], and invasive cancer cells [Sahai 2003, Khajah 2016]. However, most cells have versatile migration strategies that rely on different motility modes depending on environmental conditions. Specifically, external cues such as confinement, substrate adhesivity, and chemokine gradients, can induce transitions between blebs and lamellipodia, and even promote their coexistence and cooperation in many cell types. Therefore, a physical understanding of blebbing will shed light on bleb-based motility, with potential implications for the regulation of different cell motility modes [Paluch 2006, Yoshida 2006, Lämmermann 2009, Diz-Muñoz 2010, Bergert 2012, Paluch 2013, Tozluoğlu 2013, Tyson 2014, Liu 2015, Ruprecht 2015, Welch 2015, Mierke 2015, Diz-Muñoz 2016, Ibo 2016].

Despite their biological relevance, the physical mechanisms that govern bleb formation are not well understood. Blebs may result from membrane-cortex detachments, which can be understood in terms of the unbinding transition that we predicted in Chapter 2 for a flat membrane. However, the spontaneous formation of a bleb is driven by local fluctuations. Hence, it is a nucleation process that requires a membrane detachment of a minimum size. What determines the critical size above which a local membrane detachment grows to form a bleb? To answer this question, in this chapter we study bleb nucleation by means of the kinetic model for membrane-cortex adhesion introduced in Chapter 2.

In Section 3.2, we propose that the mechanism that governs bleb nucleation is membrane peeling from the cortex — a process whereby adjacent membrane-cortex bonds sequentially break, thus leading to bleb growth. We show that membrane peeling, which is entirely controlled by linker kinetics, completely determines the growth or decay of a local membrane detachment regardless of its energetic cost. Accordingly, we predict the critical radius for bleb nucleation through membrane

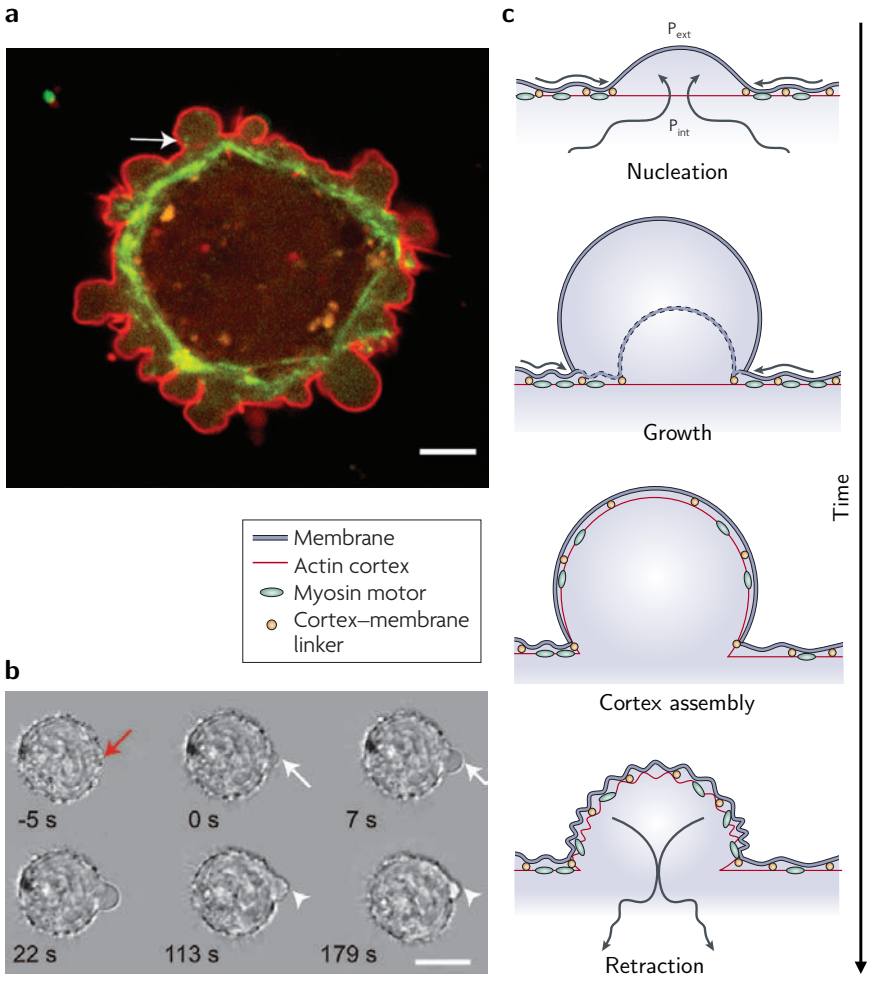

Figure 3.1 | Life cycle of a bleb. a, Blebs are balloon-like protrusions of unbound membrane. In melanoma cells lacking filamin, a membrane-cortex linker protein, the membrane (red) detaches from the cortex (myosin regulatory light chain, green), forming blebs. Some cortex foci appear in retracting blebs (arrow). Scale bar, 5 μm. From [Charras 2008a]. **b,** Local laser ablation of the cortex (red arrow) induces bleb nucleation and growth (white arrows). Later, the bleb retracts (white arrowheads). Cells are L929 fibroblasts. Scale bar, 10 μm. From [Tinevez 2009]. **c,** Sketch of the life cycle of a bleb. A bleb nucleated from a local detachment of the membrane from the cortex. Then, hydrostatic pressure in the cytoplasm inflates the bleb by driving cytosol flow through the cortex. Concomitantly, the membrane may peel from the cortex, increasing the diameter of the bleb base (dashed line). As pressure is released and bleb growth slows down, a new cortex assembles under the bleb membrane. Finally, myosin-generated contractility in the new cortex drives bleb retraction. Adapted from [Charras 2008c].

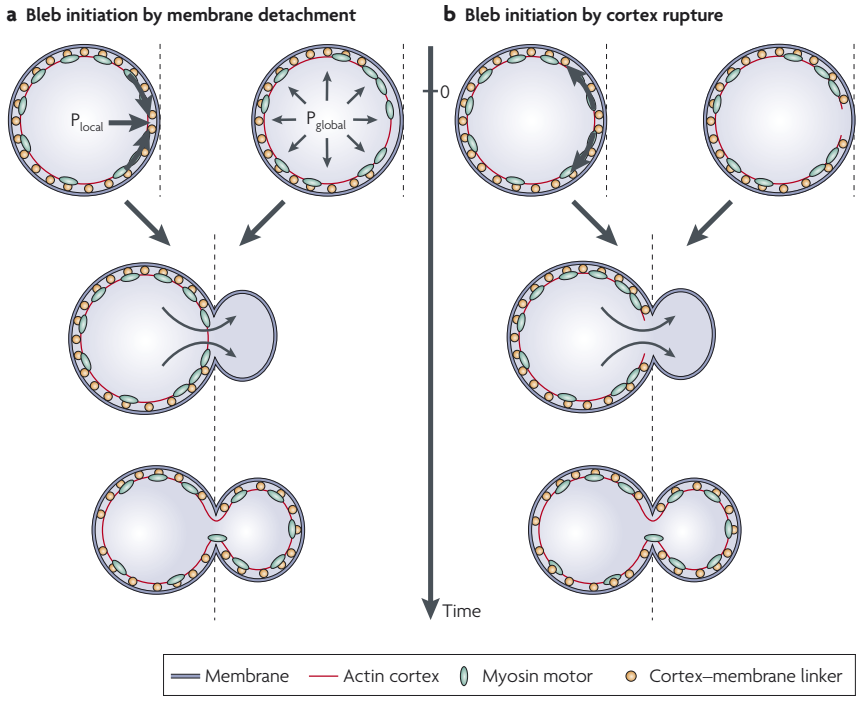

Figure 3.2 | Bleb-based motility. Bleb formation may be due to membrane-cortex detachment or to cortex rupture. **a,** Membrane-cortex detachment may be induced by a local contraction of the actomyosin cortex, which gives rise to a local increase in pressure (top left), or by a local decrease in membrane-cortex bonds (top right). **b,** The cortex can be torn by a high local contractile stress (top left) or by a local disassembly (top right). Upon bleb nucleation, the cytoplasm flows to inflate and expand the bleb. Then, the assembly of a new cortex underneath the bleb membrane is followed by a retraction of the cell rear, thus leading to cell motion. From [Charras 2008c].

peeling. In Section 3.3, we compare our predictions to those of classical nucleation theory. We estimate that the critical radius for membrane peeling is typically lower than the one predicted by classical nucleation theory. Therefore, we expect membrane peeling to entail a strong reduction of the bleb nucleation time scales. Then, in Section 3.4, we study the kinetics of bleb nucleation by means of numerical simulations of a fluctuating adhered membrane. Based on a formulation of first-passage-time statistics for the formation of a critical detachment, we obtain the probability distribution of bleb nucleation times as a function of the pressure difference across the membrane.

3.2 Bleb nucleation through membrane peeling

Upon a local membrane detachment, bleb growth could, in principle, proceed via several mechanisms: peeling of the membrane from the cortex, unfolding of membrane wrinkles, flow of membrane into the detached region, and incorporation of new cell membrane via fusion of intracellular vesicles in the vicinity of the detachment [Charras 2008a, Charras 2008b]. Experiments indicate that bleb growth occurs through a combination of membrane peeling and flow of lipids into the bleb (Fig. 3.3) [Charras 2008a, Charras 2008b]. Among these mechanisms, membrane peeling is the only one that increases the area of membrane-cortex detachment. Here, we focus on the very initial stage of bleb nucleation, in which an incipient detachment may either grow and lead to a bleb, or shrink to restore membrane-cortex adhesion.

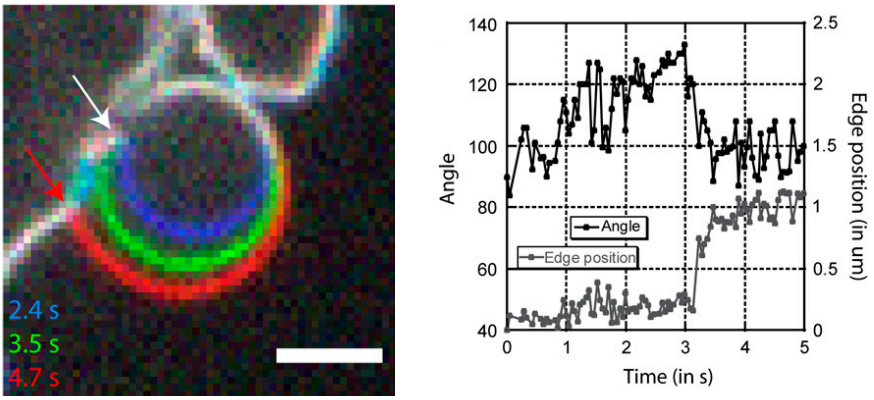

Figure 3.3 | Bleb growth through membrane peeling. Initially ($t \lesssim 3$ s), the contact point between the bleb membrane and the cell body (edge position) is pinned (white arrow), and the contact angle increases due to the flow of membrane into the bleb. However, at $t \approx 3$ s, the contact point depins and starts moving fast (~ 2 μm/s, towards red arrow), so that the area of the bleb base increases and the contact angle drops. Scale bar, 2 μm. Adapted from [Charras 2008b].

To explore this situation, we consider the interface between regions of attached and detached membrane (Fig. 3.4a). Based on the adhesion model introduced in Chapter 2, the detached region features a density of membrane-cortex bonds $\rho_b(\vec{x}, t)$ lower than the critical density $\rho_b^* = \alpha^* \rho_0 / \bar{u}^*$ for the unbinding transition. Here, ρ_0 is the density of available linkers. In turn, α^* is the solution of $\alpha^* e^{1+\alpha^*} = \chi^{-1}$, with χ the kinetic ratio $\chi \equiv k_{\text{off}}^0 / k_{\text{on}}$, which defines the critical pressure difference $f^* = \alpha^* \rho_0 k_B T / \delta$. Finally, $\bar{u}^*$ is the solution of $\bar{u}^* = \alpha^* \left(1 + \chi e^{\bar{u}^*}\right)$, which defines the critical linker stretching $u^* = \bar{u}^* u_0$, with $u_0 = k_B T / (k\delta)$ (see Section 2.2 for parameter definitions and details of the model). In contrast, in the attached region, the density of bonds is higher than the critical density ρ_b^*. Hence, we define the contact line between both regions as the set of points having exactly

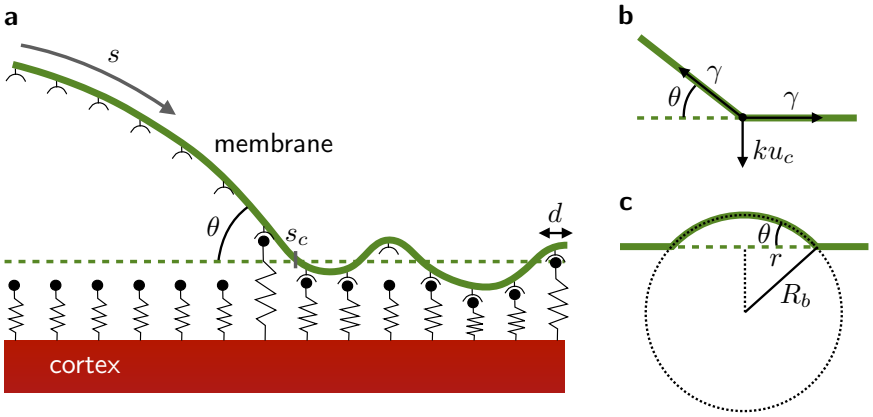

Figure 3.4 | Membrane peeling from the cortex. a, Sketch of a section of the interface between regions of attached and detached membrane, which are connected by the contact line at $s = s_c$, and form a contact angle θ. The dashed line indicates the equilibrium position of the uniformly attached membrane, u_{eq}. On the membrane, membrane-cortex bonds occupy an effective area of diameter d, due both to the lateral size of the receptor proteins and to their positional fluctuations. **b,** Normal force balance at the contact line: The adhesion force balances the vertical pulling by the unbound membrane. **c,** The unbound membrane forms a spherical cap of radius $R_b = 2\gamma/f$ with a detachment radius $r = R_b \sin\theta$.

the critical density of bonds. Thus, in terms of the arc length coordinate along the membrane, s, the contact line $s_c(t)$ is defined by the condition

$$\rho_b(s_c, t) = \rho_b^*. \tag{3.1}$$

Now, the velocity of the contact line, $v_c = ds_c/dt$, is known as the peeling speed of the membrane. If $v_c > 0$, a small detachment grows by peeling the membrane off the cortex. Conversely, if $v_c < 0$, the detachment shrinks, sequentially reforming membrane-cortex bonds to restore adhesion. To relate the peeling velocity to the binding kinetics of the linkers, we write the dynamics of the density of bonds in the reference frame co-moving with the contact line [Dembo 1988]. Defining the co-moving arc length coordinate $\bar{s}(t) \equiv s - s_c(t)$, Eq. (2.1) reads

$$\frac{d\rho_b(\bar{s})}{dt} = \frac{\partial\rho_b(\bar{s})}{\partial t} - v_c\frac{\partial\rho_b(\bar{s})}{\partial\bar{s}} = k_{\text{on}}[\rho_0 - \rho_b(\bar{s})] - k_{\text{off}}(u(\bar{s}))\,\rho_b(\bar{s}). \tag{3.2}$$

By definition, the density of bonds at the contact line, Eq. (3.1), is independent of time: $\partial_t\rho_b|_{s=s_c} = 0$. Hence, evaluating Eq. (3.2) at the contact line, we obtain

$$-v_c\left.\frac{\partial\rho_b}{\partial s}\right|_{s=s_c} = k_{\text{on}}[\rho_0 - \rho_b^*] - k_{\text{off}}(u_c)\,\rho_b^*, \tag{3.3}$$

where $u_c \equiv u(s_c, t)$ is the stretching of the bound linkers at the contact line. Then, the condition that separates detachment growth from shrinkage, namely $v_c = 0$,

corresponds to the equilibrium state of membrane-cortex adhesion, Eqs. (2.1) to (2.3), at the critical bond density ρ_b^*. Therefore, to fulfill $v_c = 0$, the bonds' stretching at the contact line must be the critical stretching, $u_c = u^*$. In conclusion, membrane peeling occurs if the stretching of the bonds at the contact line exceeds the critical value u^* defined above.

Next, to predict the critical detachment size for membrane peeling, we need to relate the stretching of the bonds at the contact line to the shape of the unbound membrane. To this end, without solving for the membrane shape across the contact region [Evans 1985,Garrivier 2002], we establish normal force balance at the contact line[1]. Neglecting bending forces, the elastic force of the linkers, ku_c, balances the vertical pulling due to the membrane tension γ of the unbound membrane (Fig. 3.4b):

$$2\pi r\gamma \sin\theta = N_c k u_c. \tag{3.4}$$

Here, θ is the contact angle formed by the detached membrane. Note that we assume that the unbound membrane is instantaneously inflated by the intracellular pressure. In turn, N_c is the number of bonds along the circular contact line of length $2\pi r$. To estimate this number, we consider that, because of their lateral size and positional fluctuations, the receptor proteins of membrane-cortex bonds cover an effective area of diameter d, presumably a few tens of nanometers, on the membrane (Fig. 3.4a). Consequently, the average number of bonds that fall in the contact line is $N_c \approx 2\pi r d\rho_b^*$.

Now, the unbound membrane is inflated by the pressure difference f to become a spherical cap of radius $R_b = 2\gamma/f$, as given by the Young-Laplace pressure drop [Dai 1999a]. In addition, the contact angle θ is geometrically related to the radius of the detachment, r, by $\sin\theta = r/R_b$ (Fig. 3.4c). Hence, the vertical pulling by the membrane at the contact line reads $2\pi r\gamma \sin\theta = \pi r^2 f$, namely the total force pushing on the unbound membrane, thus closing a relationship between r and u_c in Eq. (3.4). Thereby, the critical stretching for peeling, u^*, translates into a critical size of the detachment, r_p:

$$r_p = 2d\frac{f^*}{f}, \tag{3.5}$$

where $f^* = \rho_b^* k u^*$. Thus, r_p is a critical radius for membrane peeling. Since the peeling process ends up in a mature bleb, r_p indeed becomes a critical radius for bleb nucleation. Figure 3.5 plots r_p as a function of the pressure difference f (red line), separating those detachments that grow to form a bleb by peeling (green and blue regions) from those that shrink by healing the delamination (red region).

3.3 Comparison to classical nucleation theory

In this section, we compare our results for membrane peeling to the classical scenario for bleb nucleation. The classical approach to the nucleation of a new

[1] Note that, unlike along the normal direction, force balance in the direction parallel to the cortex involves friction forces that depend on the contact line velocity.

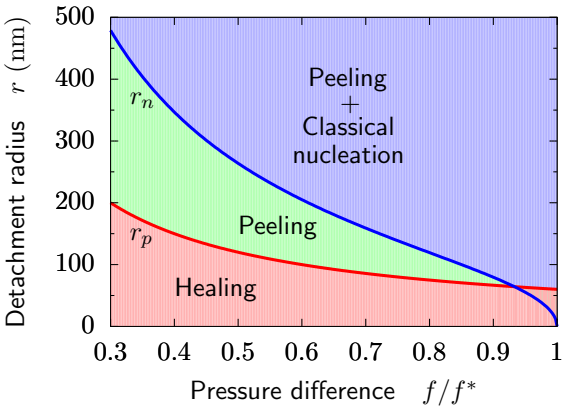

Figure 3.5 | Diagram of bleb nucleation. It indicates the predicted evolution of a local detachment of radius r of a membrane subject to a pressure difference f. Healing of the delamination occurs for $r < r_p$ (red region), whereas the membrane is peeled from the cortex for $r > r_p$ (green and blue regions). The critical radius for bleb nucleation through membrane peeling (red line) is given in Eq. (3.5). Classical bleb nucleation would occur only for $r > r_n$ (blue region), with the classical critical radius (blue line) given by Eq. (3.7). Parameter values are those in Table 2.1, plus $d = 30$ nm. For the chosen parameter estimates, membrane peeling requires smaller nucleation radii than classical energetic nucleation.

phase is based on the energy cost of forming a nucleus of such phase within the parent one. Thus, for bleb nucleation, we formulate the energy cost of a local membrane-cortex detachment (Appendix 3.A), which can be approximated by

$$E(r) \approx \pi r^2 w(f) - \frac{\pi f^2}{16\gamma} r^4. \tag{3.6}$$

Here, the first term accounts for the work of unbinding the membrane, where $w(f)$ is the pressure-dependent adhesion energy per unit area, Eq. (2.10). In turn, the second term combines the works associated to the increase in apparent membrane area and cell volume. For sufficiently small detachments, the positive contribution of adhesion loss dominates, hence favouring membrane reattachment. In contrast, for sufficiently large detachments, the negative contribution of volume expansion dominates, making detachment growth energetically favourable (Fig. 3.6). Thus, according to the classical theory, the maximum of the energy $E(r)$ indicates the critical radius for bleb nucleation (blue line in Fig. 3.5):

$$r_n = \sqrt{\frac{8\gamma\, w(f)}{f^2}}. \tag{3.7}$$

Remarkably, unlike in the classical picture, bleb nucleation through membrane peeling is not controlled by the energy cost of forming a local detachment. Instead,

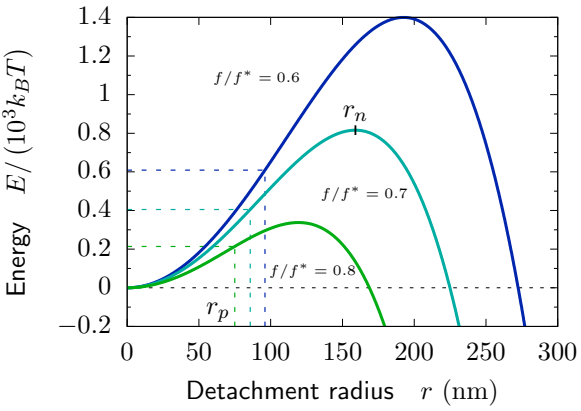

Figure 3.6 | Energy cost of a detachment. Equation (3.6) for some values of the pressure difference on the membrane. The maximum of the energy indicates the critical radius r_n for classical bleb nucleation (Eq. (3.7), see Fig. 3.5). Membrane peeling, which occurs at a critical radius r_p (Eq. (3.5), see Fig. 3.5), may yield a reduced energy barrier for bleb nucleation (dashed lines). Parameter values are those in Table 2.1, plus $d = 30$ nm.

the peeling process is entirely governed by the binding kinetics of membrane-cortex linkers. This is apparent from the fact that the critical pressure f^* is only a function of linker parameters. Hence, the critical radius in Eq. (3.5) is completely determined by the kinetics of the linkers and the force f that they withstand[2]. Indeed, compared to the rest, the linkers at the contact line sustain the additional pulling due to the unbound membrane. Consequently, even though the rest of the linkers remain below the unbinding threshold, the linkers at the contact line may unbind, thereby unchaining membrane peeling and bleb growth. This effect is not captured by the classical nucleation approach to bleb formation [Sens 2015, Sheetz 2006, Charras 2008b, Norman 2010, Lim 2012a].

Finally, we note that the classical mechanism is irrelevant even if the classical nucleation radius r_n is smaller than r_p, since any detachment of radius r such that $r_n < r < r_p$ would unavoidably shrink, even going uphill in energy. Similarly, for $r_p < r_n$, the growth of a detachment with $r_p < r < r_n$ also goes uphill in the energy landscape (see Fig. 3.6). Therefore, detachment growth or shrinkage is not controlled by its global energy $E(r)$ but by the local dynamics of the contact line, and hence by linker kinetics. Nevertheless, the probability that a fluctuation produces a detachment of a given size is still determined by the energy, Eq. (3.6). Hence, bleb nucleation through membrane peeling entails overcoming an effective

[2]Note, in particular, that, unlike in the classical approach, the critical radius for bleb nucleation through membrane peeling is independent of membrane tension γ, in agreement with recent numerical results [Manakova 2016]. This is because, although membrane tension pulls on the linkers at the contact line, it also decreases the contact angle θ by increasing the radius of the bleb, R_b, and these two effects exactly compensate in the force balance (see Eqs. (3.4) and (3.5)).

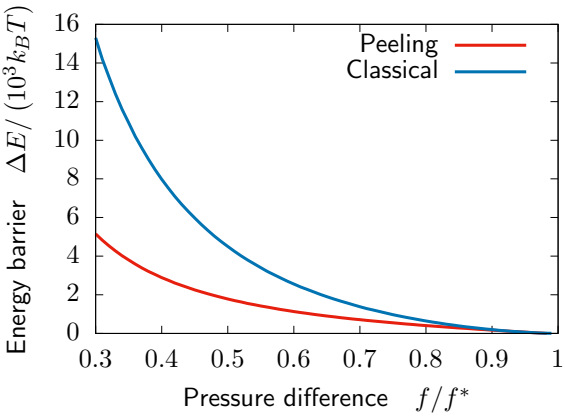

Figure 3.7 | Energy barrier for bleb nucleation. The effective energy barrier for bleb nucleation through membrane peeling, $E(r_p)$ (see details in Appendix 3.A), may be lower than that for classical bleb nucleation, $E(r_n)$, especially at low pressure differences. Parameter values are those in Table 2.1, plus $d = 30$ nm.

energy barrier $E(r_p)$ (dashed lines in Fig. 3.6, see details in Appendix 3.A). We estimate that this effective barrier is typically lower than the classical one (Fig. 3.7), so that membrane peeling would strongly reduce the bleb nucleation time, $t_{\text{nuc}} \propto e^{\beta E(r_p)}$, as compared to that of the classical nucleation mechanism, $t_{\text{nuc}} \propto e^{\beta E(r_n)}$.

3.4 Kinetics of bleb nucleation

In this section, we study the kinetics of bleb nucleation. To this end, we account for fluctuations in membrane-cortex adhesion, which give rise to spontaneous local membrane detachments.

First, to account for thermal fluctuations in membrane motion, we add a white Gaussian noise term to Eq. (2.37):

$$\begin{aligned} \partial_t \delta\tilde{u}_{\vec{0}} &= -\frac{1}{\mu}\left[k\rho_b^{\text{eq}}\,\delta\tilde{u}_{\vec{0}} + k u_{\text{eq}}\,\delta\tilde{\rho}_{b,\vec{0}}\right] + \tilde{\zeta}_{\vec{0}}(t)\,; \\ \left\langle \tilde{\zeta}_{\vec{0}}(t)\,\tilde{\zeta}_{\vec{0}}(t')\right\rangle &= \frac{2k_B T\pi\lambda_c^2}{\eta}\delta(t-t')\,, \end{aligned} \tag{3.8a}$$

$$\begin{aligned} \partial_t \delta\tilde{u}_{\vec{q}} &= -\frac{1}{4\eta q}\left[\left(\kappa q^4 + \gamma q^2 + k\rho_b^{\text{eq}}\right)\delta\tilde{u}_{\vec{q}} + k u_{\text{eq}}\,\delta\tilde{\rho}_{b,\vec{q}}\right] + \tilde{\zeta}_{\vec{q}}(t)\,; \\ \left\langle \tilde{\zeta}_{\vec{q}}(t)\,\tilde{\zeta}_{\vec{q}'}(t')\right\rangle &= \frac{k_B T}{2\eta q}\delta_{\vec{q},-\vec{q}'}\delta(t-t')\,. \end{aligned} \tag{3.8b}$$

Here, the noise terms fulfill the fluctuation-dissipation theorem. Note that the noise amplitude of the uniform ($\vec{q} = \vec{0}$) mode of membrane motion involves the membrane area. Because of thermal fluctuations, uniform membrane motion occurs

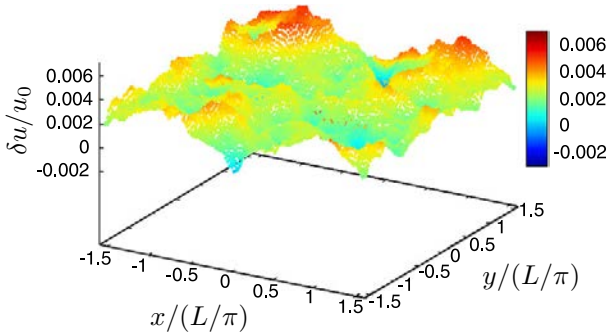

Figure 3.8 | Snapshot of membrane undulations from simulations. Simulation parameters are $L = 2\ \mu$m, $n = 1024$, and $\Delta t = 0.01 k_{\text{on}}^{-1}$. The rescaling length is $u_0 = k_B T/(k\delta)$. Parameter values are those in Table 2.1, except for $\mu = 50$ Pa·s/μm.

mainly at length scales shorter than the correlation length of membrane undulations, which we approximate by the characteristic wavelength λ_c, Eq. (2.45). Thus, we use $\pi\lambda_c^2$ as the area of uniform membrane motion.

Second, we account for fluctuations in the number of bound linkers. At the mesoscopic level of description, chemical reactions follow discrete Markov processes described by master equations. However, for a chemical reaction described by a single variable and involving a sufficiently large number of molecules, the discrete master equation can be approximated by a continuous Fokker-Planck equation [Gillespie 1980]. Hence, the stochastic reaction kinetics can be approximated by the so-called chemical Langevin equation, which features a multiplicative Gaussian white noise term [Gillespie 2000, Gillespie 2002]. Based on this approach, we include such a noise term to Eq. (2.40):

$$\begin{aligned}\partial_t \delta\rho_b(\vec{x}) = &-\rho_b^{\text{eq}}\beta k\delta k_{\text{off}}^0 e^{\beta k u_{\text{eq}}\delta}\delta u(\vec{x}) - \left[k_{\text{on}} + k_{\text{off}}^0 e^{\beta k u_{\text{eq}}\delta}\right]\delta\rho_b(\vec{x}) \\ &+ \left[k_{\text{on}}\left[\rho_0 - \rho_b^{\text{eq}}\right] + \rho_b^{\text{eq}} k_{\text{off}}^0 e^{\beta k u_{\text{eq}}\delta} + \rho_b^{\text{eq}}\beta k\delta k_{\text{off}}^0 e^{\beta k u_{\text{eq}}\delta}\delta u(\vec{x})\right. \\ &\left. + \left[k_{\text{off}}^0 e^{\beta k u_{\text{eq}}\delta} - k_{\text{on}}\right]\delta\rho_b(\vec{x})\right]^{1/2} \frac{\Gamma(t)}{\sqrt{\pi\lambda_c^2}}; \\ &\langle\Gamma(t)\Gamma(t')\rangle = \delta(t-t'), \quad (3.9)\end{aligned}$$

where we have taken the Itô prescription. Note that the noise term also involves the membrane area, which we again identify with the area of correlated membrane undulations.

Then, we simulate Eqs. (3.8) and (3.9) on a square membrane patch of side $L = n\Delta r = 2\pi/\Delta q$, with n the number of grid points per side, and periodic boundary conditions (Fig. 3.8). Thermal noise is directly implemented in Fourier space [García-Ojalvo 1992, García-Ojalvo 1999]. Simulations require two Fourier transforms at each time step to couple the Fourier-space evolution of membrane undulations to the real-space evolution of the bond density. Therefore, our numerical

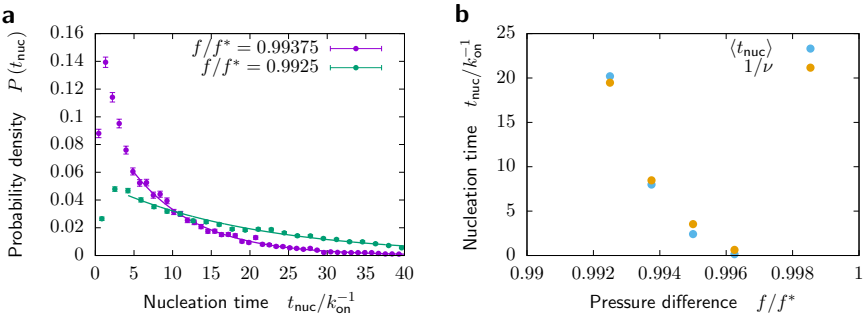

Figure 3.9 | Statistics of bleb nucleation times. a, Probability distribution of bleb nucleation times for two values of the pressure difference f. The long-time tails are fitted by an exponential $P(t_{nuc}) \propto e^{-\nu t_{nuc}}$. **b,** The average time of bleb nucleation, as well as the characteristic time scale $1/\nu$, decrease with the pressure difference across the membrane. Simulation parameters are $L = 2\ \mu$m, $n = 1024$, and $\Delta t = 0.01 k_{on}^{-1}$. Parameter values are those in Table 2.1, except for $\mu = 50$ Pa·s/μm.

procedure builds on the so-called Fourier-space Brownian dynamics (FSBD) method [Lin 2004, Brown 2008] for the simulation of continuum models of membrane dynamics, extending it to include the stochastic binding dynamics of the linkers, which must be evolved in real space.

For any simulation, at any chose pressure difference f, we let the system reach equilibrium, which we ensure by demanding that the fluctuations' correlation matrix is saturated. Then, we use an equilibrated snapshot to start a new simulation under the same conditions, with which we probe bleb nucleation. The simulation model is valid for small perturbations and hence cannot capture the complete formation of the bleb. However, it allows us to determine the statistics of bleb nucleation, which reduces to the first-passage-time statistics of finding a detachment larger than the critical size. To identify detachments, at each time step we identify the points $\vec{x}_n$ that feature a density of bonds below the critical one, $\rho_b(\vec{x}_n, t) < \rho_b^*$, which are candidates to nucleate a bleb. Then, to identify nucleation events, we apply the following criterion: A bleb of detached radius r is said to nucleate at point $\vec{x}_n$ at time t if the average density of bonds within a circle of radius $r > r_p$ centered at $\vec{x}_n$ falls below the critical density for membrane-cortex unbinding, $\langle \rho_b(\vec{x} - \vec{x}_n, t) \rangle_{|\vec{x}-\vec{x}_n| \leq r} < \rho_b^*$, whereas adhesion is restored within a slightly larger circle, $\langle \rho_b(\vec{x} - \vec{x}_n, t) \rangle_{|\vec{x}-\vec{x}_n| \leq r+\Delta r} > \rho_b^*$. Therefore, circles of increasing radius around the candidate points are considered until the nucleation criterion is fulfilled. A minimal radius $r_p(f)$ is demanded according to the critical radius for bleb nucleation through membrane peeling, Eq. (3.5) (red line in Fig. 3.5).

Employing this criterion, we obtain the histogram of bleb nucleation times at a given pressure difference f (Fig. 3.9a). We find that the probability distribution of bleb nucleation times, $P(t_{nuc})$, features an exponential tail $\propto e^{-\nu t_{nuc}}$, even for

pressures very close to that of the unbinding transition[3], f^*. This fact indicates that the nucleation process is dominated by a single time scale $1/\nu \propto e^{\beta E(r_p)}$, as is usual in activation processes [Schuss 2010, Risken 1989]. We also find that the average nucleation time $\langle t_{\mathrm{nuc}} \rangle$ decreases with increasing pressure difference (Fig. 3.9b). Moreover, the characteristic time $1/\nu$ of the exponential decay of the probability distribution, obtained from the fits in Fig. 3.9a, closely approaches the average $\langle t_{\mathrm{nuc}} \rangle$, which further confirms that it strongly dominates the kinetics of bleb nucleation.

3.5 Discussion and conclusions

In summary, we have shown that membrane peeling governs bleb nucleation, which is thus controlled by the binding kinetics of membrane-cortex linkers. We have argued that the classical approach based on the energy of bleb formation does not capture the physics of the peeling process, and hence it does not provide a complete description of bleb nucleation. We have predicted the critical radius for bleb nucleation through membrane peeling, as well as its effective energy barrier, which we have estimated to be typically lower than that of classical nucleation theory. Our predictions can be experimentally tested by inducing local membrane detachments of controlled size, for instance via laser ablation of the cortex [Tinevez 2009] or by locally controlling myosin activity or linker density, for example by means of optogenetic tools [Valon 2017]. Experiments in well-controlled reconstituted systems [Loiseau 2016] could be particularly suited to distinguish the essential mechanisms of bleb nucleation. Specifically, the dependence of the critical radius on the pressure difference on the membrane (Fig. 3.5) or its independence on membrane tension allows distinguishing whether the classical or the peeling mechanism prevails.

By means of simulations, we have studied the kinetics of bleb nucleation. Previous simulation approaches to bleb formation either imposed a maximal length of individual membrane-cortex linkers [Spangler 2011, Lim 2012a, Tyson 2014, Taloni 2015] or directly induced nucleation by removing some of them [Young 2010, Strychalski 2013, Woolley 2015, Manakova 2016]. In contrast, we have proposed a nucleation criterion based on the unbinding transition that results from the cooperative failure of membrane-cortex bonds. Moreover, by means of a first-passage-time formulation, our criterion naturally accounts for membrane peeling. Using this approach, we have obtained the distribution of bleb nucleation times as a function of the stress on the membrane. These results could be experimentally tested by measuring blebbing times in cells with perturbed cortical activity or subject to micropipette suction [Rentsch 2000, Merkel 2000, Tinevez 2009, Brugués 2010, Campillo 2012, Sliogeryte 2014].

Our results on the distribution of nucleation times for blebs (Fig. 3.9) are parallel to those reported for membrane adhesion in Figs. 4-5 of [Bihr 2012].

[3] Only pressures very close to the unbinding transition at f^* are explored because of computation time limitations.

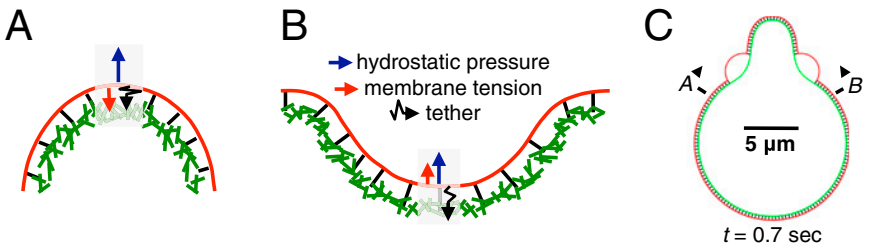

Figure 3.10 | Preferential nucleation of blebs in negatively curved sites. Depending on the sign of the membrane curvature, the normal component of membrane tension (red arrow) either opposes or adds to the pressure difference across the membrane (blue arrow). Consequently, bleb nucleation is facilitated in negatively curved regions, such as the flanks of a protrusion. From [Tyson 2014].

In cell adhesion, thermal fluctuations are typically unable to overcome the high energy barriers associated to the nucleation of adhesion domains. Consequently, processes like linker aggregation or cortical remodelling are usually required to achieve nucleation in reasonable time scales [Zhang 2008, Vink 2013]. In contrast, by yielding a reduced energy barrier essentially controlled by cortical tension (Figs. 3.6 and 3.7), we speculate that membrane peeling could allow bleb nucleation to proceed without the need of additional processes.

Finally, our model for peeling sheds light on the mechanisms of homogeneous bleb nucleation. Our results could now be generalized to address the role of membrane peeling in the nucleation of blebs at preferential sites determined by membrane curvature (Fig. 3.10) [Tyson 2014, Collier 2017]. In future studies, our approach could also be extended beyond the nucleation stage to study bleb growth, comparing the results to experiments [Charras 2008b, Tinevez 2009, Peukes 2014] and simulations [Young 2010, Spangler 2011, Lim 2012a, Strychalski 2013, Tyson 2014, Woolley 2015, Taloni 2015, Manakova 2016]. In addition, our stochastic simulation scheme could be employed to investigate the role of membrane-cortex adhesion on the statistics of membrane fluctuations (see Section 2.5).

Acknowledgements

I thank Pierre Sens and Jacques Prost for discussions.

Appendices

3.A Energy of bleb formation

In this appendix, we derive the energy of bleb formation or, more precisely, of a membrane detachment of radius r. We show that, for sufficiently large detachments, the energy can be approximated by Eq. (3.6).

We include bulk contributions due to membrane detachment and inflation, E_b, as well as interfacial contributions E_i associated to the contact region between the detached and attached membrane regions (see Fig. 3.4a). Neglecting bending forces, bleb formation has three main bulk energetic contributions associated to the increase of apparent membrane area and cell volume, and to the loss of membrane-cortex adhesion:

$$E_b \approx \gamma \Delta S - fV + w\,(f)\,A. \tag{3.A.1}$$

Here, ΔS is the increase in membrane area, V is the volume of the bleb, and $A = \pi r^2$ is the area of the detachment. Respectively, γ is the membrane tension, f is the pressure difference across the membrane, and $w\,(f)$ is the pressure-dependent membrane-cortex adhesion energy per unit area, given by Eq. (2.10). Since the bleb acquires the shape of a spherical cap, its volume is given by

$$V = \frac{\pi h^2}{3}\,(3R - h)\,, \tag{3.A.2}$$

where h is the height of the cap and R the radius of the sphere. For incipient blebs, $h \ll R$, so that the height h is related to the detachment radius r by (see Fig. 3.4c)

$$r^2 = R^2 - (R - h)^2 = 2Rh - h^2 \approx 2Rh. \tag{3.A.3}$$

Then, under this approximation, the bleb volume reads

$$V \approx \pi h^2 R \approx \frac{\pi r^4}{4R} \tag{3.A.4}$$

in terms of the detachment radius r. Respectively, the apparent membrane area of the bleb is given by $S = 2\pi Rh$. Thus, the membrane area increase associated to bleb formation is

$$\Delta S = S - A = 2\pi Rh - \pi r^2 = \pi h^2 \approx \frac{\pi r^4}{4R^2}. \tag{3.A.5}$$

Then, introducing the previous expressions into Eq. (3.A.1), the energy cost of forming an incipient bleb of radius R and detachment radius r reads:

$$E_b \approx \frac{\pi\gamma r^4}{4R^2} - \frac{\pi f r^4}{4R} + \pi r^2 w\left(f\right). \tag{3.A.6}$$

Now, energy minimization imposes the equilibrium radius of the bleb, R_b:

$$\left.\frac{\partial E_b}{\partial R}\right|_{R=R_b} = 0 \Longrightarrow R_b = \frac{2\gamma}{f}, \tag{3.A.7}$$

which corresponds to the Young-Laplace pressure difference across a spherical interface. Therefore, the energy of bleb formation reads

$$E_b\left(r\right) \approx \pi r^2 w\left(f\right) - \frac{\pi f^2}{16\gamma} r^4, \tag{3.A.8}$$

now only in terms of the detachment radius r, as given in Eq. (3.6).

Next, we include the interfacial energy associated to the contact line, and show it to be small for sufficiently large detachment radii. To this end, we start by estimating the width of the interface between the attached and detached membrane regions. To do so, we compute the decay of the membrane shape profile from the contact line towards the attached membrane region (see Fig. 3.4a). Under stationary conditions, the coupled profiles of membrane shape $u\left(\vec{x}\right)$ and density of membrane-cortex bonds $\rho_b\left(\vec{x}\right)$ follow

$$\kappa\nabla^4 u\left(\vec{x}\right) - \gamma\nabla^2 u\left(\vec{x}\right) + k\rho_b\left(\vec{x}\right) u\left(\vec{x}\right) - f = 0, \tag{3.A.9a}$$

$$k_{\text{on}}\left[\rho_0 - \rho_b\left(\vec{x}\right)\right] - k^0_{\text{off}} e^{\beta k u\left(\vec{x}\right)\delta} \rho_b\left(\vec{x}\right) = 0. \tag{3.A.9b}$$

Here, Eq. (3.A.9a) is the Euler-Lagrange equation of the membrane shape field $u\left(\vec{x}\right)$, obtained from the minimization of the membrane Hamiltonian, Eq. (2.31). In turn, Eq. (3.A.9b) is the stationary, spatially-extended version of Eq. (2.1).

The coupled nonlinear Eq. (3.A.9) can not be solved analytically in general. However, an analytical solution can be obtained for small-amplitude perturbations around the mechanical equilibrium state given by Eq. (2.4) (see Fig. 2.7):

$$u\left(\vec{x}\right) = u_{\text{eq}} + \delta u\left(\vec{x}\right), \qquad \rho_b\left(\vec{x}\right) = \rho_b^{\text{eq}} + \delta\rho_b\left(\vec{x}\right). \tag{3.A.10}$$

Then, neglecting membrane bending forces as before, and restricting to the lowest order in the perturbations, we obtain

$$\gamma\nabla^2\delta u\left(\vec{x}\right) = k\rho_b^{\text{eq}}\delta u\left(\vec{x}\right) + k u_{\text{eq}}\delta\rho_b\left(\vec{x}\right), \tag{3.A.11a}$$

$$\delta\rho_b\left(\vec{x}\right) = -\frac{\rho_b^{\text{eq}}\beta k\delta k^0_{\text{off}} e^{\beta k u_{\text{eq}}\delta}}{k_{\text{on}} + k^0_{\text{off}} e^{\beta k u_{\text{eq}}\delta}}\delta u\left(\vec{x}\right) \equiv -A\left(f\right)\delta u\left(\vec{x}\right), \tag{3.A.11b}$$

where we have defined $A\left(f\right)$, which is a positive function of the pressure difference f across the membrane. Note that Eq. (3.A.11) directly follow from Eqs. (2.39) and (2.40) under stationary conditions, and neglecting bending.

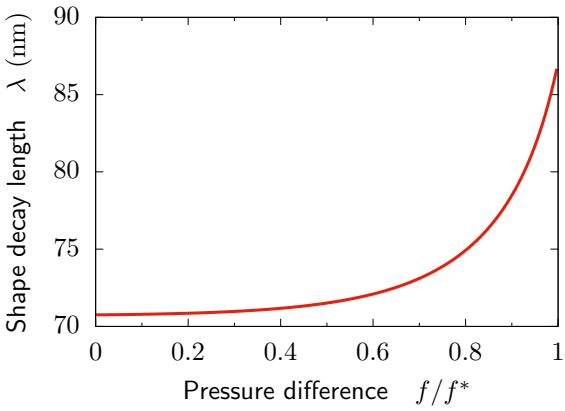

Figure 3.A.1 | Membrane shape decay length. The interface between the attached and detached membrane regions becomes flatter and wider at larger pressure differences (Eq. (3.A.13)). However, using the parameter values in Table 2.1, the variation is not pronounced, and the membrane shape typically decays within less than the interlinker spacing $\xi_0 \sim 0.1\ \mu$m.

Next, to obtain the typical decay length of the membrane shape profile from the contact line, we restrict the problem to one dimension[4], namely to a section as depicted in Fig. 3.4a, with the contact line at $x = 0$. Thus, the boundary conditions read $u(0) = u_c$ and $u(x \to \infty) = u_{\text{eq}}$, which yield the solutions

$$u(x) = u_{\text{eq}} + [u_c - u_{\text{eq}}]\, e^{-x/\lambda}, \tag{3.A.12a}$$

$$\rho_b(x) = \rho_b^{\text{eq}} - A(f)\,[u_c - u_{\text{eq}}]\, e^{-x/\lambda}. \tag{3.A.12b}$$

Therefore, the bonds' stretching decays exponentially from its value at the contact line to the asymptotic equilibrium value with a decay length

$$\lambda = \sqrt{\frac{\gamma}{k\rho_b^{\text{eq}} - k u_{\text{eq}} A(f)}}, \tag{3.A.13}$$

which depends on the pressure difference across the membrane (Fig. 3.A.1). Larger membrane tension γ and/or pressure difference f imply wider and flatter contact regions. However, using the parameter estimates in Table 2.1, the decay length varies only between $\sim 70 - 90$ nm across the whole range of possible pressures (Fig. 3.A.1). Thus, in fact, a rough estimate of the decay length is simply $\lambda \sim \sqrt{\gamma/(\rho_0 k)} \sim 70$ nm.

In conclusion, we estimate that the decay length of membrane shape and bond density perturbations is typically similar, and even slightly smaller, than the average

[4]The full solution in two dimensions with circular symmetry involves Bessel functions with the same characteristic length.

distance between linkers, $\xi_0 = \rho_0^{-1/2} \sim 0.1\ \mu$m. Therefore, the interfacial region is a circular corona of an estimated width that typically involves only one membrane-cortex bond.

At this point, we are in a position to compute the energy cost of forming the interface between the attached and detached regions of the membrane. At the interface, bonds are more stretched than in the uniformly adhered situation. Therefore, neglecting bending forces, the interfacial energy is the elastic energy associated to the extra stretching of the bonds at the interface. Since we estimated that the interfacial region contains on average a single bond in its width, the interfacial energy may be estimated as

$$E_i \approx 2\pi r d \left(\frac{k}{2} \rho_b^* u_c^2 - \frac{k}{2} \rho_b^{\text{eq}} u_{\text{eq}}^2 \right), \tag{3.A.14}$$

where d is the diameter of the effective area covered by the bonds on the membrane (see Fig. 3.4a). This expression computes the extra elastic energy stored in the bonds at the contact line (at a density ρ_b^* by definition), which withstand a stretching u_c, with respect to the uniformly adhered situation at an equilibrium pressure-dependent bond density ρ_b^{eq} and stretching u_{eq}.

Now, for detachments of radius smaller than the critical radius for membrane peeling, $r < r_p(f)$, the stretching at the contact line, u_c, is a pressure-dependent quantity determined by the balance of normal forces, Eq. (3.4):

$$u_c = \frac{fr}{2d\rho_b^* k}. \tag{3.A.15}$$

In contrast, for larger detachments, $r > r_p(f)$, the bonds at the contact line break because their stretching reaches the critical value u^*, thus giving rise to the peeling process. Therefore, whenever peeling occurs, namely for $r > r_p(f)$ (see Eq. (3.5)), the stretching of the bonds at the contact line is $u_c = u^*$. As a consequence of the saturation of bonds' stretching at the contact line, the interfacial contribution to the energy of bleb formation is given by the following piecewise function:

$$E_i(r) = \begin{cases} \pi r d \left[\frac{f^2 r^2}{4d^2 \rho_b^* k} - k\rho_b^{\text{eq}} u_{\text{eq}}^2 \right]; & r \le r_p(f) \\ \pi r d \left[\rho_b^* k (u^*)^2 - k\rho_b^{\text{eq}} u_{\text{eq}}^2 \right]; & r \ge r_p(f). \end{cases} \tag{3.A.16}$$

Note that, below the peeling radius, the interfacial energy does not behave as a line tension, meaning that is not proportional to the length of the interface, $2\pi r$. This is because increasing the length of the contact line also increases the contact angle θ (see Fig. 3.4a) and hence the stretching of the bonds, which results in the nonlinear dependence on r. In contrast, above the peeling radius, the interfacial contribution does have the form of a line tension because the bonds do not withstand further stretching.

Finally, the total energy of bleb formation includes the bulk and interfacial contributions:

$$E = E_b + E_i. \tag{3.A.17}$$

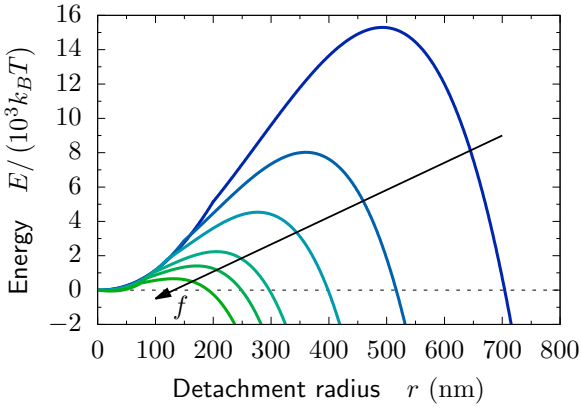

Figure 3.A.2 | Energy of bleb formation. Equation (3.A.17) with Eqs. (3.A.8) and (3.A.16). The interfacial contribution is negligible at radii $r > r_p$ because the stretching of the bonds at the interface satures for $r > r_p$. Parameter values are those in Table 2.1, plus $d = 30$ nm, and $f/f^* = 0.3 + 0.1n$; $n = 0, \ldots, 5$.

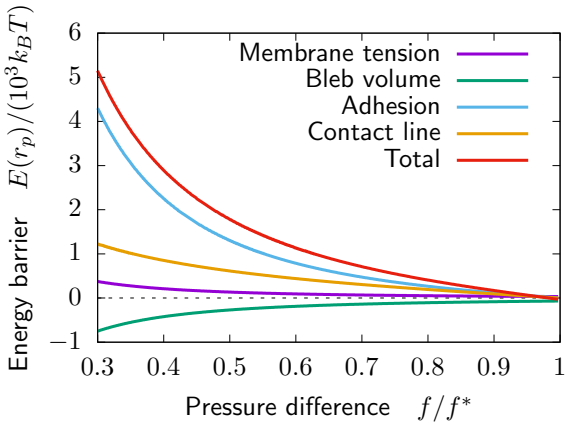

Figure 3.A.3 | Contributions to the effective energy barrier for bleb nucleation through membrane peeling. Large barriers at low pressure differences are dominated by the energy cost of breaking membrane-cortex bonds (adhesion). However, all contributions become similar for the small barriers at higher pressure differences. Parameter values are those in Table 2.1, plus $d = 30$ nm.

As expected, the interfacial contribution is subdominant respect to the bulk contributions at radii $r > r_p$ (Fig. 3.A.2). Thus, since we estimate the classical critical radius, r_n, to be larger than the critical radius for peeling, r_p, we expect the interfacial energy to have a minor impact on r_n, which will typically be well approximated

by Eq. (3.7). In contrast, the interfacial energy does substantially contribute to the effective energy barrier for bleb nucleation through membrane peeling, $E(r_p)$. Specifically, the energy cost of breaking membrane-cortex bonds is the largest contribution to the energy barrier at low pressure differences, but it becomes similar to the interfacial contribution at higher pressure differences, which correspond to smaller nucleation radii (Fig. 3.A.3).

Part II

Active gel dynamics for cells and tissues

4

Constitutive equations of active gels from nonequilibrium molecular kinetics

Contents

Abstract

Biological systems such as the cell cortex, the mitotic spindle, or epithelial tissues have been described as active gels. The constitutive equations of such materials were initially derived in the framework of nonequilibrium thermodynamics, which introduces a number of phenomenological transport coefficients. Thus, despite flows in active gels are mediated by linker proteins, the connection between their molecular kinetics and the transport coefficients remained obscure. In this chapter, we derive the constitutive equations of an active polar gel from a model for the dynamics of elastic molecules that link polar elements. Molecular binding kinetics induces the fluidization of the material, giving rise to Maxwell viscoelasticity and, provided that detailed balance is broken, to the generation of active stresses.

We give explicit expressions for the transport coefficients of active gels in terms of molecular properties, including nonlinear contributions on the departure from equilibrium. In particular, when activity favors linker unbinding, we predict a decrease of viscosity with activity — active thinning — of kinetic origin, which could explain some experimental results on cell cortex rheology. By bridging the molecular and hydrodynamic scales, our results shed light on the connection between macroscopic properties and underlying molecular processes in biological active gels.

4.1 Introduction

Active polar gels are viscoelastic media made out of orientable constituents endowed with an internal source of energy under nonequilibrium conditions [Jülicher 2007, Joanny 2009, Prost 2015]. These materials are common in cell and tissue biology [Needleman 2017], with a prominent example being the actomyosin cortex of eukaryotic cells, which generates forces that enable cell shape changes and motility (Fig. 2.2). This dynamic structure is a crosslinked network of actin polar filaments and myosin molecular motors that generates forces by transducing the chemical energy of adenosine triphosphate (ATP) hydrolysis. Other biological active gels include the mitotic spindle and epithelial tissues.

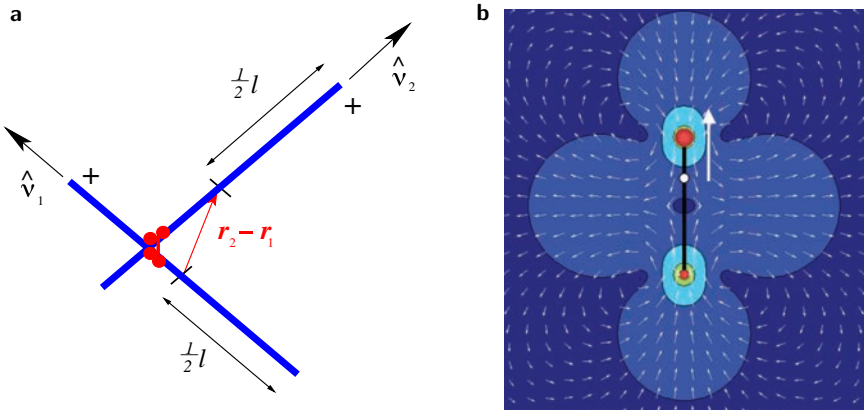

Figure 4.1 | Microscopic models of active gels. Hydrodynamic equations may be derived by coarse-graining microscopic descriptions [Marchetti 2013]. **a,** Schematic of a pair of filaments (blue) driven by an active crosslink (red) [Liverpool 2006]. From [Marchetti 2013]. **b,** Flow pattern induced by a puller microswimmer. The color denotes the amplitude of the flow, which decreases with distance (red to blue), whereas arrows only indicate the flow direction. From [Baskaran 2009].

The coarse-grained dynamics of such systems can be captured by the hydrodynamic equations of active polar gels [Joanny 2011, Marchetti 2013, Prost 2015]. Such equations can be derived relying only on symmetry arguments [Simha 2002, Hatwalne 2004, Marchetti 2013], for example in a systematic way within the formalism of linear irreversible thermodynamics [Kruse 2004, Kruse 2005, Jülicher 2011, Marchetti 2013]. These phenomenological approaches introduce a number of transport coefficients whose dependence on molecular parameters is not considered. Such relations have been obtained in derivations of the hydrodynamic equations from microscopic models [Marchetti 2013] consisting of active filaments [Liverpool 2006] or swimmers [Baskaran 2009] (Fig. 4.1), inspired by the cytoskeleton and bacterial suspensions, respectively. However, these microscopic descriptions may not be appropriate for other media such as epithelia, where cells rearrange

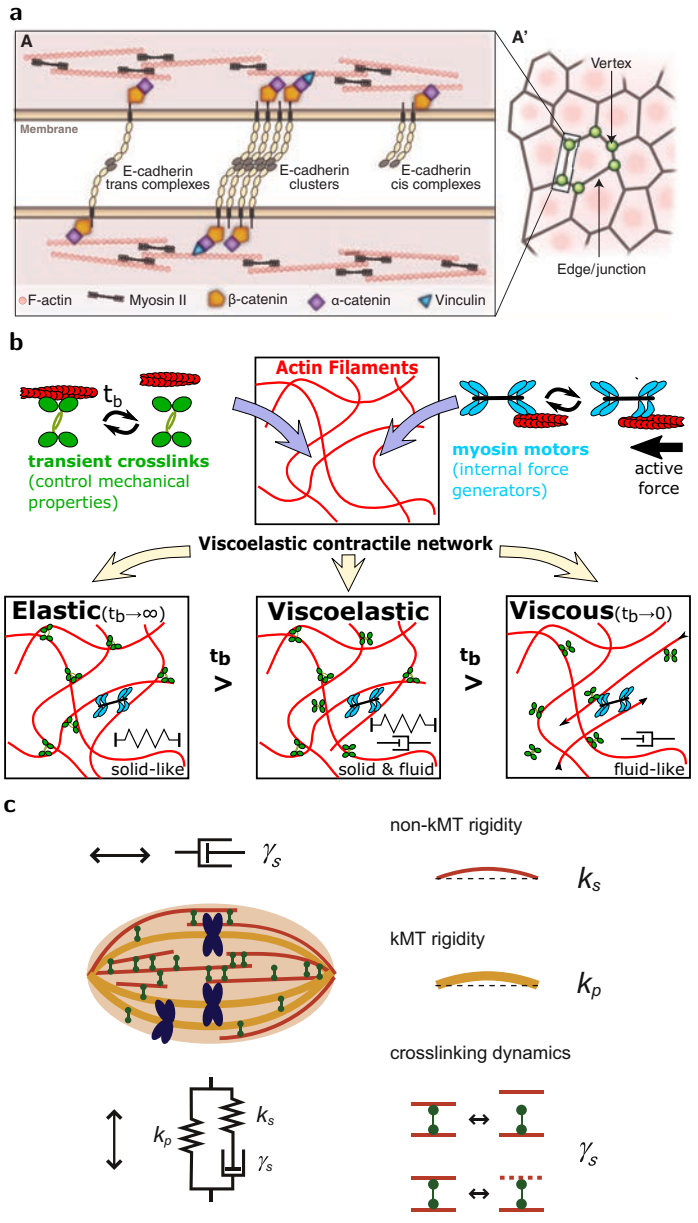

Figure 4.2 | Linker binding dynamics regulates flows in biological active gels. a, The turnover of E-cadherin proteins in cell-cell junctions enables cell-cell sliding and tissue remodeling. From [Guillot 2013]. **b,** The binding kinetics of actin crosslinkers tunes the rheological properties of the actin cytoskeleton. From [Ahmed 2015]. **c,** The binding dynamics of microtubule crosslinkers controls the rheological properties of the mitotic spindle, giving rise to a viscous response along its long axis. From [Shimamoto 2011].

while keeping confluence, thus allowing for tissue remodeling yet preserving mechanical integrity [Guillot 2013, Wyatt 2016, Khalilgharibi 2016]. Not only in tissues [Kametani 2007, Caicedo-Carvajal 2010, Garcia 2015] but also in actomyosin gels [Le Goff 2002, Humphrey 2002], in the actin cytoskeleton [Wottawah 2005, Ehrlicher 2015, Ahmed 2015], and in the metaphase spindle [Shimamoto 2011], flows are regulated by the binding dynamics of linker molecules (Fig. 4.2). Although they crucially affect the properties and dynamics of these media, a connection between molecular kinetics and the transport coefficients of continuum theories remains elusive. The goal of this chapter is to provide such a missing link by deriving the constitutive equations of active gels from a mesoscopic model for the dynamics of crosslinker molecules.

In Section 4.2, we consider a collection of polar elements linked by elastic molecules, and derive the constitutive equations of an active polar gel from the nonequilibrium dynamics of the linkers. Hence, we obtain explicit expressions for the transport coefficients of active gels in terms of molecular parameters. Some of these parameters characterize the deviation of molecular kinetics from detailed balance, thus giving nonequilibrium contributions to the transport coefficients. These active contributions are discussed in Section 4.3, which focuses, in particular, on the decrease of viscosity with molecular activity, which we term *active thinning*. We discuss how this kinetic phenomenon is different from the activity-dependent apparent viscosity of active fluids, which has a hydrodynamic origin [Hatwalne 2004, Giomi 2010, Ramaswamy 2010, Marchetti 2013]. We also discuss how *active thinning* could explain some experimental results on the rheology of the cell cortex and of other biological systems such as nucleoli and the mitotic spindle. Finally, in Section 4.4 we derive the constitutive equations of the interface of an active gel with a passive external medium. We highlight key differences in the symmetry of the active forces between the bulk and interfacial cases.

4.2 Derivation of the bulk constitutive equations

In this section, we derive the constitutive equations in the bulk of an active polar gel, such as in the cell cortex or in tissues (Figs. 4.3a and 4.3b). To this end, we consider a d-dimensional assembly of polar elements (the actin network or the cell colony, respectively, in red) with an orientation characterized by the coarse-grained nematic order parameter field $q_{\alpha\beta} = p_\alpha p_\beta - p^2\delta_{\alpha\beta}/d$, where p_α is the coarse-grained polarity vector. The polar elements are crosslinked by a density ρ of elastic molecules (for example myosin motors or cadherins in Figs. 4.3a and 4.3b, respectively, in green), so that the composite is an elastonematic material. Assuming an isotropic linear elastic response of the molecules, the free energy density of small shear deformations[1] reads

$$f = \frac{\mu}{2} u_{\alpha\beta} u_{\alpha\beta} + D\, u_{\alpha\beta} q_{\alpha\beta} + \frac{\chi}{2} q_{\alpha\beta} q_{\alpha\beta} \tag{4.1}$$

[1] Bulk deformations can be included in a similar way.

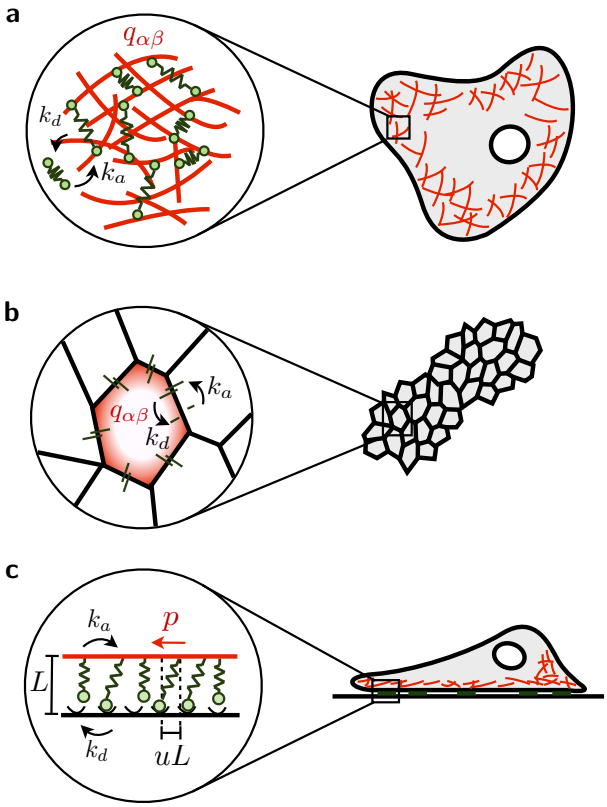

Figure 4.3 | Applications of our model to biological active gels. The elastic kinetic elements are depicted in green, and the polar structures are shown in red. **a,** Cell cortex: myosin motors are the active elastic kinetic elements within the actin network. **b,** Tissues: cell-cell adhesion molecules, such as cadherins, are the elastic kinetic elements connecting cell cortices into a multicellular active polar gel. **c,** Lamellipodium: cell adhesion molecules, such as integrins, are the elastic kinetic elements at the interface of the actomyosin gel layer.

to lowest order in $u_{\alpha\beta}$ and $q_{\alpha\beta}$, being $u_{\alpha\beta}$ the (symmetric and traceless) strain tensor, μ the shear elastic modulus, D the elastonematic coefficient, and χ the inverse nematic susceptibility [Lubensky 2002]. Thermodynamic stability requires the free energy to be a convex function, which imposes $\mu\chi > D^2$.

Assuming spatial uniformity, we define $n\left(\mathbf{u},\mathbf{q},t\right)d\mathbf{u}\,d\mathbf{q}$ as the fraction of bound molecules with strain $[\mathbf{u},\mathbf{u}+d\mathbf{u}]$ and nematic order $[\mathbf{q},\mathbf{q}+d\mathbf{q}]$ at time t. Then, the stochastic linker dynamics is captured by the following equation for the distribution of bound linkers [Tanaka 1992]

$$\frac{\partial n}{\partial t}+v_{\alpha\beta}\frac{\partial n}{\partial u_{\alpha\beta}}+\dot{Q}_{\alpha\beta}\frac{\partial n}{\partial q_{\alpha\beta}}=(1-\phi_b)k_a-nk_d. \tag{4.2}$$

Here, $v_{\alpha\beta} = \langle \dot{u}_{\alpha\beta} \rangle$ and $Q_{\alpha\beta} = \langle q_{\alpha\beta} \rangle$ are the strain rate and order parameter tensors, respectively. Brackets denote ensemble averages, so that $v_{\alpha\beta}$ and $Q_{\alpha\beta}$ are hydrodynamic variables. We assume rigid polar elements (actin fibers or cell cortices in Figs. 4.3a and 4.3b, respectively) that do not deform [Jülicher 1997], so that all the linkers shear and reorient at the same rate, consistently with $v_{\alpha\beta}$ and $\dot{Q}_{\alpha\beta}$ being spatially uniform. In turn,

$$\phi_b \equiv \int_{\mathbb{R}^m} n \, d\mathbf{u} \, d\mathbf{q} \tag{4.3}$$

is the total fraction of bound molecules, with $m = d(d+1) - 2$ being the total number of independent components of the strain and order parameter tensors. Finally, k_a and k_d are the attachment and detachment rates of the linker molecules, respectively.

In active systems, detailed balance is locally broken. This can be generically expressed as [Jülicher 1997]

$$\frac{k_a}{k_d} = e^{-\beta\varepsilon} - \Omega, \tag{4.4}$$

with $\beta \equiv (k_B T)^{-1}$. Here, $\varepsilon = \varepsilon_0 + f/\rho$ is the free energy difference between the bound and unbound states per molecule, including its chemical part ε_0. In turn, Ω defines the departure from detailed balance, hereafter referred to as 'activity'. It is an a priori unknown function of the parameters, scalar combinations of $u_{\alpha\beta}$ and $q_{\alpha\beta}$, and the chemical potential difference $\Delta\mu$ of ATP hydrolysis, with $\Omega \propto \Delta\mu$ close to equilibrium.

At this point, for each particular system, it is necessary to introduce the appropriate force dependence of the molecular unbinding rate k_d. For simplicity, and to obtain explicit expressions of the transport coefficients, we now choose a force-independent unbinding rate. This corresponds to assuming the barrier of the binding energy landscape of the molecules to be very close to the bound state [Walcott 2010]. Under this assumption, the stationary fraction of bound linkers ϕ_b is obtained by introducing Eq. (4.4) in Eq. (4.2) and integrating over $\mathbf{u}$ and $\mathbf{q}$:

$$\phi_b = \frac{\alpha - \Omega_0}{1 + \alpha - \Omega_0}, \tag{4.5}$$

where we have defined the dimensionless parameters

$$\alpha \equiv \int_{\mathbb{R}^m} e^{-\beta\varepsilon} d\mathbf{u} \, d\mathbf{q} = \left(\frac{2\pi\rho}{\beta\sqrt{\mu\chi - D^2}} \right)^{m/2} e^{-\beta\varepsilon_0} \tag{4.6}$$

and

$$\Omega_0 \equiv \int_{\mathbb{R}^m} \Omega \, d\mathbf{u} \, d\mathbf{q} \tag{4.7}$$

that characterize the equilibrium and active parts of the molecular kinetics, respectively. To ensure that the fraction of bound linkers ϕ_b is positive, the condition $\Omega_0 < \alpha$ must be fulfilled.

The stress $\sigma_{\alpha\beta}$ of the composite network [Tanaka 1992] and its nematic field $H_{\alpha\beta}$ can be defined as

$$\sigma_{\alpha\beta} = \int_{\mathbb{R}^m} n\, \sigma^{\text{el}}_{\alpha\beta}\, d\mathbf{u}\, d\mathbf{q}, \qquad H_{\alpha\beta} = \int_{\mathbb{R}^m} n\, h_{\alpha\beta}\, d\mathbf{u}\, d\mathbf{q}, \tag{4.8}$$

where

$$\sigma^{\text{el}}_{\alpha\beta} = \frac{\partial f}{\partial u_{\alpha\beta}}, \qquad h_{\alpha\beta} = \frac{\partial f}{\partial q_{\alpha\beta}} \tag{4.9}$$

are the elastic stress sustained by the linkers and the coarse-grained nematic field[2], respectively. Next, we detail the derivation of the constitutive equation for the stress. The procedure for the nematic field is analogous. First, introducing the free energy Eq. (4.1), the stress in the network can be rewritten as

$$\sigma_{\alpha\beta} = \mu \int_{\mathbb{R}^m} n\, u_{\alpha\beta}\, d\mathbf{u}\, d\mathbf{q} + D \int_{\mathbb{R}^m} n\, q_{\alpha\beta}\, d\mathbf{u}\, d\mathbf{q}. \tag{4.10}$$

Then, we compute the time derivative of $\sigma_{\alpha\beta}$:

$$\dot{\sigma}_{\alpha\beta} = \mu \int_{\mathbb{R}^m} \frac{\partial n}{\partial t} u_{\alpha\beta}\, d\mathbf{u}\, d\mathbf{q} + D \int_{\mathbb{R}^m} \frac{\partial n}{\partial t} q_{\alpha\beta}\, d\mathbf{u}\, d\mathbf{q}. \tag{4.11}$$

Note that, here, $u_{\alpha\beta}$ and $q_{\alpha\beta}$ are integration variables. Now, introducing the linker dynamics Eq. (4.2), the first term in the right-hand side of Eq. (4.11) expands into

$$\begin{aligned}\int_{\mathbb{R}^m} \frac{\partial n}{\partial t} u_{\alpha\beta}\, d\mathbf{u}\, d\mathbf{q} = &-v_{\lambda\nu} \int_{\mathbb{R}^m} \frac{\partial n}{\partial u_{\lambda\nu}} u_{\alpha\beta}\, d\mathbf{u}\, d\mathbf{q} \\ &- \dot{Q}_{\lambda\nu} \int_{\mathbb{R}^m} \frac{\partial n}{\partial q_{\lambda\nu}} u_{\alpha\beta}\, d\mathbf{u}\, d\mathbf{q} + (1-\phi_b)\, k_d \int_{\mathbb{R}^m} u_{\alpha\beta}\, e^{-\beta\varepsilon}\, d\mathbf{u}\, d\mathbf{q} \\ &- (1-\phi_b)\, k_d \int_{\mathbb{R}^m} u_{\alpha\beta}\, \Omega\, d\mathbf{u}\, d\mathbf{q} - k_d \int_{\mathbb{R}^m} n\, u_{\alpha\beta}\, d\mathbf{u}\, d\mathbf{q}.\end{aligned} \tag{4.12}$$

Integrating the first term by parts, and noticing that the second and third terms vanish, one obtains

$$\int_{\mathbb{R}^m} \frac{\partial n}{\partial t} u_{\alpha\beta}\, d\mathbf{u}\, d\mathbf{q} = v_{\alpha\beta}\phi_b - k_d\,(1-\phi_b)\,\Omega_u Q_{\alpha\beta} - k_d \int_{\mathbb{R}^m} n\, u_{\alpha\beta}\, d\mathbf{u}\, d\mathbf{q}. \tag{4.13}$$

The second term in the right-hand side of Eq. (4.11) can be computed in a similar way, leading to

$$\int_{\mathbb{R}^m} \frac{\partial n}{\partial t} q_{\alpha\beta}\, d\mathbf{u}\, d\mathbf{q} = \dot{Q}_{\alpha\beta}\phi_b - k_d\,(1-\phi_b)\,\Omega_q Q_{\alpha\beta} - k_d \int_{\mathbb{R}^m} n q_{\alpha\beta}\, d\mathbf{u}\, d\mathbf{q}. \tag{4.14}$$

[2]The minus sign in these definitions is removed because we refer the quantities to the medium, not to the linkers.

In Eqs. (4.13) and (4.14) we have defined the dimensionless parameters Ω_u and Ω_q via the relations

$$\int_{\mathbb{R}^m} \Omega\, u_{\alpha\beta}\, d\mathbf{u}\, d\mathbf{q} \equiv \Omega_u Q_{\alpha\beta}, \qquad \int_{\mathbb{R}^m} \Omega\, q_{\alpha\beta}\, d\mathbf{u}\, d\mathbf{q} \equiv \Omega_q Q_{\alpha\beta}. \tag{4.15}$$

The integrals in Eq. (4.15) must be proportional to the only intrinsic symmetry-breaking tensor of the system, $Q_{\alpha\beta}$, according to the Curie principle [Curie 1894]. Finally, introducing Eqs. (4.13) and (4.14) into Eq. (4.11), and employing Eq. (4.10) to identify the stress tensor, we obtain the constitutive equation.

The procedure outlined above yields the following constitutive equations of the active polar gel:

$$\left(1 + \tau \frac{d}{dt}\right) \sigma_{\alpha\beta} = 2\eta\, v_{\alpha\beta} - \nu\, \dot{Q}_{\alpha\beta} - \zeta\, Q_{\alpha\beta}, \tag{4.16}$$

$$\left(1 + \tau \frac{d}{dt}\right) H_{\alpha\beta} = \gamma\, \dot{Q}_{\alpha\beta} + \nu\, v_{\alpha\beta} - \omega\, Q_{\alpha\beta}, \tag{4.17}$$

where $\tau = k_d^{-1}$ is the viscoelastic relaxation time. The viscoelastic behavior stems from the linker kinetics, which fluidizes the initially elastic network, leading to a viscous response at times longer than τ [Tanaka 1992], with shear viscosity η and rotational viscosity γ. In addition, Eqs. (4.16) and (4.17) feature flow alignment terms coupling flow to orientation by the coefficient ν. Finally, the equations have terms corresponding to an active stress and an active alignment, with coefficients ζ and ω, respectively. In our derivation, these coefficients are naturally obtained in terms of the mechanical and kinetic molecular parameters:

$$\eta = \frac{\mu\phi_b}{2k_d}, \qquad \gamma = \frac{\chi\phi_b}{k_d}, \qquad \nu = -\frac{D\phi_b}{k_d},$$
$$\zeta = (D\,\Omega_q + \mu\,\Omega_u)\,(1-\phi_b)\,, \qquad \omega = (D\,\Omega_u + \chi\,\Omega_q)\,(1-\phi_b)\,, \tag{4.18}$$

where

$$\phi_b = \frac{\alpha - \Omega_0}{1 + \alpha - \Omega_0}, \tag{4.19}$$

with α and Ω_0 defined in Eqs. (4.6) and (4.7), and Ω_u and Ω_q defined in Eq. (4.15). Physically, Ω_u and Ω_q correspond to an *active strain* and an *active orientation* induced by the departure from detailed balance, which are ultimately responsible for the shear active stress and alignment, respectively.

Equations (4.16) and (4.17) are the constitutive equations of an active polar gel [Salbreux 2009]. Here, the passive transport coefficients η, ν, γ respectively emerge from the mechanical parameters in the free energy, μ, D, χ, via the fluidization induced by linker kinetics. In turn, the active coefficients ζ, ω are constructed by coupling scalars derived from Ω to the mechanical parameters. This clearly denotes that the generation of shear (dipolar) active forces requires breaking rotational invariance ($Q_{\alpha\beta} \neq 0$) and detailed balance (nonzero Ω_u and/or Ω_q), which is a fundamental feature of active gels [Prost 2015]. Finally, as in the fluidization of

tissues by cell proliferation [Ranft 2010], the Maxwell operator $(1 + \tau\, d/dt)$ affects $\sigma_{\alpha\beta}$ and $H_{\alpha\beta}$ but not the nematic terms in Eqs. (4.16) and (4.17), differing from the form often adopted for active gels [Kruse 2004, Kruse 2005, Jülicher 2011].

4.3 Active thinning by molecular kinetics

Equation (4.18) unveils that transport coefficients depend on activity at the molecular level, characterized by the parameters Ω_0, Ω_u, and Ω_q, which can be experimentally modified by tuning the ATP concentration. In the Onsager approach to the equations of active gels, such dependencies are absent at the linear level and could only arise from nonlinear flux-force couplings [Prost 2015]. In our derivation, in contrast, while the constitutive equations are still linear due to having restricted the free energy to lowest order, the transport coefficients include contributions of all orders in the activity.

Figure 4.4 shows the dependence of the transport coefficients on the departure from equilibrium, Ω_0, for the simple case $\Omega_u = 0$ and $\Omega_q = \Omega_0$ (i.e. neglecting fluctuations of $q_{\alpha\beta}$). In general, the sign of Ω_0 is not determined. For instance, for myosin, ATP binding directly causes its dissociation from actin filaments (Fig. 4.5) [Howard 2001, Jacobs 2013], suggesting that $\Omega_0 > 0$. For adhesion molecules such as integrins [Fournier 2010] or cadherins [Borghi 2012], the same behaviour may stem from the fact that activity (ATP consumption) generates cortical contractile forces that pull on them, hence favouring their detachment. However, more complex responses such as catch-bond behaviour [Evans 2007, Rakshit 2014] might yield $\Omega_0 < 0$.

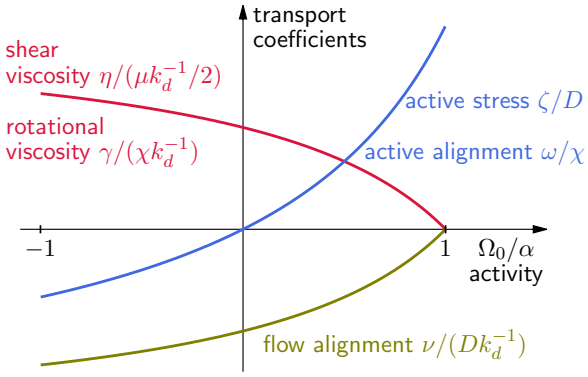

Figure 4.4 | Activity-dependent transport coefficients. The plotted dependencies correspond to Eq. (4.18) with Eq. (4.19) for the case $\Omega_u = 0$ and $\Omega_q = \Omega_0$. For $\Omega_0 > 0$ (see text), the viscosity $\eta = \mu\phi_b/(2k_d)$ decreases with activity (*active thinning*, Eq. (4.20)) due to the reduced fraction of bound molecules.

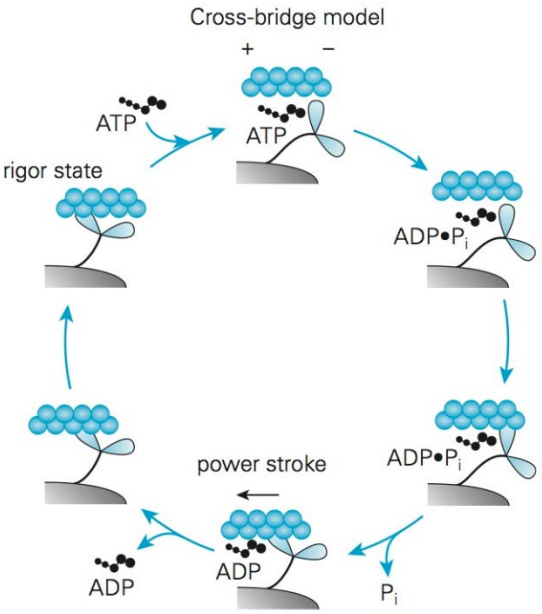

Figure 4.5 | Mechanochemical cycle of myosin interacting with actin. The detailed sequence of steps corresponds to the cross-bridge model. ATP binding induces myosin unbinding from the actin filament. Thus, a higher ATP concentration leads to a larger fraction of unbound myosin. From [Jacobs 2013].

For $\Omega_0 > 0$, the viscosity decreases with activity (see Fig. 4.4):

$$\eta = \frac{\mu}{2k_d}\frac{\alpha - \Omega_0}{1 + \alpha - \Omega_0}. \tag{4.20}$$

We call this phenomenon *active thinning*. The modification of viscosity with activity that we predict has a kinetic origin, since it stems from the dependence of the fraction of bound linkers ϕ_b on the departure from detailed balance, Ω_0 (Eq. (4.5)). Thus, it must be distinguished from the activity-dependent effective viscosity of active nematic fluids, η_{eff}, which is a hydrodynamic effect due to flow alignment (Fig. 4.6) [Hatwalne 2004, Giomi 2010, Ramaswamy 2010, Marchetti 2013]. In these fluids, the dynamics of the average orientation is given by

$$\dot{Q}_{\alpha\beta} = -\frac{1}{\tau_q}\left(Q_{\alpha\beta} - Q^0_{\alpha\beta}\right) + \nu\, v_{\alpha\beta}, \tag{4.21}$$

where τ_q is the orientational relaxation time and $Q^0_{\alpha\beta}$ denotes a preferred orientation. Hence, in the steady state, the average orientation has a contribution due to shear flows:

$$Q_{\alpha\beta} = Q^0_{\alpha\beta} + \tau_q \nu\, v_{\alpha\beta}. \tag{4.22}$$

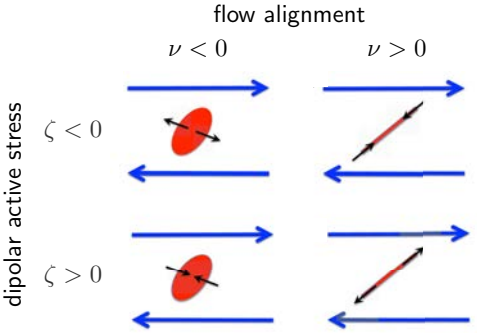

Figure 4.6 | Effective viscosity of active nematic fluids. Shear (blue arrows) orients disk-like (left) or rod-like (right) constituents (red). Then, the contractile (top) or extensile (bottom) active force dipoles generated by these constituents (black arrows) oppose or enhance the shear flow, hence yielding an increased or decreased effective viscosity, respectively, Eq. (4.24). Adapted from [Marchetti 2013].

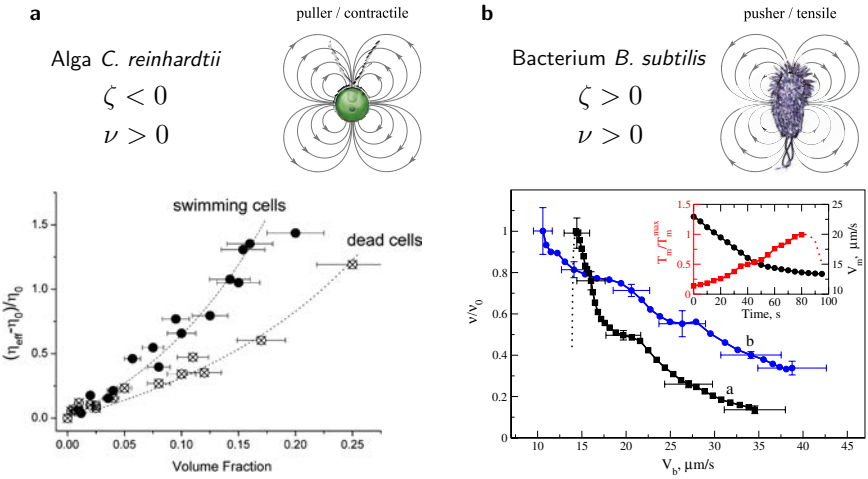

Figure 4.7 | Effective viscosity of microswimmer suspensions. a, The alga *C. reinhardtii* swims by exerting contractile dipolar stresses on the surrounding fluid. The apparent viscosity of suspensions of swimming algae ($\zeta < 0$) is higher than that of dead algae ($\zeta = 0$). Adapted from [Rafaï 2010, Giomi 2010]. **b,** The bacterium *B. subtilis* swims by exerting extensile dipolar stresses on the surrounding fluid. The apparent viscosity of suspensions of these bacteria decreases with their swimming speed. Adapted from [Sokolov 2009, Giomi 2010]. Both microorganisms behave as rod-like particles (Fig. 4.6). Similar results have been obtained for suspensions of the bacterium *E. coli* [Gachelin 2013, López 2015]. These findings are consistent with the predicted effective viscosity of active nematic fluids, Eq. (4.24). Our model does not apply to microswimmer suspensions.

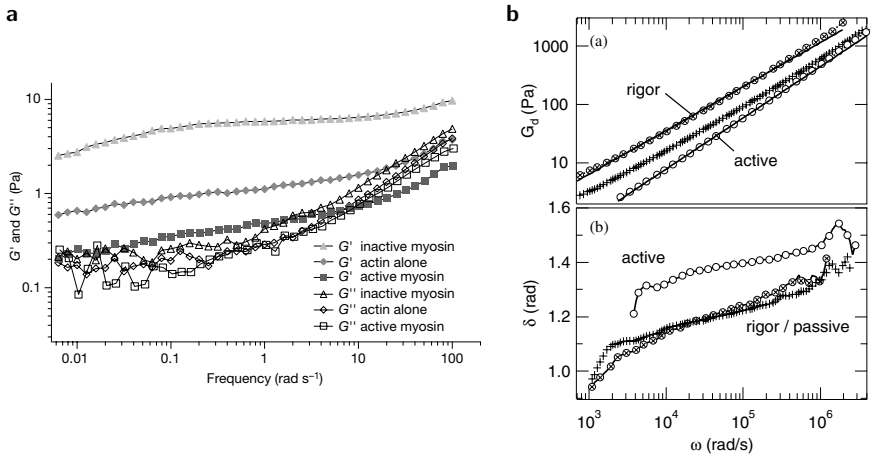

Figure 4.8 | Active fluidization and softening of actomyosin gels. a, Myosin activation decreases the complex shear modulus $G = G' + iG''$ of an actomyosin gel. The storage shear modulus G', which quantifies the non-dissipative, elastic-like shear response, decreases more pronouncedly than the loss shear modulus G'', which quantifies the dissipative, viscous-like shear response. Hence, the viscoelastic relaxation time of the gel is also decreased. From [Humphrey 2002]. **b,** Myosin activation decreases the loss shear modulus $G_d = G''$ and increases the phase angle δ of an actomyosin gel. The complex shear modulus is $G = G_d e^{i\delta}$. Hence, myosin induces a more fluid response. From [Le Goff 2002]. These findings are consistent with the predicted *active thinning* of actomyosin gels, Fig. 4.4.

Introducing this expression into Eq. (4.16), we obtain an effective constitutive equation at long times,

$$\sigma_{\alpha\beta} = 2\eta\, v_{\alpha\beta} - \zeta\, Q^0_{\alpha\beta}, \tag{4.23}$$

with the effective viscosity

$$\eta_{\text{eff}} = \eta - \frac{\zeta \tau_q \nu}{2}. \tag{4.24}$$

Therefore, whereas the effective viscosity Eq. (4.24) depends on (the sign of) other transport coefficients, such as the active stress and the flow alignment, our nonequilibrium kinetic correction to viscosity is intrinsic and does not.

Thus, activity modifies the viscosity of active gels through two different mechanisms: one based on flow alignment and one on molecular kinetics. The hydrodynamic mechanism was associated to the reduction (increase) of the apparent viscosity measured in active extensile (contractile) suspensions of microswimmers (Fig. 4.7) [Marchetti 2013, Sokolov 2009, Rafaï 2010, Gachelin 2013, López 2015]. However, in some biological active gels, to which our linker-based model applies, the opposite effect was observed. For instance, myosin activity was shown to fluidize and soften actin gels (Fig. 4.8) [Le Goff 2002, Humphrey 2002] or even cells in suspension[3] [Chan 2015] and the cell cortex in mitosis [Fischer-Friedrich 2016],

[3] Myosin-generated contractile stresses are often found to stiffen adherent cells but soften cells

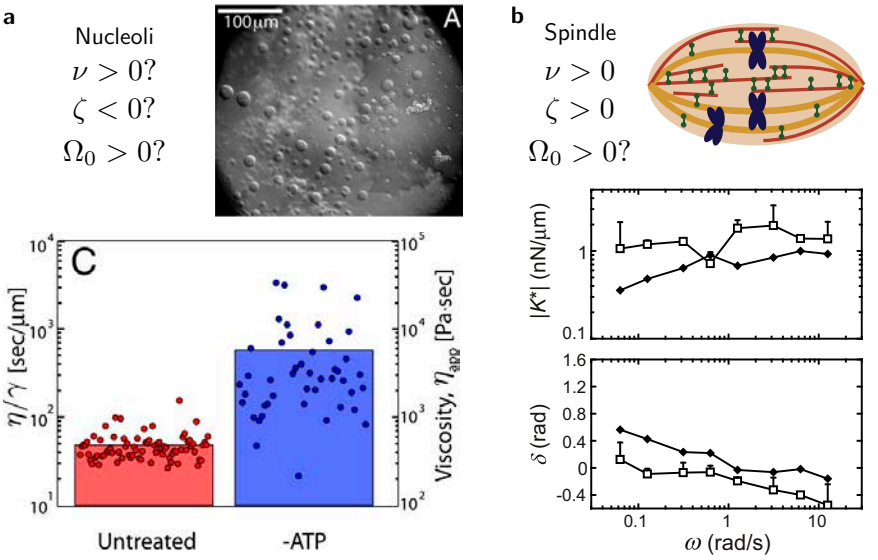

Figure 4.9 | Active fluidization in nucleoli and the spindle. a, The apparent viscosity of nucleoli increases upon ATP depletion. Adapted from [Brangwynne 2011]. This finding is consistent with the *active thinning* phenomenon, suggesting that chromatin remodeling proteins, which have been suggested to be contractile [Bruinsma 2014], might have $\Omega_0 > 0$ (Fig. 4.4). **b,** Upon treatment with a slowly hydrolyzing analog of ATP that locks kinesins in a microtubule-bound (rigor) state, metaphase spindles increase their dynamic stiffness $|K^*|$ and decrease their phase angle δ. Therefore, decreasing activity induces a more elastic response. Adapted from [Shimamoto 2011]. These findings are consistent with *active thinning*, suggesting that ATP-dependent microtubule crosslinkers such as kinesin might have $\Omega_0 > 0$ (Fig. 4.4). However, since the spindle has been found to exert extensile active stresses [Brugués 2014b], these results could also due to the hydrodynamic decrease of effective viscosity, Eq. (4.24).

decreasing both their stiffness and viscosity. Since actomyosin gels, and hence the cortex, are contractile ($\zeta < 0$), the flow alignment effect would render an increased effective viscosity η_{eff}, which seems inconsistent with the measurements. Hence, we propose that the measured active softening could be partially due to the kinetic effect predicted here (red line in Fig. 4.4), which is independent of the contractile/extensile nature of the system. ATP binding would promote myosin dissociation

in suspension. We suggest that this distinct behavior stems from a markedly different cytoskeletal architecture. Cells attached to a substrate often feature prominent actin stress fibers connected to focal adhesions [Schwarz 2013]. Hence, their cytoskeleton tends to be quite anisotropic and elastic. Thus, the strongly crosslinked cytoskeletal network can resist the myosin-generated forces, leading to a strain stiffening response [Broedersz 2014]. In contrast, the lack of adhesions in suspended and mitotic cells leads to a more isotropic and fluid cytoskeleton, which mainly concentrates in a cortical layer [Salbreux 2012]. Therefore, in this case, the cytoskeleton is only transiently crosslinked, and hence it can flow under myosin-generated forces, thus experiencing the predicted *active thinning*.

from actin, thus leading to a decreased viscosity. Combined with increased active stress (blue line in Fig. 4.4), this effect would allow a network remodeling resulting in the observed fluidization.

Similar considerations might hold for suspensions of nucleic acids and proteins. Indeed, rheological measurements [Hameed 2012] and the observation of collective flows [Zidovska 2013] suggest that chromatin behaves as a gel with active polar processes associated to chromatin remodeling enzymes [Bruinsma 2014, Chu 2017]. In this line, ATP was shown to lower the apparent viscosity of nucleoli (Fig. 4.9a) [Brangwynne 2011], consistently with our prediction. Similarly, the metaphase spindle behaves as an active polar fluid [Brugués 2014b], with an increased viscosity when the rate of ATP hydrolysis is reduced (Fig. 4.9b) [Shimamoto 2011], also in line with our result.

4.4 Interfacial constitutive equations

In this section, we derive the constitutive equations at the boundary of an active polar gel, such as to account for traction forces exerted by lamellipodia on substrates via focal adhesions (Fig. 4.3c). With this purpose, we consider a polar surface (lamellipodium, red) coated with a density ρ of elastic molecules (e.g. integrins, green) that transiently bind to an apolar surface (substrate, black). Now, taking the $\hat{z}$ axis perpendicular to the surface, the strain is effectively a vector $u_\alpha \equiv u_{\alpha z}$ that can directly couple to the polarity p_α. Hence, the free energy density reads

$$f = \frac{\mu}{2} u_\alpha u_\alpha + D\, u_\alpha p_\alpha + \frac{\chi}{2} p_\alpha p_\alpha, \tag{4.25}$$

where μ is the shear elastic modulus, D is the elastopolar coefficient, and χ is the inverse orientational susceptibility.

Parallel to the bulk case, the force F_α exerted by the bound molecules on the substrate [Schwarz 2013] and the average molecular field H_α are defined as

$$F_\alpha = \int_{\mathbb{R}^k} n\, F_\alpha^{\text{el}}\, d\mathbf{u}\, d\mathbf{p}, \qquad H_\alpha = \int_{\mathbb{R}^k} n\, h_\alpha\, d\mathbf{u}\, d\mathbf{p}, \tag{4.26}$$

with $k = 2(d-1)$, and

$$F_\alpha^{\text{el}} = \frac{1}{\rho} \frac{\partial f}{\partial u_\alpha}, \qquad h_\alpha = \frac{1}{\rho} \frac{\partial f}{\partial p_\alpha} \tag{4.27}$$

being the elastic force sustained by the linkers and the molecular field, respectively. Then, via a procedure analogous to that in Section 4.2, we find the constitutive equations at the interface of an active polar gel:

$$\left(1 + \tau \frac{d}{dt}\right) F_\alpha = \xi_i v_\alpha - \nu_i \dot{P}_\alpha - \zeta_i P_\alpha, \tag{4.28}$$

$$\left(1 + \tau \frac{d}{dt}\right) H_\alpha = \gamma_i \dot{P}_\alpha + \nu_i v_\alpha - \omega_i P_\alpha, \tag{4.29}$$

where $P_\alpha = \langle p_\alpha \rangle$, and $v_\alpha = \langle \dot{u}_\alpha \rangle L$ is the gel-substrate relative velocity, with L the gel-substrate distance (Fig. 4.3c). The interfacial transport coefficients read

$$\xi_i = \frac{\mu\phi_b}{2k_d\rho L}, \qquad \gamma_i = \frac{\chi\phi_b}{k_d\rho}, \qquad \nu_i = -\frac{D\phi_b}{k_d\rho},$$
$$\zeta_i = (D\,\Omega_p + \mu\,\Omega_u)\frac{1-\phi_b}{\rho}, \qquad \omega_i = (D\,\Omega_u + \chi\,\Omega_p)\frac{1-\phi_b}{\rho}, \tag{4.30}$$

where we have defined

$$\int_{\mathbb{R}^k} \Omega\, u_\alpha \, d\mathbf{u}\, d\mathbf{p} \equiv \Omega_u P_\alpha, \qquad \int_{\mathbb{R}^k} \Omega\, p_\alpha \, d\mathbf{u}\, d\mathbf{p} \equiv \Omega_p P_\alpha. \tag{4.31}$$

As for the bulk case, molecular kinetics entails the fluidization of the ensemble of elastic linkers, thereby leading to friction with coefficient ξ_i and to an interfacial rotational viscosity γ_i. In turn, ν_i is the interfacial flow alignment coefficient, and ζ_i, ω_i are the interfacial active force and active alignment coefficients, respectively.

Equations (4.28) and (4.29) correspond to the constitutive equations at the interface of an active polar fluid (Eqs. 20-22 in [Jülicher 2009], omitting chemical potential gradients), thus giving their coefficients in terms of molecular parameters. A key point is that the interfacial active force $\zeta_i P_\alpha$ is polar whereas the bulk active stress $\zeta Q_{\alpha\beta}$ features apolar symmetry.

4.5 Discussion and conclusions

We have derived the constitutive equations for the active polar gel that emerges from the nonequilibrium dynamics of a single species of elastic molecules that link polar elements. This minimal bottom-up approach is inspired by biological materials such as the lamellipodium, the cell cortex, or tissues (Fig. 4.3). Assuming a constant unbinding rate of the linker molecules yields simple explicit expressions of the transport coefficients in terms of molecular parameters. In particular, the coefficients include nonlinear dependencies on activity, by means of three unknowns $(\Omega_0, \Omega_u, \Omega_q)$ that characterize the departure from detailed balance. For general linker kinetics k_d, the approach is still valid but explicit expressions may not be obtained. Although spatial uniformity is assumed, the ensuing constitutive equations and transport coefficients can be used in the hydrodynamic limit, namely to the lowest order in a gradient expansion.

The Onsager formalism identifies three generalized forces for an active polar medium: the strain rate tensor $v_{\alpha\beta}$, the molecular field h_α, and the chemical potential difference $\Delta\mu$ of a reaction (typically ATP hydrolysis in biological systems) that maintains the system out of equilibrium. Hence, this approach yields constitutive equations for the three corresponding fluxes, namely the stress tensor $\sigma_{\alpha\beta}$, the rate of change of the polarity $\dot{P}_\alpha$, and the reaction rate r [Kruse 2004, Kruse 2005, Jülicher 2011, Marchetti 2013]. In contrast, our approach yields only two constitutive relations, for the stress tensor and for the polarity. In our model, the

nonequilibrium driving of the chemical reaction is encoded in the function Ω that explicitly breaks the detailed balance of the molecular kinetics. However, the relation between Ω and the generalized force $\Delta\mu$ is, in principle, unknown [Jülicher 1997]. Consequently, a constitutive equation for the reaction rate r does not readily follow from our current model.

Beyond phenomenological approaches, the mechanical response of active solids had been derived from microscopic models [Liverpool 2009, Banerjee 2011, Hawkins 2014]. However, in contrast, the viscoelastic relaxation of active fluids remained only included at the hydrodynamic level [Callan-Jones 2011, Hemingway 2015], thus unrelated to underlying molecular processes. In our derivation, the binding kinetics of linker molecules fluidizes the material, giving rise to a viscoelastic fluid response typically postulated in active gel theory. In general, other fluidization mechanisms may be at play. Examples include actin depolymerization in the cortex [Chan 2015] and, in the context of tissues, cell division and apoptosis [Ranft 2010, Matoz-Fernandez 2017], as well as topological transitions and cell shape changes [Etournay 2015, Popović 2017]. We expect the fluidization mechanism associated to molecular kinetics to be generic in cells and tissues, and to combine with others in the corresponding time scales.

Our model builds on previous theoretical approaches to transiently crosslinked networks [Tanaka 1992, Broedersz 2014], extending them to account for orientational degrees of freedom of the gel, as well as to include a nonequilibrium contribution to the binding kinetics of the linkers. Active stresses and torques naturally emerge from this contribution, which also modifies the passive transport coefficients of the system. Finally, bulk and interfacial active forces are shown to exhibit different symmetries, yet depend on common parameters. Thus, in tissues, our unified treatment of intercellular (bulk) and traction (interfacial) forces may help understand their interdependence [Maruthamuthu 2011]. Hence, our results could shed light on active-gel models of epithelial dynamics.

More generally, our work contributes to bridging the gap between the hydrodynamics of active gels and the underlying molecular dynamics. Typically, whereas macroscopic quantities such as stress and shear are measured, molecular concentrations and kinetic parameters are under experimental control [Bazellières 2015]. Therefore, our results may help interpret the effects of molecular perturbations on the mechanical properties of biological active gels, from subcellular structures such as the actomyosin cortex or the mitotic spindle to multicellular tissues. In this line, we have unveiled a dependence of viscosity on ATP consumption that could explain some experimental findings.

Contributions and acknowledgements

The work in this chapter was done jointly with David Oriola (UB, Barcelona).

I thank Madan Rao for insightful comments and discussions, and for pointing out Ref. [Tanaka 1992]. I also thank Carles Blanch-Mercader, Pierre Sens, Raphaël Voituriez, and Jean-François Joanny for discussions.

Part III

Collective cell migration and tissue morphology

5

Emergent structures and dynamics of cell colonies

Contents

Abstract

Cells in tissues can organize in a broad spectrum of structures according to their function. To study how such organizations emerge from cell-cell interactions, this chapter introduces a particle-based model of two-dimensional cell colonies. To capture generic cellular behaviours, particles self-propel and interact through a soft short-range potential that accounts for cell-cell and cell-substrate adhesion, and that allows for cell-cell overlapping. In addition, we model the so-called contact inhibition of locomotion (CIL), which repolarizes cell migration away from cell-cell contacts, as a torque on the self-propulsion direction. We explicitly show how CIL yields an effective repulsion between cells, which allows the analytical

prediction of transitions between cohesive, non-cohesive, and three-dimensional cell arrangements. In simulations, we reproduce structures and collective dynamics observed in several existing tissue phenotypes, such as regular distributions of cells, dynamic cell clusters, gel-like networks, collectively migrating monolayers, and 3D aggregates. Finally, we discuss experimental findings from the perspective of our phase diagram, providing support for the correspondence between the organizations that emerge from our model and different tissue phenotypes.

5.1 Introduction

Cell colonies exhibit a broad range of phenotypes. In terms of structure, collections of cells can arrange into distributions of single cells, assemble into continuous monolayers or multi-layered tissues, or even form 3D agglomerates. In terms of dynamics, cell motility may be simply absent, or produce random, directed or collective migration of cells. Transitions between these states of tissue organization are characteristic of morphogenetic events and are also central to tumor formation and dispersal [Friedl 2003, Friedl 2009, Thiery 2009, Nieto 2013]. Therefore, a physical understanding of the collective behavior of cell colonies will shed light on many multicellular processes involved in development and disease.

However, a complete physical picture of multicellular organization is not yet available, partly due to the challenge of modeling the complex interactions between cells. In this chapter, we address this problem by modeling cell colonies as collections of self-propelled particles endowed with interactions capturing generic cellular behaviors. Models of self-propelled particles with polarity interactions have been used to investigate collective motion in cell monolayers (Fig. 5.1) [Méhes 2014, Szabó 2016, Camley 2017, Szabó 2006, Belmonte 2008, Henkes 2011, Basan 2013, Sepúlveda 2013, Deforet 2014, Woods 2014, Tarle 2015, Mones 2015, Garcia 2015, Zimmermann 2016, Camley 2016, George 2017]. Here, we extend this approach to unveil how the different structures and collective dynamics of cell colonies emerge from cell-cell interactions.

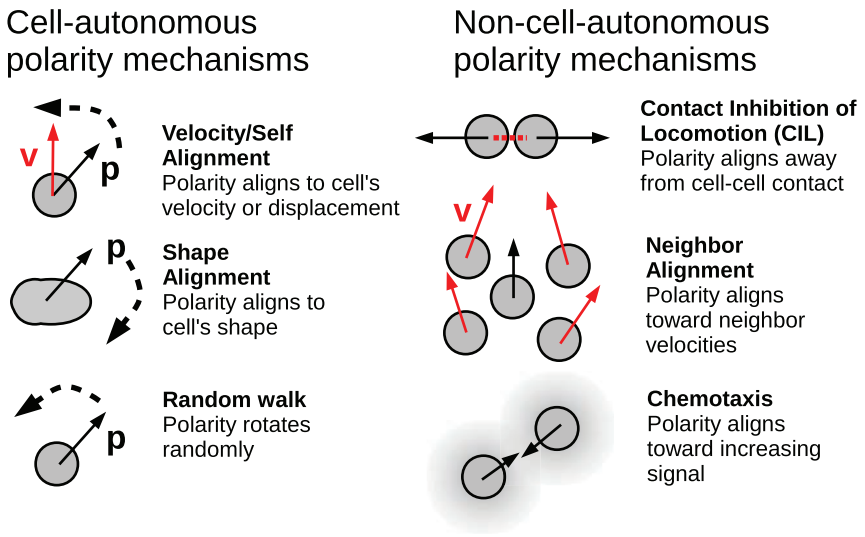

Figure 5.1 | Cell polarization mechanisms. Particle-based models of collective cell migration usually implement some of these mechanisms. Our model accounts for the random walk and CIL mechanisms. From [Camley 2017].

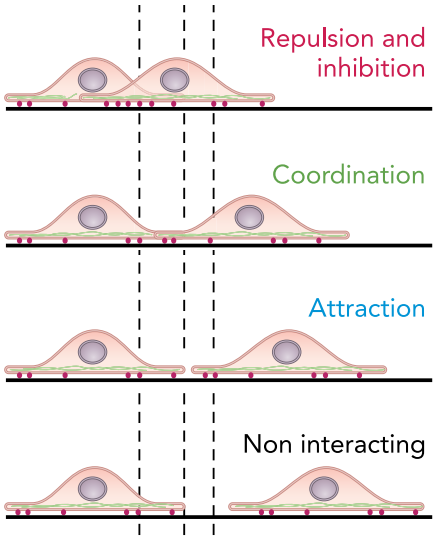

Figure 5.2 | Cell-cell interactions. When overlapping, cells exhibit a repulsive interaction due to excluded volume effects and to the resistance to decrease cell-substrate adhesion area. Moreover, they also exhibit inhibition of locomotion in the direction of the cell-cell contact. At an intermediate cell-cell distance, cell migration is optimally coordinated. When further separated, cells attract because of intercellular adhesion. Finally, when cells are separated more than their maximal spread size, they lose contact and they do not interact. From [Vedula 2013].

In addition to an excluded-volume repulsion, cells generally feature a short-range attraction as a consequence of their active cortical contractility transmitted through cell-cell junctions (Fig. 5.2). With no additional interactions, this attraction would typically lead to cohesive tissues. However, not all cell types form cohesive tissues. Whereas epithelial cells tend to form continuous monolayers, mesenchymal cells separate after division despite the presence of cell-cell junctions. This observation calls for an extra effective repulsion to drive the separation, which may ultimately have a deep impact on the overall organization of the colony.

Such a repulsive interaction mediated by adhesion is indeed present in many cell types upon cell-cell contact, and is known as contact inhibition of locomotion (CIL) [Mayor 2010, Stramer 2017] after Abercrombie and Heaysman [Abercrombie 1954]. Upon a cell-cell collision, the cell front adheres to the colliding cell, which hinders further cell protrusions. Subsequently, repolarization of the cell's cytoskeleton creates a new front away from the adhesion zone, and the two cells thus separate [Abercrombie 1958, Davis 2015] (Fig. 5.3). This interaction has been shown to be crucial in determining the collective behavior of cell groups in several contexts [Mayor 2010, Desai 2013, Vedula 2013, Mayor 2016, Hakim 2017, Stramer 2017]. For example, CIL guides the directional migration of neural crest cells [Carmona-Fontaine 2008], and also ensures the correct dispersion of Cajal-Retzius cells in the cerebral cortex [Villar-Cerviño 2013] or of hemocytes in the embryo [Davis 2012].

In Section 5.2, we introduce a particle-based description of cell colonies that models cellular interactions by means of an attraction due to intercellular adhesion, and a soft repulsion associated to the reduction of cell-substrate adhesion area. In addition, CIL is modeled as an interaction orienting cell motility away from cell-cell contacts. In Section 5.3, we derive a mean-field repulsive potential associated to CIL. Then, in Sections 5.4 to 5.6, we employ the mean-field potential to predict transitions between non-cohesive, cohesive, and overlapped organizations of the

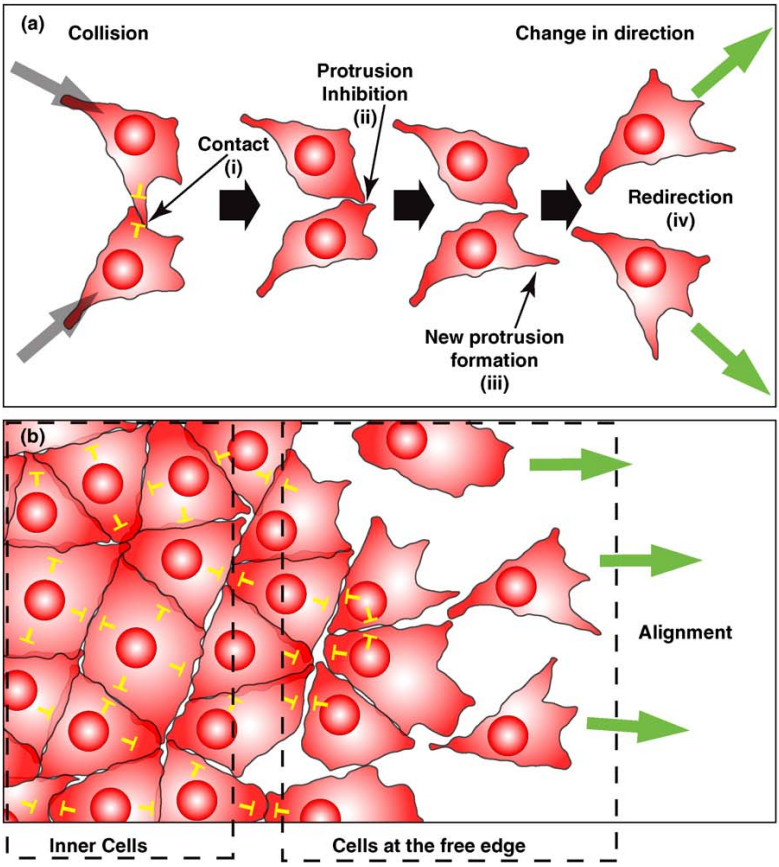

Figure 5.3 | Contact inhibition of locomotion. a, Contact between migrating cells produces the collapse and subsequent repolarization of cell protrusions to migrate in a new direction. **b,** In a group of cells, inhibition of protrusions yields inner cells unpolarized, whereas cells at the free edge polarize and may drive collective directional migration. From [Mayor 2010].

colonies as a function of cell-cell adhesion and CIL strength. These transitions are also observed in large-scale simulations performed by Bart Smeets (KU, Leuven). In simulations, we further identify states with different structures and emergent dynamics, including ordered or dynamic arrangements of cell clusters, gel-like networks, active gas and polar liquid states, and 3D aggregates. Finally, in Section 5.7, we interpret the results in biological terms by associating each state to a common tissue phenotype, namely grid-like distributions of mesenchymal cells, collectively migrating epithelial monolayers, and cellular spheroids.

5.2 Particle-based model

We model a 2D cell colony as a suspension of overdamped self-propelled disks of radius R. Neglecting translational fluctuations, the equation of motion of cell i with position $\vec{r}_i$ and polarity $\hat{p}_i$ reads

$$F_m \hat{p}_i = \gamma_s \dot{\vec{r}}_i + \sum_{j \in \text{nn}} \left[F_{ij}^{cc} \, \hat{n}_{ij} + \gamma \left(\dot{\vec{r}}_i - \dot{\vec{r}}_j \right) \right], \tag{5.1}$$

for contacting nearest neighbor cells j, with $\hat{n}_{ij} = (\vec{r}_j - \vec{r}_i)/d_{ij}$ the intercellular direction and $d_{ij} = |\vec{r}_j - \vec{r}_i|$ the cell-cell distance. Here, F_m is the magnitude of the cell self-propulsion force, and γ_s and γ are cell-substrate and cell-cell friction constants, respectively.

The central force F_{ij}^{cc} includes a soft repulsion F_{ij}^{r} associated to the reduction of the cell-substrate adhesion area when two cells are closer than their spread size $2R$, and an attractive force F_{ij}^{a} that accounts for cellular contractility transmitted through cell-cell adhesions. The repulsive force F_{ij}^{r} is assumed to increase linearly with decreasing intercellular distance d_{ij} up to $d_{ij} = R$. Hence,

$$F_{ij}^{r} = \frac{2W_s}{R^2} (2R - d_{ij}), \tag{5.2}$$

with

$$W_s = \int_R^{2R} F_{ij}^{r} \, \mathrm{d}d_{ij} \tag{5.3}$$

the cell-substrate adhesion energy (gray in Fig. 5.4a). No further reduction of the cell-substrate contact area is allowed for $d_{ij} < R$. As a result, cells can approach at smaller distances under compression. In this regime cells do not exert any force on the substrate and are considered to be extruded from the monolayer (Figs. 5.4a and 5.4b). Cell extrusions may lead to 3D tissues, whose structure and dynamics are not described by our 2D model. Respectively, the attractive force F_{ij}^{a} is assumed to increase linearly with distance up to $d_{ij} = 2R$. Hence,

$$F_{ij}^{a} = -\frac{2W_c}{R^2} (d_{ij} - R), \tag{5.4}$$

with

$$W_c = -\int_R^{2R} F_{ij}^{a} \, \mathrm{d}d_{ij} \tag{5.5}$$

the cell-cell adhesion energy (red in Fig. 5.4a). Accordingly, the total interaction force (black in Fig. 5.4a) reads

$$F_{ij}^{cc}(d_{ij}) = F_{ij}^{r} + F_{ij}^{a} = \begin{cases} \frac{2}{R}[W_s - \frac{W_s + W_c}{R}(d_{ij} - R)], & \text{if } R \le d_{ij} \le 2R \\ 0, & \text{else.} \end{cases} \tag{5.6}$$

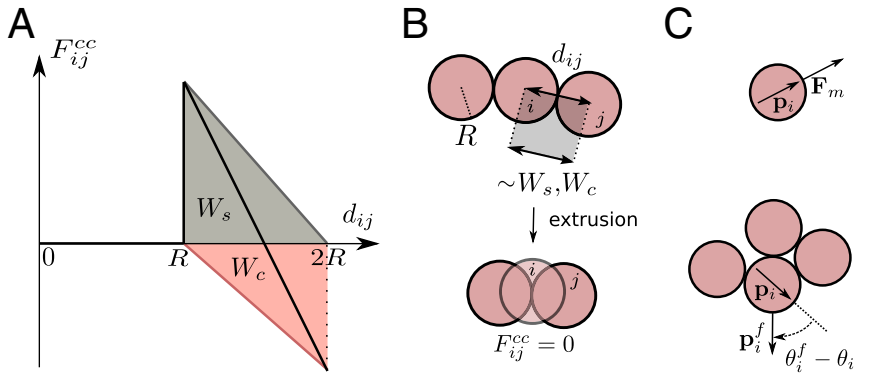

Figure 5.4 | A model of self-propelled particles with cell-like interactions. **a,** Central cell-cell force F_{ij}^{cc} (black) including a soft repulsion due to reduction of cell-substrate adhesion area (gray) and attraction due to cell-cell adhesions (red). **b,** Cell extrusion for intercellular distances $d_{ij} < R$, resulting in vanishing cell-cell forces in the plane. **c,** Cellular self-propulsion force F_m in the direction of the cell polarity $\hat{p}_i$. CIL rotates the polarity towards the direction $\hat{p}_i^f$ pointing away from cell-cell contacts.

In turn, CIL tends to orient cell polarity towards free space. Specifically, we define the free direction as pointing away from the weighted average position of the contacting cells (Fig. 5.4c):

$$\vec{p}_i^f = -\sum_{j \in \text{nn}} \frac{R^2}{d_{ij}^2} \hat{n}_{ij}. \tag{5.7}$$

This way, the more two cells overlap, the stronger they contribute to their respective free direction. Then, we model the CIL interaction as a rotation of the polarity $\hat{p}_i = (\cos\theta_i, \sin\theta_i)$ towards the free direction $\hat{p}_i^f = \vec{p}_i^f / |\vec{p}_i^f| = (\cos\theta_i^f, \sin\theta_i^f)$ (Fig. 5.4c) driven by a harmonic potential for the polarity angle θ_i [Camley 2016]. In addition, we include fluctuations of cell motion direction with a rotational diffusion coefficient D_r. Thus, the polarity dynamics is given by

$$\dot{\theta}_i = -f_{\text{cil}}(\theta_i - \theta_i^f) + \sqrt{2D_r}\,\xi, \tag{5.8}$$

where f_{cil} is the cellular repolarization rate upon cell-cell contact, namely the angular speed of the polarity vector rotation, and $\xi(t)$ is a typified Gaussian white noise.

The parameters of the model may be reduced to five dimensionless quantities: the packing fraction of cells ϕ, two ratios between adhesion and motility energies $\overline{W}_c = W_c/(2RF_m)$ and $\overline{W}_s = W_s/(2RF_m)$, a ratio between cell-cell and cell-substrate friction $\overline{\gamma} = \gamma/\gamma_s$, and a parameter $\psi = f_{\text{cil}}/(2D_r)$ that compares the timescale of cytoskeletal repolarization associated to CIL to the rotational diffusion. In the simulations performed by Bart Smeets, we set $\phi = 0.85$, $\overline{W}_s = 1$, $\overline{\gamma} = 0$,

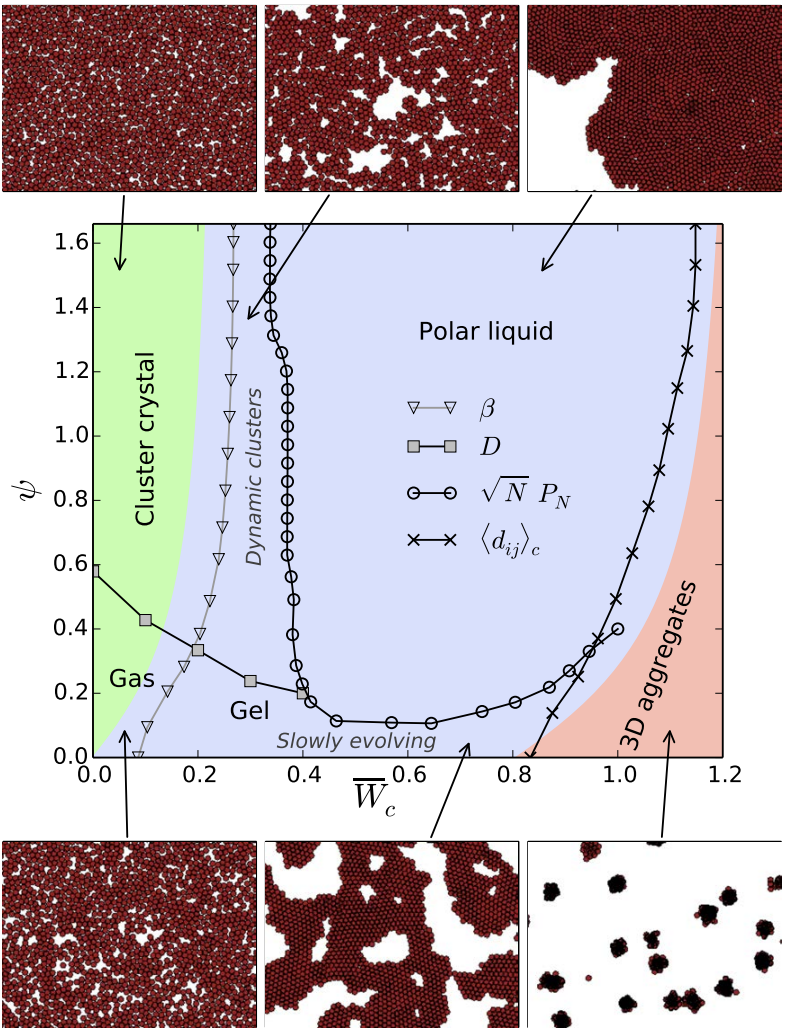

Figure 5.5 | Phase behavior of cell colonies. The dimensionless parameters are the ratio between cell-cell adhesion and motility energies $\overline{W}_c = W_c/(2RF_m)$, and the ratio between CIL repolarization rate and rotational diffusivity $\psi = f_{\text{cil}}/(2D_r)$. Colors indicate the predicted regions for non-cohesive (green), cohesive (blue), and overlapped (red) organizations. In addition to capturing these structural transitions, simulations identify dynamically distinct states such as an active gas, a cluster crystal, a gel-like percolated network, dynamic clusters, and an active polar liquid, as illustrated in snapshots.

and focus on the effects of intercellular adhesion and CIL on the organization of cell colonies. The results are summarized in the phase diagram of Fig. 5.5.

5.3 Effective repulsion by contact inhibition of locomotion

The repolarization of cell motility away from neighbors leads to cell-cell separation, thus acting as an effective repulsive interaction. In a mean-field approach, the CIL-induced effective repulsive force between two migrating cells is the orientational average of the cell self-propulsion force:

$$\vec{F}_{ij}^{p} = F_m \left\langle \hat{p}_i \right\rangle_{\theta_i} = F_m \int_{-\pi}^{\pi} \left(\cos\theta_i \, \hat{x} + \sin\theta_i \, \hat{y}\right) P\left(\theta_i\right) d\theta_i, \tag{5.9}$$

where $P\left(\theta_i\right)$ is the probability distribution of the polarity angle θ_i. This distribution is determined by the stationary solution of the Fokker-Planck equation associated to the Ornstein-Uhlenbeck stochastic process in Eq. (5.8) [Coffey 2004]:

$$\partial_t P\left(\alpha_i, t\right) = f_{\text{cil}} \partial_{\alpha_i} \left[\alpha_i P\left(\alpha_i, t\right)\right] + D_r \partial_{\alpha_i}^2 P\left(\alpha_i, t\right), \tag{5.10}$$

where we have introduced the angle $\alpha_i = \theta_i - \theta_i^f$ between the cell polarity and the free direction[1]. Solving Eq. (5.10) in the stationary state with periodic boundary conditions $P\left(\pi\right) = P\left(-\pi\right)$ yields

$$P\left(\alpha_i\right) = \sqrt{\frac{\psi}{\pi}} \frac{e^{-\psi \alpha_i^2}}{\operatorname{erf}\left(\sqrt{\psi}\,\pi\right)}, \tag{5.11}$$

where we have identified the dimensionless parameter $\psi = f_{\text{cil}}/(2D_r)$ that compares the two sources of repolarization, namely CIL and rotational diffusion.

Now, for two contacting cells, the free direction coincides with the intercellular axis. Thus, decomposing the polarity vector in the direction of the intercellular axis $\hat{n}_{ij}$ and the ortogonal direction $\hat{t}_{ij}$, Eq. (5.9) can be rewritten as

$$\vec{F}_{ij}^{p} = F_m \int_{-\pi}^{\pi} \left(\cos\alpha_i \, \hat{n}_{ij} + \sin\alpha_i \, \hat{t}_{ij}\right) P\left(\alpha_i\right) d\alpha_i. \tag{5.12}$$

Then, introducing Eq. (5.11) we obtain

$$\vec{F}_{ij}^{p} = \frac{F_m e^{-1/(4\psi)}}{2\operatorname{erf}\left(\sqrt{\psi}\,\pi\right)} \left[\operatorname{erf}\left(\frac{i + 2\pi\psi}{2\sqrt{\psi}}\right) - \operatorname{erf}\left(\frac{i - 2\pi\psi}{2\sqrt{\psi}}\right)\right] \hat{n}_{ij}. \tag{5.13}$$

Typically, $\psi \gg 1/(2\pi)$, and hence the CIL-induced repulsive pairwise force can be approximated by

$$\vec{F}_{ij}^{p} \approx F_m e^{-1/(4\psi)} \, \hat{n}_{ij}. \tag{5.14}$$

[1] Since θ_i^f depends on the positions of the neighbor cells, it indirectly depends on θ_i, which influences the neighbor's positions through the force balance. However, we neglect this coupling when introducing the new variable α_i, which leads to a closed equation for the polarity dynamics, namely Eq. (5.10).

5.4 Non-cohesive phase

First, we study the transition between a cohesive phase in which cells remain in contact, $d_{ij} < 2R$, and a non-cohesive phase in which they lose contact. Loss of cell contact is only possible if the CIL-induced repulsive force obtained above is stronger than the maximal attractive force at $d_{ij} = 2R$, $F_{ij}^{cc}(2R) = -2W_c/R$. Thus, within the mean-field approximation introduced in Section 5.3, the condition

$$F_{ij}^{p} + F_{ij}^{cc}(2R) = 0 \tag{5.15}$$

gives a prediction for the transition between the non-cohesive (green in Fig. 5.5) and cohesive (blue in Fig. 5.5) phases. This condition gives a critical cell-cell adhesion energy

$$\overline{W}_c^{\mathrm{coh}} = \frac{1}{4} e^{-1/(4\psi)} \tag{5.16}$$

above which cells are expected to be in contact or, alternatively, a critical CIL rate above which cohesiveness is lost. Therefore, at low cell-cell adhesion, CIL promotes cell dispersal, thereby hindering the formation of cohesive tissues.

In simulations, we quantify this transition in terms of particle number fluctuations. Phase separated self-propelled disks feature giant number fluctuations [Henkes 2011, Fily 2012, Fily 2014]. In this state, the standard deviation of the number of particles N in a given region scales as $\sigma_N \sim N^{\beta}$ for large N, with $\beta \approx 1$, whereas a system at equilibrium would feature $\beta = 1/2$. Similarly, we compute the exponent β (Fig. 5.6a) and identify the regions with $\beta > 1/2$ as phase-separated, and thus cohesive. Consequently, we identify the transition to the cohesive phase from the onset of giant number fluctuations (triangles in Fig. 5.5), which qualitatively agrees with the mean-field analytical prediction.

Within the non-cohesive phase (green in Fig. 5.5), the colony forms an active gas state with equilibrium-like statistics ($\beta \approx 1/2$) at low CIL repolarization rates ψ. At larger ψ, cells get hyperuniformly distributed, with $\beta < 1/2$ (Fig. 5.6a), forming a crystal of small cell clusters. This state is reminiscent of the equilibrium cluster crystals formed by purely repulsive soft spheres [Mladek 2006]. In our case, an effective repulsion arises from anti-aligned propulsion forces via CIL (Section 5.3). To identify the clustering transition, we set a dynamical criterion based on the cell diffusion coefficient D obtained from the long-time mean-squared displacement (MSD) [Levis 2014], $\lim_{t\to\infty}\langle(\Delta\vec{r})^2\rangle = 4Dt$. Increasing the repolarization rate ψ initially enhances diffusion by promoting cluster evaporation. However, the stronger effective repulsion at larger ψ progressively prevents cells from escaping the clusters, hence reducing diffusion until it is eventually solely due to intercluster hopping events [Moreno 2007]. Consequently, we locate the clustering transition (squares in Fig. 5.5) from the maximum of $D(\psi)$ at each $\overline{W}_c$ (Fig. 5.6b). Increasing cell-cell adhesion favors clustering, thereby enabling the short-range CIL-associated repulsion responsible for the crystalline order.

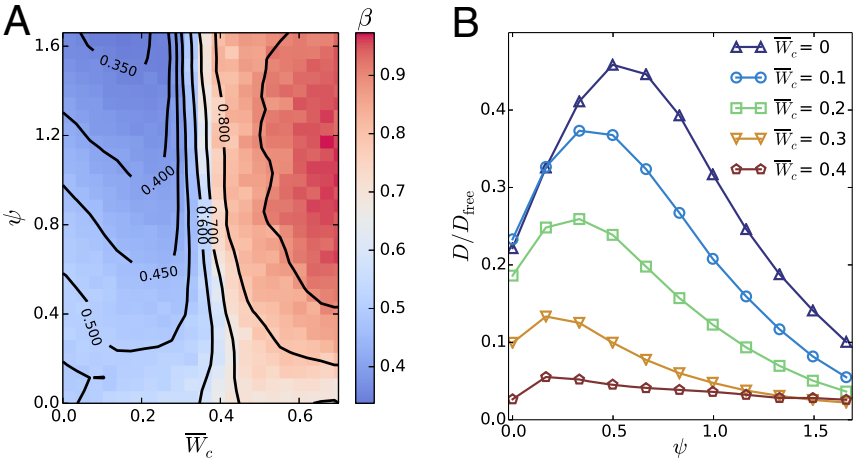

Figure 5.6 | Number fluctuations and diffusion in cell colonies. a, Exponent of number fluctuations $\sigma_N \sim N^\beta$ as a function of $\overline{W}_c$ and ψ. Phase-separated states feature giant number fluctuations ($\beta > 1/2$) whose onset identifies the transition to the cohesive phase (triangles in Fig. 5.5). In the non-cohesive phase, colonies of slowly repolarizing cells (low ψ) feature equilibrium-like fluctuations ($\beta \approx 1/2$), whereas faster repolarizations (higher ψ) induce a hyperuniform distribution of cells ($\beta < 1/2$). **b,** Cell diffusion coefficient D as a function of ψ for some values of $\overline{W}_c$. For increasing repolarization rate ψ, D initially increases but then decreases as clusters form. The maximum of $D(\psi)$ identifies the onset of clustering (squares in Fig. 5.5). $D_{\text{free}} = F_m/(2\gamma_s D_r)$ is the translational diffusion coefficient of a persistent random walker with rotational diffusion [Coffey 2004].

5.5 Cohesive phase

Increasing cell-cell adhesion beyond the transition to the cohesive phase (blue in Fig. 5.5), the colony initially forms a percolating structure of clusters. At low CIL repolarization rate ψ, cells arrange in a network with very slow, subdiffusive dynamics, as shown by the MSD $\langle(\Delta\vec{r})^2\rangle \sim t^\alpha$ with $\alpha < 1$ (Fig. 5.7a). Thus, due to cell-cell adhesion, the colony forms a near-equilibrium attractive gel [Redner 2013a] with few cell rearrangements. At larger repolarization rates ψ (above squares in Fig. 5.5, see Fig. 5.6b), the effective CIL-associated repulsion yields smaller, dynamic, and locally crystalline clusters. They arise from a kinetic balance between the CIL-enhanced evaporation and the adhesion-induced condensation of clusters that prevents the completion of phase separation into a continuous dense phase.

Complete phase separation occurs at larger cell-cell adhesion, $\overline{W}_c \gtrsim 0.4$. The coarsening dynamics (Figs. 5.7b and 5.7c) are much faster than in a passive system, for which particle domains grow by diffusion as $\mathfrak{L}(t) \sim t^{1/3}$ [Bray 1994]. By orienting cell motility towards free space, CIL induces an advective coarsening of the cell domains that enables a fast phase separation of cell colonies.

Upon phase separation, the colony forms a continuous cell monolayer that ex-

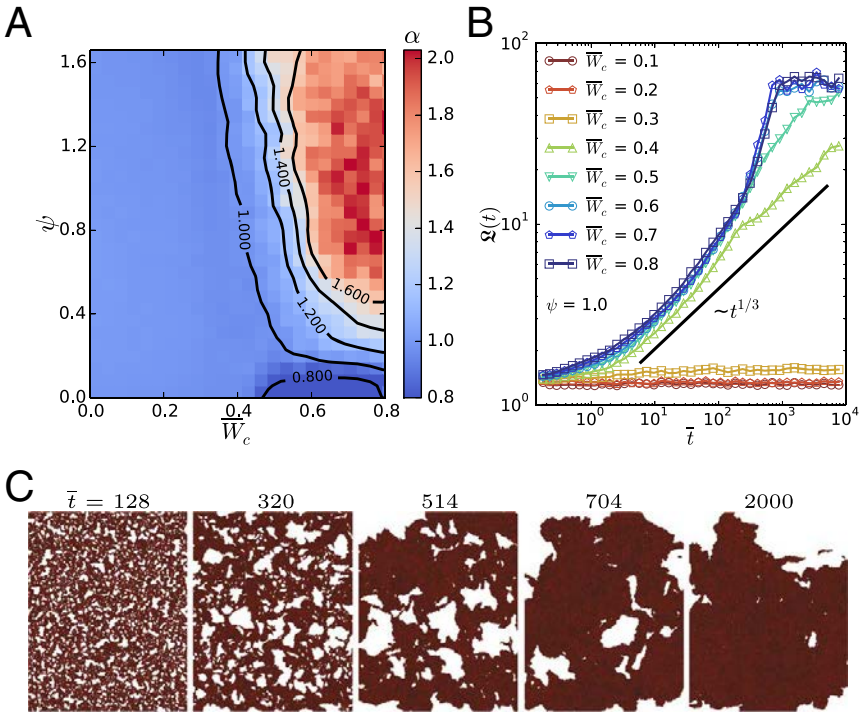

Figure 5.7 | Dynamics and phase-separation kinetics in cell colonies. a, MSD exponent α, $\langle(\Delta\vec{r})^2\rangle \sim t^{\alpha}$, as a function of $\overline{W}_c$ and ψ. The colony forms a gel-like network with subdiffusive dynamics ($\alpha < 1$) at low ψ. Faster CIL gives rise to collective cell motion as indicated by almost ballistic dynamics ($\alpha = 2$). **b,** Evolution of the average domain size $\mathfrak{L}(t)$, computed from the structure factor, for different $\overline{W}_c$ at $\psi = 1$. Dimensionless time reads $\bar{t} = F_m/(2R\gamma_s)t$. The colony phase separates for $\overline{W}_c \gtrsim 0.4$. CIL yields faster phase-separation kinetics than the diffusive coarsening dynamics of passive systems, for which $\mathfrak{L}(t) \sim t^{1/3}$ [Bray 1994]. **c,** Illustration of the phase separation from an initial random configuration towards the active polar liquid at $\psi = 1$ and $\overline{W}_c = 0.7$.

hibits self-organized collective motion. This is reflected in the MSD exponent, that evolves from diffusive ($\alpha = 1$) towards almost ballistic ($\alpha = 2$) above $\overline{W}_c \approx 0.4$ (Fig. 5.7a). CIL induces a coupling between cell polarity and density fluctuations in the fluid phase that gives rise to a macroscopic polarization via a spontaneous symmetry breaking. The outward motion of cells at the boundary of the monolayer creates free space behind them, which polarizes neighboring cells before the leading cell can reorient back. Through this mechanism, self-organized collective cell motion emerges from CIL, leading to an active polar liquid state.

The polar order is stable if the confinement imposed by neighbors restores the position and orientation of a cell before its polarity turns towards a new free direction. The repolarization occurs within a timescale $1/f_{\mathrm{cil}}$, and the characteristic

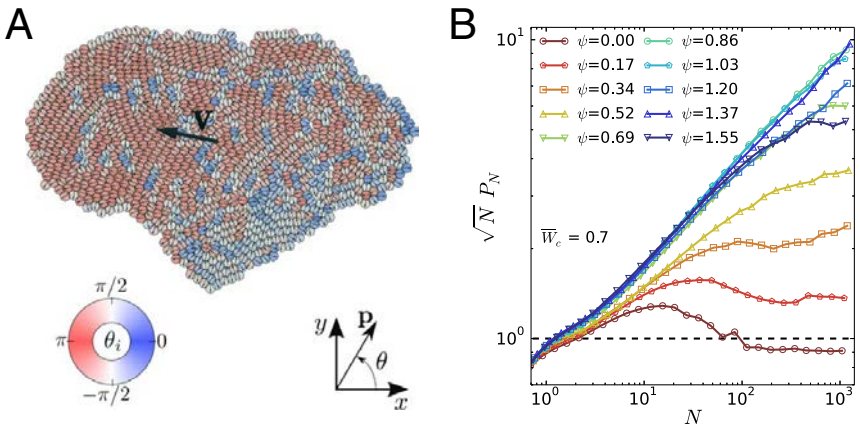

Figure 5.8 | Collective motion in cell colonies. a, Snapshot of a globally polarized, collectively migrating cell monolayer. **b,** Rescaled average polarity $\sqrt{N}\,P_N$ of a monolayer of N cells for different CIL repolarization rates ψ at a cell-cell adhesion $\overline{W}_c = 0.7$. $\sqrt{N}\,P_N = 1$ corresponds to randomly oriented cells. CIL induces a global polarity ($\sqrt{N}\,P_N > 1$) that gives rise to collective motion. The appearance of several polarity domains reduces the average polarity of large cell groups. The transition to the active polar liquid state (circles in Fig. 5.5) is defined by the condition that the maximum of $\sqrt{N}\,P_N$ is at $N = 75$.

time of position relaxation in a dense environment is $\sim \gamma_s/k$, with $k = 4(W_s + W_c)/R^2$ the stiffness of a two-neighbor confinement. Thus, an approximate stability criterion reads $\gamma_s/k \lesssim f_{\rm cil}^{-1}$, which is satisfied for the whole parameter range in Fig. 5.5.

As illustrated in Fig. 5.8a, isolated fluid monolayers may acquire a global polarity, and consequently perform persistent random walks with a persistence much larger than that of single cells. For randomly oriented cells, the average polarity of N cells scales as $P_N = |\sum_{i=1}^{N} \hat{p}_i|/N \sim N^{-1/2}$. If cell polarities align, the average polarity of a small region of cells decreases slower with its size, so that $\sqrt{N}P_N > 1$. At sufficiently large sizes, multiple misaligned polarity domains appear that restore the random scaling (Fig. 5.8b). Hence, we define the onset of macroscopic polarization (circles in Fig. 5.5) by the condition that $\sqrt{N}\,P_N$ has a maximum at $N = 75$, namely that connected clusters consisting of up to 75 cells may form a single polarity domain. The appropriate choice of N depends on system size. However, for the sizes explored, the transition line (circles in Fig. 5.5) is hardly sensitive to values around $N = 75$ (Fig. 5.9). In conclusion, by ensuring a complete phase separation while still allowing for cell rearrangements, sufficiently strong cell-cell adhesion and CIL are required to form a polar, collectively moving cell monolayer.

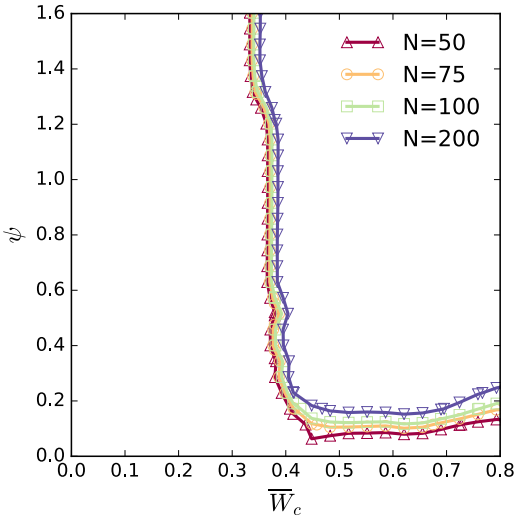

Figure 5.9 | Criterion for the onset of macroscopic polarity in cell monolayers. For the system sizes explored, the transition line (circles in Fig. 5.5 for $N = 75$) hardly depends on the choice of N, namely the size of the larger cluster that is fully polarized, forming a single polarity domain. Thus, the criterion is robust.

5.6 Overlapped phase

In this section, we focus on the transition to 3D tissues. When the average total cell-cell force is attractive, cells eventually overcome the energy barrier associated to the soft repulsive potential (Fig. 5.4a), which corresponds to cell extrusion events. Extruded cells are confined at distances smaller than R, where they exert neither cell-cell nor traction forces. Thus, our model can predict the onset of the transition to 3D cell arrangements. Assuming a homogeneous distribution of cells, and using Eq. (5.6), the average interaction force reads

$$\left\langle F_{ij}^{cc} \right\rangle = \frac{\int_R^{2R} 2\pi d_{ij} F_{ij}^{cc} \, \mathrm{d}d_{ij}}{\int_R^{2R} 2\pi d_{ij} \, \mathrm{d}d_{ij}} = \frac{2}{9R} \left(4W_s - 5W_c\right). \tag{5.17}$$

This force adds to the effective repulsion F_{ij}^{p} associated to anti-aligned self-propulsion forces (Eq. (5.14)), so that the transition between monolayers (blue in Fig. 5.5) and 3D cell arrangements (red in Fig. 5.5) is predicted by the condition

$$\left\langle F_{ij}^{cc} \right\rangle + F_{ij}^{p} = 0. \tag{5.18}$$

This condition sets a critical cell-cell adhesion energy

$$\overline{W}_c^{\mathrm{3D}} = \frac{1}{5}\left[4\overline{W}_s + \frac{9}{4} e^{-1/(4\psi)}\right] \tag{5.19}$$

above which cells are expected to fully overlap or, alternatively, a critical CIL repolarization rate above which cell extrusion is prevented. Therefore, by opposing cell extrusion, CIL hinders the collapse of cell monolayers into 3D aggregates. Indeed, a sufficiently fast repolarization of cell motility may stabilize cell monolayers even

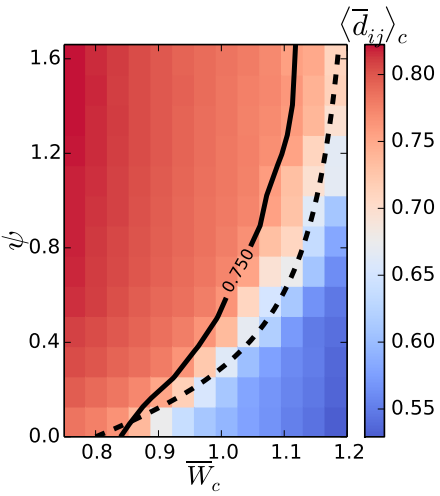

Figure 5.10 | Wetting transition of cell monolayers. Average distance between contacting cells $\langle \overline{d}_{ij} \rangle_c = \langle d_{ij} \rangle_c / (2R)$ as a function of $\overline{W}_c$ and ψ. The transition between cell monolayers and 3D aggregates is predicted to occur at a vanishing average cell-cell force (dashed line, Eqs. (5.18) and (5.19)), and identified by the condition $\langle d_{ij} \rangle_c = 3R/2$ (solid line, crosses in Fig. 5.5).

when cell-cell adhesion is stronger than cell-substrate adhesion, $\overline{W}_c > \overline{W}_s = 1$ (Fig. 5.5).

In simulations, we characterize the degree of cell overlap in terms of the average distance between contacting cells $\langle d_{ij} \rangle_c$ (Fig. 5.10). We identify the transition point to the overlapped phase by the condition that $\langle d_{ij} \rangle_c$ is the average of the critical distance for extrusion, $d_{ij} = R$, and the distance between fully spread cells, $d_{ij} = 2R$. Hence, the transition is defined by $\langle d_{ij} \rangle_c = (R + 2R)/2 = 3R/2$ (crosses in Fig. 5.5), in qualitative agreement with the mean-field analytical prediction.

Monolayer instability occurs through a dewetting process whereby holes appear in the cell monolayer, which rapidly evolves into a network structure, as experimentally observed (Fig. 6.3) [Douezan 2012a]. Subsequently, different regions of the network slowly collapse into separate aggregates. In general, the 3D aggregate-monolayer transition can be viewed as a wetting transition of the cell colony [Douezan 2011] enabled by cell insertion or extrusion [Beaune 2014]. Thus, our results show how CIL favors tissue wetting by orienting cell motility towards free space.

5.7 Discussion of experiments

In this section, based on experimental observations, we propose that the different organizations of cell colonies that emerge from our generic model correspond to different well-known tissue phenotypes (Fig. 5.11). First, the non-cohesive phase, in which cells are not in contact, might correspond to mesenchymal tissues. Experiments show that CIL leads to regular distributions of mesenchymal cells during development [Villar-Cerviño 2013, Davis 2012]. This result is consistent with the transition towards an ordered structure of cell clusters by increasing CIL strength ψ (Fig. 5.5).

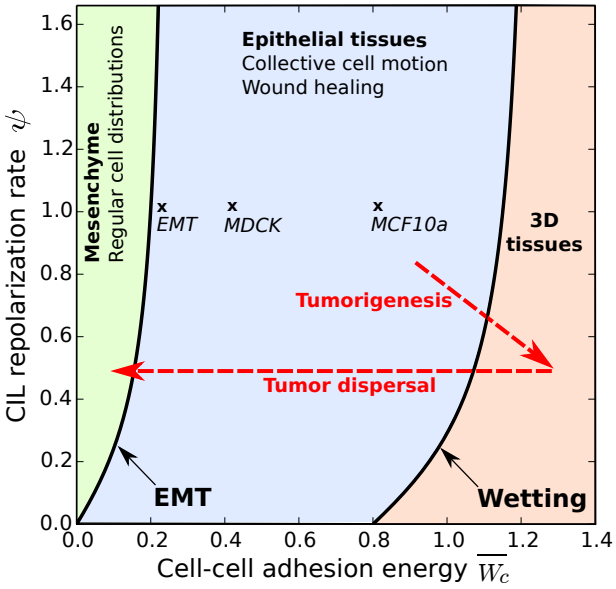

Figure 5.11 | Proposed correspondence of tissue phenotypes to phases of the model. The association between phenotypes (bold) and phases (colors) is based on the indicated features, and supported by the parameter estimates for two epithelial tissues [Vincent 2015], and an EMT [Bazellières 2015] (crosses, see text). Speculated trajectories in cellular interaction parameter space during cancer progression are also indicated (dashed arrows).

The cohesive phase, in which cells maintain contact, can correspond to epithelial tissues. In the active polar liquid state, CIL induces cells to spontaneously invade empty spaces within the tissue, similarly to wound healing processes characteristic of epithelia. Indeed, simulations of prepared wounds reproduce the closure dynamics observed in experiments [Cochet-Escartin 2014] (Fig. 5.12). In the absence of CIL, healing is severely impaired (Fig. 5.13), in agreement with experiments upon inhibition of Rac1 [Anon 2012], a key protein for CIL behavior [Roycroft 2016].

In addition, the parameters of our phase diagram can be estimated from experiments on two epithelial cell lines. By fitting the MSD of the motion of a self-propelled particle with rotational diffusion (persistent random walk) [Cofey 2004],

$$\langle(\Delta\vec{r})^2\rangle = 2v_m^2/D_r^2\left(D_r t + e^{-D_r t} - 1\right), \tag{5.20}$$

to experimental data for MCF10a cells (Fig. 5.14), we estimate a self-propulsion velocity $v_m = F_m/\gamma_s \approx 1$ μm/min, and a diffusion coefficient $D_r \approx 0.05$ min^{-1}. These estimates give a Péclet number $\mathrm{Pe} = 3v_m/(2RD_r) \approx 2$, too low to produce motility-induced phase separation [Redner 2013b, Redner 2013a]. In turn, we estimate the rate of cell motility repolarization, f_{cil}, from the duration of cell-cell contact during CIL events. From experimental data on two mesenchymal cell types, hemocytes [Davis 2015] and fibroblasts [Kadir 2011], we estimate $f_{\mathrm{cil}} \approx 0.1$

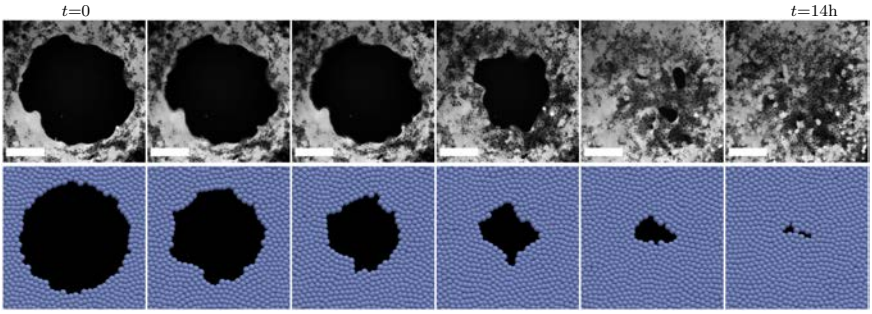

Figure 5.12 | The active polar liquid state recapitulates wound healing. The closure dynamics of a circular gap of radius $R_0 = 250$ μm in an MDCK cell monolayer in vitro (top, actin-GFP) [Cochet-Escartin 2014] is well reproduced in simulations (bottom). Simulation parameter values are $R = 16$ μm, $v_m = 1$ μm/min, $D_r = 0.05$ min^{-1}, $F_m = 25$ nN, $\overline{W}_c = 0.42$, $\overline{W}_s = 0.35$, and $\psi = 1$, which we estimate for MDCK monolayers (see text), and correspond to the polar liquid region of our phase diagram (Fig. 5.5). Scale bar, 100 μm.

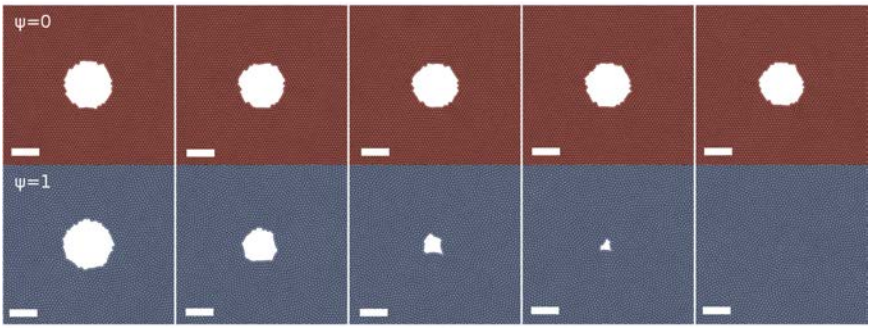

Figure 5.13 | CIL enables wound healing by collective cell migration. Simulated healing of a circular gap of radius $R_0 = 100$ μm for 15 h. In the absence of CIL (red), wound healing is severely impaired compared to the typical case with $\psi = 1$ (blue, see text). The simulation is performed for a cell monolayer in the polar liquid state ($\overline{W}_c = 0.7$, see Fig. 5.5). Scale bar, 100 μm.

min^{-1}. The same estimate is obtained for epithelial MDCK cell monolayers from the time that a wound needs to start closing [Brugués 2014a]. Then, assuming that these parameter values are similar for MCF10a and MDCK cells, we estimate $\psi = f_{\text{cil}}/(2D_r) \approx 1$ for both cell lines. Self-propulsion forces can be estimated from traction force measurements, which yield $F_m \approx 60$ nN for MCF10a and $F_m \approx 25$ nN for MDCK cells in monolayers [Bazellières 2015]. Finally, cell-cell and cell-substrate adhesion energies can be related to an effective elastic modulus Γ of an expanding monolayer, and to the total cellular strain ϵ_{tot} at which the expansion stops [Vincent 2015]. From Eq. (5.6), $\Gamma \approx (W_s + W_c)/R^2$. Respectively, ϵ_{tot}

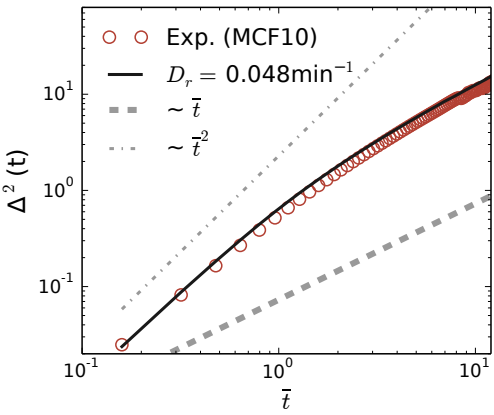

Figure 5.14 | Mean-squared displacement of cell migration. The evolution of the MSD of migrating MCF10a cells is fit by that of a persistent random walk, Eq. (5.20), which yields estimates for the velocity $v_m \approx 1$ μm and rotational diffusivity $D_r \approx 0.048$ min^{-1} of the motion. Dimensionless time reads $\bar{t} = F_m/(2R\gamma_s)t$.

corresponds to the cell-cell distance at mechanical equilibrium, $d_{ij}^{\text{eq}} = (1 + \epsilon_{\text{tot}})\, R$, namely the distance at which the total cell-cell force vanishes, $F_{ij}^{cc} + F_{ij}^{p} = 0$:

$$d_{ij}^{\text{eq}} = \frac{R}{W_s + W_c}\left[2W_s + W_c + \frac{R}{2}F_m e^{-\frac{1}{4\psi}}\right]. \tag{5.21}$$

Then, using $R = 16$ μm and the values of Γ and ϵ_{tot} reported in [Vincent 2015], we infer $\overline{W}_s \approx 1.1$ and $\overline{W}_c \approx 0.8$ for the MCF10a tissue, and $\overline{W}_s \approx 0.35$ and $\overline{W}_c \approx 0.42$ for the MDCK tissue. The transition to 3D structures would then occur at $\overline{W}_c^{\text{3D}} \approx 1.3$ for the MCF10a tissue. Thus, this tissue type falls well within the polar liquid state, in which cells form a collectively migrating continuous monolayer as experimentally observed. Respectively, the MDCK tissue is closer to the wetting transition, which we estimate at $\overline{W}_c^{3D} \approx 0.63$. Thus, although the MDCK monolayer also falls within the polar liquid state, it may form 3D structures more easily, in line with experimental observations [Deforet 2014].

Now, the transition from cohesive to non-cohesive phases should correspond to the epithelial-mesenchymal transition (EMT), which is associated to down-regulation of cell-cell adhesion proteins (Fig. 5.15) [Thiery 2009, Nieto 2013]. Our prediction sheds light on the role of CIL in the EMT (Fig. 5.11). As above, we can estimate the parameters for an EMT in an expanding MCF10a monolayer. Upon a knockdown of cell-cell adhesion proteins, the epithelial tissue disaggregates at an intercellular stress $\sigma_{xx}^{\text{coh}} \approx 300$ Pa [Bazellières 2015]. From this value, we can obtain the critical cell-cell adhesion for the loss of cohesiveness as $\overline{W}_c^{\text{coh}} \approx \sigma_{xx}^{\text{coh}} h R^2$, with $h \approx 5$ μm the height of the monolayer. Hence, we estimate $\overline{W}_c^{\text{coh}} \approx 0.2$, consistent with the prediction $\overline{W}_c^{\text{coh}} \approx 0.19$ at $\psi = 1$.

A tissue may also disaggregate by increasing cell traction forces, such as upon treatment with hepatocyte growth factor [Vincent 2015, Maruthamuthu 2014]. In our diagram, an increased self-propulsion force F_m yields a lower value of $\overline{W}_c = W_c/(2RF_m)$, whereas its critical value depends only on CIL (Eq. (5.16)). Hence, an increase in traction force asymmetry may also cause an EMT (Fig. 5.15).

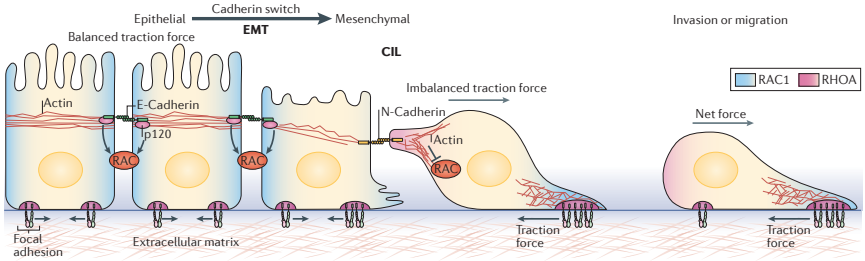

Figure 5.15 | Epithelial-mesenchymal transition. This transition involves loss of cell-cell adhesion, and acquisition of planar cell polarity, asymmetric traction forces, and CIL behavior. This is consistent with the association of the EMT to the cohesive-noncohesive phase transition of our model (Fig. 5.11). In neural crest cells, the EMT is triggered by a switch from E-cadherin to N-cadherin as a cell-cell adhesion protein [Scarpa 2015]. From [Stramer 2017].

In conclusion, the estimates and observations support the association of epithelial tissues to the cohesive phase. Nevertheless, some mesenchymal cells can also migrate collectively as a consequence of CIL [Carmona-Fontaine 2008, Woods 2014, Szabó 2016] or of increased cell-cell adhesion [Plutoni 2016]. Therefore, these specific phenotypes might also correspond to the active polar liquid state. However, whether the features of collective mesenchymal cell migration [Theveneau 2013] fully agree with our results deserves further exploration.

Finally, in our model, the overlapped phase corresponds to 3D tissues. Their structure is not captured by our 2D model, which only predicts the onset of their appearance. In experiments, the transition from a cell monolayer to a 3D aggregate can be induced in many ways [Gonzalez-Rodriguez 2012] (Fig. 6.1), such as by increasing the density of cell-cell adhesion proteins [Ryan 2001, Douezan 2011]. Alternatively, one can reduce the density of cell-substrate proteins [Ryan 2001, Ravasio 2015] which, in our diagram, entails a decrease of the critical cell-cell adhesion for the wetting transition, Eq. (5.19). 3D aggregates also form when the substrate is softened [Douezan 2012c] (Fig. 6.A.3), which simultaneously decreases cell tractions F_m and cell-substrate adhesion W_s. This increases $\overline{W}_c = W_c/(2RF_m)$ while keeping $\overline{W}_s = W_s/(2RF_m)$, and hence $\overline{W}_c^{3D}$, constant.

The monolayer-spheroid transition has been put forward as an in vitro model for tumor formation and spreading [Gonzalez-Rodriguez 2012]. In this context, our predictions may contribute to appreciate the role of CIL in cancer progression [Abercrombie 1979] (Fig. 5.11). Indeed, downregulation of cell-cell adhesion and enhanced traction forces promote metastasis, which may proceed through many steps involving collective cell migration, dissemination of cell clusters, and a final EMT [Friedl 2003, Friedl 2009, Thiery 2009, Nieto 2013, Cheung 2016].

5.8 Conclusions

In summary, we have studied the organization of cell colonies by means of an active-particle model. The interparticle interactions (Fig. 5.4) capture specific cellular behaviors such as CIL, and give rise to several structures and collective dynamics (Fig. 5.5). Our results show how CIL leads to regular cell arrangements, and hinders the formation of cohesive tissues. Self-organized collective motion in continuous cell monolayers, including wound healing, also emerges from CIL interactions. The soft character of the intercellular potential allows for the extrusion-mediated collapse of cell monolayers into 3D aggregates, which is opposed by CIL. Thus, our work highlights the prominent role of CIL in determining the emergent structures and dynamics of cell colonies. From a more general perspective, our results underscore the need to include specific cellular interactions in particle-based models of tissues to recapitulate observed organizations and collective behaviors of cell colonies.

In addition, we have analytically derived an effective CIL-induced cellular repulsion force, which yields explicit predictions for transitions between non-cohesive, cohesive, and 3D colonies. Based on experimental observations and parameter estimates, we associate these phases to mesenchymal, epithelial, and 3D tissue phenotypes (Fig. 5.11). Thus, our predictions might have implications for processes that modify the tissue phenotype, both in development and disease. In general, this chapter illustrates how a soft active matter approach may provide insight into multicellular organization and collective cell migration.

Contributions and acknowledgements

The work described in this chapter is the result of a collaboration between simulations and theory. Bart Smeets (KU, Leuven) and Romaric Vincent (IBEC, Barcelona & CEA, Grenoble) conceived the research. Bart performed simulations, Romaric performed experiments (Fig. 5.14), and I derived analytical predictions. Ignacio Pagonabarraga (UB, Barcelona), Jiří Pešek and Herman Ramon (KU, Leuven) also contributed to the interpretation of results. Bart prepared most figures.

6

Active wetting of epithelial tissues

Contents

Abstract

The transition from an epithelial monolayer to a spheroidal cell aggregate holds an analogy with the dewetting process whereby a fluid layer collapses into a droplet. Exploiting this analogy, this chapter is devoted to studying the wetting transition of epithelial monolayers from a mechanical point of view. First, we describe the experiment that motivated this study, which shows the dewetting of an epithelial

cancer cell monolayer in vitro. Then, we introduce a continuum active polar fluid model of the monolayer that predicts its traction and flow profiles. By fitting the predicted traction profiles to the experimental kymographs, we infer the mechanical parameters of the monolayer. The model also predicts the existence of a critical size for the wetting transition in the monolayer, in contrast with the classical wetting transition in regular fluids. We verify this prediction by studying cell monolayers of different sizes.

6.1 Introduction

When a cell aggregate is placed on a flat substrate, it may spread on it by extending a cell monolayer or it may remain as a cellular spheroid. Whether one or the other process actually takes place depends on the cohesion of the aggregate and its interactions with the substrate. More precisely, the transition between a spheroidal aggregate and a monolayer was associated to a competition between cell-cell and cell-substrate adhesion [Ryan 2001].

In this sense, a direct analogy can be drawn with the wetting transition of a droplet of a simple fluid on a solid substrate. Depending on the surface tensions of the liquid-gas, liquid-solid, and solid-gas interfaces, which are directly related to their corresponding adhesion energies, the droplet either remains as a spherical cap with a non-zero contact angle or spreads over the substrate as a fluid film. This wetting analogy for cell colonies was firmly established by a series of experiments that studied the spreading of cell aggregates [Gonzalez-Rodriguez 2012]. In these experiments, the cell-cell and cell-substrate adhesivity was varied by different means, such as tuning the expression levels of cell-cell adhesion proteins [Ryan 2001, Douezan 2011], the surface treatment of the substrate [Ryan 2001, Douezan 2011], or its rigidity [Douezan 2012c].

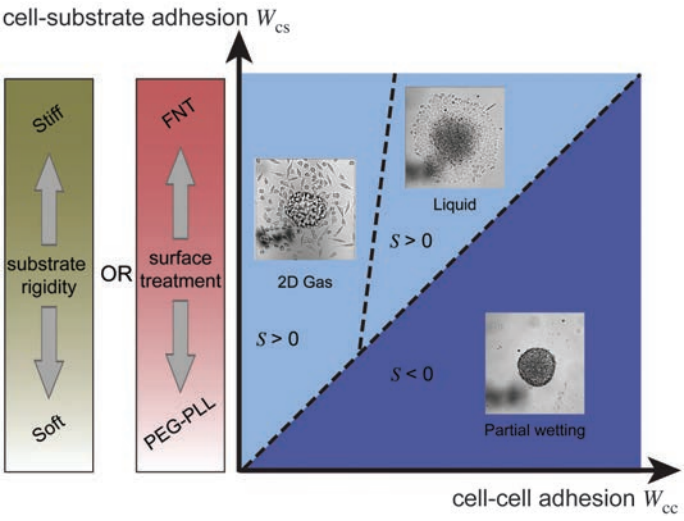

Figure 6.1 | Phase diagram of tissue wetting. For negative values of the spreading parameter, cell-cell adhesion dominates over cell-substrate adhesion, so that the cell colony forms an aggregate (partial wetting). For positive values of the spreading parameter, cell-substrate adhesion wins over cell-cell adhesion, thus driving the spreading of the colony into either a cohesive fluid monolayer or a gas-like state of scattered cells. The adhesivity of the substrate may be modified either by tuning its surface treatment or its rigidity. From [Gonzalez-Rodriguez 2012].

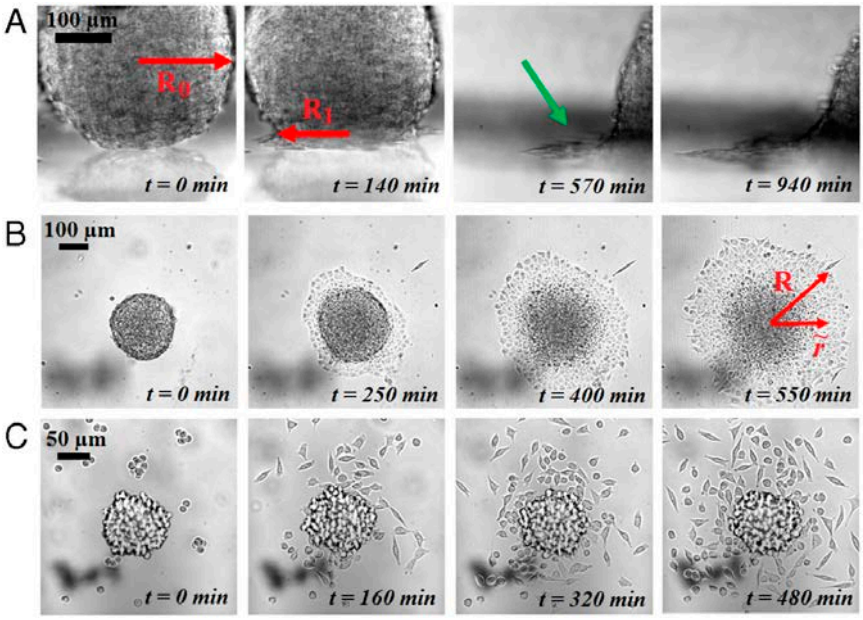

Figure 6.2 | Spreading dynamics of a cell aggregate. a, A precursor film extends from the aggregate. **b,** A cohesive cell monolayer spreads on the substrate in the complete wetting phase. **c,** The aggregate disgregates into a gas-like state of scattered cells when cell-cell adhesion is too weak to sustain a cohesive monolayer. From [Douezan 2011].

All the phenomenology found in these experiments was rationalized by complete analogy with the classical wetting transition picture, namely in terms of the spreading parameter S, as summarized in Fig. 6.1. For cell colonies, the spreading parameter can be written as $S = W_{cs} - W_{cc}$ [Douezan 2011], which encodes the competition between cell-cell and cell-substrate adhesion energies in a direct way. Thus, a positive spreading parameter corresponds to a cell-substrate adhesion stronger than cell-cell adhesion, so that aggregate spreading is energetically favourable. In this case, a precursor film of cells radially extends from the aggregate until it completely wets the substrate as a cell monolayer (Figs. 6.2a and 6.2b) [Douezan 2011, Beaune 2014]. In fact, the cell monolayer may even disgregate into a gas-like phase of scattered cells if cell-cell adhesion is sufficiently weak (Fig. 6.2c) [Douezan 2011, Guo 2006]. In contrast, a negative spreading parameter corresponds to cell-cell adhesion winning over cell-substrate adhesion, and hence to the partial wetting phase in which the cells remain as an aggregate. Under these conditions, a large cell monolayer was also shown to dewet from the substrate by the nucleation and growth of holes (Fig. 6.3), as would occur in a viscous film on a slipping surface [Douezan 2012a, Beaune 2014].

In addition to setting the physical basis of the tissue wetting transition, some

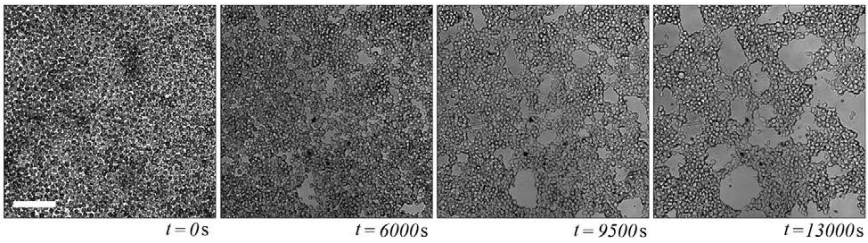

Figure 6.3 | Dewetting of a cell monolayer on a nonadhesive substrate by nucleation and growth of holes. Scale bar, 100 μm. From [Douezan 2012a].

of these studies also characterized the dynamics of aggregate spreading [Douezan 2011, Douezan 2012b, Douezan 2012c, Beaune 2014] and monolayer dewetting [Douezan 2012a]. However, the detailed mechanics of the wetting transition were unknown. In particular, the connection between the spreading parameter and the forces involved in the collective migration of the monolayer remained elusive. Therefore, it is the objective of this chapter to elucidate how the tissue wetting transition arises from the competition of forces in a cell monolayer.

To this end, traction force microscopy experiments were performed by Carlos Pérez-González in the lab of Xavier Trepat (IBEC, Barcelona), which are briefly described in Section 6.2. Section 6.3 introduces the active polar fluid model of the monolayer that was proposed to understand the observations. The model is solved in Section 6.4 to yield predictions for the traction and flow profiles, which are contrasted with experimental data. In Section 6.5, the model is employed to study the wetting transition of the monolayer, giving the spreading parameter in terms of the model parameters characterizing the active cellular forces in the monolayer. The model predicts the existence of a critical size for the wetting transition in the monolayer, which is verified in further experiments on monolayers of different radii.

6.2 Dewetting of an epithelial monolayer

The main idea of the experiment is to induce the dewetting of an epithelial monolayer by an increasing expression of E-cadherin, one of the main molecular components of cell-cell adhesions in epithelial tissues. An increasing expression of this protein should increase cell-cell adhesion, and thus eventually induce tissue dewetting. To this end, the experiments use MDA-MB-231 cells, which are metastatic human epithelial breast cancer cells, that were genetically engineered to have an inducible promoter of the gene responsible for the expression of E-cadherin [Sarrió 2009]. This way, the expression of E-cadherin can be induced by the addition of dexamethasone.

These cells are then plated on polyacrylamide gels with embedded fluorescent beads, which allows the traction forces exerted by the cells on the substrate to

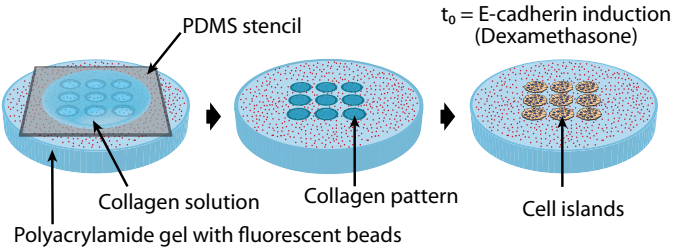

Figure 6.4 | Cells are confined within circular adherent regions of the substrate. A pattern of collagen coating defines the adherent regions. The substrate is an elastic polyacrylamide gel with embedded fluorescent beads (red dots) used for traction force and monolayer stress microscopy.

Figure 6.5 | Addition of dexamethasone induces E-cadherin expression. The concentration of E-cadherin is quantified from Western Blot analyses, in arbitrary units defined with respect to the signal intensity of tubulin.

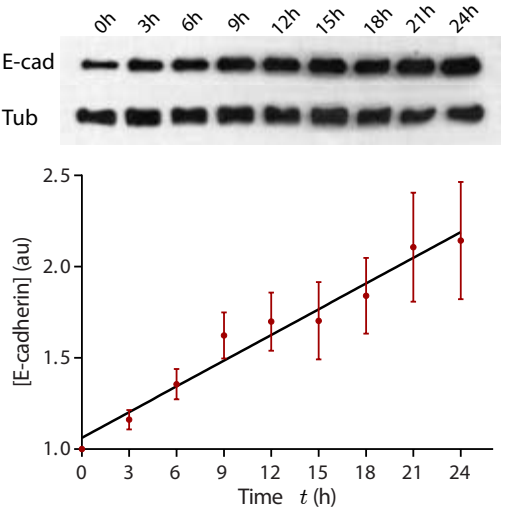

be measured via traction force microscopy [Serra-Picamal 2015]. The tension in the monolayer is also measured from traction force fields via monolayer stress microscopy [Serra-Picamal 2015, Tambe 2013, Zimmermann 2014b]. In the present experiments, the elastic substrate is coated with circular regions of collagen, which is a common extracellular matrix protein to which cells can attach. Therefore, the substrate features circular adherent islands to which cells are confined (Fig. 6.4).

Upon addition of dexamethasone, cells increase their expression of E-cadherin (Fig. 6.5) and progressively turn from moving as individual cells to forming a cohesive epithelial monolayer (Fig. 6.6a). Traction force measurements show that weak and randomly oriented traction forces initially appear throughout the cell island. Later, with the formation of a cohesive monolayer, traction forces become stronger, oriented along the radial direction, and localized at the edge of

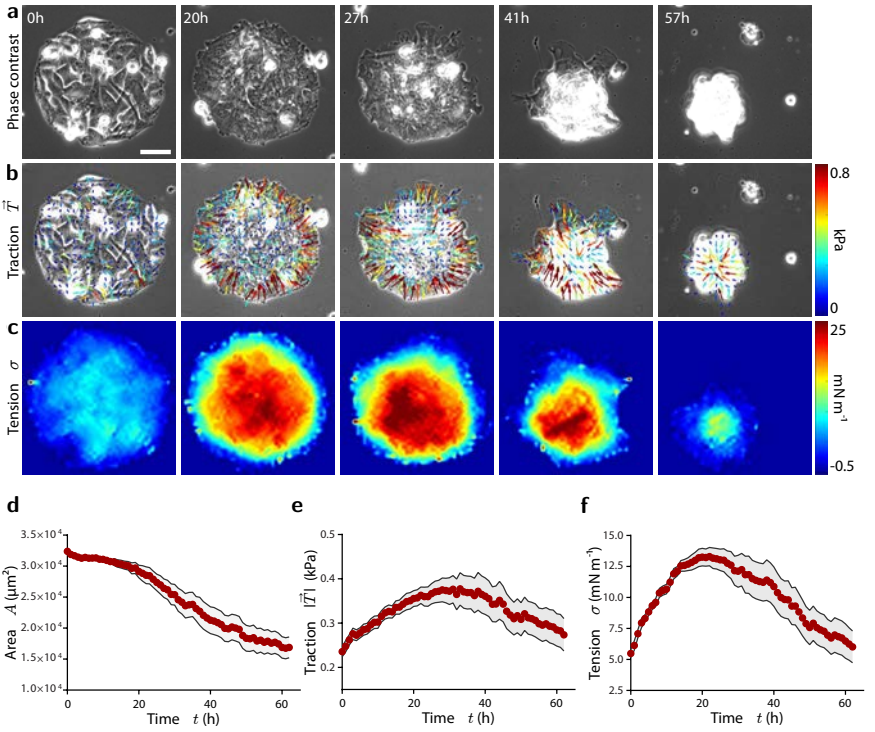

Figure 6.6 | Mechanics of monolayer dewetting. a, The expression of E-cadherin induces the formation of a cohesive cell monolayer. Later, the monolayer dewets from the substrate. Scale bar, 40 μm. **b,** The initially weak and random traction forces progressively localize at the monolayer edge, becoming stronger and radially oriented. **c,** Monolayer tension is maximal at the center of the monolayer, and increases in time. **d,** The dewetting process is reflected in a decreasing area of the monolayer. **e, f,** The average magnitude of the traction forces **e,** and monolayer tension **f,** increase in time until the onset of dewetting.

the cell island (Fig. 6.6b and 6.7), consistently with previous findings [Mertz 2012, Mertz 2013]. In turn, the internal tension is maximal at the center of the monolayer (Fig. 6.6c). The average magnitude both of traction forces and monolayer tension is found to increase with time (Figs. 6.6e and 6.6f) [Harris 2014].

Eventually, the monolayer dewets from the substrate and ends up forming a spheroidal aggregate (Fig. 6.6a and 6.8). It is worth noting that the monolayer always collapses into a single tissue droplet. This contrasts with the dewetting of much larger monolayers [Douezan 2012a], which tear apart into several aggregates by the nucleation and growth of holes (Fig. 6.3). In fact, the dewetting process of a passive liquid film into a single droplet was only experimentally realized very recently (Fig. 6.9), unveiling remarkable differences between the dynamics of wetting and dewetting [Edwards 2016].

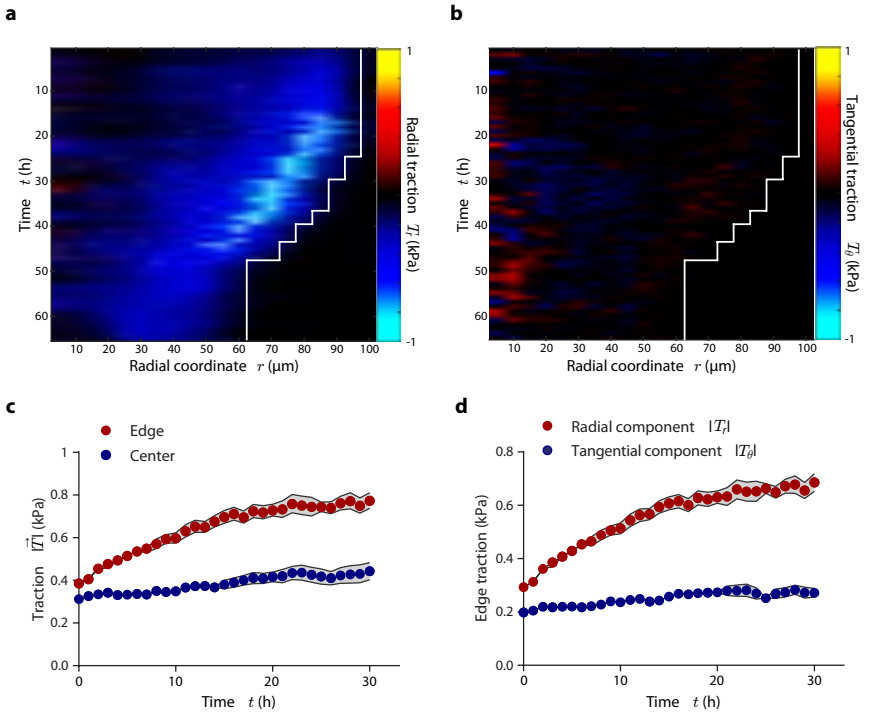

Figure 6.7 | Traction forces localize at the edge and are mainly radial. a, b, Kymographs of the radial component **a,** and of the absolute value of the ortoradial component **b,** of the traction force field. The radial component is larger and more localized. **c,** Tractions at the edge are stronger and increase in time more significantly than those at the center of the monolayer. **d,** The radial component of edge tractions increases in time, whereas the ortoradial component remains constant.

To understand the wetting transition, we asked what is the origin of the increasing cellular forces, and whether these forces are responsible for the transition. Western blot analyses show that the increasing expression of E-cadherin is paralleled by an increase in myosin phosphorylation (Fig. 6.10a), which should account for the increasing forces. It is worth noting that the total concentration of myosin is not affected by the expression of E-cadherin (Fig. 6.10b). In addition, single isolated cells do not feature increasing traction forces upon the treatment with dexamethasone (Fig. 6.11), suggesting that myosin phosphorylation and the ensuing increase in forces result from a mechanosensing process associated to cell-cell adhesion [Harris 2014]. The molecular or cellular mechanism whereby an increasing expression of E-cadherin may result in myosin phosphorylation remains, to our knowledge, unknown. Indeed, if based on a mechanosensing pathway, our measurements would suggest a mechanosensitive response in the opposite direction compared to the well-known reinforcement of cell-cell junctions under

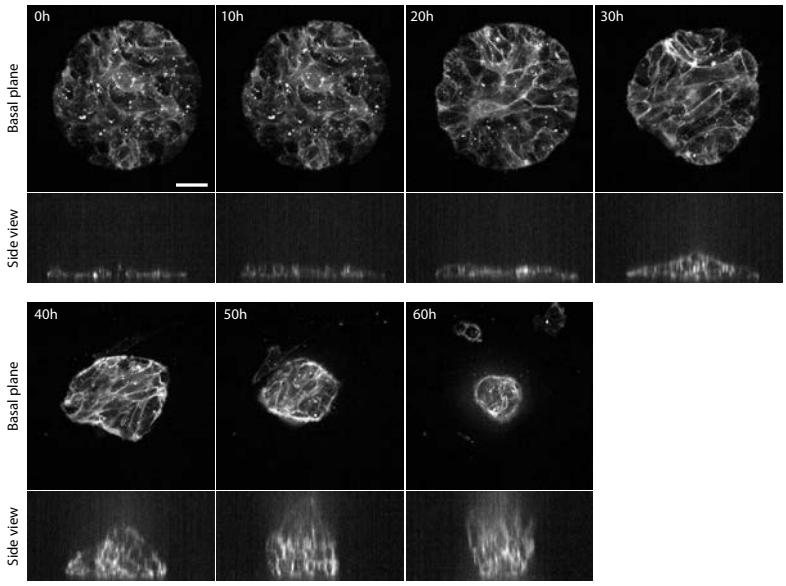

Figure 6.8 | Monolayer dewetting. The tissue-substrate contact area decreases pronouncedly upon dewetting (basal plane). The tissue evolves from a cell monolayer to a spheroidal cell aggregate, resembling a droplet. The contact angle increases up to values above 90° (side view). Scale bar, 40 μm.

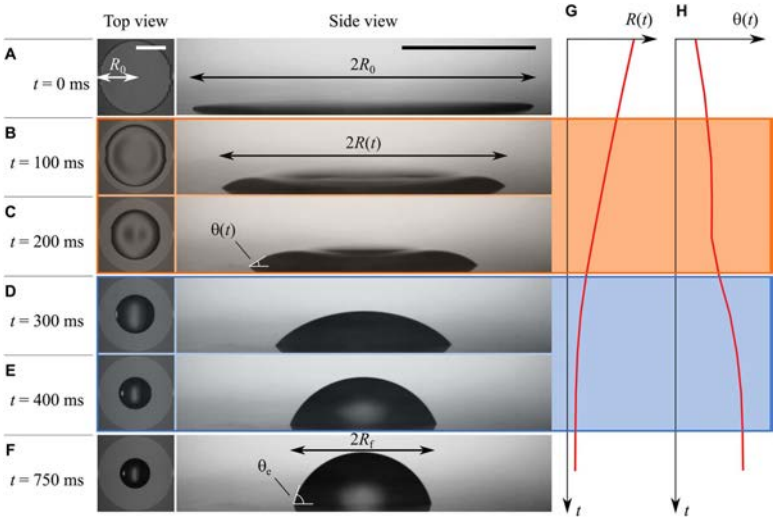

Figure 6.9 | Dewetting of a passive liquid film into a single droplet. The initial radius of the film is $R_0 = 2.5$ mm. Scale bar, 2 mm. From [Edwards 2016].

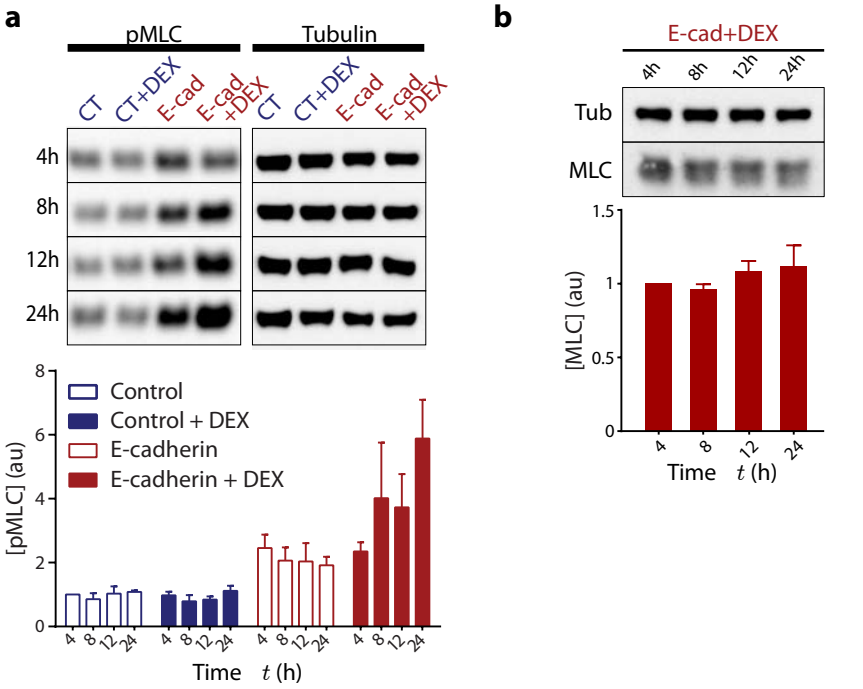

Figure 6.10 | E-cadherin expression is paralleled by myosin phosphorylation. a, The concentration of phosphorylated myosin increases upon induction of E-cadherin expression by dexamethasone. **b,** Under the same conditions, the total concentration of myosin does not increase. Concentrations are quantified in arbitrary units from Western blot analyses as in Fig. 6.5.

Figure 6.11 | Traction forces of a single cell do not increase in time. This suggests that the expression of E-cadherin induces myosin phosphorylation through a mechanosensing process associated to cell-cell junctions.

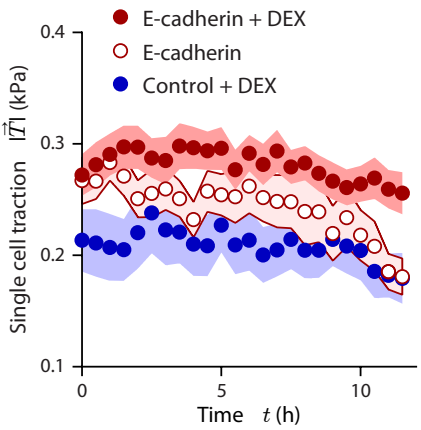

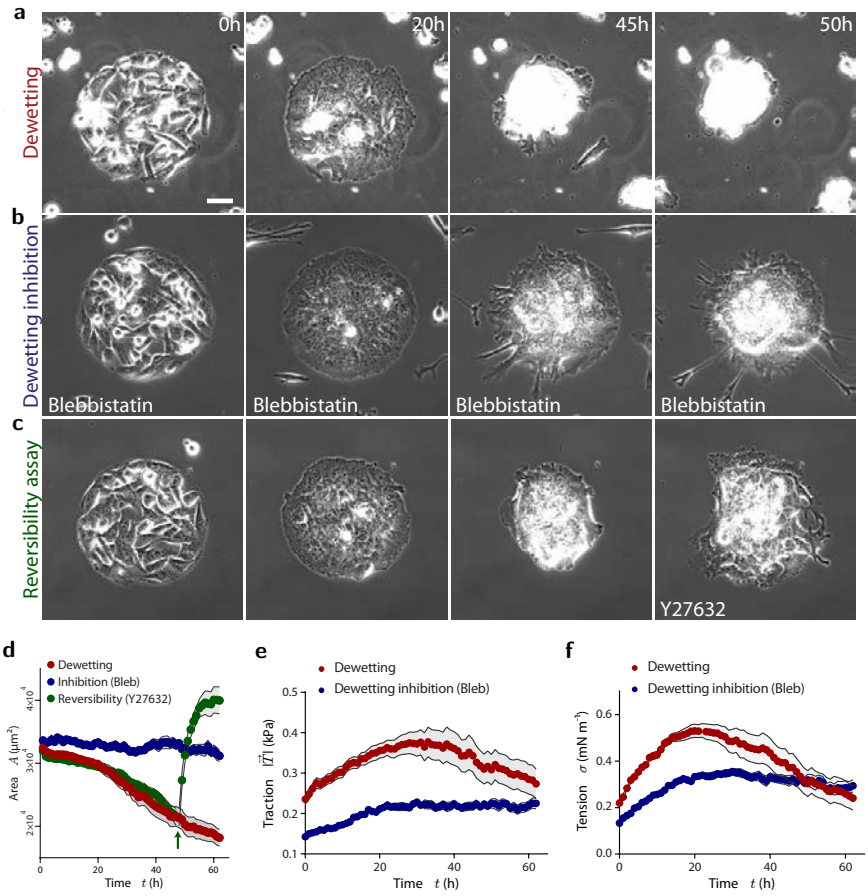

Figure 6.12 | Monolayer dewetting is induced by tissue tension. **a,** Control monolayer dewetting. Scale bar, 40 μm. **b,** Treatment with blebbistatin inhibits, or at least strongly impairs, tissue dewetting. **c,** Dewetting can be reversed back to wetting by inhibiting contractility via application of Y27632. **d,** Monolayer area does not substantially decrease in the presence of blebistattin. Upon application of Y27632 (arrow), a dewetting monolayer spreads again. **e, f,** The magnitude of traction forces **e,** and monolayer tension **f,** is reduced under the action of blebbistatin.

force application [Schwartz 2008, Liu 2010, Gomez 2011, Leckband 2011, Dufour 2013, Engl 2014, Hoffman 2015, Lecuit 2015].

Next, to check whether the increase in forces induces monolayer dewetting, we inhibit myosin activity. Upon treatment with blebbistatin, monolayer dewetting is prevented or, at least, significantly delayed (Figs. 6.12b and 6.12d). Traction forces and tissue tension are substantially reduced under these conditions (Figs. 6.12e and 6.12f). In addition, the dewetting process can be reversed by the application

of the ROCK inhibitor Y27632, which causes the monolayer to wet the substrate again (Figs. 6.12c and 6.12d). Hence, we conclude that, when they overcome a certain threshold, cell-generated contractile forces drive the dewetting of the monolayer. Note that the increasing expression of E-cadherin could trigger the dewetting process on its own, simply by strengthening cell-cell junctions and hence increasing the cell-cell adhesion energy (see Fig. 6.1). However, our observations show that this is not the case but that, instead, a competition between active cellular forces drives the monolayer through the wetting transition. Therefore, the increasing expression of E-cadherin is only indirectly responsible for the dewetting of the monolayer in our experiments.

6.3 Active polar fluid model of epithelial spreading

The observation of the active wetting transition described above motivated the formulation of a physical model to understand it quantitatively. Instead of formulating a model based on adhesion energies, similar to those previously proposed to describe tissue wetting, our aim is to see how the wetting transition arises from mechanical models of collective cell migration. To this end, we extend a previously introduced continuum model of epithelial spreading [Blanch-Mercader 2017b] to the present problem. This continuum model takes a coarse-grained approach that describes the long-time and large-scale dynamics of the tissue as those of an active polar liquid. Below, we briefly justify this description, which has already been applied to the spreading of tissue monolayers [Blanch-Mercader 2017b, Lee 2011b, Lee 2011a]. In fact, a very similar model has also been proposed for traction force and velocity profiles of single crawling cells [Roux 2016].

We remark that, although the dewetting process involves an out-of-plane reorganization of the initial cell monolayer, the model below only describes the 2D dynamics of the monolayer. Therefore, the model can not capture the 3D flows and shape of the tissue, nor the dynamics of the contact angle. However, our 2D description is sufficient to predict the onset and initial dynamics of the wetting transition, which is the focus of our study.

6.3.1 Polarity dynamics

In monolayers, cells often acquire anisotropic cytoskeletal organizations and shapes, which gives rise to planar orientational order in the tissue. Nematic orientational order has been experimentally found and characterized, becoming apparent by the observation of topological defects in the orientation field [Gruler 1999, Kemkemer 2000, Duclos 2014, Duclos 2017, Saw 2017, Kawaguchi 2017, Hirst 2017]. Therefore, tissue monolayers may form nematic liquid crystal phases.

In our monolayer, cells at the center do not exhibit any clear sign of planar polarity, and they exert weak and random traction forces (Fig. 6.6b-6.7). In contrast, cells at the edge extend large lamellipodia towards the outside and exert strong inward-pointing traction forces on the substrate, indicating that they are polarized

(Fig. 6.6b-6.7). The outwards polarization of cells at the border is likely due to contact inhibition of locomotion, a cell-cell interaction whereby cells repolarize in opposite directions upon contact [Mayor 2010, Stramer 2017]. In fact, this interaction is mediated by cell-cell adhesion, with front-rear differences in cadherin-based junctions acting as a cue for the repolarization [Desai 2009, Khalil 2010, Weber 2012, Theveneau 2013, Vedula 2013, Ladoux 2016]. Although originally proposed for mesenchymal cells, contact inhibition of locomotion is being increasingly recognized to play a key role in orchestrating the collective migration of epithelial monolayers [Mayor 2010, Theveneau 2013, Vedula 2013, Ladoux 2016, Mayor 2016, Hakim 2017, Zimmermann 2016, Coburn 2016, Smeets 2016] (see also Chapter 5). In a cohesive monolayer, this interaction naturally leads to polarization of cells at the edge towards free space, leaving cells at the center unpolarized (Fig. 6.13). Such a polarity profile, in turn, explains the localization of traction forces at the edge and the build-up of tension at the center of epithelial monolayers [Zimmermann 2016, Coburn 2016]. Therefore, upon the expression of E-cadherin, we expect the polarity field $\vec{p}\,(\vec{r},t)$ to be entirely set by contact inhibition of locomotion, and hence to remain essentially independent of flows in the monolayer. Consequently, within a phenomenological approach, we propose the polarity field to follow a purely relaxational dynamics given by

$$\frac{\partial p_\alpha}{\partial t} = -\frac{1}{\gamma_1}\frac{\delta F}{\delta p_\alpha}, \tag{6.1}$$

where $F\,[p]$ is the coarse-grained free energy functional of the orientational degrees of freedom. Thus, the functional derivative of F, which is known as molecular field $h_\alpha = -\delta F/\delta p_\alpha$, gives the generalized restoring force that changes the polarity field at a rate controlled by the orientational friction coefficient γ_1, known as rotational viscosity.

For the sake of comparison with the general case, the full constitutive equation for the polarity of a d-dimensional active polar fluid reads [Kruse 2005, Jülicher 2011, Marchetti 2013, Prost 2015]

$$\left(\partial_t + v_\beta \partial_\beta\right) p_\alpha + \omega_{\alpha\beta} p_\beta = \frac{1}{\gamma_1} h_\alpha - \frac{\bar{\nu}_1}{d} v_{\gamma\gamma} p_\alpha - \nu_1 \tilde{v}_{\alpha\beta} p_\beta + \epsilon p_\alpha. \tag{6.2}$$

Here, v_α is the velocity field, with $\tilde{v}_{\alpha\beta} = 1/2\left(\partial_\alpha v_\beta + \partial_\beta v_\alpha\right) - v_{\gamma\gamma}/d\ \delta_{\alpha\beta}$ and $\omega_{\alpha\beta} = 1/2\left(\partial_\alpha v_\beta - \partial_\beta v_\alpha\right)$ are the traceless symmetric and antisymmetric parts of the strain rate tensor, with $v_{\gamma\gamma} = \partial_\gamma v_\gamma$. In turn, $\bar{\nu}_1$ and ν_1 are the bulk and shear flow alignment coefficients, and ϵ is the active alignment coefficient. Thus, with respect to the most general situation of Eq. (6.2), we do not consider polarity advection and corotation, nor flow alignment and active spontaneous polarization effects in Eq. (6.1). Note that these simplifications are based on the contact inhibition of locomotion mechanism for tissue polarity, and that they may not apply to other experimental situations.

Then, the coarse-grained free energy F has a local polynomial contribution that specifies the preferred polarity, in addition to spatial coupling terms resulting

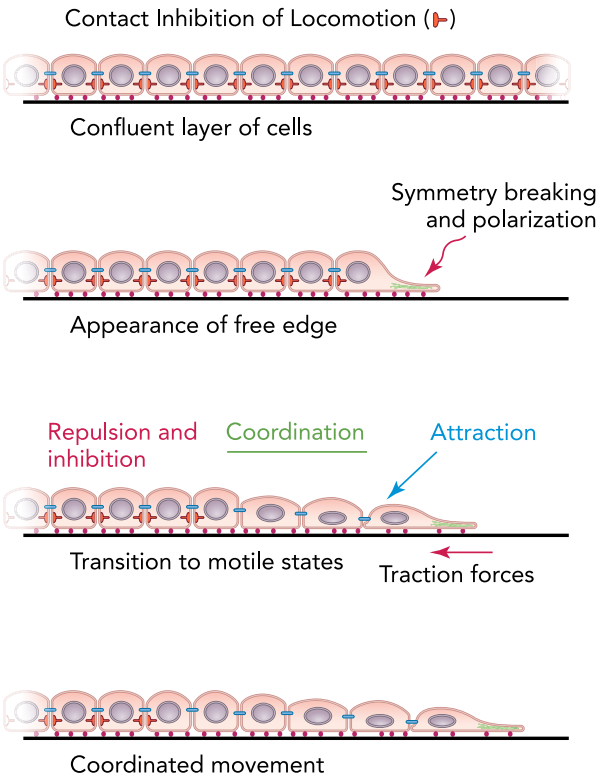

Figure 6.13 | Polarization of cells in a monolayer by contact inhibition of locomotion. The motility of cells in a confluent monolayer is symmetrically inhibited by their neighbours. In contrast, at a free edge, this symmetry in the contact inhibition of locomotion is broken, which results in polarization of cells at the edge towards free space. Polarized cells start migrating, thus pulling on their neghbouring cells. This asymmetric force transmission force polarizes follower cells [Ladoux 2016], which establishes a polarity profile that results in the collective migration of the monolayer. From [Vedula 2013].

from nematic elasticity, known as the Frank elastic free energy [de Gennes 1993, Stewart 2004, Stephen 1974, Singh 2002]. For a planar polarity field, it reads

$$F = \int_{\mathcal{V}} \left[\frac{a}{2} p^2 + \frac{b}{4} p^4 + \frac{K_1}{2} \left(\vec{\nabla} \cdot \vec{p} \right)^2 + \frac{K_2}{2} \left(\vec{\nabla} \times \vec{p} \right)^2 \right] d^3\vec{r}, \qquad (6.3)$$

where a and b are the coefficients of the Landau expansion of the local free energy density, and K_1 and K_2 are the Frank elastic constants associated to splay and bend distortions of the polarity field, respectively. In our case, cells in the bulk of the tissue remain unpolarized, so that the free energy must favour a vanishing polarity. Hence, $a > 0$, and only the quadratic term in the Landau expansion is kept. In addition, for the sake of simplicity, we assume $K_1 = K_2 \equiv K$, which is the usual

one-constant approximation for the nematic elasticity. Thus, Eq. (6.3) reduces to

$$F = \int_{\mathcal{V}} \left[\frac{a}{2} p^2 + \frac{K}{2} \left(\partial_\alpha p_\beta \right) \left(\partial_\alpha p_\beta \right) \right] d^3 \vec{r}, \tag{6.4}$$

so that the dynamics of the polarity is specified by

$$\partial_t p_\alpha = \frac{1}{\gamma_1} \left(-a p_\alpha + K \nabla^2 p_\alpha \right). \tag{6.5}$$

Finally, we also assume that the dynamics of the polarity is fast compared to the spreading dynamics, and hence that it adapts to the shape of the monolayer adiabatically, namely with $\partial_t p_\alpha = 0$. For two mesenchymal cell types, hemocytes [Davis 2015] and fibroblasts [Kadir 2011], cell polarization events associated to contact inhibition of locomotion usually occur within a time scale of $\tau_{\text{CIL}} \sim 10$ min [Smeets 2016]. This is much faster than the monolayer speading time scale given by the strain rate, usually $\tau_s \sim 100$ min [Blanch-Mercader 2017b]. Hence, the adiabatic approximation for the polarity dynamics seems generally reasonable. In fact, specific support to this approximation will be given in Section 6.4 by the fits of the model to experimental data in our system. Therefore, under this approximation, the polarity field is given by

$$L_c^2 \nabla^2 p_\alpha = p_\alpha, \tag{6.6}$$

where the characteristic length $L_c \equiv \sqrt{K/a}$ of the nematic order has been defined.

6.3.2 Force balance

Next, we establish momentum conservation as

$$\rho_m \left(\partial_t + v_\beta \partial_\beta \right) v_\alpha = \partial_\beta \left(\sigma^s_{\alpha\beta} + \sigma^a_{\alpha\beta} + \sigma^{E,s}_{\alpha\beta} \right) + f_\alpha, \tag{6.7}$$

where ρ_m is the density of the monolayer, v_α is the velocity field, $\sigma^s_{\alpha\beta}$ and $\sigma^a_{\alpha\beta}$ are the symmetric and antisymmetric parts of the deviatoric stress tensor, and f_α is the external force density. Finally, $\sigma^{E,s}_{\alpha\beta}$ is the symmetric part of the Ericksen tensor. This tensor generalizes the pressure P to include anisotropic elastic stresses associated to the orientational degrees of freedom in liquid crystals [de Gennes 1993]:

$$\sigma^E_{\alpha\beta} = -P \delta_{\alpha\beta} - \frac{\partial f}{\partial \left(\partial_\beta p_\gamma \right)} \partial_\alpha p_\gamma, \tag{6.8}$$

where f is the Frank free energy density, namely the integrand of Eq. (6.3) or Eq. (6.4). Consequently, the orientational contribution to the Ericksen tensor is of second order in gradients of the polarity field, and hence we neglect it. Thus, force balance reads

$$\rho_m \left(\partial_t + v_\beta \partial_\beta \right) v_\alpha = -\partial_\alpha P + \partial_\beta \left(\sigma^s_{\alpha\beta} + \sigma^a_{\alpha\beta} \right) + f_\alpha. \tag{6.9}$$

Now, flows in cell monolayers occur at very low Reynolds numbers. Estimating the density of the monolayer by that of water, $\rho_m \sim 10^3$ kg/m^3, and taking typical cell migration velocities $v_c \sim 10$ μm/min, monolayer sizes of $R \sim 200$ μm, and tissue viscosities $\eta \sim 10^5$ Pa·s [Forgacs 1998, Marmottant 2009, Guevorkian 2010, Stirbat 2013], we obtain $\mathrm{Re} = \rho_m v_c R/\eta \sim 10^{-13}$. Therefore, inertial forces are negligible, and momentum conservation reduces to the force balance condition:

$$0 = -\partial_\alpha P + \partial_\beta \left(\sigma^s_{\alpha\beta} + \sigma^a_{\alpha\beta}\right) + f_\alpha. \tag{6.10}$$

Then, the pressure is related to the cell number surface density ρ by the equation of state of the monolayer[1]. For the sake of an estimate, we assume the simplest form for an equation of state, $P(\rho) = B(\rho - \rho_0)/\rho_0$, where B is the bulk modulus of the monolayer, and ρ_0 is a reference density defined by $P(\rho_0) = 0$. Taking the pressure origin at the monolayer edge, $\rho_0 \sim 3 \cdot 10^3$ cells/mm^2 (Fig. 6.14). In turn, density differences in the monolayer are, at most, $\rho - \rho_0 \sim 10^3$ cells/mm^2 (Fig. 6.14). Then, the monolayer is expected to be highly compressible because area changes can in principle be accommodated by changes in height, resisted only by the shear modulus of the tissue. Hence, we estimate the bulk modulus of the monolayer by typical shear moduli of cell aggregates, which are in the range $G \sim 10^2 - 10^3$ Pa [Forgacs 1998, Marmottant 2009, Guevorkian 2010]. Thus, the pressure in the monolayer should be $P \lesssim 30 - 300$ Pa. In fact, isotropic compressive stresses (pressures) of ~ 50 Pa were recently shown to induce cell extrusion [Saw 2017]. In conlusion, in the absence of significant cell proliferation [Basan 2013, Recho 2016, Yabunaka 2017a], the magnitude of the pressure in the monolayer is expected to be much smaller than the tensile stress (tension) induced by traction forces, as measured by monolayer stress microscopy, which is of the order of several kPa (Fig. 6.6c, with a monolayer height of $h \sim 5$ μm). Hence, we neglect the pressure in the force balance[2]:

$$0 = \partial_\beta \left(\sigma^s_{\alpha\beta} + \sigma^a_{\alpha\beta}\right) + f_\alpha. \tag{6.11}$$

Now, for a nematic medium, the antisymmetric part of the stress tensor is given by $\sigma^a_{\alpha\beta} = 1/2\,(p_\alpha h_\beta - h_\alpha p_\beta)$. From Eq. (6.1), the adiabatic approximation for the polarity dynamics, $\partial_t p_\alpha = 0$, means that $h_\alpha = 0$. Therefore, the antisymmetric part of the stress tensor vanishes under this approximation, $\sigma^a_{\alpha\beta} = 0$. Thus, force balance reduces to

$$0 = \partial_\beta \sigma^s_{\alpha\beta} + f_\alpha. \tag{6.12}$$

Finally, multiplying Eq. (6.12) by the height h of the monolayer, the force balance can be rewritten in terms of the experimentally measured traction stress $T_\alpha(\vec{r}, t)$ and monolayer tension $\sigma_{\alpha\beta}(\vec{r}, t)$ fields:

$$\partial_\beta \sigma_{\alpha\beta} = T_\alpha, \tag{6.13}$$

from where

$$T_\alpha = -f_\alpha h, \qquad \sigma_{\alpha\beta} = \sigma^s_{\alpha\beta} h. \tag{6.14}$$

[1] Note that the equation of state actually relates the pressure to the mass density. Here, we assume that cells have a typical volume that proportionally relates the mass density to the cell number density.

[2] Note that this corresponds to allowing the tissue to be compressible also in 3D.

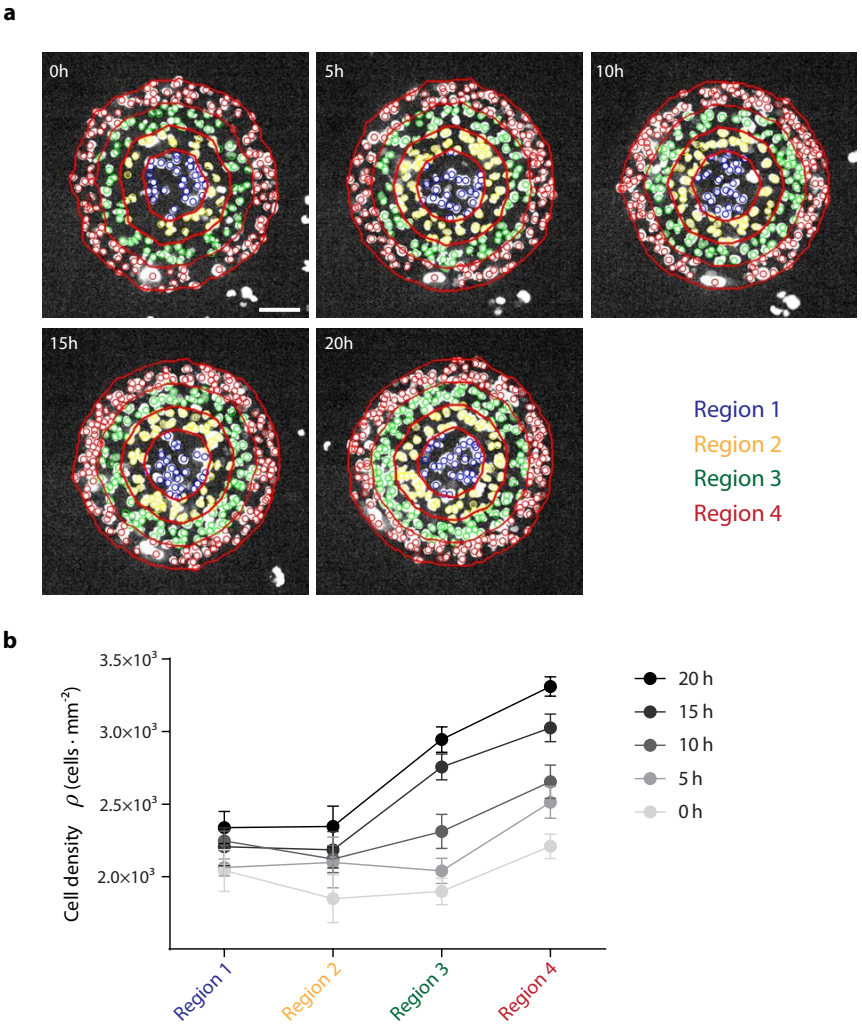

Figure 6.14 | Cell density increases towards the edge. **a,** The cell density profile is measured by counting cell nuclei in four concentric regions. Scale bar, 40 μm. **b,** The cell density profile develops a gradient towards the edge of the monolayer.

6.3.3 Constitutive equations

Next, constitutive equations must be given to specify the deviatoric stress tensor $\sigma^s_{\alpha\beta}$ and the external force f_α in terms of the polarity and velocity fields. The generic constitutive equations of an active liquid crystal are provided by active gel theory. Here, based on the previous assumptions on the dynamics of the polarity field, we propose a simplified version of the generic constitutive equations of an

active polar gel to describe epithelial spreading.

First, spreading occurs at strain rates that define a time scale $\tau_s \sim 100$ min [Blanch-Mercader 2017b], at which the tissue should have a fluid rheology. This timescale is much slower than the turnover time scales of proteins in the cytoskeleton or in cell-cell junctions, which are of the order of tens of minutes at most [Wyatt 2016, Khalilgharibi 2016]. Intra- or intercellular processes such as cytoskeletal reorganizations or cell-cell slidings dissipate energy over these time scales, so that elastic energy may only be stored in the tissue at shorter times. Therefore, to describe the slow spreading dynamics, we will not consider the elastic response of the tissue at short time scales. Note that incessant cell-cell sliding and neighbour exchanges are observed throughout the experiments, which provides further support to the purely fluid behaviour of the monolayer at the experimentally relevant time scales.

Then, in the viscous limit, the constitutive equations for the internal stress and the interfacial force of an active polar medium are:

$$\sigma^s_{\alpha\beta} = 2\eta\tilde{v}_{\alpha\beta} + \frac{\nu_1}{2}\left(p_\alpha h_\beta + h_\alpha p_\beta - \frac{2}{d}p_\gamma h_\gamma \delta_{\alpha\beta}\right) - \zeta q_{\alpha\beta} + \left(\bar{\eta}\, d\, v_{\gamma\gamma} + \bar{\nu}_1\, d\, p_\gamma h_\gamma - \bar{\zeta} - \zeta' p_\gamma p_\gamma\right)\delta_{\alpha\beta}, \quad (6.15)$$

$$f_\alpha = -\xi v_\alpha + \nu_i \dot{p}_\alpha + \zeta_i p_\alpha, \quad (6.16)$$

where, $q_{\alpha\beta} = p_\alpha p_\beta - p_\gamma p_\gamma / d\ \delta_{\alpha\beta}$ is the traceless symmetric nematic order parameter tensor, and v_α is the velocity of the fluid with respect to the substrate. The coefficients η and $\bar{\eta}$ are the shear and bulk viscosities of the medium, ζ is the anisotropic active stress coefficient, and $\bar{\zeta}$ and ζ' are two isotropic active stress coefficients[3]. Finally, ξ, ν_i, and ζ_i are the corresponding interfacial counterparts of the viscosity (viscous friction), flow alignment (polar friction), and active stress (active force) coefficients. The constitutive equation for the internal stress, Eq. (6.15), is that of an active polar gel with a variable modulus of the polarity [Jülicher 2011]. In turn, the constitutive equation for the interfacial force, Eq. (6.16), is less conventional [Jülicher 2009], but it was recently derived from a mesoscopic model of an active polar gel [Oriola 2017] (see Eq. (4.28), Chapter 4).

Now, as stated in Section 6.3.2, the adiabatic approximation for the polarity dynamics implies $h_\alpha = 0$, so that flow alignment terms do not contribute to the stress tensor or the interfacial force. Next, we assume that polarized cells generate much higher active stresses than unpolarized cells. Hence, we neglect the active stress coefficient $\bar{\zeta}$ in front of ζ and ζ'. Note that, to capture the wetting transition with a model for a two-dimensional fluid layer, the fluid must be compressible, meaning that bulk coefficients must be retained. Then, for simplicity, we assume $\zeta = \zeta'\, d = 2\zeta'$ and $2\eta = \bar{\eta}\, d = 2\bar{\eta}$. Under these simplifications, the constitutive

[3]Note that, to simplify notation, the active coefficients have been redefined to incorporate the chemical potential difference $\Delta\mu$ of the ATP hydrolysis reaction that acts as a generalized force in the standard linear irreversible thermodynamics formulation of active gel theory [Kruse 2005, Jülicher 2011, Marchetti 2013, Prost 2015].

equations reduce to

$$\sigma^s_{\alpha\beta} = \eta\left(\partial_\alpha v_\beta + \partial_\beta v_\alpha\right) - \zeta p_\alpha p_\beta, \tag{6.17}$$

$$f_\alpha = -\xi v_\alpha + \zeta_i p_\alpha, \tag{6.18}$$

which close the set of equations defining our active polar fluid model of the spreading of an epithelial monolayer.

6.4 Traction and flow profiles

In this section, the model is solved in a circular geometry. There are two unknown fields: the polarity field $\vec{p}(\vec{r},t)$ and the flow field $\vec{v}(\vec{r},t)$. The polarity field is completely specified by Eq. (6.6). Once the polarity profile is known, introducing the constitutive equations Eqs. (6.17) and (6.18) into the force balance condition Eq. (6.12) sets a closed equation for the flow field. The equations for both the polarity and the flow field are time-independent. Therefore, the time dependence of these fields arises solely from the boundary conditions at the free interface, which moves according to $dR/dt = v_r(R)$.

6.4.1 Traction profile

Since traction forces are mainly along the radial direction (Fig. 6.6b-6.7), we assume the polarity field to be radial: $\vec{p} = p(r)\,\hat{r}$. Hence, in polar coordinates, Eq. (6.6) reads

$$r^2 p''(r) + r p'(r) - \left[1 + \frac{r^2}{L_c^2}\right] p(r) = 0, \tag{6.19}$$

which is a modified Bessel equation of first order. Because of the strong outwards polarization of cells at the edge of the cell island (see Section 6.3.1 for details), we impose $p(R) = 1$, namely the maximal polarity value, as a boundary condition. Finitude and symmetry of the profile also require $p(0) = 0$. Hence, the solution for the radial polarity profile is

$$p(r) = \frac{I_1(r/L_c)}{I_1(R/L_c)}. \tag{6.20}$$

where I_1 is the modified Bessel function of the first kind and first order. Therefore, the nematic length L_c characterizes the decay of the tissue polarity from its maximal value at the boundary towards its vanishing value in the bulk (red gradient in Fig. 6.15).

Next, we may compare the two sources of dissipation, the viscosity and the friction coefficient, whose ratio defines the hydrodynamic screening length $\lambda = \sqrt{\eta/\xi}$. For monolayers smaller than this length, $R < \lambda$, viscosity dominates over friction, and the monolayer stress profile features a central plateau of maximal stress. In contrast, for monolayers larger than this length, $R > \lambda$, friction dominates over viscosity, and the monolayer stress decays at the center, thus featuring its maximum

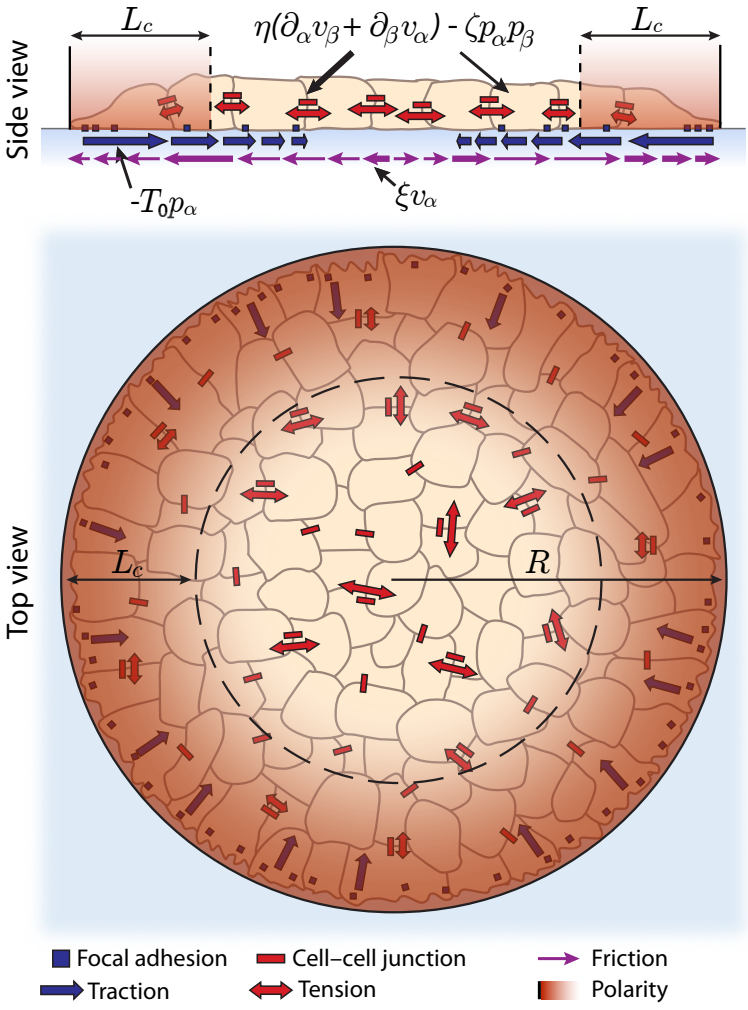

Figure 6.15 | Sketch of the cell monolayer. Cells at the edge are strongly polarized, whereas cells at the center are unpolarized, which establishes a radial polarity profile, indicated by the red color gradient, that decays over a length scale L_c. Cell polarity is associated to active traction forces transmitted between the cells and the substrate through focal adhesions, and to active contractile stress generated in the monolayer. Tension is transmitted throughout the tissue through cell-cell junctions. Cell flows generate viscous stress in the monolayer and friction forces on the substrate.

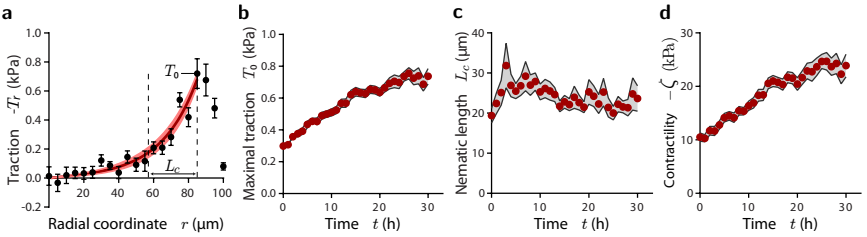

Figure 6.16 | Fits to traction force profiles determine the evolution of model parameters. **a,** The radial traction profile is fit by $T_r(r) = -T_0 p(r)$, with $p(r)$ given by Eq. (6.20). When performed at each time point, these fits yield the evolution of the model parameters $T_0(t)$ and $L_c(t)$. **b,** The maximal traction at the edge of the monolayer increases in time, reflecting the increasing forces in the monolayer. **c,** The nematic length characterizing the decay of the traction profile remains constant. **d,** Through the boundary condition $v(R) = 0$, the confinement of the monolayer sets the value of the contractility $-\zeta(t)$, which also increases in time.

close to the monolayer edge [Blanch-Mercader 2017b]. In our case, the stress is always maximal at the center of the monolayer (Fig. 6.6c), meaning that $R > \lambda$. Hence, we neglect cell-substrate friction hereafter. This corresponds to the so-called wet limit [Marchetti 2013], $\lambda \to \infty$, in which the flows in the monolayer are fully hydrodynamically coupled, with no screening effects due to the release of stress to the substrate through friction. In this limit, the force balance reduces to

$$\partial_\beta \sigma_{\alpha\beta} = -T_0 p_\alpha, \tag{6.21}$$

where we have defined the active traction stress coefficient $T_0 = \zeta_i h$, which gives the maximal traction stress exerted at the edge of the monolayer.

Then, we fit the predicted radial traction force profile $T_r(r) = -T_0 p(r)$ to the experimentally measured profiles at different times, as represented in kymographs as in Fig. 6.7a. At each time point, the fitting algorithm searches for the radial position of the maximum of the experimental traction force profile, which sets the monolayer radius $R(t)$. Then, the theoretical prediction is fit up to this point, discarding the outer region where the traction force progressively vanishes[4]. (Fig. 6.16a). From the fits, one obtains the time evolution of the maximal traction stress $T_0(t)$ and the nematic length $L_c(t)$. The maximal traction increases in time (Fig. 6.16b), reflecting the increasing traction forces associated to myosin phosphorylation. In contrast, after an initial transient, the nematic length remains essentially constant throughout the experiment (Fig. 6.16c), taking a value $L_c \sim 25\ \mu$m. This gives support to the assumption that the polarity field is set by a flow-independent mechanism, and that its dynamics is quasi-static.

[4]Traction forces measured in this outer region may arise from poorly attached protrusions or be an artifact due to the long-range propagation of deformations in the elastic substrate used for traction force microscopy. These effects are not described by the model.

Symbol	Description	Estimate
h	monolayer height	$5\ \mu$m
ξ	friction coefficient	100 Pa·s/μm^2
T_0	maximal traction	$0.2 - 0.8$ kPa
L_c	nematic length	$25\ \mu$m
$-\zeta$	contractility	$5 - 50$ kPa
γ_1	rotational viscosity	10 kPa·s
a	polarity restoring coefficient	20 Pa
K	Frank constant	10 nN
η	monolayer viscosity	$3 - 30$ MPa·s
λ	hydrodynamic screening length	$0.2 - 0.6$ mm
D	noise intensity of tissue shape fluctuations	$0.05 - 1.5\ \mu$m^2/h

Table 6.1 | Estimates of model parameters. The estimates in the lowest part of the table are obtained in Chapter 7.

Now, by combining the inferred value of the nematic length L_c with estimates for typical traction forces and cell migration velocities, we can estimate all the parameters of the polarity dynamics, namely the rotational viscosity γ_1, the restoring force coefficient a, and the Frank elastic constant K. To this end, we start by estimating the cell-substrate friction coefficient as $\xi \sim T/(vh)$. Taking typical values of traction stresses $T \sim 100$ Pa and speeds $v \sim 10\ \mu$m/min for cell migration [Basan 2013], and estimating the cell height $h \sim 5\ \mu$m (Fig. 6.8), we get $\xi \sim 100$ Pa·s/μm^2, consistent with previous estimates [Cochet-Escartin 2014]. Then, we assume that the rotational viscosity mainly arises from the friction between the substrate and polarized cytoskeletal structures such as the lamellipodia [Lee 2011b]. Thus, considering the polarized structures to be rods of length $\ell \sim 10\ \mu$m comparable to cell length, the rotational friction may be estimated as $\gamma_1 \sim \xi \ell^2 \sim 10$ kPa·s. Now, together with the restoring force coefficient a, the rotational friction γ_1 determines the time scale of the polarity field: $\tau_p \sim \gamma_1/a$. As argued in Section 6.3.1, the polarity field should be essentially set by contact inhibition of locomotion interactions, so that the time scale of the polarity field may be estimated by that of contact inhibition events, $\tau_p \sim \tau_{\mathrm{CIL}} \sim 10$ min [Smeets 2016] (see Section 5.7). This gives an estimate for the polarity restoring force coefficient $a \sim 20$ Pa. Finally, we estimate the Frank constant as $K = aL_c^2 \sim 10$ nN. The estimates of model parameters are collected in Table 6.1.

Finally, knowing the value of K allows us to check that the orientational contribution of the Ericken tensor in Eq. (6.8) is negligible as argued in Section 6.3.2. Using Eq. (6.4) and the polarity profile in Eq. (6.20), this contribution can be estimated as $K\left(p'\right)^2 \sim K/L_c^2 = a \sim 20$ Pa. Therefore, it is much smaller than the typical tensile stresses measured in the monolayer, of the order of several kPa, and it can be safely neglected.

6.4.2 Flow profile

The next step is to solve the force balance equation to obtain the velocity field. Since traction forces were assumed to be purely radial, we also assume a radial velocity field, $\vec{v} = v(r)\,\hat{r}$, which was indeed observed in spreading aggregates [Beaune 2014]. Thus, in polar coordinates, the nonvanishing components of the stress tensor are

$$\frac{1}{h}\sigma_{rr} = \eta v' - \zeta p^2, \qquad \frac{1}{h}\sigma_{\theta\theta} = \eta\frac{v}{r}, \tag{6.22}$$

and the force balance reads

$$\sigma'_{rr} + \frac{\sigma_{rr} - \sigma_{\theta\theta}}{r} = -T_0 p. \tag{6.23}$$

Hence, the equation for the velocity profile is

$$\eta\left[v'' + \frac{1}{r}v' - \frac{1}{r^2}v\right] = -\frac{T_0}{h}p + \zeta\left[\frac{1}{r}p^2 + 2pp'\right]. \tag{6.24}$$

Finitude and symmetry of the velocity profile impose $v(0) = 0$. In addition, since the external fluid has a much smaller viscosity than that of the monolayer, we consider it to be an ideal fluid, hence imposing normal stress-free boundary conditions at the tissue boundary: $n_\alpha \sigma_{\alpha\beta} n_\beta|_{r=R} = 0$, in agreement with the experimental measurements. This translates into $\sigma_{rr}(R) = 0$, which is the same condition employed to compute the monolayer tension via monolayer stress microscopy. Under these conditions, the velocity profile reads

$$\begin{aligned} v(r) = \frac{1}{2\eta}\Bigg[\Bigg[\zeta - 2T_0\frac{L_c^2}{hR} + \left[\zeta\frac{L_c}{R} + 2T_0\frac{L_c}{h}\right]\frac{I_0(R/L_c)}{I_1(R/L_c)} - \zeta\frac{I_0^2(R/L_c)}{I_1^2(R/L_c)}\Bigg] r \\ + \left[\zeta\frac{I_0(r/L_c)}{I_1(R/L_c)} - 2T_0\frac{L_c}{h}\right] L_c\frac{I_1(r/L_c)}{I_1(R/L_c)}\Bigg], \end{aligned} \tag{6.25}$$

which is plotted in Fig. 6.17 (red curve).

Now, the previous solution is general for a freely spreading cell monolayer. However, the monolayers in our experiment are confined within circular adherent regions. While the tissue is wetting the substrate, confinement imposes $v(R) = 0$. With no integration constants left, this extra boundary condition sets a relationship between model parameters. Since the values of $T_0(t)$ and $L_c(t)$ are set by traction profiles, this condition directly determines the active stress coefficient $\zeta(t)$ in terms of the other parameters:

$$\zeta = -2T_0\frac{L_c}{h}\frac{I_2(R/L_c)}{I_1(R/L_c) - I_0(R/L_c)\left[\frac{I_0(R/L_c)}{I_1(R/L_c)} - \frac{2L_c}{R}\right]}. \tag{6.26}$$

Thus, whereas all model parameters are free in a spreading or retracting monolayer, they are not independent in a confined monolayer. Equation (6.26) shows that, under confinement, the active stress parameter is negative, hence corresponding to

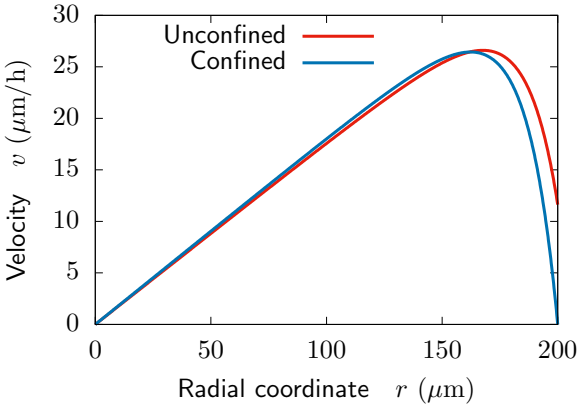

Figure 6.17 | Velocity profile in the monolayer. Equation (6.25). Parameters are $T_0 = 0.5$ kPa, $L_c = 25$ μm, $R = 200$ μm, $h = 5$ μm, and $\eta = 50$ MPa·s. For the unconfined case, the contractility is $\zeta = -20$ kPa, under which the monolayer expands ($v(R) > 0$). For the confined case, the condition $v(R) = 0$ sets the contractility to be given by Eq. (6.26).

a so-called contractile active stress. Accordingly, the coefficient $-\zeta$ will be called *contractility* hereinafter. When the tissue dewets from the substrate, the confinement restriction is released, and hence the contractility becomes an independent parameter, not governed by Eq. (6.26) anymore. Thus, up to the onset of dewetting, the evolution of the contractility can be obtained from Eq. (6.26). To check the resulting values, we extract the contractility via two other methods. First, it can be obtained from fits of the radial tension profile in the monolayer:

$$\begin{aligned}\sigma_{rr}(r) = T_0 L_c \left[\frac{I_0^2(R/L_c)}{I_1^2(R/L_c)} - \frac{L_c}{R}\right] - T_0 L_c \frac{I_0(r/L_c)}{I_1(R/L_c)} \\ + \frac{\zeta h}{2}\left[1 + \frac{L_c}{R}\frac{I_0(R/L_c)}{I_1(R/L_c)} - \frac{I_0^2(R/L_c)}{I_1^2(R/L_c)}\right] \\ + \frac{\zeta h}{2}\frac{1}{I_1^2(R/L_c)}\left[\frac{1}{2} I_0(r/L_c)\left[I_0(r/L_c) + I_2(r/L_c)\right] - I_1^2(r/L_c)\right]. \quad (6.27)\end{aligned}$$

In the fits of the tension kymographs, the monolayer radius $R(t)$ is determined from the radial coordinate at which the stress vanishes, $\sigma_{rr}(R) = 0$. Second, the

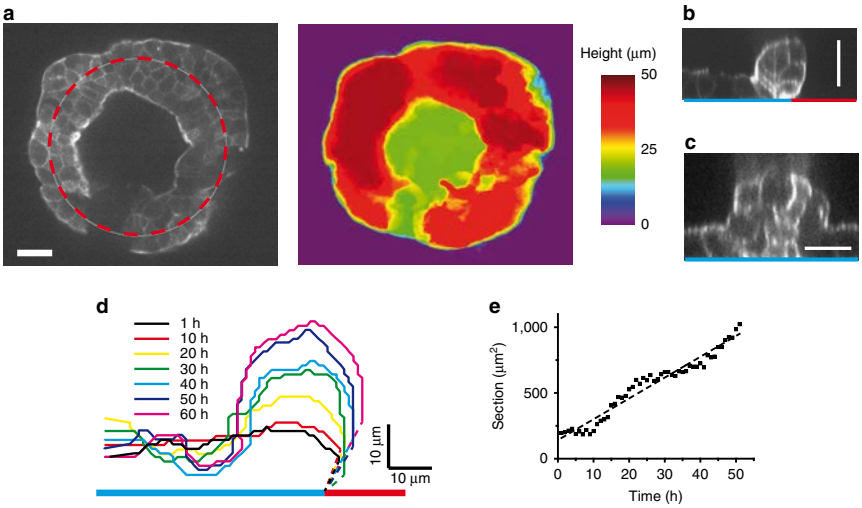

Figure 6.18 | Formation of a 3D peripheral cell rim in a confined monolayer. a, Planar section of the rim at 15 μm above the basal plane (left), and reconstruction of the tissue height (right). The dashed line indicates the limit of the adhesive region on the substrate. **b,** Transversal section of the rim. The blue/red lines indicate the adhesive/nonadhesive regions of the substrate. **c,** Transversal section of a bulge growing on top of the monolayer. All images are of actin-GFP. Scale bars, 20 μm. **d,** Dynamics of rim formation, shown through tissue height profiles. **e,** The section of the rim increases in time. From [Deforet 2014].

contractility can also be obtained from the average radial tension

$$\begin{aligned}\sigma &= \frac{1}{\pi R^2}\int_0^{2\pi} d\theta \int_0^R \sigma_{rr}\, r\, dr \\ &= T_0 L_c \left[\frac{I_0\left(R/L_c\right)}{I_1\left(R/L_c\right)} - 3\frac{L_c}{R} + 2\frac{L_c^2}{R^2}\frac{I_0\left(R/L_c\right) I_1\left(R/L_c\right) - 1}{I_1^2\left(R/L_c\right)}\right] \\ &\quad - \frac{\zeta h}{2}\left[1 - \frac{I_0^2\left(R/L_c\right)}{I_1^2\left(R/L_c\right)} + \frac{L_c}{R}\frac{I_0\left(R/L_c\right)}{I_1\left(R/L_c\right)} + \frac{L_c^2}{R^2}\frac{I_0^2\left(R/L_c\right) - 1}{I_1^2\left(R/L_c\right)}\right]\end{aligned} \tag{6.28}$$

All three methods yield fully compatible results, which are shown in Fig. 6.16d. Note that, at the lowest order in the small dimensionless parameter L_c/R, the average tension is completely given by traction forces: $\sigma = T_0 L_c + \mathcal{O}\left(L_c/R\right)$. Therefore, the contractility only contributes to the average stress at the first-order level in L_c/R, which explains the large values of this parameter compared to the stress in the monolayer.

Both for confined and free monolayers, a general feature of the predicted velocity profiles is their nonmonotonicity (Fig. 6.17). The model predicts an outwards flow at a velocity that, close to the center, has a linearly increasing profile, with a slope controlled by traction forces: $v\left(r\right) \approx T_0 L_c/(\eta h)\ r$; $r \ll R$, as

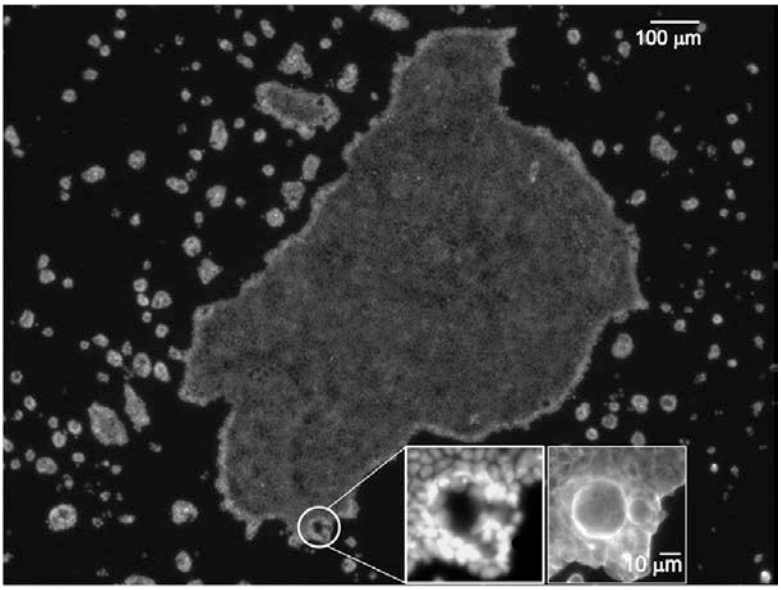

Figure 6.19 | Cell extrusion from the 3D peripheral rim of an expanding monolayer. The image of cell nuclei shows the presence of the 3D peripheral rim, from which live-cell extrusion events occur (inset: nuclei, left; actin, right), giving rise to an archipelago of new cell colonies surrounding the main one. From [Kaliman 2014].

obtained from Eq. (6.25) in the limit $L_c \ll R$. In contrast, through Eq. (6.22), the stress-free boundary condition $\sigma_{rr}(R) = 0$ imposes the slope of the velocity at the boundary to be $v'(R) = \zeta/\eta < 0$. Hence, the contractility causes the velocity to drop at the peripheral polarized region of width L_c. Therefore, the velocity a bit behind the boundary is always higher than at the very boundary (Fig. 6.17). As a consequence, cells are expected to accumulate close to the monolayer edge as they flow outwards. Experimentally, a gradient of increasing cell density towards the edge develops in the monolayer (Fig. 6.14), consistently with the predicted flow profile.

The increase in peripheral cell density might promote the extrusion of live cells from the monolayer [Eisenhoffer 2012, Marinari 2012, Eisenhoffer 2013], eventually leading to the formation of 3D structures at the monolayer edge. This is indeed what seems to occur in our monolayers (Fig. 6.8). In fact, 3D structures in the form of cell rims were previously observed both in confined [Deforet 2014] (Fig. 6.18) and unconfined [Kaliman 2014] (Fig. 6.19) monolayers. We suggest that the formation of these structures might partially stem from the predicted flow-induced accumulation of cells at the tissue edge. The appearance of 3D rims seems more favourable in confined monolayers, in which the contractility is not a free parameter and the confinement may facilitate the accommodation of extruded cells in upper layers [Deforet 2014]. In expanding monolayers, the absence of the

velocity drop close to the boundary [Blanch-Mercader 2017b, Lee 2017] suggests much lower values of the contractility, which can often be neglected.

6.5 Critical size for tissue wetting

We now focus on deriving the wetting transition, defined by a vanishing spreading parameter, $S = 0$ (Fig. 6.1). The spreading parameter is directly related to the spreading velocity [Beaune 2014], $S = \eta V$, so that using Eq. (6.25) it reads

$$S = \frac{\zeta R}{2} - 2\frac{T_0 L_c^2}{h} + \left[\zeta L_c + \frac{T_0 L_c R}{h}\right] \frac{I_0\left(R/L_c\right)}{I_1\left(R/L_c\right)} - \frac{\zeta R}{2} \frac{I_0^2\left(R/L_c\right)}{I_1^2\left(R/L_c\right)}. \tag{6.29}$$

In the experimentally relevant limit $L_c \ll R$, it reduces to

$$S = \frac{T_0 L_c}{h} R + \left(\zeta - \frac{3 T_0 L_c}{h}\right) \frac{L_c}{2}, \tag{6.30}$$

This result gives the spreading parameter in terms of the active forces responsible for collective cell migration, thus addressing the main objective of this chapter. Equation (6.30) encodes the competition between the positive contribution of traction forces, which drive the spreading of the monolayer, and the negative contribution of tissue contractility ($\zeta < 0$), which drives the retraction of the monolayer. As shown in Fig. 6.20, the spreading parameter depends on the radius of the monolayer. As a consequence, a critical monolayer radius

$$R^* \approx \frac{1}{2}\left(3L_c - \frac{\zeta h}{T_0}\right) \tag{6.31}$$

exists above which the tissue spreads and below which it retracts. This implies that the transition point is an unstable equilibrium point, much like the critical radius in nucleation processes.

The classical wetting transition does not feature a critical radius. In other words, the spreading parameter does not depend on the radius of the droplet or the fluid film but only on the surface tensions of the contacting interfaces[5]. Therefore, the predicted existence of a critical radius for wetting in epithelial monolayers, modelled as active polar fluids, constitutes a fundamental difference between the wetting transition in these materials and in passive fluids.

[5]The classical wetting transition is usually of first order. Thus, an energy barrier must be overcome to reach the final stable state, namely complete or partial wetting. Therefore, a nucleation process takes place, which entails the formation of a nucleus of the final phase larger than a critical radius defined by the interfacial and bulk energy difference between both phases [Bonn 2001]. However, the actual stable phase is entirely determined by the thermodynamic properties of the interfaces, regardless of the lateral size of the fluid film or droplet. In addition, a critical thickness exists below which a wetting fluid film is metastable to dewetting [de Gennes 2003]. It is important to distinguish these critical sizes, which do not determine the sign of the spreading parameter, from our critical radius for wetting, which does define a change of sign of the spreading parameter.

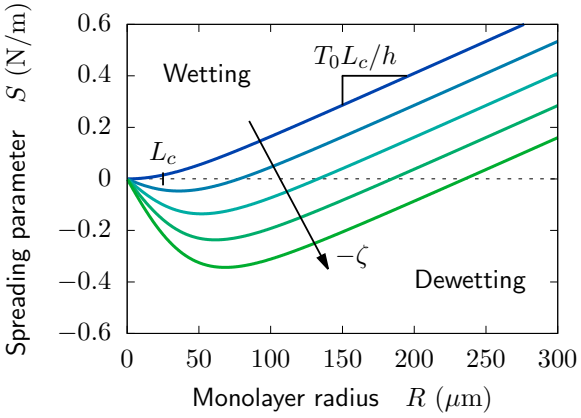

Figure 6.20 | Critical radius for tissue wetting. Starting from a negative value set by contractility, the spreading parameter of the monolayer increases with its radius with a slope determined by traction forces. As a consequence, for any values of the contractility and maximal traction, a critical radius exists above which the spreading parameter of the monolayer is positive (wetting) and below which it is negative (dewetting). Parameter values are $T_0 = 0.5$ kPa, $L_c = 25$ μm, $h = 5$ μm, and $-\zeta = -10n$ kPa; $n = 0, \ldots, 4$.

Our predictions imply that the wetting transition in cell islands can be induced by changes of the size of the colony, with no modification of its mechanical parameters. We suggest that this prediction might explain the experimentally observed nucleation of cell monolayers from spheroidal cell aggregates [Kaliman 2014]. Kaliman et al. seeded MDCK cells on a soft polyacrylamide gel ($E = 0.6$ kPa), on which they formed spheroidal cell aggregates. Whenever the cell-substrate contact area overcomes a given threshold, for instance via cell proliferation, a cell monolayer nucleates and grows from the center of the aggregate (Fig. 6.21). This observation is consistent with the prediction that large enough monolayers should wet the substrate whereas small enough monolayers should dewet from it, thus remaining droplet-like aggregates.

The wetting transition can also be induced by changing the mechanical parameters of the monolayer or of the extracellular matrix[6]. For instance, dewetting will occur whenever the contractility exceeds a critical value

$$-\zeta^* = 2T_0 \frac{L_c}{h} \frac{I_2\left(R/L_c\right)}{I_1\left(R/L_c\right) - I_0\left(R/L_c\right)\left[\frac{I_0(R/L_c)}{I_1(R/L_c)} - \frac{2L_c}{R}\right]} \approx \frac{T_0}{h}\left(2R - 3L_c\right), \tag{6.32}$$

which increases with the radius of the monolayer (Fig. 6.22). Therefore, larger

[6] In cell aggregates, the wetting transition was also shown to be induced by changing the rigidity of the substrate [Douezan 2012c]. In Appendix 6.A, we incorporate the role of substrate rigidity in our model. We show how the different effect of substrate rigidity on traction and contractile stresses leads to a rigidity-induced wetting transition, which still exhibits a critical size.

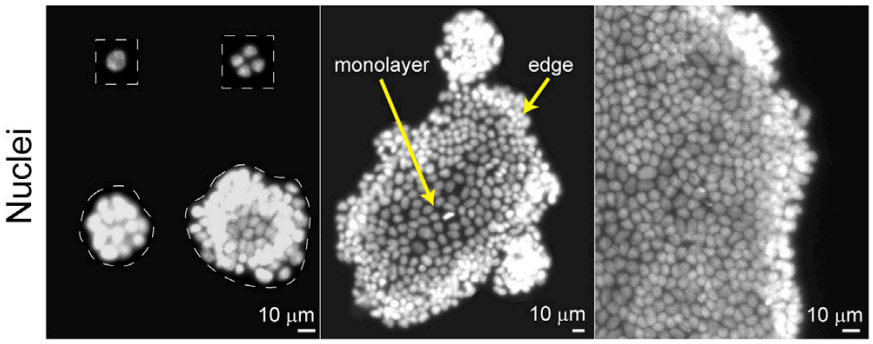

Figure 6.21 | Monolayer nucleation. A monolayer nucleates from the center of spheroidal aggregates whenever its contact area with the substrate exceeds a given threshold. A 3D rim of cells remains at the edge of the monolayer. Cell nuclei are imaged. From [Kaliman 2014].

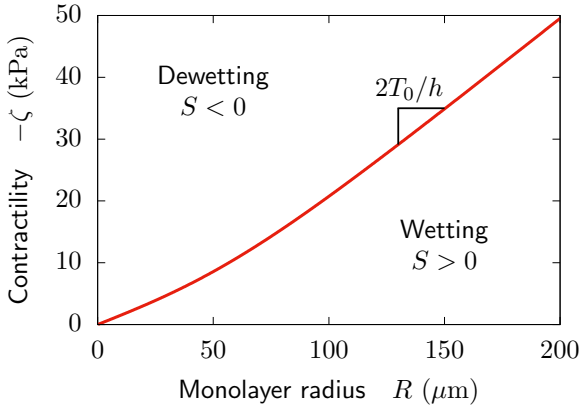

Figure 6.22 | Size-dependent critical contractility for monolayer dewetting. In the regime $L_c \ll R$, the slope is set by the maximal traction T_0. Parameter values are $T_0 = 0.75$ kPa, $L_c = 25$ μm, and $h = 5$ μm.

monolayers require a higher contractility to induce the dewetting. This can be understood by looking at the velocity profiles of monolayers of different radii. As explained in Section 6.4.2, traction forces at the edge impose a linearly increasing velocity profile at the central region of the monolayer. As a result, larger monolayers reach higher velocities right behind the narrow polarized peripheral region of width L_c (Fig. 6.23). In turn, the wetting transition condition imposes a vanishing velocity at the boundary. As also explained in Section 6.4.2, the contractility is responsible for the velocity drop across the strongly polarized peripheral layer. Thus, larger monolayers require a higher contractility to bring the velocity down to zero at the boundary.

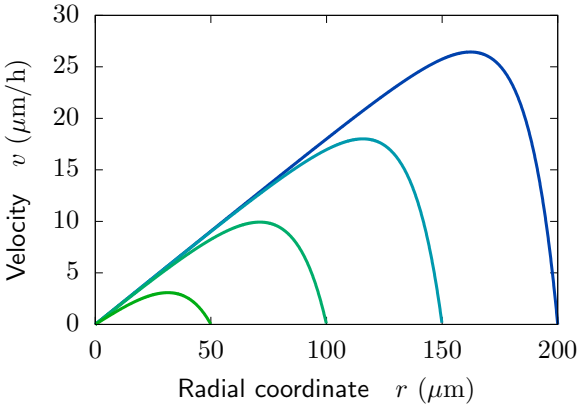

Figure 6.23 | Velocity profile for monolayers of different radius. The velocity right behind the polarized peripheral region of width L_c is higher in larger monolayers. Therefore, to meet the wetting transition condition ($V = 0$), the critical contractility must reach higher values in larger monolayers (Fig. 6.22). Parameters are $T_0 = 0.5$ kPa, $L_c = 25$ μm, $h = 5$ μm, $\eta = 50$ MPa·s. The different profiles correspond to monolayers of radii $R = 50, 100, 150, 200$ μm, with the critical contractility $-\zeta^*$ given by Eq. (6.32).

Note that the critical contractility $-\zeta^*$ is precisely the contractility under confinement, Eq. (6.26), since confinement also imposes the condition $V = 0$ in the wetting phase. Therefore, while fully spread, our confined monolayers are in a resting state ($V = 0$) maintained by the parallel increase of traction $T_0(t)$ and contractility $-\zeta(t)$, continuously fulfilling Eq. (6.32).

Then, we propose that, in our experiments, the dewetting is triggered by the failure of integrin-based cell-substrate adhesions at a critical traction T_0^*. Focal adhesions are unable to transmit higher tractions to the substrate, and hence $T_0(t)$ eventually saturates at T_0^*. In contrast, E-cadherin-based cell-cell junctions remain able to transmit the stress generated by the increasing activity of myosin molecular motors, thereby enabling the contractility to keep rising. Thus, once the traction threshold T_0^* is reached, traction forces can no longer follow the increasing contractility as required by Eq. (6.32) to maintain the monolayer boundary at rest. As a consequence, the dewetting process starts. In other words, because of the saturation of traction forces, the increasing critical contractility $-\zeta^*(t)$ eventually saturates to the value $-\zeta^* \approx T_0^*/h(2R - 3L_c)$. This causes the actual contractility $-\zeta(t)$, which keeps increasing, to overcome its critical value, thus inducing the dewetting of the monolayer.

Within this picture, the critical traction T_0^* should emerge from the mechanics and kinetics of integrin-ECM bonds in focal adhesions[7] [Schwarz 2013], thus

[7] Following this rationale, a naive mesoscopic model of focal adhesions is proposed in Appendix 6.B, which gives the critical traction T_0^* in terms of kinetic and mechanical parameters of integrin-ligand bonds.

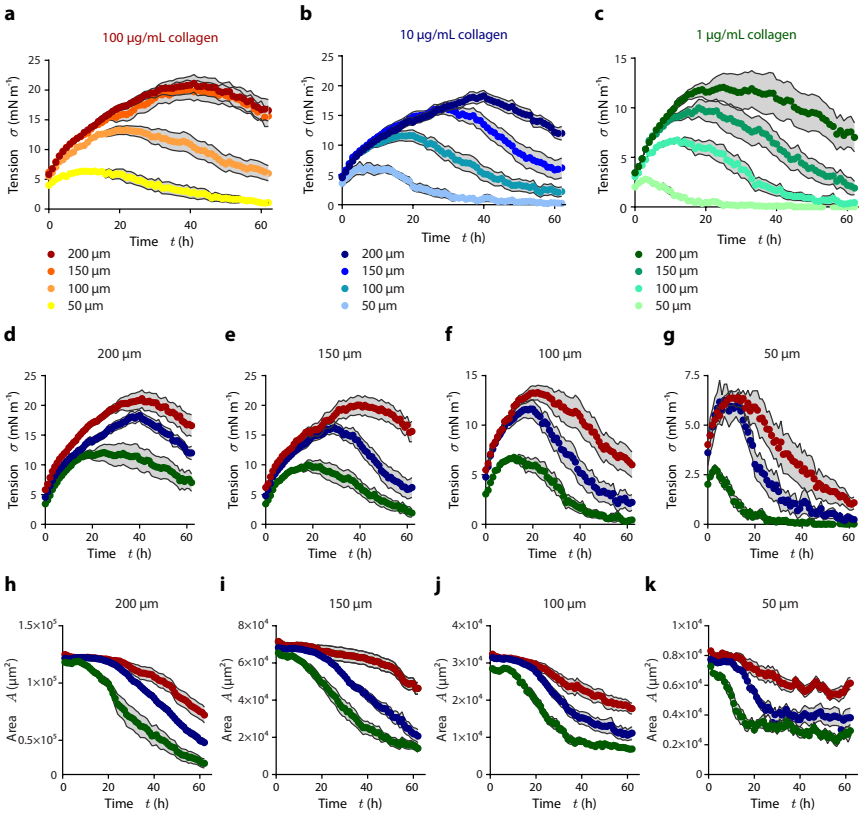

Figure 6.24 | Mechanics of monolayer dewetting for different island radii and collagen concentrations. For larger monolayers, as well as for monolayers on substrates coated with more collagen, dewetting occurs later and at higher tension.

being independent of the size of the tissue. In contrast, the critical contractility $-\zeta^*$ should depend on the radius of the monolayer as predicted by Eq. (6.32) and Fig. 6.22.

To test these predictions, we proposed dewetting experiments with cell islands of different radii, as well as on substrates coated with different concentrations of collagen. Figure 6.24 shows that monolayers on substrates with more collagen dewet later, reaching higher tensions. For a given collagen concentration, larger monolayers also dewet later and at higher tension. Then, we fit the predicted traction force profiles to the experimental traction kymographs (see Section 6.4 for details) to obtain the evolution of the parameters of the model, $T_0\,(t)$, $L_c\,(t)$, and $-\zeta\,(t)$ for all different conditions (Fig. 6.25).

Now, to quantitatively compare the onset of the dewetting under the different conditions, we need a criterion to identify the wetting transition. Since confinement

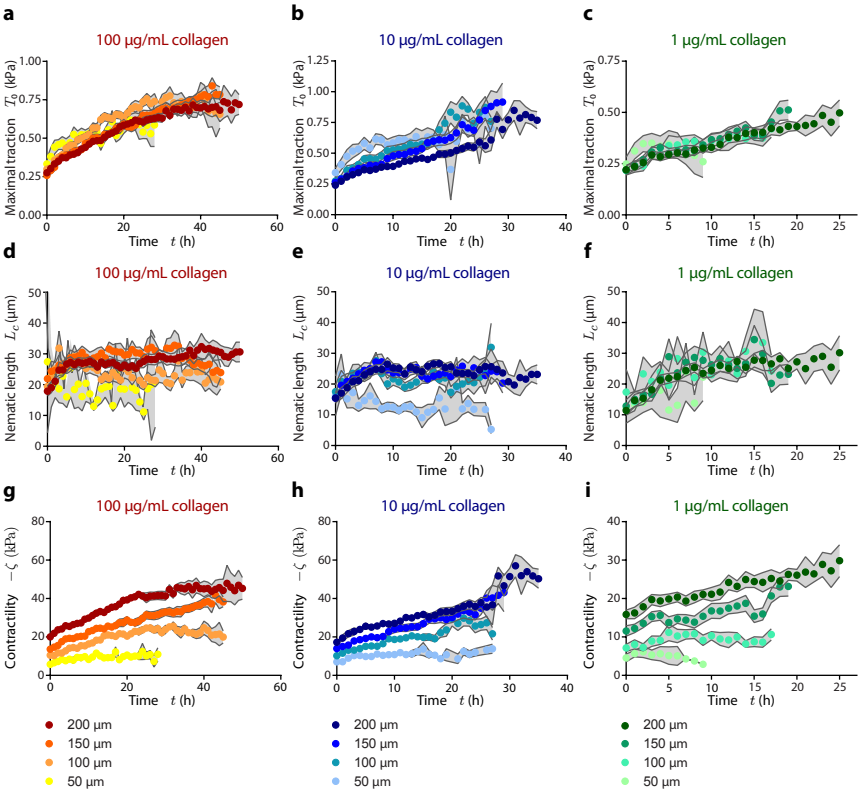

Figure 6.25 | Evolution of the parameters of the model for islands of different radii and collagen concentrations. The parameters are obtained from fits of the predicted traction force profile to the experimental traction kymographs, as detailed in Section 6.4.

imposes $V \leq 0$, the natural criterion based on the change of sign of the spreading velocity turns out to be impractical. Instead, we introduce the following criterion based on the decrease of the monolayer radius upon the onset of dewetting. We divide cell islands in circular sectors of a fixed arc length $s = 50\pi/3\ \mu\text{m} \approx 52\ \mu\text{m}$, so that islands of radius R will be divided into $M = 2\pi R/s$ sectors. Then, the evolution of the average radius $R_m(t)$ of each sector $m = 1, \ldots, M$ is computed from phase contrast images of the monolayer. Then, the time of the dewetting onset in a given sector m is identified whenever its average radius falls below a threshold $R_m^w = 0.95 R_m(0)$. In other words, the wetting transition time of sector m, t_m^*, is defined by the condition $R_m(t_m^*) = R_m^w$. Finally, the onset of dewetting of the full monolayer is defined to occur when $M/6$ sectors have started dewetting. Figure 6.26 illustrates this criterion, which we checked to robustly and reliably yield the wetting-dewetting transition time t^*.

Figure 6.27a shows the transition time t^* for cell islands of different radii on

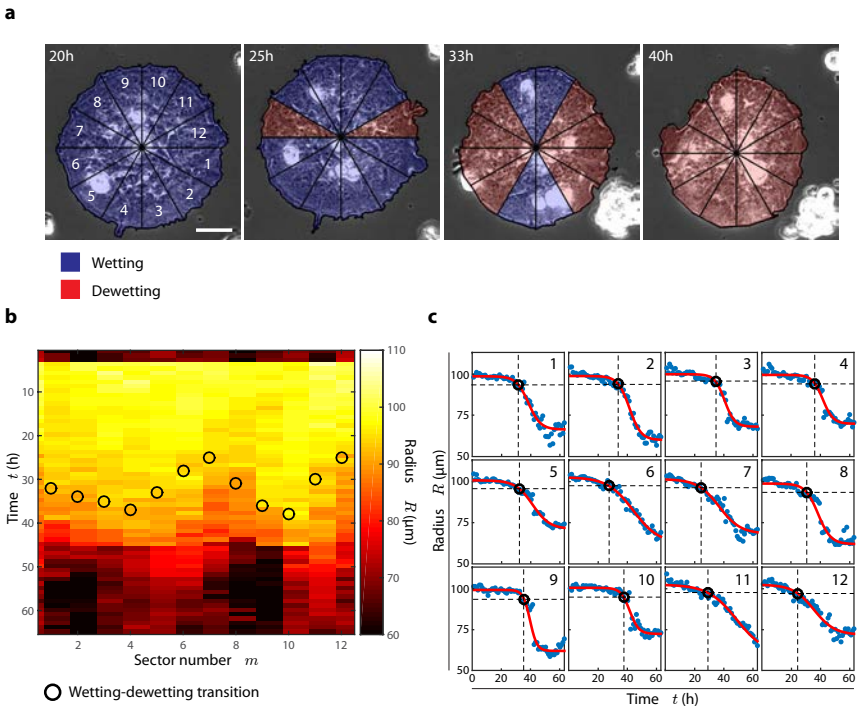

Figure 6.26 | Criterion for the identification of the onset of dewetting. a, Cell islands are divided in circular sectors. Scale bar, 40 μm. **b, c,** Evolution of the average radius of each sector, $R_m\,(t)$. The onset of dewetting in each sector is identified whenever its average radius falls below a threshold $R_m^w = 0.95R_m\,(0)$ (horizontal dashed lines in **c**). This condition, namely $R_m\,(t_m^*) = R_m^w$, identifies the transition time t_m^* for each sector (vertical dashed lines and open circles). Red lines in **c** show sigmoidal fits to $R_m\,(t)$. When dewetting has started in $M/6$ sectors, the whole island is considered to have started the dewetting process.

substrates coated with different collagen concentrations. The wetting-dewetting transition is found to occur later for larger monolayers (see also Fig. 6.28), consistent with them having to reach higher critical contractilities. Dewetting also starts later for islands on more concentrated collagen coatings (see also Fig. 6.29), consistent with them featuring higher critical tractions, and hence higher critical contractilities. Then, using the measured transition times, the critical values of the model parameters can be evaluated. As expected, the critical traction $T_0^* = T_0\,(t^*)$ is found to depend on the concentration of collagen coating the substrate, but it is independent of the island radius for each collagen concentration (Fig. 6.27b). Therefore, averaging over all islands of different radii, we can define an average critical traction $\overline{T_0^*}$ for each collagen concentration (lines in Fig. 6.27b). In turn, the critical contractility $-\zeta^* = -\zeta\,(t^*)$ increases both with the radius of the monolayer and with the concentration of collagen (Fig. 6.27c). Then, introducing the average

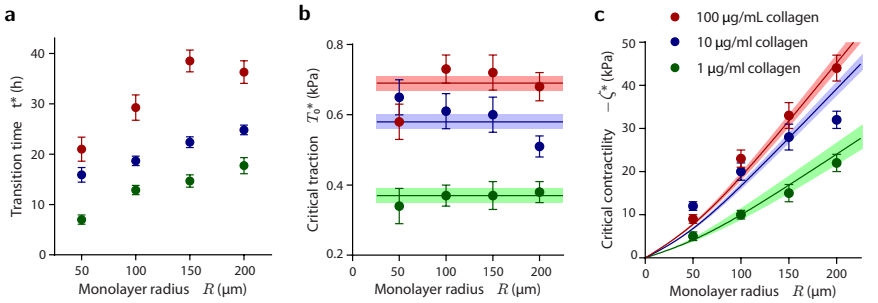

Figure 6.27 | Critical parameter values. a, The wetting-dewetting transition times increase with the radius of the monolayer, as well as with the concentration of collagen coating the substrate. **b,** The critical traction $T_0^* = T_0\,(t^*)$ is independent of the monolayer radius but depends on the concentration of collagen on the substrate. For each collagen concentration, the line indicates the average critical traction $\overline{T_0^*}$ over all monolayers of all radii. Shadows indicate error margins. **c,** The critical contractility $-\zeta^* = -\zeta\,(t^*)$ increases with the radius of the monolayer, with a slope that increases with collagen concentration. For each collagen concentration, the line indicates the average size-dependent critical contractility $-\overline{\zeta^*}\,(R)$, obtained by introducing $\overline{T_0^*}$ and $\overline{L_c^*}$ into Eq. (6.32). The slope of $-\overline{\zeta^*}\,(R)$ is set by the collagen-dependent average critical traction $\overline{T_0^*}$. Shadows indicate error margins.

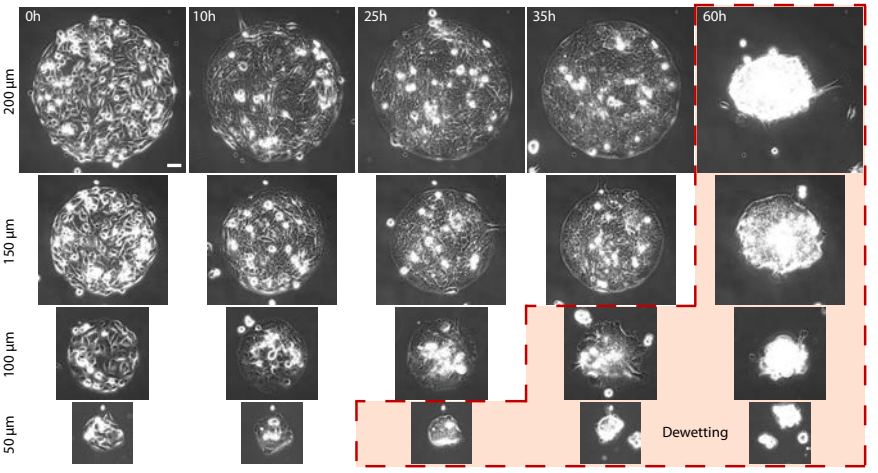

Figure 6.28 | Dewetting starts later for larger monolayers. Phase contrast images. Collagen concentration is 100 μg/mL. Scale bar, 40 μm.

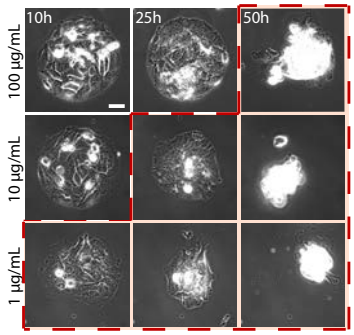

Figure 6.29 | Dewetting starts later for higher collagen concentrations. Phase contrast images. The shaded region denotes dewetting monolayers, as in Fig. 6.28. The island radius is 100 μm. Scale bar, 40 μm.

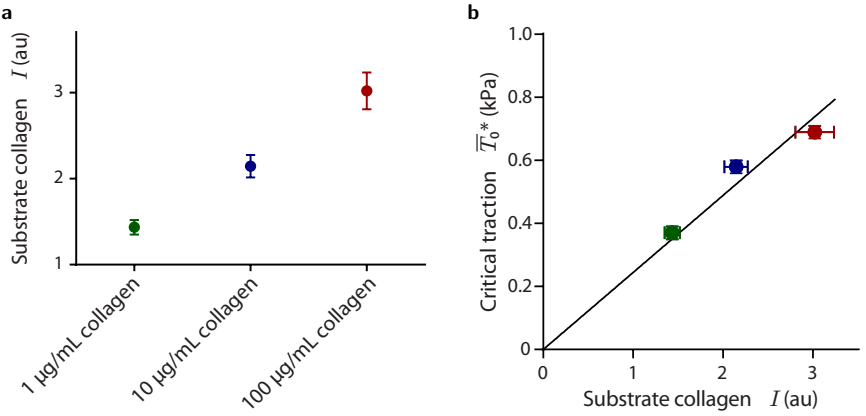

Figure 6.30 | The critical traction is proportional to the density of collagen on the substrate. a, Quantification of the fluorescence intensity of collagen coating the substrate for the different collagen concentrations in solution. **b,** The average critical traction $\overline{T_0^*}$ scales linearly with this intensity, which quantifies the density of collagen on the substrate.

values $\overline{T_0^*}$ and $\overline{L_c^*}$ into Eq. (6.32), we obtain an averaged dependence of the critical contractility on the monolayer radius, $-\overline{\zeta^*}\,(R)$, for each collagen concentration (lines in Fig. 6.27c). The transition times and the corresponding critical values of all model parameters are summarized in Table 6.2.

Finally, to study the dependence of the average critical traction $\overline{T_0^*}$ on the collagen density, we quantified the actual density of collagen on the substrate, as opposed to its concentration in solution, from fluorescence images. This way, the average critical traction $\overline{T_0^*}$ is found to increase linearly with the density of collagen on the substrate (Fig. 6.30), as expected from simple models of focal adhesions (Appendix 6.B).

Collagen coating concentration	Wetting transition	Island radius R (μm) 200	150	100	50	Average
100 μg/mL	N	17	15	18	11	
	t^* (h)	36 ± 2	39 ± 2	29 ± 2	21 ± 3	
	L_c^* (μm)	27 ± 2	30 ± 4	23 ± 2	19 ± 7	26 ± 2
	T_0^* (kPa)	0.68 ± 0.04	0.72 ± 0.05	0.73 ± 0.04	0.58 ± 0.05	0.69 ± 0.02
	$-\zeta^*$ (kPa)	44 ± 3	33 ± 3	23 ± 2	9 ± 1	
10 μg/mL	N	17	15	17	10	
	t^* (h)	25 ± 1	22 ± 1	19 ± 1	16 ± 2	
	L_c^* (μm)	26 ± 2	24 ± 2	20 ± 2	12 ± 5	22 ± 1
	T_0^* (kPa)	0.51 ± 0.03	0.60 ± 0.05	0.61 ± 0.05	0.65 ± 0.05	0.58 ± 0.02
	$-\zeta^*$ (kPa)	32 ± 2	28 ± 3	20 ± 2	12 ± 1	
1 μg/mL	N	11	10	8	8	
	t^* (h)	18 ± 2	15 ± 1	13 ± 1	7 ± 1	
	L_c^* (μm)	28 ± 2	31 ± 5	25 ± 6	19 ± 7	27 ± 2
	T_0^* (kPa)	0.38 ± 0.03	0.37 ± 0.04	0.37 ± 0.03	0.34 ± 0.05	0.37 ± 0.02
	$-\zeta^*$ (kPa)	22 ± 2	15 ± 2	10 ± 1	5 ± 1	

Table 6.2 | Critical parameter values. The number of islands N, along with the averages of the transition time t^*, the critical polar length L_c^*, the critical active traction $T_0^* h$, and the critical contractility $-\zeta^*$ are given for cell islands of different radius and for different concentrations of collagen coating the substrate.

6.6 Discussion and conclusions

We have studied the mechanics of the wetting transition in epithelial tissues by means of a continuum model for epithelial spreading. The model describes a cell monolayer as an active polar fluid that, in addition to sustaining viscous stresses, generates active contractile stresses and exerts traction forces on the substrate. Based on the model, we have extended the classical concept of the wetting transition to such an active medium. Specifically, we have explicitly obtained the spreading parameter, whose change of sign defines the wetting transition, in terms of parameters that characterize the active cellular forces involved in collective cell migration. This result allows to understand the wetting transition as a result of the competition between traction forces and tissue contractility.

Strikingly, in contrast to the classical wetting scenario, the spreading parameter of the epithelial monolayer depends on its size. As a consequence, a critical monolayer size exists for the wetting transition. In fact, since contractility is a bulk stress and traction forces are an interfacial force, their competition requires a length scale, which naturally defines the aforementioned critical size. Therefore, the existence of a critical size for tissue wetting is generic, applying to cell monolayers of any geometry. In experiments, by fitting the predicted traction and tension profiles to those measured in monolayers of different sizes, we have inferred the evolution of the model parameters, which has allowed us to verify the prediction of a critical size for tissue wetting. The characterization of the wetting transition in terms of the contractility and size of the monolayer and the density of collagen on the substrate is summarized in Fig. 6.31.

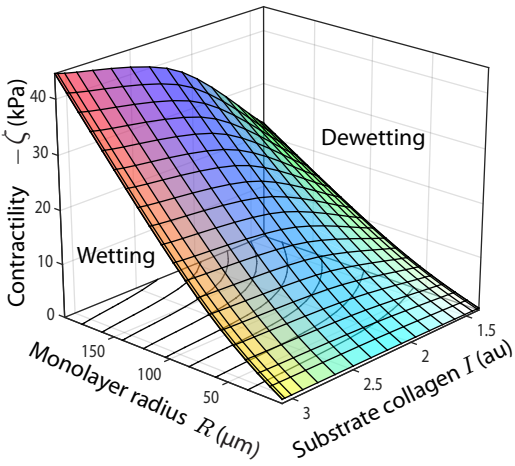

Figure 6.31 | Phase diagram of active tissue wetting. Equation (6.32) gives the projection of the surface in the contractility-radius plane. The value of the critical traction T_0^* as a function of the density of collagen on the substrate is extrapolated from the data in Fig. 6.30.

Experimentally, an increasing expression of E-cadherin is induced in the cells. Concomitantly with the formation of cell-cell junctions, this leads to a progressive phosphorylation of myosin, hence increasing traction forces and contractility in the monolayer. The competition of these two opposing forces results in the observed wetting-dewetting transition. Therefore, we conclude that E-cadherin regulates active cellular forces in the epithelium, thereby controlling the wetting properties of the tissue.

Nevertheless, the molecular mechanism whereby E-cadherin expression leads to myosin phosphorylation remains unknown. Therefore, our findings open new questions about the molecular crosstalk between cell-cell junctions and the force-generating cytoskeletal machinery. A better understanding of these aspects would bring insight into mechanotransduction processes at cell-cell junctions and, more in general, into mechanical homeostasis in epithelial tissues.

Both contractility and traction forces ultimately stem from myosin-generated forces. As a consequence, they are found to parallely strengthen due to the increasing phosphorylation of myosin. Eventually, the monolayer dewetting process is triggered by the failure of focal adhesions, which prevents traction forces from overcoming a critical value. In contrast, the greater stability of cell-cell junctions enables the contractility to keep rising, hence inducing the dewetting of the monolayer. We have inferred the critical traction and critical contractility from experimental data, and characterized their dependencies on the monolayer size and the density of extracellular-matrix ligand. Therefore, the experiment illustrates the differences between the two competing driving forces of epithelial spreading. Despite sharing many aspects of the force generation mechanism, which makes them interdependent, contractility and traction forces differ in their transmission — between cells through cell-cell junction and to the substrate via focal adhesions, respectively. Yet another crucial difference is the polar symmetry of traction forces, in contrast to the apolar nature of contractile stresses. These essential differences are reflected in the introduction of two distinct terms, with independent parameters, accounting for these forces in the model.

In the context of the soft active matter approach to living systems, our findings contribute to the understanding of epithelial tissues as active viscous liquid crystals [Hirst 2017]. Specifically, our theoretical analysis has considered the wetting transition of active liquid crystal films [Joanny 2012, Joanny 2013], showing that essential aspects of the wetting transition in such active media are fundamentally different from their equilibrium counterparts. In particular, our findings allow to understand how the wetting properties of a tissue emerge from its active and liquid-crystalline features, evidencing the active nature of the wetting transition in tissues. In other words, we show that the wetting behaviour of a tissue is not independent of the active character of these materials, but it rather arises from active forces, hence the term “active wetting”. In this line, our results also underscore the crucial role of planar tissue polarity in establishing the competition between traction and contractile forces that determines the wetting transition.

In the biological context, our findings might have implications for tumour formation or spreading [Gonzalez-Rodriguez 2012], as well as for developmental

processes that involve tissue spreading, such as zebrafish epiboly [Behrndt 2012, Campinho 2013, Morita 2017]. By unveiling the mechanics of tissue wetting, our results define how changes in the polarity, active forces, mechanical properties and, remarkably, size of a tissue may lead to monolayer-spheroid transitions in epithelia. Hence, our study provides a physical framework to interpret the mechanical outcome of the phenotypic changes that trigger tumour formation or spreading, as well as key developmental processes during embryonic morphogenesis.

Contributions and acknowledgements

The work described in this chapter is the result of a close collaboration between theory and experiments. Experiments were performed by Carlos Pérez-González in the "Integrative cell and tissue dynamics" group led by Xavier Trepat (IBEC, Barcelona). Elsa Bazellières (IBEC, Barcelona, then IBDM, Marseille) assisted in the experiments. Tomasz Kolodziej performed the single-cell experiments (Fig. 6.11). With the help of Carles Blanch-Mercader (UB, Barcelona, then Institut Curie, Paris), I performed the theoretical analysis, as well as the fits to the experimental data. Carlos Pérez-González prepared most figures.

I thank all members of the labs of Xavier Trepat and Pere Roca-Cusachs for discussions during their lab meetings. I also thank Romaric Vincent for early discussions about monolayer dewetting and related processes. Finally, I thank Françoise Brochard-Wyart for her keen interest in this project during my stay at Institut Curie.

Appendices

6.A Role of substrate rigidity in tissue wetting

In this appendix, we study the role of substrate rigidity in the tissue wetting transition. To this end, we minimally extend the continuum model for epithelial spreading of Chapter 6 to include the effects of a finite substrate rigidity. In our minimal approach, we do not consider the nonlocal elasticity problem of the substrate. Thus, we do not solve for the deformation field of the substrate, which would give rise to elastic long-range interactions. Rather, we simply consider that the model parameter directly characterizing monolayer-substrate interactions, namely the active traction coefficient T_0 (see Eq. (6.21)), depends on the rigidity of the substrate.

The dependence of the magnitude of traction forces on the rigidity of the substrate has been studied before [Ghibaudo 2008, Ladoux 2010]. Several theoretical approaches [Walcott 2010, Marcq 2011, Gupta 2015] have derived expressions that can be rewritten as

$$T_0\left(E\right) = T_0^{\infty}\frac{E}{E+E_0}, \tag{6.A.1}$$

where T_0^{∞} is the maximal traction on an infinitely rigid substrate, E is the Young modulus of the substrate, and E_0 is a characteristic Young modulus associated to cell-substrate adhesion complexes. In fact, this generic result ultimately arises from the in-series connection of two linear elastic media, namely the substrate and the substrate-bound cellular structures. The dependence in Eq. (6.A.1), which has been shown to fit experimental data (Fig. 6.A.1), encodes a linear increase of traction forces at low substrate rigidity that crosses over to a saturation at rigidities much higher than E_0. A very similar dependence was numerically obtained when accounting for the long-range elasticity of the substrate [Banerjee 2012, Lelidis 2013].

When introduced in Eq. (6.29), the dependence of traction forces on substrate rigidity (Eq. (6.A.1)) yields a critical substrate rigidity for tissue wetting,

$$\begin{aligned} E^* = E_0\frac{\frac{R}{L_c}\left[1-\frac{I_0^2(R/L_c)}{I_1^2(R/L_c)}\right]+2\frac{I_0(R/L_c)}{I_1(R/L_c)}}{\frac{2T_0^{\infty}L_c}{\zeta h}\left[2-\frac{R}{L_c}\frac{I_0(R/L_c)}{I_1(R/L_c)}\right]-\frac{R}{L_c}\left[1-\frac{I_0^2(R/L_c)}{I_1^2(R/L_c)}\right]-2\frac{I_0(R/L_c)}{I_1(R/L_c)}} \\ \approx \frac{E_0}{-\frac{T_0^{\infty}}{\zeta h}\left(2R-3L_c\right)-1}, \end{aligned} \tag{6.A.2}$$

which decreases with the size of the monolayer (Fig. 6.A.2). Thus, even if larger than the critical radius, only monolayers on sufficiently rigid substrates are able to

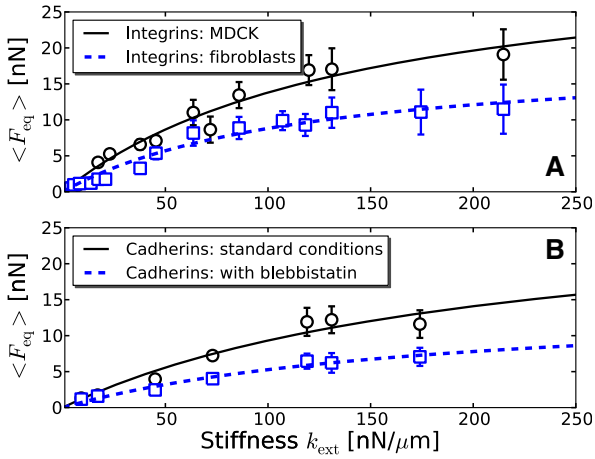

Figure 6.A.1 | Dependence of traction forces on substrate rigidity. Equation (6.A.1) fits experimental data on various conditions. From [Marcq 2011].

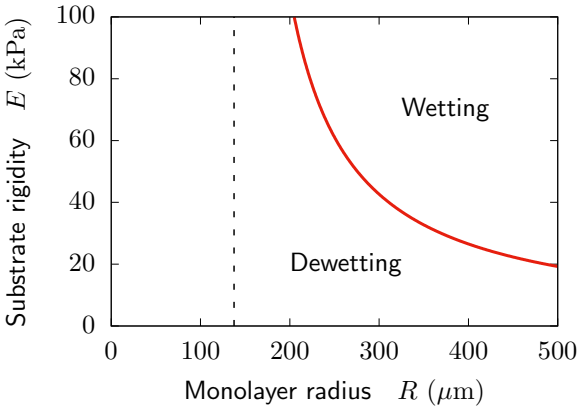

Figure 6.A.2 | Size-dependent critical substrate rigidity for tissue wetting. The critical radius for tissue wetting decreases with substrate rigidity, down to $R^* \approx 1/2\,(3L_c - \zeta h/T_0^\infty)$ (dashed line). Parameter values are $E_0 = 70$ kPa [Douezan 2012c], $T_0^\infty = 0.5$ kPa, $L_c = 25$ μm, $h = 5$ μm, $\zeta = -20$ kPa.

exert the traction forces required to overcome contractility and wet the substrate. Alternatively, the critical radius for tissue wetting monotonically decreases with substrate rigidity,

$$R^* \approx \frac{1}{2}\left(3L_c - \frac{\zeta h}{T_0^\infty}\left(\frac{E_0}{E}+1\right)\right), \tag{6.A.3}$$

tending to $R^* \approx 1/2\,(3L_c - \zeta h/T_0^\infty)$ for infinitely rigid substrates (dashed line in Fig. 6.A.2).

Therefore, the tissue wetting transition can be induced by substrate rigidity, in agreement with experimental findings on cell aggregates [Douezan 2012c] (Fig. 6.A.3). In fact, our result for the spreading parameter as a function of the substrate rigidity, Eq. (6.29) with Eq. (6.A.1), provides a physical basis for the ansatz in [Douezan 2012c].

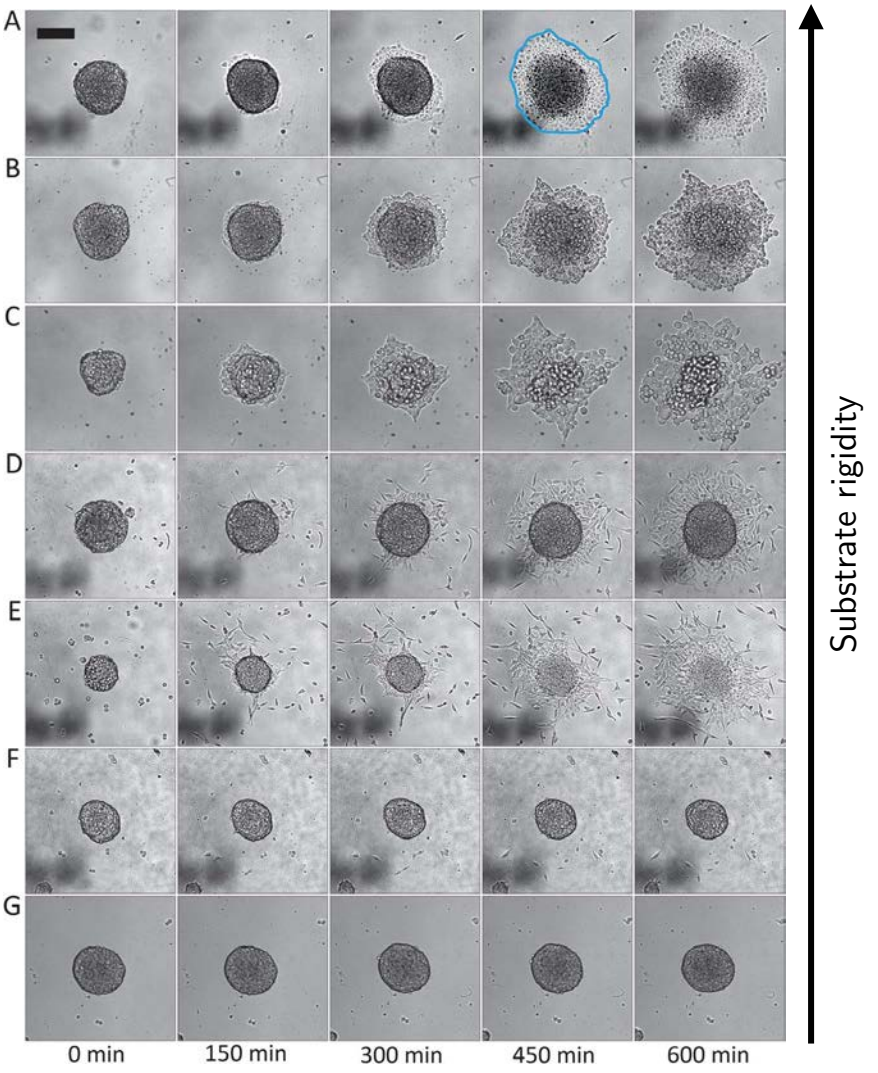

Figure 6.A.3 | Tissue wetting transition induced by substrate rigidity. Cell aggregates spread over sufficiently rigid substrates, and remain as a spheroidal aggregate on softer ones. **a,** Glass coverslip, $E = 70$ GPa. **b,** PDMS gel, $E = 1.8$ MPa. **c,** PDMS gel, $E = 0.5$ MPa. **d,** PAA gel, $E = 16.7$ kPa. **e,** PAA gel, $E = 10.6$ kPa. **f,** PAA gel, $E = 7.4$ kPa. **g,** PAA gel, $E = 2.8$ kPa. Scale bar, 100 μm. Adapted from [Douezan 2012c].

6.B Stochastic sliding friction model for the traction force

The goal of this appendix is to obtain a prediction for the critical traction force sustained by focal adhesions, which we have experimentally measured under different conditions in Section 6.5 in the context of the tissue wetting transition. To this end, we present the simplest version of available models of stochastic sliding friction to predict cellular traction forces [Schwarz 2013, Sens 2013].

The approach is to model a focal adhesion at the mesoscopic level as a collection of elastic linkers, which represent the proteins connecting the actin cytoskeleton to the extracellular matrix substrate. The elastic linkers of stiffness k stochastically bind and unbind from the cytoskeleton (through the weakest link of the molecular complex) at rates k_{on} and k_{off}, respectively. In turn, due to a combination of actin polymerization and myosin-generated contractility, the cytoskeleton experiences a retrograde flow with respect to the substrate at speed v over the adhesion site (Fig. 6.B.1).

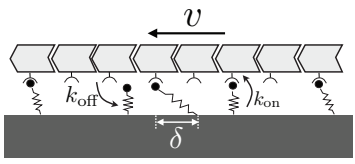

Figure 6.B.1 | Mesoscopic model for a focal adhesion. The cytoskeleton moves at a speed v with respect to the substrate, to which it is adhered through a collection of linkers that bind and unbind at rates k_{on} and k_{off}, respectively. Here, δ stands for u in the text. From [Sens 2013].

The relative motion between the cytoskeleton and the substrate induces an average stretch $\langle u \rangle = v/k_{\text{off}}$ on the bound linkers, since k_{off}^{-1} is the average time that a linker remains bound. This assumes that the unbinding of the linkers is a Poissonian process. Then, we assume that each bond withstands a force $f = ku$. Therefore, the total force transmitted by the adhesion to the substrate, namely the traction force, is

$$T = N\phi_b f, \tag{6.B.1}$$

where N is the total number of linkers and

$$\phi_b = \frac{k_{\text{on}}}{k_{\text{on}} + k_{\text{off}}} \tag{6.B.2}$$

is the fraction of them that are bound.

In general, the binding and unbinding rates of the linkers depend on the force that they are subject to [Rakshit 2014]. In our situation, this force stems from the stretching of the linkers imposed by the retrograde flow of actin. We assume that the cytoskeleton-substrate distance is essentially constant and comparable to the rest length of the linkers, so that they do not need to stretch substantially to bind. Therefore, the binding rate is assumed to be independent of the sliding velocity of the cytoskeleton. In contrast, bound linkers are stretched by the cytoskeletal flow, and hence the unbinding rate depends on the sliding velocity v [Wolfenson 2011].

To capture this fact, we employ Bell's model for the unbinding rate, which endows it with an exponential dependence on the force [Bell 1978, Evans 2007]:

$$k_{\text{off}}(f) = k_{\text{off}}^0 e^{f/f_0}, \tag{6.B.3}$$

where k_{off}^0 is the unbinding rate in the absence of force, and f_0 is a scale characterizing force fluctuations. Assuming that force fluctuations stem from the thermal fluctuations of the linkers, $f_0 = k_B T/a$, where a is a molecular-scale length that measures the distance between the bound state and the transition state of the binding energy lanscape, which should be comparable to the ligand-receptor (integrin-collagen) interaction range. In the case that force fluctuations were essentially active, f_0 should be estimated by other means.

Now, in a mean-field approximation that neglects fluctuations, we replace the force f sustained by a linker by its average $\langle f\rangle = k\langle u\rangle = kv/k_{\text{off}}$. When combined with Eq. (6.B.3), this approximation yields the following implicit relation between the average force and the sliding velocity:

$$v = \frac{k_{\text{off}}^0}{k}\langle f\rangle e^{\langle f\rangle/f_0}. \tag{6.B.4}$$

In turn, this allows to implictly relate the average traction force on the substrate to the sliding velocity through

$$\langle T\rangle = N\langle\phi_b\rangle\langle f\rangle = \frac{N\langle f\rangle}{1+\chi e^{\langle f\rangle/f_0}}; \qquad \chi \equiv \frac{k_{\text{off}}^0}{k_{\text{on}}}. \tag{6.B.5}$$

This relation is plotted as a function of the velocity in Fig. 6.B.2a, which shows that it is non-monotonic. At low velocities, the traction increases with the velocity because the linkers are more stretched and hence widthstand and transmit more force. However, higher velocities induce the linkers to unbind faster, which causes the number of bound linkers to decrease. As a consequence, even if each individual bond sustains a large force, the decreasing number of bonds makes the total traction force decrease at sufficiently large speeds. This biphasic traction-velocity curve entails the existence of a maximum traction force, which is given by

$$T^* = Nf_0\left(\frac{f^*}{f_0} - 1\right), \tag{6.B.6}$$

with f^* being the solution of

$$\chi e^{f^*/f_0} = \frac{1}{f^*/f_0 - 1}. \tag{6.B.7}$$

The critical traction force that the linkers can sustain depends only on their binding kinetics, namely on the kinetic ratio χ (Fig. 6.B.2b), and on the scale of force fluctuations f_0.

Equations (6.B.4) and (6.B.5) define the relationship between the traction force and the cytoskeletal sliding velocity, $T(v)$. However, the actual velocity of the

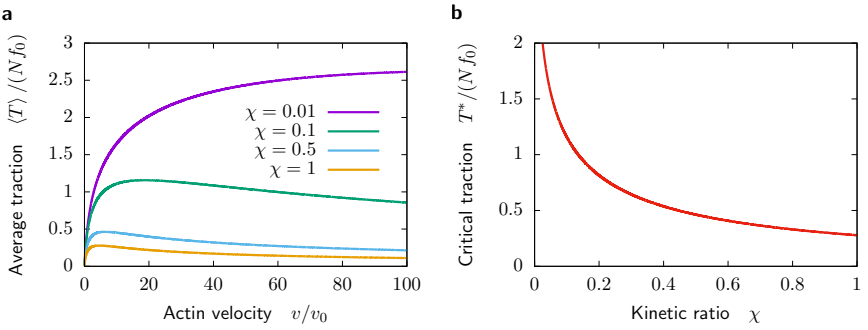

Figure 6.B.2 | Traction force by actin sliding friction. **a,** The traction force is non-monotonic with the sliding velocity of actin. The plotted dependence is obtained by introducing the implicit relation in Eq. (6.B.4) into Eq. (6.B.5). The velocity scale is $v_0 \equiv k_{\text{off}}^0 f_0 / k$. **b,** The critical traction force, namely the maximum of $T(v)$ in (a), is determined by the binding kinetics of the linkers, encoded in the kinetic ratio $\chi \equiv k_{\text{off}}^0 / k_{\text{on}}$, through Eqs. (6.B.6) and (6.B.7).

retrograde flow of actin is determined by the forces driving and opposing it. The forces driving this flow are due to actin polymerization, F_p, and myosin-generated contractility, F_c. In the absence of cell-substrate adhesion, and hence of traction forces, the only force limiting the retrograde flow of actin is the viscous friction of the cytoskeleton with the cytosol, γv. In the presence of adhesion, traction forces $T(v)$ also oppose the retrograde flow, so that the force balance reads

$$F_p + F_c = \gamma v + T(v) . \tag{6.B.8}$$

Thus, combined with Eqs. (6.B.4) and (6.B.5), Eq. (6.B.8) gives the relation between the contractile force F_c and the velocity of actin v. This relation is plotted in Fig. 6.B.3a, which shows that for sufficiently small cytoskeletal friction γ, there is a region of bistability, namely that two different actin velocities are stable for a given contractility. This bistable behaviour leads to a hysteresis loop for the velocity as a function of the contractility. This means that, under an increasing contractility, the velocity may increase up to the stability limit of the low-velocity phase, above which it discontinuously jumps to a the value of the high-velocity phase. An analogous behaviour takes place under a decreasing contractility. Finally, in the presence of noise, stochastic switching between the two stable velocities may occur when the contractility value lies within the bistable region, which gives rise to stick-slip motion of the cell lamellipodium.

For the experimental situation of Chapter 6, in which the contractility is increasing in time, we propose that a critical contractility exists at which the actin velocity experiences a discontinuous transition to larger values (Fig. 6.B.3a). Upon such a transition to high actin speeds, the traction force becomes much smaller (see Fig. 6.B.2a). The discontinuous transition of the traction force as a function of contractility, with the associated hysteresis loop, is shown in Fig. 6.B.3b. For the

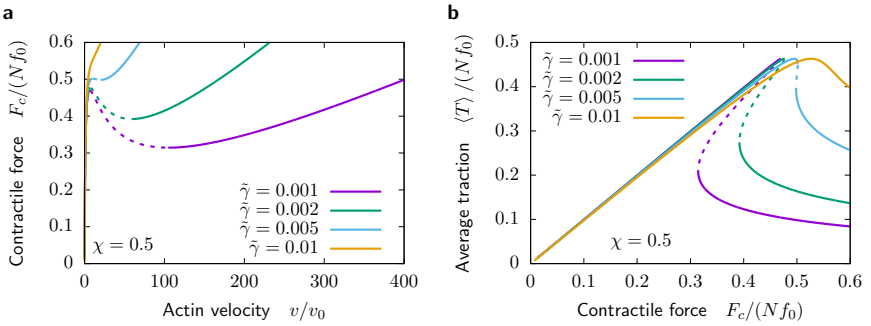

Figure 6.B.3 | Bistability in actin sliding friction. For sufficiently small friction $\tilde{\gamma} \equiv \gamma v_0/(Nf_0)$, a region of mechanical instability (dashed lines) exists between two stable values of actin velocitiy **a,** and traction force **b,** for a given contractility. Therefore, a continuous increase in contractility leads to a discontinuous stick-slip transition from a state of low actin velocity and high traction force to a state of high actin velocity and low traction force. In these graphs, the polymerization force is neglected ($F_p = 0$); including it simply shifts the F_c axis.

regime of viscous friction coefficients γ in which this bistable behaviour occurs, the critical value of the traction force may be approximated by the maximal traction force in Fig. 6.B.2, as given by Eqs. (6.B.6) and (6.B.7).

Note that, in the absence of force fluctuations, the model does not account for a complete detachment of the focal adhesion, but simply for stick-slip motion[8]. However, in the presence of force fluctuations, the complete detachment eventually occurs, at much shorter times in the low-traction phase. Even in the presence of noise, due to the constant rebinding rate, the complete detachment is not an absorbing state of the model. Nevertheless, in the experimental system, the tissue-scale contractile forces will in general remove the cell from the substrate upon a complete detachment event, which prevents the rebinding. Consequently, we may associate the critical traction force of the tissue wetting transition to the critical traction force of the stick-slip transition of the focal adhesion model above which, in turn, is approximated by T^* in the low friction regime.

Finally, we check that the viscous friction of the actin cytoskeleton with the cytosol is low enough to ensure that the stick-slip transition exists. In addition, the lower the cytoskeletal friction, the larger the velocity jump, and hence the better the interpretation of the tissue wetting transition as the stick-slip transition. The friction coefficient γ may be estimated from the permeability of the cytoplasm, understood as a poroelastic medium made of a fluid cytosol permeating an elastic cortex [Charras 2005, Charras 2008b, Charras 2009]. In this picture, the volume

[8]This contrasts with what occurs if the cytoskeleton perpendicularly pulls on the focal adhesion instead of sliding over it. Under a normal pulling force, a complete detachment transition takes place [Schwarz 2013]. In general, the total force on a focal adhesion will have components in the directions normal and parallel to the substrate, but we expect the latter to dominate in lamellipodia.

permeability K_p characterizes the resistance of the Darcy flow of the cytosol through the cytoskeleton:

$$\vec{v} = -K_p \vec{\nabla} P. \tag{6.B.9}$$

Experimental estimates indicate $K_p \sim 4 \cdot 10^{-15} - 2.5 \cdot 10^{-14}$ m^2/(Pa· s) [Charras 2008b]. The friction coefficient is then estimated as

$$\gamma \sim \frac{V}{K_p}, \tag{6.B.10}$$

where V is the fluid volume driven across the cytoskeleton. For a typical actin cortical layer in the lamellipodium of height $h \sim 200$ nm, width $w \sim 5 - 10$ μm, and length $\ell \sim 1 - 5$ μm, and neglecting the volume of the cytoskeletal filaments, $V \sim 1 - 10$ μm^3, which gives $\gamma \sim 2.5 \cdot 10^{-3} - 4 \cdot 10^{-5}$ Ns/m.

On the other hand, using $a \sim 1$ nm, we can estimate $f_0 \sim k_B T/a \sim 5$ pN. Then, using estimates for the rate of unforced unbinding of integrin from the extracellular matrix, $k_{\text{off}}^0 \sim 1$ s^{-1}, and for typical molecular bond rigidities $k \sim 1$ pN/nm [Sens 2013], the velocity scale of actin flows is $v_0 \sim 5$ nm/s. Finally, assuming a number of adhesion molecules of the order $N \sim 100$ in a focal adhesion, we obtain $\tilde{\gamma} \sim 0.0004 - 0.02$. These estimates are compatible with the existence of the stick-slip instability, which should indeed occur in cells as suggested by the observation of a biphasic relation between traction forces and actin velocity [Gardel 2008, Schwarz 2013].

7

Morphological instability during epithelial spreading

Contents

Abstract

In this chapter, we study the stability of the advancing front of a spreading epithelial monolayer. Based on the continuum active polar fluid model introduced in Chapter 6, we analytically predict a long-wavelength instability of the front. Cellular traction forces destabilize the interface against the stabilizing effect of tissue contractility. Long-range viscous stresses in the tissue yield a fastest-growing

mode with a finite wavelength, typically of a few hundreds of micrometers. This wavelength is determined either by the width of the monolayer or by the hydrodynamic screening length $\lambda = \sqrt{\eta/\xi}$ defined by the tissue viscosity η and the cell-substrate friction coefficient ξ. Thus, the predicted instability may account for the formation of finger-like protrusions observed during epithelial spreading. Our analysis shows that, despite their role in the developed fingers, leader cells are not required to trigger the fingering instability. The instability is also predicted for the retracting fronts of the dewetting monolayers presented in Chapter 6. We quantitatively compare the predicted growth rates to the experimentally measured ones, which yields an estimate of the increasing viscosity of the dewetting monolayers, $\eta \sim 3 - 30$ MPa·s.

7.1 Introduction

When exposed to available space, epithelial cell monolayers under wetting conditions spread. Often, the initially flat front becomes undulated by the growth of multicellular protrusions called fingers (Fig. 7.1) [Vedula 2013, Saw 2014, Hakim 2017]. The fingers exhibit a fast and strongly oriented cellular flow field along their long axis [Petitjean 2010, Reffay 2011, Reffay 2014]. At their tip, phenotypically different "leader cells" have been identified (Fig. 7.2) that exert large traction forces, driving the collective migration of the finger [Omelchenko 2003, Poujade 2007, Reffay 2011, Reffay 2014]. Leader cells are not pre-existent in the tissue but emerge with the fingers, as the outcome of a self-organization process driven by the complex cellular flows in the epithelium [Reffay 2011, Reffay 2014]. On the sides of the finger, supracellular actomyosin cables (Fig. 7.2) under tension provide mechanical coherence to the structure and prevent the formation of nearby fingers [Poujade 2007, Klarlund 2012, Reffay 2014].

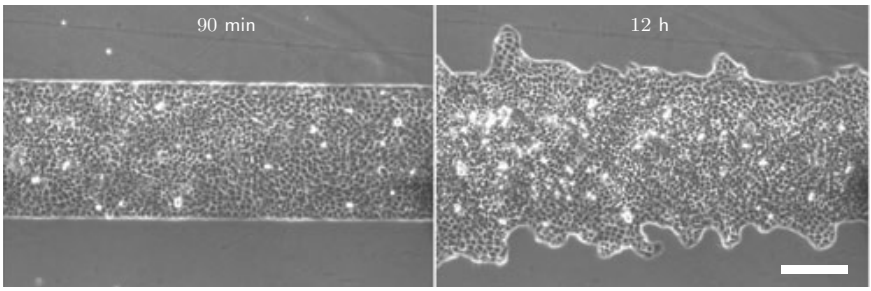

Figure 7.1 | Fingering in epithelial spreading. The initially flat front of an MDCK cell monolayer develops multicellular finger-like protrusions during spreading. Scale bar, 200 μm. Adapted from [Poujade 2007].

Several models have been proposed to explain the fingering instability in expanding cell monolayers [Hakim 2017]. Some of the models directly implement leader-cell behaviour to induce the fingers. For instance, special particles with distinct mechanical properties were introduced in a particle-based model of collective cell migration [Sepúlveda 2013]. A similar spirit was followed in a continuum model of the epithelial front as an active membrane, which includes elastic restoring forces and an active normal force accounting for cell motility [Mark 2010]. To capture the self-organized appearance of leader cells, a phenomenological dependence of the cell motility force on the local curvature of the interface was proposed. This interfacial model, which neglects the long-range hydrodynamic interactions through the monolayer, yields a simple analytical prediction of a long-wavelength instability of the front (Fig. 7.3). The same motility-curvature coupling was then implemented in the aforementioned particle-based model to reproduce the fingering [Tarle 2015].

In a different approach, the fingering instability was also recapitulated by a particle-based model that introduced an alignment interaction between cell motility

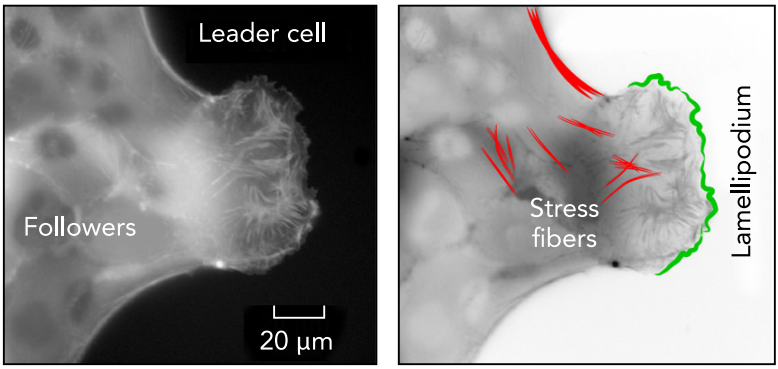

Figure 7.2 | Leader cells in epithelial fingers. Cells at the tip of the fingers exhibit a different, more mesenchymal phenotype with a large lamellipodium at the front and polarized stress fibers, yet retaining strong cell-cell adhesions with the cells behind. A supracellular actin cable forms along the side of the finger. From [Vedula 2013].

forces and the local velocity field of the tissue [Basan 2013]. Later on, assuming a complete alignment between velocity and traction forces, a continuum model was formulated in the form of Toner-Tu equations for a dry[1] and incompressible active fluid [Zimmermann 2014a, Nesbitt 2017]. This model predicts a moving front to be stable and non-moving front to exhibit an instability with an unbounded growth rate for a number of finite wavelengths (Fig. 7.4). In yet a different approach, fingering, or at least interface roughening, was obtained by coupling chemotactic fields to different models and numerical schemes for the mechanics of epithelial spreading [Ouaknin 2009, Salm 2012, Köpf 2013, Ben Amar 2016]. Finally, an undulation of the interface was observed in the numerical solution of continuum models of epithelial expansion, treated as an active polar fluid [Lee 2011b] and as an active nematic with cell proliferation [Doostmohammadi 2015]. Recently, fingering was also found in a given parameter range of an active vertex model [Barton 2017].

Thus, despite the many efforts, the physical mechanism of the fingering instability in epithelia remains a matter of debate. In this chapter, we analize the stability of the front of an expanding epithelial monolayer by means of the continuum active polar fluid model introduced in Chapter 6. The model includes hydrodynamic interactions through the tissue, and it does not implement any kind of leader-cell behaviour, nor alignment interactions between traction forces and the flow field. Yet, we analytically predict a long-wavelength instability of the moving front due to the sole effect of active traction forces. The fastest-growing mode has a finite wavelength, typically of hundreds of micrometers, consistent with the experimentally observed spacing of the fingers. This characteristic wavelength emerges from

[1] Here, dry denotes that friction dominates over viscosity as a dissipation source [Marchetti 2013]. Thus, the dry limit corresponds to a vanishing hydrodynamic screening length $\lambda = \sqrt{\eta/\xi} \to 0$. See Section 6.4.1 for a discussion of this point.

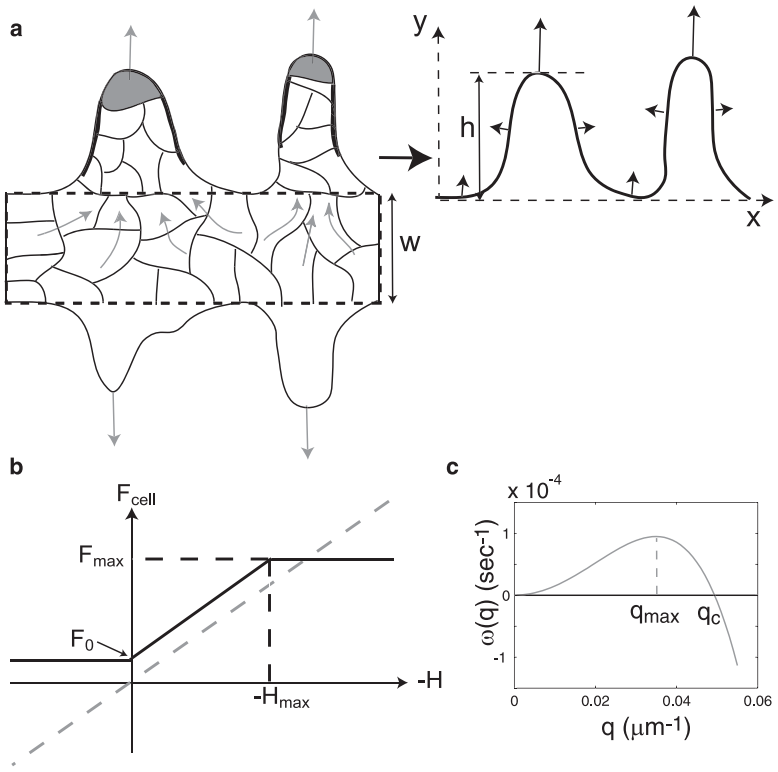

Figure 7.3 | Interfacial instability in an active membrane model with motility-curvature coupling. a, Sketch of epithelial fingering, with tissue flow, actin cables, and leader cells depicted. The dashed lines indicate the initial width of the monolayer (left). The model assumes an active motility force on the interface proportional to its local curvature (right). **b,** The proposed dependence of the cell motility force on the interfacial curvature. The grey dashed line indicates the simpler linear dependence employed in the linear stability analysis. **c,** Growth rate of interfacial perturbations of wavevector q. Long-wavelength perturbations with $q < q_c$ are unstable, with the fastest growth occurring at $q_{\max}$. From [Mark 2010].

the long-range viscous stresses in the tissue, whose propagation is either limited by the lateral width of the monolayer or screened by friction forces. The model also shows that tissue contractility stabilizes short-wavelength perturbations of the monolayer boundary. The stabilizing effect of contractility is typically stronger than that of surface tension. In all, our analysis explicitly shows how a morphological instability may naturally take place in an expanding or retracting cell monolayer, as a result of the flows induced by the traction force field. Leader cells could then appear upon the onset of the instability, influencing the collective dynamics of the fully developed finger structures.

Section 7.2 presents the linear stability analysis of the flat front of an expanding

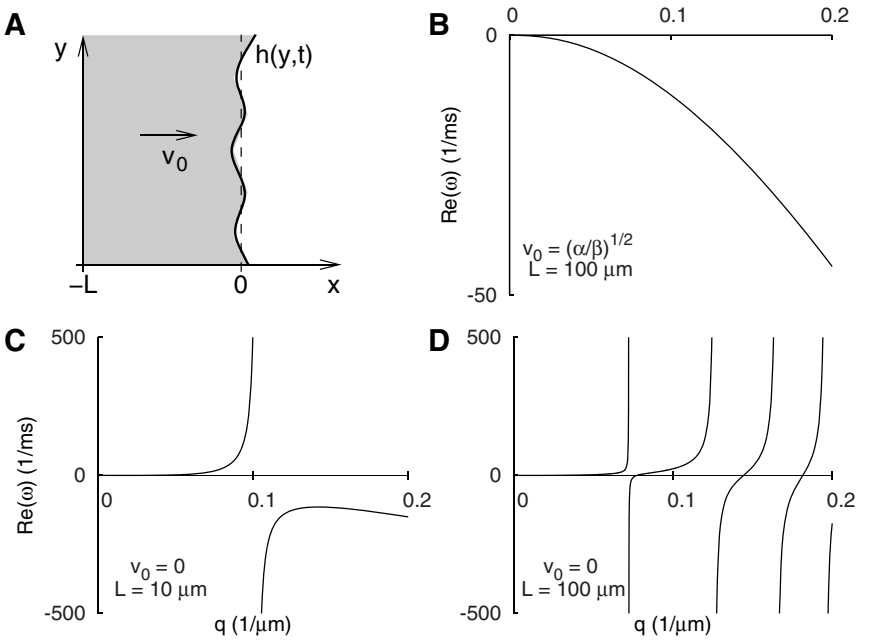

Figure 7.4 | Interfacial instability in a Toner-Tu model of epithelial expansion. a, Sketch of the tissue geometry. **b, c, d,** Growth rate of interfacial perturbations of wavevector q for a moving monolayer **b,** a narrow non-moving monolayer **c,** and a wider non-moving monolayer **d,**. The interface of the non-moving tissue is unstable, with a number of divergences of the growth rate that increases with the tissue width L. From [Zimmermann 2014a].

rectangular monolayer. The origin of the morphological instability and the role of all the mechanical parameters of the monolayer is discussed. Then, Section 7.3 presents the linear stability analysis for the circular dewetting monolayers of Chapter 6. The analytically predicted growth rates at the onset of dewetting are compared to the experimentally measured ones. In combination with the critical values of the model parameters inferred from the wetting transition in Chapter 6, this comparison of the monolayer dynamics allows to estimate the viscosity of the monolayer under different conditions.

7.2 Long-wavelength instability of the tissue front

7.2.1 Linear stability analysis

A continuum active polar fluid model for epithelial spreading was introduced in Section 6.3. The model describes the hydrodynamics of a cell monolayer by means of a polarity field and a flow field. Under the assumptions and approximations

introduced in Section 6.3, the polarity field $\vec{p}\,(\vec{r},t)$ is given by Eq. (6.6):

$$L_c^2 \nabla^2 p_\alpha = p_\alpha, \tag{7.1}$$

and it adiabatically adapts to the boundary imposed by the flow field. Here, L_c is the so-called nematic length that characterizes the decay of the polarity from the maximally polarized boundary of the monolayer towards its unpolarized interior (Figs. 6.15 and 6.16a). In turn, the flow field $\vec{v}\,(\vec{r},t)$ is determined by the force balance condition in the monolayer Eq. (6.12), combined with the suitable constitutive relations of a compressible active polar fluid, Eqs. (6.17) and (6.18):

$$\partial_\beta \sigma^s_{\alpha\beta} + f_\alpha = 0; \tag{7.2}$$

$$\sigma^s_{\alpha\beta} = \eta\left(\partial_\alpha v_\beta + \partial_\beta v_\alpha\right) - \zeta p_\alpha p_\beta, \qquad f_\alpha = -\xi v_\alpha + \frac{T_0}{h} p_\alpha. \tag{7.3}$$

Here, η is an effective viscosity of the monolayer, ζ is the active stress coefficient, and $T_0 = \zeta_i h$ is active traction stress coefficient. In contrast to Section 6.4.1, here we retain the viscous friction force between the cells and the substrate[2], with a friction coefficient ξ.

To study the stability of the advancing front, we consider a monolayer with a rectangular geometry, typical of in vitro monolayer spreading experiments (Fig. 7.1). Thus, in Cartesian coordinates, Eq. (7.1) reads

$$L_c^2\left(\partial_x^2 + \partial_y^2\right) p_x = p_x, \tag{7.4a}$$
$$L_c^2\left(\partial_x^2 + \partial_y^2\right) p_y = p_y. \tag{7.4b}$$

In turn, the force balance equation Eq. (7.2) reads

$$\partial_x \sigma^s_{xx} + \partial_y \sigma^s_{xy} = \xi v_x - T_0/h\, p_x, \tag{7.5a}$$
$$\partial_x \sigma^s_{yx} + \partial_y \sigma^s_{yy} = \xi v_y - T_0/h\, p_y, \tag{7.5b}$$

where the components of the stress tensor are given by

$$\sigma^s_{xx} = 2\eta\, \partial_x v_x - \zeta p_x^2, \tag{7.6a}$$
$$\sigma^s_{xy} = \sigma^s_{yx} = \eta\left(\partial_x v_y + \partial_y v_x\right) - \zeta p_x p_y, \tag{7.6b}$$
$$\sigma^s_{yy} = 2\eta\, \partial_y v_y - \zeta p_y^2. \tag{7.6c}$$

We first obtain the flat front solution in rectangular geometry, which will be the reference state of the linear stability analysis. The long ($\hat{y}$) axis of the rectangle is much longer than the short ($\hat{x}$) axis. Hence, we assume translational invariance along the long axis of the monolayer [Blanch-Mercader 2017b]. Moreover, traction forces are mainly perpendicular to the monolayer boundary [Trepat 2009], so that we take the polarity field along the $\hat{x}$ direction: $\vec{p} = p_x^0\,(x)\,\hat{x}$, where the superindex

[2]This is because the problem including the friction term can be analytically solved in the rectangular geometry considered in this section. Cell-substrate friction is negligible for the monolayers in Chapter 6, but it is not negligible for sufficiently large monolayers, which we wish to consider in a general situation.

indicates the zeroth order in the perturbations of the front. Now, imposing symmetry and boundary conditions $p_x^0(L_0) = 1$ and $\sigma_{xx}^0(L_0) = 0$ as in Section 6.4, one obtains the polarity and velocity profiles:

$$p_x^0(x) = \frac{\sinh(x/L_c)}{\sinh(L_0/L_c)}, \tag{7.7}$$

$$\begin{aligned} v_x^0(x) = \frac{\bar{\lambda}}{2\eta}\Bigg[\zeta + \frac{T_0 L_c \bar{\lambda}^2/h}{\bar{\lambda}^2 - L_c^2}\coth(L_0/L_c) \\ - \frac{2\zeta\bar{\lambda}^2}{4\bar{\lambda}^2 - L_c^2}\left[2 + \operatorname{csch}^2(L_0/L_c)\right]\Bigg]\frac{\sinh\left(x/\bar{\lambda}\right)}{\cosh\left(L_0/\bar{\lambda}\right)} \\ + \frac{L_c}{\xi\sinh(L_0/L_c)}\left[\frac{\zeta}{4\bar{\lambda}^2 - L_c^2}\frac{\sinh(2x/L_c)}{\sinh(L_0/L_c)} - \frac{T_0 L_c/h}{\bar{\lambda}^2 - L_c^2}\sinh(x/L_c)\right], \end{aligned} \tag{7.8}$$

where $\bar{\lambda} = \sqrt{2\eta/\xi} = \sqrt{2}\,\lambda$ is a redefined hydrodynamic screening length, and L_0 is the semi-width of the monolayer, which changes according to $dL_0/dt = v_x^0(L_0)$.

Next, we introduce peristaltic small-amplitude perturbations of the flat interface of the monolayer, namely those that modify the monolayer width[3] (Fig. 7.5):

$$L(y) = L_0 + \delta L(y). \tag{7.9}$$

Under these perturbations, the polarity and velocity fields take the form

$$p_x(x,y) = p_x^0(x) + \delta p_x(x,y), \qquad p_y(x,y) = \delta p_y(x,y), \tag{7.10}$$

$$v_x(x,y) = v_x^0(x) + \delta v_x(x,y), \qquad v_y(x,y) = \delta v_y(x,y). \tag{7.11}$$

In turn, boundary conditions must keep imposing a normal and maximal polarity, as well as vanishing normal and shear stresses at the interface, which is now curved. To this end, we define the normal and tangential vectors of each interface,

$$\hat{n}_\pm = \pm\cos\theta\,\hat{x} + \sin\theta\,\hat{y} \approx \pm\hat{x} - \frac{d\delta L}{dy}\,\hat{y}, \tag{7.12a}$$

$$\hat{t}_\pm = \mp\sin\theta\,\hat{x} + \cos\theta\,\hat{y} \approx \pm\frac{d\delta L}{dy}\,\hat{x} + \hat{y}, \tag{7.12b}$$

where θ is defined in Fig. 7.5, and the $\pm$ index stands for the right and left interfaces, respectively. Thus, the boundary conditions for the polarity read

$$\vec{p}\cdot\hat{n}_\pm\big|_{x=\pm L} = 1, \qquad \vec{p}\cdot\hat{t}_\pm\big|_{x=\pm L} = 0. \tag{7.13}$$

For the x-component, the conditions imply $p_x(\pm L) \approx \pm 1$. This expands into

$$p_x(\pm L) = p_x^0(\pm L) + \delta p_x(\pm L) \approx p_x^0(\pm L_0) \pm \partial_x p_x^0(\pm L_0)\,\delta L + \delta p_x(\pm L) \approx \pm 1, \tag{7.14}$$

[3] The introduction of peristaltic perturbations, instead of perturbations that locally conserve the width of the monolayer, is motivated by the experimental observations, in which the monolayers exhibit local differences in width along their long axis (Fig. 7.1).

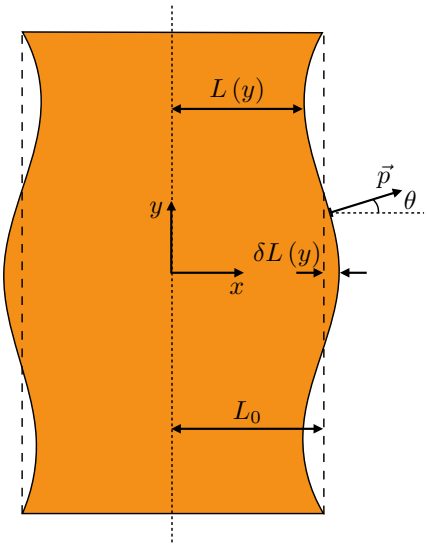

Figure 7.5 | Sketch of the peristaltic perturbations of the monolayer boundary. Dashed lines indicate the position of the flat, unperturbed interface. The dotted line indicates the symmetry axis of the monolayer.

which yields

$$\delta p_x(\pm L) = \mp \partial_x p_x^0(\pm L_0)\,\delta L \tag{7.15}$$

as a boundary condition on the polarity perturbation. For the y-component of the polarity perturbation, the boundary condition imposes

$$\delta p_y(\pm L) = -\frac{d\delta L}{dy}. \tag{7.16}$$

Then, the boundary conditions on the stress read

$$\hat{n}_\pm \cdot \boldsymbol{\sigma} \cdot \hat{n}_\pm\big|_{x=\pm L} = 0, \qquad \hat{t}_\pm \cdot \boldsymbol{\sigma} \cdot \hat{n}_\pm\big|_{x=\pm L} = 0, \tag{7.17}$$

which respectively ensure vanishing normal and shear stress at the interfaces. Here, for simplicity, we neglect interfacial tension and bending rigidity, which would contribute stabilizing terms to the growth rate. The condition on the normal stress gives $\sigma_{xx}(\pm L) = 0$ which, after expanding as previously, leads to

$$\delta\sigma_{xx}(\pm L) = \mp \partial_x \sigma_{xx}^0\left(\pm L^0\right)\delta L \tag{7.18}$$

for the stress perturbation. In turn, the condition on the shear stress directly gives

$$\delta\sigma_{xy}(\pm L) = 0. \tag{7.19}$$

Next, we decompose all perturbations in their Fourier modes, identified by the

wave number q:

$$\delta L\left(y,t\right)=\int_{-\infty}^{\infty}\delta\tilde{L}\left(q,t\right)e^{iqy}\,\frac{dq}{2\pi}, \tag{7.20a}$$

$$\delta p_{\alpha}\left(x,y,t\right)=\int_{-\infty}^{\infty}\delta\tilde{p}_{\alpha}\left(x,q,t\right)e^{iqy}\,\frac{dq}{2\pi}, \tag{7.20b}$$

$$\delta v_{\alpha}\left(x,y,t\right)=\int_{-\infty}^{\infty}\delta\tilde{v}_{\alpha}\left(x,q,t\right)e^{iqy}\,\frac{dq}{2\pi}, \tag{7.20c}$$

In terms of the Fourier modes, the equations for the polarity components read

$$L_{c}^{2}\left(\partial_{x}^{2}-q^{2}\right)\delta\tilde{p}_{x}=\delta\tilde{p}_{x}, \tag{7.21a}$$

$$L_{c}^{2}\left(\partial_{x}^{2}-q^{2}\right)\delta\tilde{p}_{y}=\delta\tilde{p}_{y}. \tag{7.21b}$$

In turn, the components of the force balance equation, once the constitutive relation is introduced, read

$$\begin{aligned}&\eta\left(2\partial_{x}^{2}-q^{2}-\frac{1}{\lambda^{2}}\right)\delta\tilde{v}_{x}+iq\eta\,\partial_{x}\delta\tilde{v}_{y}\\&\quad+\left[T_{0}/h-2\zeta\left(\partial_{x}p_{x}^{0}+p_{x}^{0}\partial_{x}\right)\right]\delta\tilde{p}_{x}-iq\zeta\,p_{x}^{0}\,\delta\tilde{p}_{y}=0,\end{aligned} \tag{7.22a}$$

$$\begin{aligned}&iq\eta\,\partial_{x}\delta\tilde{v}_{x}+\eta\left(\partial_{x}^{2}-2q^{2}-\frac{1}{\lambda^{2}}\right)\delta\tilde{v}_{y}\\&\quad+\left[T_{0}/h-\zeta\left(\partial_{x}p_{x}^{0}+p_{x}^{0}\partial_{x}\right)\right]\delta\tilde{p}_{y}=0.\end{aligned} \tag{7.22b}$$

The boundary conditions must also be translated into the Fourier domain, reading

$$\delta\tilde{p}_{x}\left(\pm L\right)=\mp\partial_{x}p_{x}^{0}\left(\pm L_{0}\right)\delta\tilde{L},\qquad\delta\tilde{p}_{y}\left(\pm L\right)=-iq\,\delta\tilde{L}, \tag{7.23}$$

$$\delta\tilde{\sigma}_{xx}\left(\pm L\right)=\mp\partial_{x}\sigma_{xx}^{0}\left(\pm L_{0}\right)\delta\tilde{L},\qquad\delta\tilde{\sigma}_{xy}\left(\pm L\right)=0. \tag{7.24}$$

Then, the four coupled differential equations Eqs. (7.21) and (7.22) are analytically solved for $\delta\tilde{p}_{\alpha}\left(x,q\right)$ and $\delta\tilde{v}_{\alpha}\left(x,q\right)$. From the Fourier modes of the velocity field, the perturbed spreading velocity V can be computed as

$$V=\vec{v}\cdot\hat{n}|_{x=L}=\left[\vec{v}^{\,0}\cdot\hat{n}+\delta\vec{v}\cdot\hat{n}\right]_{x=L}\approx v_{x}^{0}\left(L_{0}\right)+\partial_{x}v_{x}^{0}\left(L_{0}\right)\delta L+\delta v_{x}\left(L_{0}\right), \tag{7.25}$$

so that

$$\delta V\left(y\right)=V\left(y\right)-V_{0}=\partial_{x}v_{x}^{0}\left(L_{0}\right)\delta L\left(y\right)+\delta v_{x}\left(L_{0},y\right). \tag{7.26}$$

Thus, the growth rate $\omega\left(q\right)$ of the tissue shape perturbations follows from

$$\delta\tilde{V}\left(q\right)=\int_{-\infty}^{\infty}\delta V\left(y\right)e^{-iqy}dy=\frac{d\delta\tilde{L}\left(q\right)}{dt}=\omega\left(q\right)\delta\tilde{L}\left(q\right). \tag{7.27}$$

Hence,

$$\omega\left(q\right)=\partial_{x}v_{x}^{0}\left(L_{0}\right)+\frac{\delta\tilde{v}_{x}\left(L_{0},q\right)}{\delta\tilde{L}\left(q\right)}. \tag{7.28}$$

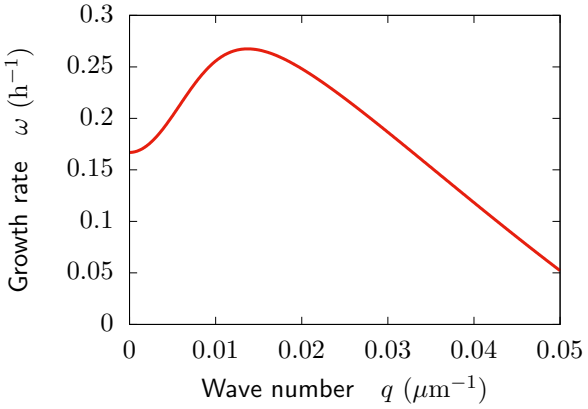

Figure 7.6 | Long-wavelength instability of the monolayer front. Parameter values are $L_0 = 200$ μm, $T_0 = 0.5$ kPa, $L_c = 25$ μm, $h = 5$ μm, $\zeta = -20$ kPa, $\eta = 25$ MPa·s, $\xi = 100$ Pa·s/μm^2, typical for the monolayers in Chapter 6 (see Table 6.1).

The resulting growth rate, whose expression is omitted here due to its length, is a real number under any conditions, so that no oscillatory instability is expected. However, the growth rate evidences a long-wavelength instability of the monolayer front. Moreover, the fastest growing perturbation has a finite wavelength[4] (Fig. 7.6).

7.2.2 Origin and contributions to the instability

Here, we give an argument for the origin of a long-wavelength morphological instability in the tissue, which singles out its physical mechanism. It is based on a simple calculation of the flat front velocity that does not require solving for the full flow profile. To this end, we consider a limit case without contractility and cell-substrate friction, $\zeta, \xi \to 0$, which might be close to the experimental situation of an expanding monolayer [Blanch-Mercader 2017b]. In addition, we also consider the experimentally relevant limit $L_c \ll L_0$. In this limit, most of the tissue behaves as a passive viscous fluid, since it experiences essentially no traction force, which is strongly concentrated at a polarized boundary layer of width L_c. Thus, outside this narrow layer, force balance can be approximated by

$$\partial_x \sigma^s_{xx} \approx 0, \qquad \sigma^s_{xx} \approx 2\eta \frac{dv_x}{dx}. \tag{7.30}$$

[4] In our free-boundary problem, the amplitude of the front perturbations does not grow exponentially in time. This is because the growth rate depends on time through the monolayer width $L_0\,(t)$. Consequently, Eq. (7.27) yields

$$\delta\tilde{L}\,(q,t) = \delta\tilde{L}\,(q,0) \exp\left[\int_0^t \omega\,(q,t')\,dt'\right]. \tag{7.29}$$

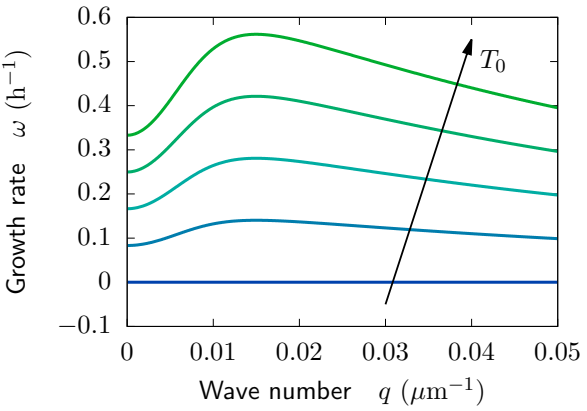

Figure 7.7 | Traction forces completely destabilize the monolayer front. Parameter values are $L_0 = 200$ μm, $L_c = 25$ μm, $h = 5$ μm, $\eta = 25$ MPa·s, $\xi, \zeta \to 0$, and $T_0 = 0.25n$ kPa; $n = 0, \ldots, 4$.

Therefore, the stress is uniform throughout most of the tissue, with a value given by the stress accumulated across the boundary layer, namely $\sigma^s_{xx} \approx T_0 L_c/h$. Consequently, the velocity gradient is also constant,

$$\frac{dv_x}{dx} \approx \frac{T_0 L_c}{2\eta h}, \tag{7.31}$$

and hence the spreading velocity $v_x(L_0) = V_0$ reads

$$V_0 \approx \frac{T_0 L_c}{2\eta h} L_0, \tag{7.32}$$

where we have used that $v_x(0) = 0$. This result means that the flat front has an accelerated expansion due to the sole action of a constant traction force. Consequently, the $q = 0$ perturbation mode is unstable, $\omega(0) > 0$, since any uniform displacement of the advancing front makes it depart from its original velocity. This fact already implies a long-wavelength instability of the front, since the growth rate $\omega(q)$ is continuous and must eventually become negative at short wavelengths because of stabilizing effects such as surface tension. In fact, under the sole presence of traction forces, the flat front is unstable with respect to a perturbation of any wavelength (Fig. 7.7). Such a complete instability stems from the fact that, similarly to the acceleration of the flat front (Eq. (7.32)), the bulged regions of the interface locally expand at a higher velocity than the depressed regions (Fig. 7.5).

The previous argument explains why long-wavelength modes are unstable under only traction forces. However, it does not explain why the most unstable mode occurs at a finite wavelength (Fig. 7.7). In fact, the existence of a peak in the growth rate is due to the long-range viscous forces that span the entire monolayer in the

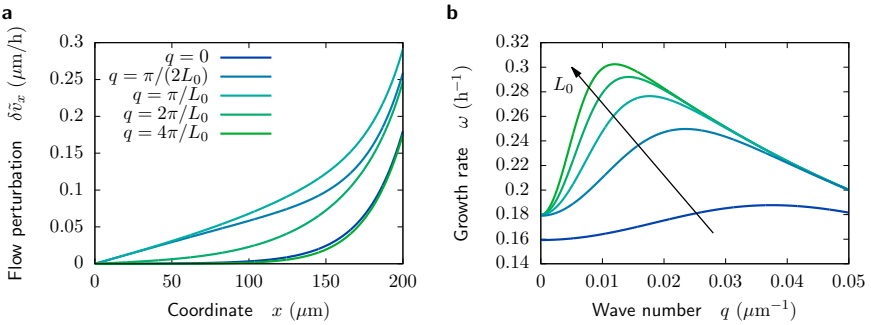

Figure 7.8 | Long-range viscous flows select the fastest growing mode. a, Flow perturbations induced by the longest-wavelength shape perturbations ($q < \pi/L_0$) are screened. In turn, flows induced by shorter wavelength perturbations ($q > \pi/L_0$) naturally have a shorter range. Finally, shape pertubations at a wavelength that matches the monolayer width ($q \sim \pi/L_0$) are optimal; they span the whole monolayer, thus yielding the fastest front velocity. $L_0 = 200$ μm. **b,** The growth rate features a peak at $q \sim \pi/L_0$. $L_0 = 50n$ μm; $n = 1, \ldots, 5$. Note that for $L_0 = 50$ μm, $\omega(0)$ departs from the value given in Eq. (7.33) because the limit $L_c \ll L_0$ does not hold. Parameter values are $T_0 = 0.5$ kPa, $L_c = 25$ μm, $h = 5$ μm, $\eta = 25$ MPa·s, and $\xi, \zeta \to 0$.

wet limit $\lambda = \sqrt{\eta/\xi} \gg L_0$. Thus, a given perturbation of the front generates a flow perturbation that propagates over a length scale $\sim \pi/q$ into the monolayer. For $\pi/q > L_0$, these flows have a longer range than the width of the monolayer. Since they do not fit in the monolayer, they are strongly screened. In turn, flows generated by perturbations of wavelength comparable to the monolayer width span the whole monolayer, giving the strongest contribution to the motion of the perturbed front. Finally, flows arising from shorter-wavelength perturbations have a shorter range, thus having a smaller impact to the motion of the tissue interface (Fig. 7.8a). Thus, viscous flows in the monolayer are responsible for the peak in the growth rate at $q \sim \pi/L_0$ (Fig. 7.8b).

In fact, the presence of a peak of the growth rate at $q \sim \pi/L_0$ can also be deduced from an expansion of the growth rate at long wavelengths:

$$\omega(q) \approx \frac{T_0 L_c}{2\eta h}\left[1 + \frac{1}{3}(L_0 q)^2 - \frac{2}{45}(L_0 q)^4 + \mathcal{O}\left(q^6\right)\right], \tag{7.33}$$

which applies in the limit $\zeta, \xi \to 0$ and $L_c \ll L_0$. The positive curvature of the growth rate at $q \to 0$ ensures the presence of a peak at a finite wavelength. From Eq. (7.33), the fastest growing mode can be estimated as $q^* \approx \sqrt{15}/(2L_0) \sim 2/L_0$, in agreement with the argument above.

The presence of a surface tension γ of the monolayer interface[5] might induce a negative curvature of the growth rate at $q \to 0$, hence making the peak disappear.

[5]The surface tension of the interface, γ, quantifies the work per unit area required to expand it. Thus, it must not be confused with other interfacial forces, such as traction forces and tissue contractility. Even

Surface tension modifies the boundary condition for the normal stress, Eq. (7.17), which becomes

$$\hat{n}_{\pm} \cdot \boldsymbol{\sigma}^{s} \cdot \hat{n}_{\pm}|_{x=\pm L} = -\gamma \vec{\nabla} \cdot \hat{n}_{\pm}\Big|_{x=\pm L} \approx \pm\gamma \frac{d^2 \delta L}{dy^2}. \tag{7.34}$$

In this case, Eq. (7.33) becomes

$$\omega(q) \approx \frac{T_0 L_c}{2\eta h} + \left[\frac{T_0 L_c L_0^2}{6\eta h} - \frac{\gamma L_0}{2\eta}\right] q^2 + \mathcal{O}\left(q^4\right). \tag{7.35}$$

This expression reveals the existence of a critical size

$$L_\gamma \approx \frac{3\gamma h}{T_0 L_c} \tag{7.36}$$

above which the growth rate features a peak at a finite wavelength, and hence tissue fingers arise at the linear level of the instability. Alternatively, fingers are expected to easily form if the surface tension is lower than the size-dependent critical value $\gamma^* \approx T_0 L_c L_0/(3h)$.

For typical values of tissue surface tension measured in cell aggregates[6], $\gamma \sim 1 - 10$ mN/m [Foty 1994, Forgacs 1998, Guevorkian 2010, Stirbat 2013], the critical monolayer width for fingering is $L_\gamma \sim 0.3 - 10$ μm, where we have used $T_0 = 0.2 - 0.8$ kPa, $L_c = 25$ μm, and $h = 5$ μm (see Table 6.1). Therefore, we expect surface tension not to play a major role in the fingering instability in monolayers of typical widths $L_0 \sim 0.1 - 1$ mm. Thus, fingers should be formed by the sole destabilizing action of traction forces at the edge of the monolayer which, due to the ensuing long-range viscous stresses in the tissue, lead to the selection of a finite wavelength for the most unstable mode.

Cell-substrate friction screens the propagation of viscous stresses over distances larger than $\lambda = \sqrt{\eta/\xi}$. Therefore, friction is expected to affect the selection of the fastest growing mode. In fact, because of the screening of viscous stresses, the peak of the growth rate occurs at $q \sim \pi/\lambda$ if $\lambda \lesssim L_0$, namely if friction is not negligible (Fig. 7.9). Thus, for a sufficiently strong friction, the preferred wavelength of finger formation is limited by the hydrodynamic screening length λ instead of the monolayer width L_0. For typical values of the friction coefficient $\xi \sim 100$ Pa·s/μm^2 and the monolayer viscosity $\eta \sim 25$ MPa·s (see Table 6.1), the hydrodynamic screening length is $\lambda \sim 0.5$ mm. Therefore, the crossover from a viscosity-dominated to a friction-dominated monolayer spreading and fingering should be observable in usual in vitro experiments.

for a flat monolayer edge with a constant length, these interfacial forces drive the spreading or retraction of the tissue. In contrast, the surface tension γ of the interface only gives rise to a normal force at the interface under curvature.

[6] In principle, one of the main contributions to the surface tension of the monolayer should be the peripheral actin cables usually found at the monolayer edge, specially on the sides of tissue fingers. Measurements of the traction forces associated to the retraction of such supracellular actin cables upon laser ablation (Fig. S2C in Ref. [Reffay 2014]) suggest their tension to be $\gamma \sim 0.2$ mN/m, even lower than the tissue surface tension of cell aggregates. In addition, the cortical tension in cells is also usually in the range $\sim 0.1 - 5$ mN/m.

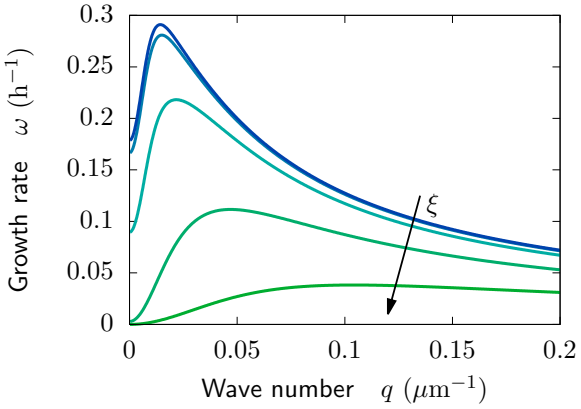

Figure 7.9 | Friction screens viscous stresses to limit the most unstable mode. If friction is not negligible ($\lambda \lesssim L_0$), the fastest growing mode is set by the hydrodynamic screening length $\lambda = \sqrt{\eta/\xi}$, $q \sim \pi/\lambda$. Parameter values are $L_0 = 200$ μm, $T_0 = 0.5$ kPa, $L_c = 25$ μm, $h = 5$ μm, $\eta = 25$ MPa·s, $\zeta \to 0$, and $\xi = 10^n$ Pa·s/μm^2; $n = 1, \ldots, 5$.

Finally, contractility has a stabilizing effect on the monolayer front, since it decreases the spreading velocity (Fig. 7.10). The effect of contractility is opposite to that of traction, albeit size-independent. This is because contractile forces are an internal stress concentrated at the polarized layer of width L_c at the monolayer edge, and hence do not generate long-range viscous stresses as external forces do. In the limit $L_\gamma, L_c \ll L_0 \ll \lambda$, contractility has no impact on the growth rate of the uniform mode, $\omega(0)$, but contributes a stabilizing term to the quadratic term in the expansion at long wavelengths:

$$\omega(q) \approx \frac{T_0 L_c}{2\eta h} + \left[\frac{T_0 L_c L_0^2}{6\eta h} + \frac{\zeta L_c^2}{8\eta}\right] q^2 + \mathcal{O}\left(q^4\right). \tag{7.37}$$

Thus, as surface tension, it defines a critical size

$$L_\zeta \approx \sqrt{-\frac{3\zeta L_c h}{4T_0}} \tag{7.38}$$

above which the growth rate features a peak at a finite wavelength. In other words, fingers are expected at the linear level of the instability if the contractility is smaller than the size-dependent critical value $\zeta^* \approx -4T_0 L_0^2/(3hL_c)$.

For typical values of the contractility, $\zeta \sim -50 - 1$ kPa, the critical monolayer width for fingering is $L_\zeta \sim 10 - 100$ μm, where we have used $T_0 = 0.2 - 0.8$ kPa, $L_c = 25$ μm, and $h = 5$ μm (see Table 6.1). Therefore, we do not expect contractility to prevent fingering. However, our estimates indicate that contractility is probably one of the main responsibles for stabilizing short-wavelength perturbations of the monolayer front. Thus, the competition between the destabilizing

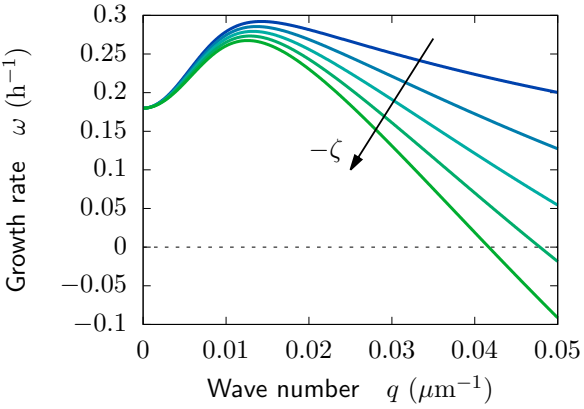

Figure 7.10 | Contractility stabilizes short-wavelength perturbations of the monolayer front. Parameter values are $L_0 = 200$ μm, $T_0 = 0.5$ kPa, $L_c = 25$ μm, $h = 5$ μm, $\eta = 25$ MPa·s, $\xi \to 0$, and $\zeta = 10n$ kPa; $n = 0, \ldots, 4$.

effect of traction forces and the stabilizing effect of contractility defines the critical wavelength of the long-wavelength instability of the front or, in other words, the band of unstable modes.

7.3 Morphological instability during monolayer dewetting

Chapter 6 studied the mechanics of the wetting transition in epithelial tissues. The experiments showed the dewetting of confined epithelial monolayers towards droplet-like aggregates. The theoretical analysis described the dynamics of the confined monolayer in the wetting phase, and then focused on the transition to dewetting. However, the dynamics of the dewetting process was not studied. In this section we address this aspect, showing that the circular shape of the monolayer is lost during dewetting (Fig. 7.11). The monolayer acquires an elliptic-like shape in the initial stages of the retraction, finally collapsing into a spheroidal cell aggregate. We propose that the observed symmetry breaking of the tissue shape results from the morphological instability presented in Section 7.2, which is enabled by the release of the confinement constraint upon the onset of dewetting.

We first present the linear stability analysis, which predicts that the morphological instability should also occur during monolayer dewetting. Then, we compare the predicted growth rate to the experimentally measured one. Except for the monolayer viscosity, all the model parameters characterizing the monolayer mechanics at the onset of dewetting were already inferred in Chapter 6 from the analysis of the wetting transition. This allows the monolayer viscosity to be estimated from the

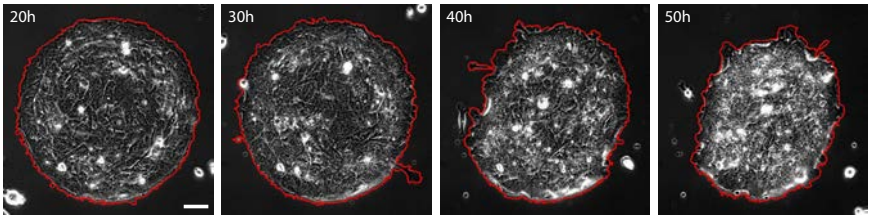

Figure 7.11 | Symmetry breaking of monolayer shape during dewetting. The monolayer loses its initial circular shape, acquiring an elliptic-like shape. Phase contrast images. The red contour indicates the monolayer boundary. Scale bar, 30 μm.

retraction dynamics. The results under different conditions reveal that the viscosity increases with the increasing expression of E-cadherin.

7.3.1 Linear stability analysis

In this section, we study the stability of the retracting front of the dewetting epithelial monolayers in Chapter 6. With respect to Section 7.2, and consistent with Section 6.4, the linear stability analysis is performed in a circular geometry (see Fig. 6.15), considering the wet limit $\lambda = \sqrt{\eta/\xi} \to \infty$, and neglecting surface tension. Thus, the polarity field $\vec{p}\,(\vec{r},t)$ in the epithelium is given by Eq. (6.6):

$$L_c^2 \nabla^2 p_\alpha = p_\alpha. \tag{7.39}$$

In turn, the flow field $\vec{v}\,(\vec{r},t)$ is determined from the force balance condition Eq. (6.21) and the constitutive equation of the medium Eq. (6.17):

$$\partial_\beta \sigma^s_{\alpha\beta} = -\frac{T_0}{h} p_\alpha; \tag{7.40}$$

$$\sigma^s_{\alpha\beta} = \eta\left(\partial_\alpha v_\beta + \partial_\beta v_\alpha\right) - \zeta p_\alpha p_\beta. \tag{7.41}$$

In polar coordinates, Eq. (7.39) reads

$$\left(\partial_r^2 + \frac{1}{r}\partial_r - \frac{1}{r^2}\right) p_r + \frac{1}{r^2}\partial_\theta^2 p_r - \frac{2}{r^2}\partial_\theta p_\theta = \frac{1}{L_c^2} p_r, \tag{7.42a}$$

$$\left(\partial_r^2 + \frac{1}{r}\partial_r - \frac{1}{r^2}\right) p_\theta + \frac{1}{r^2}\partial_\theta^2 p_\theta + \frac{2}{r^2}\partial_\theta p_r = \frac{1}{L_c^2} p_\theta. \tag{7.42b}$$

Force balance is expressed as

$$\frac{1}{r}\partial_r\left(r\sigma^s_{rr}\right) + \frac{1}{r}\partial_\theta \sigma^s_{\theta r} - \frac{1}{r}\sigma^s_{\theta\theta} = -T_0/h\, p_r, \tag{7.43a}$$

$$\frac{1}{r}\partial_r\left(r\sigma^s_{r\theta}\right) + \frac{1}{r}\partial_\theta \sigma^s_{\theta\theta} + \frac{1}{r}\sigma^s_{\theta r} = -T_0/h\, p_\theta, \tag{7.43b}$$

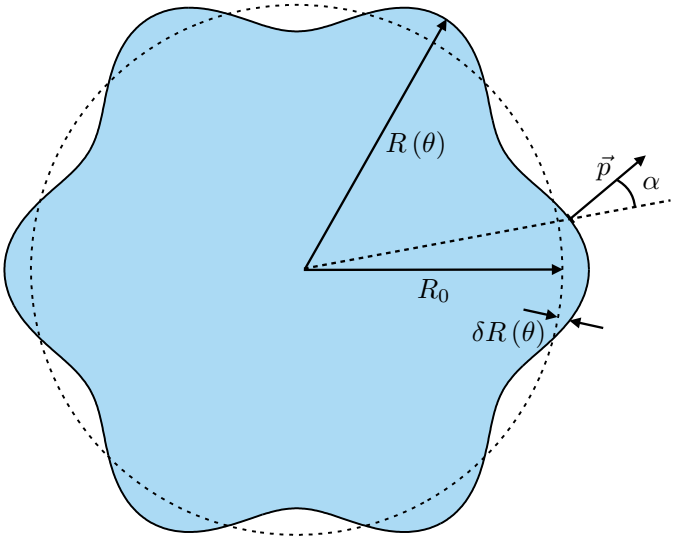

Figure 7.12 | Sketch of the perturbations of the circular monolayer shape. The dashed line indicates the circular, unperturbed interface.

with the components of the stress tensor given by

$$\sigma^s_{rr} = 2\eta\,\partial_r v_r - \zeta p_r^2, \tag{7.44a}$$

$$\sigma^s_{r\theta} = \sigma^s_{\theta r} = \eta\left[r\partial_r\left(\frac{v_\theta}{r}\right) + \frac{1}{r}\partial_\theta v_r\right] - \zeta p_r p_\theta, \tag{7.44b}$$

$$\sigma^s_{\theta\theta} = \frac{2\eta}{r}\left(v_r + \partial_\theta v_\theta\right) - \zeta p_\theta^2. \tag{7.44c}$$

The solution for the unperturbed state, which preserves circular symmetry, is given by Eqs. (6.20) and (6.25):

$$p_r^0(r) = \frac{I_1(r/L_c)}{I_1(R_0/L_c)}, \tag{7.45}$$

$$v_r^0(r) = \frac{1}{2\eta}\left[\left[\zeta - 2T_0\frac{L_c^2}{hR_0} + \left[\zeta\frac{L_c}{R_0} + 2T_0\frac{L_c}{h}\right]\frac{I_0(R_0/L_c)}{I_1(R_0/L_c)} - \zeta\frac{I_0^2(R_0/L_c)}{I_1^2(R_0/L_c)}\right]r + \left[\zeta\frac{I_0(r/L_c)}{I_1(R_0/L_c)} - 2T_0\frac{L_c}{h}\right]L_c\frac{I_1(r/L_c)}{I_1(R_0/L_c)}\right], \tag{7.46}$$

where R_0 is the monolayer radius, which changes according to $dR_0/dt = v_r^0(R_0)$.

Next, we introduce small-amplitude perturbations of the circular monolayer boundary (Fig. 7.12):

$$R(\theta) = R_0 + \delta R(\theta). \tag{7.47}$$

In contrast to the peristaltic perturbations of the rectangular tissue in Section 7.2, the perturbations of the circular interface are generic, accounting for all possible deformations of tissue shape. Then, the polarity and velocity fields are correspondingly perturbed:

$$p_r(r,\theta) = p_r^0(r) + \delta p_r(r,\theta), \qquad p_\theta(r,\theta) = \delta p_\theta(r,\theta), \tag{7.48}$$

$$v_r(r,\theta) = v_r^0(r) + \delta v_r(r,\theta), \qquad v_\theta(r,\theta) = \delta v_\theta(r,\theta). \tag{7.49}$$

To impose boundary conditions, we define the normal and tangential vectors at the boundary,

$$\hat{n} = \cos\alpha\,\hat{r} + \sin\alpha\,\hat{\theta} \approx \hat{r} - \frac{1}{R_0}\frac{d\delta R}{d\theta}\hat{\theta}, \tag{7.50a}$$

$$\hat{t} = -\sin\alpha\,\hat{r} + \cos\alpha\,\hat{\theta} \approx \frac{1}{R_0}\frac{d\delta R}{d\theta}\hat{r} + \hat{\theta}, \tag{7.50b}$$

where α is defined in Fig. 7.12. In terms of these vectors, the conditions that impose a normal and maximal polarity at the boundary read

$$\vec{p}\cdot\hat{n}\big|_{r=R} = 1, \qquad \vec{p}\cdot\hat{t}\big|_{r=R} = 0. \tag{7.51}$$

For the radial component, these conditions imply $p_r(R) \approx 1$, which expands into

$$p_r(R) = p_r^0(R) + \delta p_r(R) \approx p_r^0(R_0) + \partial_r p_r^0(R_0)\,\delta R + \delta p_r(R) \approx 1, \tag{7.52}$$

so that

$$\delta p_r(R) = -\partial_r p_r^0(R_0)\,\delta R. \tag{7.53}$$

For the ortoradial component,

$$\delta p_\theta(R) = -\frac{1}{R_0}\frac{d\delta R}{d\theta}. \tag{7.54}$$

In turn, the boundary conditions on the stress impose a vanishing normal and shear stress at the interface:

$$\hat{n}\cdot\boldsymbol{\sigma}\cdot\hat{n}\big|_{r=R} = 0, \qquad \hat{t}\cdot\boldsymbol{\sigma}\cdot\hat{n}\big|_{r=R} = 0. \tag{7.55}$$

The condition on the normal stress gives $\sigma_{rr}(R) = 0$ which, after expanding as previously, yields

$$\delta\sigma_{rr}(R) = -\partial_r\sigma_{rr}^0(R_0)\,\delta R. \tag{7.56}$$

Finally, the condition on the shear stress imposes $\sigma_{r\theta}(R) = 0$, which translates into

$$\delta\sigma_{r\theta}(R) = \frac{1}{R_0}\frac{d\delta R}{d\theta}\sigma_{\theta\theta}^0(R_0) = \frac{2\eta}{hR_0^2}v_r^0(R_0)\frac{d\delta R}{d\theta}. \tag{7.57}$$

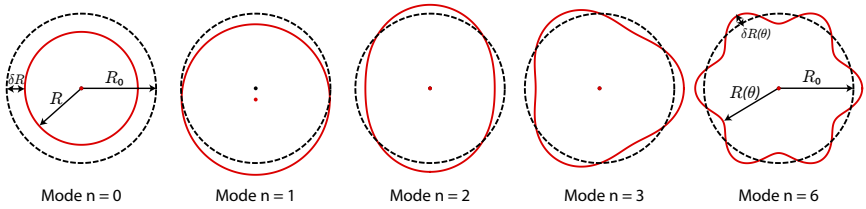

Figure 7.13 | Illustration of the perturbation modes of the circular monolayer shape. The dashed lines indicate the unperturbed interface. The mode number n indicates the number of bulges of each perturbation mode.

Next, we decompose the perturbations in their Fourier modes, identified by an index n (Fig. 7.13):

$$\delta R\left(\theta,t\right)=\sum_{n=0}^{\infty}\delta\tilde{R}_n\left(t\right)e^{in\theta}, \tag{7.58a}$$

$$\delta p_\alpha\left(r,\theta,t\right)=\sum_{n=0}^{\infty}\delta\tilde{p}_{\alpha,n}\left(r,t\right)e^{in\theta}, \tag{7.58b}$$

$$\delta v_\alpha\left(r,\theta,t\right)=\sum_{n=0}^{\infty}\delta\tilde{v}_{\alpha,n}\left(r,t\right)e^{in\theta}. \tag{7.58c}$$

In contrast to the rectangular monolayer, which has an infinitely long interface, the circular interface has a finite length. Consequently, as opposed to the continuum spectrum of the infinite interface, there is a discrete set of possible wavelengths $\lambda_n = 2\pi R_0/n$; $n \in \mathbb{N}$ along the finite circular interface. Now, in terms of the Fourier modes, the equations for the polarity components read

$$\left(\partial_r^2+\frac{1}{r}\partial_r-\frac{1+n^2}{r^2}-\frac{1}{L_c^2}\right)\delta\tilde{p}_r=\frac{2in}{r^2}\delta\tilde{p}_\theta, \tag{7.59a}$$

$$\left(\partial_r^2+\frac{1}{r}\partial_r-\frac{1+n^2}{r^2}-\frac{1}{L_c^2}\right)\delta\tilde{p}_\theta=-\frac{2in}{r^2}\delta\tilde{p}_r. \tag{7.59b}$$

In turn, the components of the force balance, once the constitutive equation has been introduced, are expressed as

$$\begin{aligned}&2\eta\left(\partial_r^2+\frac{1}{r}\partial_r-\frac{1+n^2/2}{r^2}\right)\delta\tilde{v}_r+\frac{in\eta}{r}\left(\partial_r-\frac{3}{r}\right)\delta\tilde{v}_\theta\\&\quad+\left[T_0/h-2\zeta\left(\left(\partial_r+\frac{1}{r}\right)p_r^0+p_r^0\partial_r\right)\right]\delta\tilde{p}_r-\frac{in\zeta}{r}p_r^0\delta\tilde{p}_\theta=0,\end{aligned} \tag{7.60a}$$

$$\begin{aligned}&\frac{in\eta}{r}\left(\partial_r+\frac{3}{r}\right)\delta\tilde{v}_r+\eta\left(\partial_r^2+\frac{1}{r}\partial_r-\frac{1+2n^2}{r^2}\right)\delta\tilde{v}_\theta\\&\quad+\left[T_0/h-\zeta\left(\left(\partial_r+\frac{2}{r}\right)p_r^0+p_r^0\partial_r\right)\right]\delta\tilde{p}_\theta=0.\end{aligned} \tag{7.60b}$$

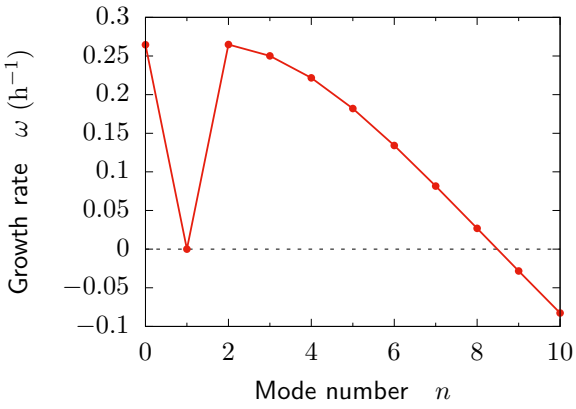

Figure 7.14 | Long-wavelength morphological instability during monolayer dewetting. Parameter values are $R_0 = 200$ μm, $T_0 = 0.75$ kPa, $L_c = 25$ μm, $h = 5$ μm, $\zeta = -40$ kPa, $\eta = 25$ MPa·s, typical for the onset of dewetting (see Fig. 6.27 and Table 6.2). The line is a guide to the eye.

Finally, in Fourier space, the boundary conditions read

$$\delta\tilde{p}_{r,n}(R) = -\partial_r p_r^0(R_0)\,\delta\tilde{R}_n, \qquad \delta\tilde{p}_{\theta,n}(R) = -\frac{in}{R_0}\delta\tilde{R}_n, \tag{7.61}$$

$$\delta\tilde{\sigma}_{rr,n}(R) = -\partial_r\sigma_{rr}^0(R_0)\,\delta\tilde{R}_n, \qquad \delta\tilde{\sigma}_{r\theta,n}(R) = \frac{2in\eta}{hR_0^2}v_r^0(R_0)\,\delta\tilde{R}_n. \tag{7.62}$$

At this point, the four coupled ordinary differential equations Eqs. (7.59) and (7.60) are solved for $\delta\tilde{p}_{\alpha,n}(r)$ and $\delta\tilde{v}_{\alpha,n}(r)$. The procedure to solve these equations is outlined in Appendix 7.A. The solution is completely analytical for mode $n = 0$ and almost analytical for the rest of modes, meaning that it has an analytical expression that involves two integrals that need to be numerically evaluated. Then, from the Fourier modes of the velocity field, the perturbed spreading velocity can be obtained as

$$V = \vec{v}\cdot\hat{n}|_{r=R} = \left[\vec{v}^{\,0}\cdot\hat{n} + \delta\vec{v}\cdot\hat{n}\right]_{r=R} \approx v_r^0(R_0) + \partial_r v_r^0(R_0)\,\delta R + \delta v_r(R_0), \tag{7.63}$$

which implies

$$\delta V(\theta) = V(\theta) - V_0 = \partial_r v_r^0(R_0)\,\delta R(\theta) + \delta v_r(R_0,\theta). \tag{7.64}$$

Thus, the growth rate ω_n of the tissue shape perturbations follows from

$$\delta\tilde{V}_n = \frac{1}{2\pi}\int_0^{2\pi}\delta V(\theta)\,e^{-in\theta}d\theta = \frac{d\delta\tilde{R}_n}{dt} = \omega_n\delta\tilde{R}_n. \tag{7.65}$$

Hence,

$$\omega_n = \partial_r v_r^0 (R_0) + \frac{\delta \tilde{v}_{r,n} (R_0)}{\delta \tilde{R}_n}. \tag{7.66}$$

The resulting growth rate is a real number under any conditions, showing that there is no oscillatory instability. At the onset of dewetting, namely using typical critical parameter values T_0^*, L_c^*, and $-\zeta^*$ that define the tissue wetting transition (Fig. 6.27 and Table 6.2), the cell monolayer exhibits a long-wavelength morphological instability (Fig. 7.14). Several modes corresponding to deformations of the tissue shape ($n \geq 2$, Fig. 7.13) are unstable. Hence, we propose that this instability is at the root of the observed shape changes during monolayer dewetting (Fig. 7.11).

7.3.2 Tissue shape dynamics, fluctuations, and monolayer viscosity

Next, we compare our predictions for the morphological instability during monolayer dewetting to experiments. To this end, we experimentally characterized the dynamics of tissue shape by tracking the position of the monolayer boundary during dewetting (red line in Fig. 7.11). Thus, the evolution of the local monolayer radius $R(\theta, t)$ quantifies the loss of the circular shape of the monolayer (Fig. 7.15a).

To quantitatively assess the theoretical predictions, we experimentally tracked the growth or decay of the shape perturbation modes. By Fourier-transforming the shape perturbations $\delta R(\theta, t) = R(\theta, t) - R_0$ (Fig. 7.15a), we obtained the time evolution of the amplitude of each perturbation mode: $|\delta \tilde{R}_n(t)|$. These amplitudes stay roughly constant before the dewetting and grow upon its onset (Fig. 7.15b). To compare to the theoretical results, we must restrict the analysis to the linear regime of the instability. In practice, we defined the linear regime by the criterion $|\delta \tilde{R}_n| < 0.1\lambda_n$, namely that the amplitude of a given perturbation mode is less than 10% of its wavelength. This criterion is generally fulfilled at short times after dewetting starts, and is eventually violated. Consequently, we restrict to a short time span after the onset of dewetting, $t_f - t^* = 7$ h (Fig. 7.15b).

We quantified the relevance of the different modes at the final time t_f by means of the structure factor of the interface, $S_n(t_f) = \langle |\delta \tilde{R}_n(t_f)|^2 \rangle$. For all conditions of monolayer size and collagen concentration, long-wavelength modes have larger amplitudes, and hence are more prominent than short-wavelength modes, consistent with a long-wavelength instability of the monolayer front (Fig. 7.16). An exception is mode $n = 1$, corresponding to translations of the monolayer, which often features a much smaller amplitude. This is consistent with the expected vanishing growth rate of mode $n = 1$ (Fig. 7.14), which follows from the translational symmetry of the problem.

To theoretically compute the structure factor, we add a noise term to the dynamics of the perturbation modes, Eq. (7.65). Thus, the corresponding Langevin equation reads

$$\frac{d\delta \tilde{R}_n}{dt} = \omega_n \delta \tilde{R}_n + \tilde{\xi}_n(t). \tag{7.67}$$

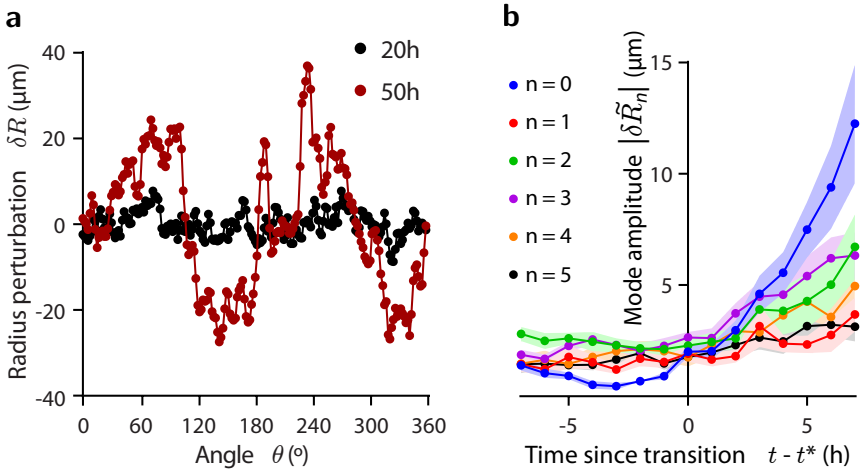

Figure 7.15 | Dynamics of the shape perturbation modes. a, The circular shape is lost during dewetting, as apparent from the appearance of perturbations in the local radius along the monolayer boundary, $\delta R(\theta, t) = R(\theta, t) - R_0$. **b,** The amplitude of the Fourier modes of the shape perturbations grow upon the onset of monolayer dewetting. n is the mode number, which characterizes the number of bulges of the corresponding perturbation (Fig. 7.13).

In principle, shape fluctuations have an active origin, and hence the fluctuation-dissipation theorem does not hold. For simplicity, although active shape fluctuations could have a memory, we take a Gaussian white noise:

$$\left\langle \tilde{\xi}_n(t) \right\rangle = 0, \qquad \left\langle \tilde{\xi}_n(t)\, \tilde{\xi}_m^*(t') \right\rangle = 2D\delta_{n,m}\delta(t-t'), \tag{7.68}$$

where D is the effective diffusion coefficient of shape fluctuations, which we assume independent of the mode number n. Now, under the approximation of a constant growth rate ω_n in the short time span $t_f - t^* = 7$ h, the solution to Eq. (7.67) can be formally expressed as[7]

$$\delta\tilde{R}_n(t) = \delta\tilde{R}_n(t^*)\, e^{\omega_n(t-t^*)} + e^{\omega_n t}\int_{t^*}^{t} \tilde{\xi}_n(t')\, e^{-\omega_n t'}\, dt'. \tag{7.70}$$

Considering no shape perturbations at the onset of dewetting, $\delta\tilde{R}_n(t^*) = 0$, the

[7] As pointed out in Section 7.2.1, the growth rate of free-boundary problems is, in general, not constant. Here, the radius $R_0(t)$ and the mechanical parameters of the monolayer, $T_0(t)$, $\zeta(t)$, and $\eta(t)$ depend on time, yielding a time-dependent growth rate. Consequently, the perturbation growth or decay is not purely exponential but rather follows

$$\delta\tilde{R}_n(t) = \delta\tilde{R}_n(t^*) \exp\left[\int_{t^*}^{t} \omega_n(t')\, dt'\right]. \tag{7.69}$$

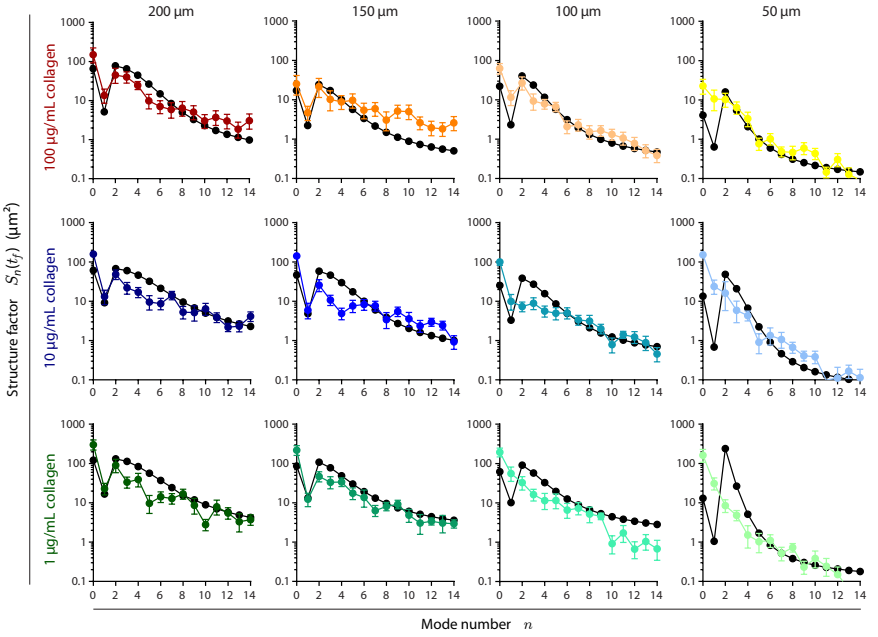

Figure 7.16 | Structure factor of the monolayer interface. At the final time t_f of the linear regime of the instability, long-wavelength modes have developed larger amplitudes for all different conditions, consistent with a long-wavelength instability of tissue shape. Mode $n = 1$, which corresponds to translations of the monolayer, often exhibits a much lower amplitude than its adjacent modes, which correspond to shape or area changes (Fig. 7.13). This is consistent with the expected translational symmetry of the problem, which makes the translational mode marginal (Fig. 7.14). The theoretical prediction (Eq. (7.71), black), is fit to the experimental data (colours), yielding estimates of the effective diffusion coefficient D under the different experimental conditions (Fig. 7.19). Lines are guides to the eye.

equal-time structure factor reads

$$S_n(t) = \left\langle |\delta \tilde{R}_n(t)|^2 \right\rangle = e^{2\omega_n t} \int_{t^*}^{t} \int_{t^*}^{t} \left\langle \tilde{\xi}_n(t') \, \tilde{\xi}_n^*(t'') \right\rangle e^{-\omega_n (t'+t'')} \, dt' \, dt'' = \frac{D}{\omega_n} \left[e^{2\omega_n (t-t^*)} - 1 \right], \quad (7.71)$$

where we have employed Eq. (7.68).

The predicted structure factor Eq. (7.71) has two unknowns: the diffusion coefficient D, and the growth rate ω_n. To predict the growth rate at the onset of dewetting, we use the critical values of the model parameters, T_0^*, L_c^*, and $-\zeta^*$, given in table Table 6.2. Once these parameter values are introduced, the growth rate is left with a single unknown parameter, the monolayer viscosity at the wetting transition, η^*. This parameter can be inferred from the retraction rate of the

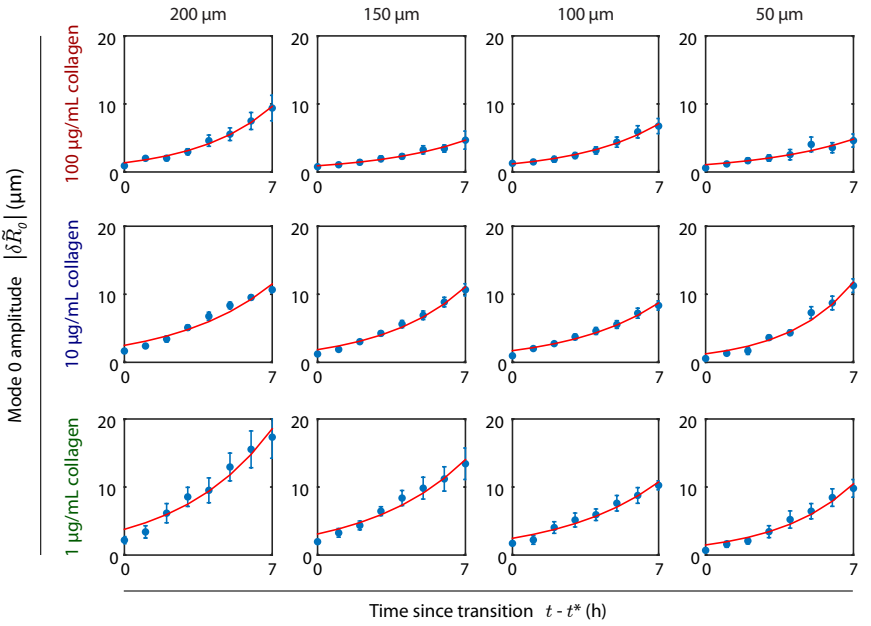

Figure 7.17 | Fits to obtain the retraction rate of the monolayer. For all different conditions, an exponential growth $\delta\tilde{R}_0(t) = \delta\tilde{R}_0(t^*)\, e^{\omega_0(t-t^*)}$ is fitted to the experimental data in the time span $t_f - t^* = 7$ h after the onset of dewetting.

monolayer, ω_0. which we experimentally measure by fitting the exponential growth of the zeroth perturbation mode[8] (Fig. 7.17):

$$\delta\tilde{R}_0(t) = \delta\tilde{R}_0(t^*)\, e^{\omega_0(t-t^*)}. \tag{7.72}$$

Then, we obtain the monolayer viscosity η^* by comparing to the theoretical prediction (see Appendix 7.A for the derivation):

$$\omega_0 = \frac{1}{4\eta}\left[2T_0\frac{R_0}{h} + 3\zeta + 2\left[\zeta\left[\frac{L_c}{R_0} - \frac{R_0}{L_c}\right] + 2T_0\frac{L_c}{h}\right]\frac{I_0(R_0/L_c)}{I_1(R_0/L_c)} - \left[2T_0\frac{R_0}{h} + 5\zeta\right]\frac{I_0^2(R_0/L_c)}{I_1^2(R_0/L_c)} + 2\zeta\frac{R_0}{L_c}\frac{I_0^3(R_0/L_c)}{I_1^3(R_0/L_c)}\right], \tag{7.73}$$

which is approximated by

$$\omega_0 \approx \frac{T_0 L_c}{2\eta h} \tag{7.74}$$

in the limit $L_c \ll R_0$. The measured retraction rate is similar for islands of different size, as well as for the different collagen concentrations (Fig. 7.18a). In contrast,

[8] Since the zeroth mode is always unstable, its amplitude grows fast with time, soon becoming much larger than the noise level. Hence, we neglect noise and approximate the dynamics of the amplitude of the mode $n = 0$ by its average, exponential growth.

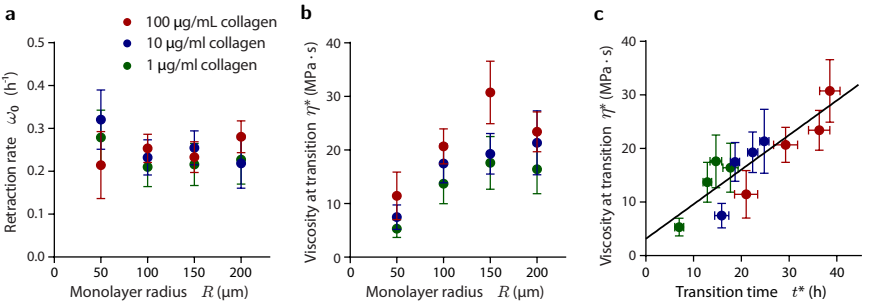

Figure 7.18 | Monolayer viscosity. a, The retraction rate of the monolayer is independent of its size and of the collagen concentration. **b,** The viscosity at the wetting transition, obtained from the measured retraction rate (**a**) via Eq. (7.73), increases with monolayer size and with the collagen concentration. **c,** Monolayer viscosity correlates well with the transition time, suggesting that the increasing E-cadherin expression entails an increasing viscosity.

Figure 7.19 | Effective diffusion coefficient of monolayer shape fluctuations. The diffusion coefficient, estimated from the fits of Eq. (7.71) to the experimental structure factors (Fig. 7.16), increases with monolayer radius and decreases with collagen concentration. This behaviour is consistent with active shape fluctuations, driven by traction forces and damped by cell-substrate friction. The error bars given by the least-squares fits are likely overestimated, and hence not shown.

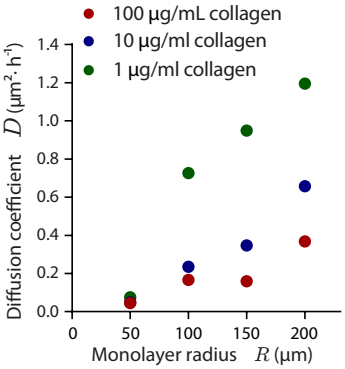

the inferred monolayer viscosity at the wetting transition point, η^*, increases with the monolayer radius and with collagen concentration (Fig. 7.18b). In fact, the tendency exhibited by the viscosity is similar to that of the wetting transition time t^* (Fig. 6.27a). Indeed, these two quantities correlate well (Fig. 7.18c), suggesting that the monolayer viscosity increases with time due to the increasing expression of E-cadherin.

Next, using the predicted growth rates, we fit the theoretical structure factor Eq. (7.71) to the experimental data (Fig. 7.16), which yields estimates for D. The inferred diffusion coefficient of tissue shape increases with monolayer size and decreases with collagen concentration (Fig. 7.19). This behaviour is consistent with shape fluctuations being driven by the total active force in the tissue, which scales like $T_0 L_c R_0$ (see Eq. (6.30)), and damped by cell-substrate friction, which increases with collagen concentration.

Finally, we experimentally determine the growth rate from the structure factor

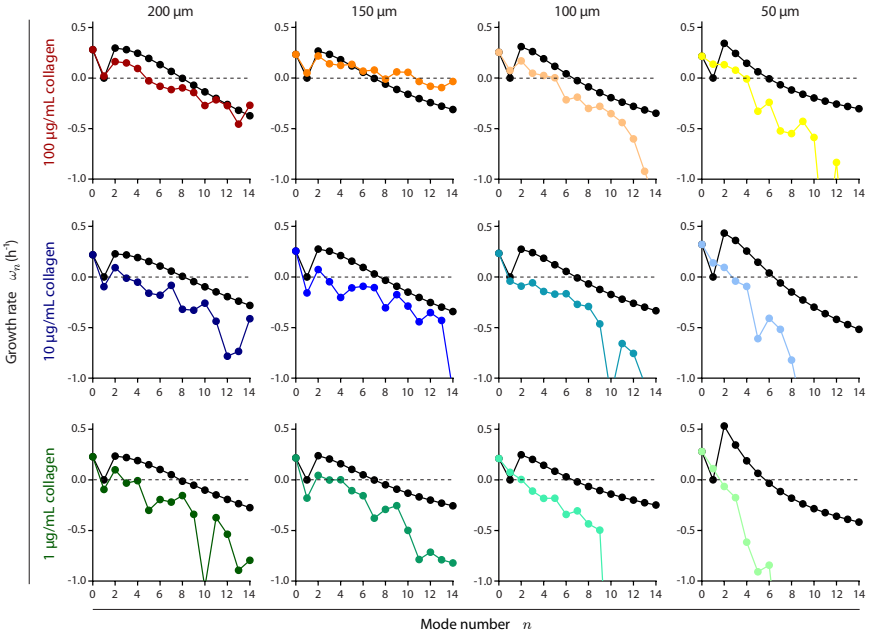

Figure 7.20 | Growth rate of shape perturbation modes. The theoretical predictions (black) are obtained by evaluating the growth rate at the wetting transition point, namely using the critical values of the parameters, T_0^*, L_c^*, $-\zeta^*$, and η^* for each condition, as collected in Table 6.2. The experimental growth rates (colours) are obtained from the measured structure factors (Fig. 7.16) by means of Eq. (7.75). Lines are guides to the eye.

by numerically inverting the relation

$$\frac{S_n\left(t_f\right)}{S_0\left(t_f\right)} = \frac{\omega_0}{\omega_n} \frac{e^{2\omega_n\left(t_f - t^*\right)} - 1}{e^{2\omega_0\left(t_f - t^*\right)} - 1}, \tag{7.75}$$

which is independent of the diffusion coefficient D. For all different experimental conditions, the results show a long-wavelength instability of the shape of the monolayer during dewetting (Fig. 7.20). Larger islands tend to have a larger number of unstable modes, in qualitative agreement with the theoretical predictions. In addition, as reflected in the structure factor, the growth rate of the translation mode $n = 1$ is often smaller than the growth rate of adjacent modes. Figure 7.20 also shows the predicted growth rates at the onset of dewetting (black), namely using the critical values of the model parameters, T_0^*, L_c^*, and $-\zeta^*$, given in Table 6.2.

Although their qualitative agreement is remarkable, the theoretical and experimental growth rates feature some quantitative discrepancy (Fig. 7.20). Most notably, in the experiments, the retraction rate ω_0 is often larger than the growth rate of the rest of the modes. In contrast, there is no such marked difference in the theory, which predicts the elliptic mode $n = 2$ to be even faster than the retraction mode

in some cases. This discrepancy might be due to the fact that the theory considers shape perturbations that protrude outside of the initial monolayer radius R_0. However, due to the confinement imposed by the collagen coating pattern on the substrate, such outwards protrusions are not possible in the experiments. Therefore, confinement hinders the initial growth of all modes except for the retraction mode $n = 0$, which might explain its preponderance in the experiments. Finally, measuring the growth rate of stable modes ($\omega_n < 0$) accurately is challenging. Inferring the growth rate from temporal correlations of mode amplitudes might help improve the accuracy.

7.4 Discussion and conclusions

Motivated by the observation of finger-like protrusions during the spreading of epithelial monolayers, we have theoretically studied the stability of the advancing front. We model the cell monolayer as a compressible active polar fluid that exerts traction forces on the substrate. Based on this continuum model, we have analytically shown that active traction forces are responsible for a generic long-wavelength instability of the monolayer front. Moreover, the fastest-growing mode has a finite wavelength comparable to that of the experimentally observed undulations of the monolayer edge. The existence of such an optimal wavelength for the growth of front perturbations is due to the limitation of the propagation of viscous stresses across the tissue, either by the finite size of the monolayer or by the screening due to cell-substrate friction. The results also show that the contractility of polarized cells stabilizes short-wavelength perturbations.

Our analysis clearly identifies the physical mechanism of the instability. Cellular traction forces at the monolayer edge set the velocity gradient in the spreading monolayer. Hence, under the same traction force, a larger monolayer spreads faster. Consequently, when the monolayer front is perturbed, the protruding regions of the interface advance faster than the trailing regions, thus causing the growth of the perturbation. Therefore, we conclude that traction forces naturally lead to a generic instability of the monolayer front. Thus, neither leader-cell behaviour nor couplings of cell motility to curvature or external fields are necessary for the fingering instability of spreading epithelia. Therefore, our results are consistent with the emergence of leader cells at later stages of the fingering process. However, long-range viscous flows in the monolayer are indeed essential for the instability. On the one hand, they enable the accelerated spreading that renders the interface unstable and, on the other, their range determines the characteristic wavelength of the interfacial undulations.

Our predictions can be experimentally tested by analysing the dynamics of the front perturbations. For instance, one could test whether decreasing traction forces hinders the instability, or whether the characteristic wavelength of the fingering is determined by either the monolayer width or the hydrodynamic screening length $\lambda = \sqrt{\eta/\xi}$.

The predicted instability is generic, occurring for any values of the parameters,

even during monolayer dewetting. For dewetting monolayers, we have experimentally characterized the dynamics of the tissue shape, verifying the long-wavelength instability of the front. By comparison to the theoretical predictions, we estimated the monolayer viscosity at the wetting-dewetting transition point. Our results show that the viscosity correlates well with the transition time, suggesting that the increasing E-cadherin expression entails an increasing viscosity. This might indicate that epithelial viscosity mainly stems from intercellular adhesion [Garcia 2015, Blanch-Mercader 2017b]. Nevertheless, the increasing cell number density due to proliferation could also contribute to the increase of viscosity [Garcia 2015]. In addition, the increasing E-cadherin expression causes an increasing cellular contractility (Figs. 6.6 and 6.10), which might modify tissue viscosity [Stirbat 2013]. Therefore, our results do not preclude a relevant intracellular contribution to the monolayer viscosity.

More generally, our findings emphasize the role of collective hydrodynamic modes in spreading epithelia, illustrating how epithelial morphodynamics arises from long-range hydrodynamic interactions throughout the tissue. In this sense, our results support the physical description of epithelial tissues as active viscous liquid crystals [Hirst 2017]. In particular, we propose that epithelial fingering may naturally emerge as the outcome of a generic morphological instability in a fluid film driven by interfacial active polar forces. Thus, our results illustrate the relevance of interfacial instabilities in driven [Troian 1989, Melo 1989, Ben Amar 2001] and active [Callan-Jones 2008, Sankararaman 2009, Sarkar 2012, Sarkar 2013] fluids for collective behaviours in migrating epithelial tissues.

Finally, in the biological context, the formation of collectively migrating multicellular protrusions is often observed in embryonic development and tumor invasion [Friedl 2009]. These observations have led to propose that fingering instabilities might be involved in developmental processes or tumor progression [Basan 2011, Risler 2013, Pham 2011, Giverso 2016, Hakim 2017]. In fact, migrating fingers have also been proposed to constitute an intermediate state of the epithelial-mesenchymal phenotypic transition [Revenu 2009, Friedl 2012]. Nevertheless, in-vivo migrating fingers are often led by cells with a clearly different phenotype, even of a different cell type, such as cancer-associated fibroblasts leading invasive tumoral fingers [Khalil 2010]. Thus, the actual in-vivo relevance of fingering instabilities in tissues deserves further investigation.

Contributions and acknowledgements

Section 7.2 presents a purely theoretical analysis, motivated by published experimental observations. In contrast, Section 7.3 is the result of a close collaboration between theory and experiments. This collaboration stems from the project on tissue wetting presented in Chapter 6. Experiments were performed by Carlos Pérez-González, with the help of Manuel Gómez-González, in the "Integrative cell and tissue dynamics" group led by Xavier Trepat (IBEC, Barcelona). With the help of Carles Blanch-Mercader (UB, Barcelona, and then Institut Curie, Paris), I

performed the theoretical analysis, as well as fits to the experimental data. Carlos Pérez-González prepared most figures in Section 7.3.

I thank Genís Torrents Verdaguer for suggesting the change of variable that enabled the analytical solution of the linear stability analysis for the circular monolayer geometry. I thank all the members of the labs of Xavier Trepat and Pere Roca-Cusachs for discussions during their lab meetings.

Appendices

7.A Solution of the linear stability analysis of the circular monolayer boundary

In this appendix, we outline the procedure to obtain the profiles of the polarity and velocity perturbation modes, $\delta\tilde{p}_{\alpha,n}(r)$ and $\delta\tilde{v}_{\alpha,n}(r)$, associated to the morphological instability of the tissue shape during monolayer dewetting described in Section 7.3. The mentioned perturbation modes obey a system of four coupled ordinary differential equations, Eqs. (7.59) and (7.60):

$$\left(\partial_r^2+\frac{1}{r}\partial_r-\frac{1+n^2}{r^2}-\frac{1}{L_c^2}\right)\delta\tilde{p}_r=\frac{2in}{r^2}\delta\tilde{p}_\theta, \tag{7.A.1a}$$

$$\left(\partial_r^2+\frac{1}{r}\partial_r-\frac{1+n^2}{r^2}-\frac{1}{L_c^2}\right)\delta\tilde{p}_\theta=-\frac{2in}{r^2}\delta\tilde{p}_r, \tag{7.A.1b}$$

$$\begin{aligned}&2\eta\left(\partial_r^2+\frac{1}{r}\partial_r-\frac{1+n^2/2}{r^2}\right)\delta\tilde{v}_r+\frac{in\eta}{r}\left(\partial_r-\frac{3}{r}\right)\delta\tilde{v}_\theta\\&+\left[T_0/h-2\zeta\left(\left(\partial_r+\frac{1}{r}\right)p_r^0+p_r^0\partial_r\right)\right]\delta\tilde{p}_r-\frac{in\zeta}{r}p_r^0\delta\tilde{p}_\theta=0,\end{aligned} \tag{7.A.2a}$$

$$\begin{aligned}&\frac{in\eta}{r}\left(\partial_r+\frac{3}{r}\right)\delta\tilde{v}_r+\eta\left(\partial_r^2+\frac{1}{r}\partial_r-\frac{1+2n^2}{r^2}\right)\delta\tilde{v}_\theta\\&+\left[T_0/h-\zeta\left(\left(\partial_r+\frac{2}{r}\right)p_r^0+p_r^0\partial_r\right)\right]\delta\tilde{p}_\theta=0,\end{aligned} \tag{7.A.2b}$$

with boundary conditions given by Eqs. (7.61) and (7.62) (see derivation and details in Section 7.3.1):

$$\delta\tilde{p}_{r,n}(R)=-\partial_r p_r^0(R_0)\,\delta\tilde{R}_n,\qquad \delta\tilde{p}_{\theta,n}(R)=-\frac{in}{R_0}\delta\tilde{R}_n, \tag{7.A.3}$$

$$\delta\tilde{\sigma}_{rr,n}(R)=-\partial_r\sigma_{rr}^0(R_0)\,\delta\tilde{R}_n,\qquad \delta\tilde{\sigma}_{r\theta,n}(R)=\frac{2in\eta}{hR_0^2}v_r^0(R_0)\,\delta\tilde{R}_n. \tag{7.A.4}$$

The equations for the polarity perturbations, Eq. (7.A.1), are uncoupled from the force balance equations Eq. (7.A.2). Hence, they can be solved separately. To solve

this system of coupled differential equations, we diagonalize it. The eigenvalues of the system are the following differential operators:

$$\Lambda_{\pm} = \partial_r^2 + \frac{1}{r}\partial_r - \frac{(1 \mp n)^2}{r^2} - \frac{1}{L_c^2}, \tag{7.A.5}$$

which give the following eigenvectors:

$$\delta\tilde{p}_+ = \frac{1}{\sqrt{2}}\left(-i\,\delta\tilde{p}_r + \delta\tilde{p}_\theta\right), \qquad \delta\tilde{p}_- = \frac{1}{\sqrt{2}}\left(\delta\tilde{p}_r - i\,\delta\tilde{p}_\theta\right). \tag{7.A.6}$$

Then, in the base of the eigenvectors, the system is diagonal, and hence their eigenvector components become uncoupled:

$$\left(\partial_r^2 + \frac{1}{r}\partial_r - \frac{(1-n)^2}{r^2} - \frac{1}{L_c^2}\right)\delta\tilde{p}_+ = 0, \tag{7.A.7a}$$

$$\left(\partial_r^2 + \frac{1}{r}\partial_r - \frac{(1+n)^2}{r^2} - \frac{1}{L_c^2}\right)\delta\tilde{p}_- = 0. \tag{7.A.7b}$$

Thus, these equations can be solved in terms of Bessel functions. Subsequently, the eigenvectors are transformed back to the original perturbation fields by inverting Eq. (7.A.6). Finally, application of the boundary conditions Eq. (7.A.3) yields

$$\begin{aligned}\delta\tilde{p}_{r,n}(r) = &\left[\left[1 - n - \frac{R_0}{L_c}\frac{I_0(R_0/L_c)}{I_1(R_0/L_c)}\right]\frac{I_{n-1}(r/L_c)}{I_{n-1}(R_0/L_c)}\right.\\ &\left. + \left[1 + n - \frac{R_0}{L_c}\frac{I_0(R_0/L_c)}{I_1(R_0/L_c)}\right]\frac{I_{n+1}(r/L_c)}{I_{n+1}(R_0/L_c)}\right]\frac{\delta\tilde{R}_n}{2},\end{aligned} \tag{7.A.8a}$$

$$\begin{aligned}\delta\tilde{p}_{\theta,n}(r) = &\left[\left[1 - n - \frac{R_0}{L_c}\frac{I_0(R_0/L_c)}{I_1(R_0/L_c)}\right]\frac{I_{n+1}(r/L_c)}{I_{n+1}(R_0/L_c)}\right.\\ &\left. - \left[1 + n - \frac{R_0}{L_c}\frac{I_0(R_0/L_c)}{I_1(R_0/L_c)}\right]\frac{I_{n-1}(r/L_c)}{I_{n-1}(R_0/L_c)}\right]\frac{i\,\delta\tilde{R}_n}{2}.\end{aligned} \tag{7.A.8b}$$

The force balance equations Eq. (7.A.2) are also coupled, but they can not be directly diagonalized because of the specific dependencies of the differential operators in the system of equations. However, the diagonalization is possible upon the change of variable[9] $z = \ln r$. In this new variable, the equations read

$$\begin{aligned}&2\eta\left(\partial_z^2 - 1 - n^2/2\right)\delta\tilde{v}_r + in\eta\left(\partial_z - 3\right)\delta\tilde{v}_\theta\\ &+ \left[r^2\left[T_0/h - 2\zeta\left(\left(\partial_r + \frac{1}{r}\right)p_r^0 + p_r^0\partial_r\right)\right]\delta\tilde{p}_r - in\zeta r p_r^0\delta\tilde{p}_\theta\right]_{r=e^z} = 0,\end{aligned} \tag{7.A.9a}$$

$$\begin{aligned}&in\eta\left(\partial_z + 3\right)\delta\tilde{v}_r + \eta\left(\partial_z^2 - 1 - 2n^2\right)\delta\tilde{v}_\theta +\\ &r^2\left[T_0/h - \zeta\left(\left(\partial_r + \frac{2}{r}\right)p_r^0 + p_r^0\partial_r\right)\right]\delta\tilde{p}_\theta\Big|_{r=e^z} = 0.\end{aligned} \tag{7.A.9b}$$

[9] I am indebted to Genís Torrents Verdaguer for pointing out this change of variable.

In this form, the system of equations can be formally solved. Applying the operator $\partial_z + 3$ on Eq. (7.A.9a) and operating, one can obtain the following fourth-order equation for $\delta\tilde{v}_r$:

$$\frac{\eta}{n^2-4}\left[\partial_z^4 - 2\left(1+n^2\right)\partial_z^2 + \left(1-n^2\right)^2\right]\delta\tilde{v}_{r,n}(z) = f_n(z), \tag{7.A.10}$$

where $f_n(z)$ is a function that properly combines the inhomogeneous terms of the force balance equations. The corresponding homogeneous equation can be integrated analytically, but the inhomogeneous term can not. Therefore, the solution to the full equation is formally expressed as

$$\begin{aligned}\delta\tilde{v}_{r,n}(r) = \frac{n^2-4}{8n\eta}\Bigg[&\frac{C_1}{r^{n+1}} + \frac{C_2}{r^{n-1}} + C_3 r^{n-1} + C_4 r^{n+1} \\ &+ \frac{1}{(n+1)\,r^{n+1}}\int_r^{R_0} x^n f_n(x)\,dx - \frac{1}{(n-1)\,r^{n-1}}\int_r^{R_0} x^{n-2} f_n(x)\,dx \\ &+ \frac{r^{n-1}}{(n-1)}\int_r^{R_0}\frac{1}{x^n} f_n(x)\,dx - \frac{r^{n+1}}{(n+1)}\int_r^{R_0}\frac{1}{x^{n+2}} f_n(x)\,dx\Bigg],\end{aligned} \tag{7.A.11}$$

where $x = e^z$ is a newly defined integration variable, and $C_1, \ldots, C_4$ are undetermined integration constants. This formal solution is valid for $n \geq 2$, for which the four superposed solutions of the homogeneous equation are independent. For the modes $n = 0, 1$, these four solutions are not independent, which requires two new independent solutions to be included. In the following, we will focus on the $n \geq 2$ modes. The growth rate for the $n = 0, 1$ modes will be computed separately afterwards.

For $n \geq 2$, avoiding a divergence at $r = 0$ requires

$$C_1 = -\frac{1}{n+1}\int_0^{R_0} x^n f_n(x)\,dx, \qquad C_2 = \frac{1}{n-1}\int_0^{R_0} x^{n-2} f_n(x)\,dx. \tag{7.A.12}$$

In turn, the boundary conditions for the stress, Eq. (7.A.4), set the values of C_3 and C_4. The ortoradial component $\delta\tilde{v}_\theta$ of the velocity perturbations can be then computed from the solution for the radial component $\delta\tilde{v}_r$. Finally, these results allow to compute the growth rate through Eq. (7.66). Remarkably, the result is a not-so-long expression with only two pieces that need to be numerically evalutated, namely the integrals in C_1 and C_2.

Next, we compute the growth rate of the modes $n = 0, 1$. The latter corresponds to translations of the center of the cell monolayer (Fig. 7.13). Therefore, this mode must be marginal to preserve spatial translational symmetry: $\omega_1 = 0$. In contrast, mode $n = 0$ corresponds to an expansion or retraction of the monolayer (Fig. 7.13), which is allowed in our compressible fluid model. Then, the solution to Eq. (7.A.10)

for $n = 0$ can be formally written as

$$\delta\tilde{v}_{r,0}(r) = \frac{1}{\eta}\left[\frac{C_1}{r} + C_2\, r + C_3\,\frac{\ln r}{r} + C_4\, r \ln r \right. \\ + \frac{1}{r}\int_0^{R_0} [1 - \ln x]\, f_0(x)\, dx - r\int_r^{R_0} \frac{1+\ln x}{x^2} f_0(x)\, dx \\ \left. + \frac{\ln r}{r}\int_0^{R_0} f_0(x)\, dx + r\,\ln r \int_r^{R_0} \frac{f_0(x)}{x^2} dx\right]. \quad (7.A.13)$$

As previously, to avoid a divergence at $r = 0$,

$$C_1 = -\int_0^{R_0} [1 - \ln x]\, f_0(x)\, dx, \qquad C_3 = -\int_0^{R_0} f_0(x)\,, \quad (7.A.14)$$

and the boundary conditions Eq. (7.A.4) set the remaining integration constants, C_2 and C_4. From the solution for $\delta\tilde{v}_{r,0}(r)$, one can also compute the ortoradial component of the velocity mode, which vanishes: $\delta\tilde{v}_{\theta,0}(r) = 0$. Finally, employing Eq. (7.66), we obtain the growth rate of the uniform mode:

$$\omega_0 = \frac{1}{4\eta}\left[2T_0\frac{R_0}{h} + 3\zeta + 2\left[\zeta\left[\frac{L_c}{R_0} - \frac{R_0}{L_c}\right] + 2T_0\frac{L_c}{h}\right]\frac{I_0(R_0/L_c)}{I_1(R_0/L_c)}\right. \\ \left. - \left[2T_0\frac{R_0}{h} + 5\zeta\right]\frac{I_0^2(R_0/L_c)}{I_1^2(R_0/L_c)} + 2\zeta\frac{R_0}{L_c}\frac{I_0^3(R_0/L_c)}{I_1^3(R_0/L_c)}\right]. \quad (7.A.15)$$

In the limit $L_c \ll R_0$, this is approximated by

$$\omega_0 \approx \frac{T_0 L_c}{2\eta h}. \quad (7.A.16)$$

8 Conclusions and perspectives

This thesis has addressed some mechanical aspects of cellular behaviour, both in single cells and in tissues, developing theoretical models rooted in the physics of soft active matter. Here, we summarize the main conclusions (•) and future perspectives (▷) for each chapter. More general conclusions (⋆) of each part of the thesis are also drawn.

At the cell scale, Part I has focused on the mechanics of the adhesion between the plasma membrane and the actin cortex. In Chapter 2, we proposed a model for membrane-cortex adhesion that couples membrane motion to the binding kinetics of membrane-cortex linker proteins, from which we draw the following conclusions:

- The coupling between membrane motion and linker kinetics leads to a membrane-cortex unbinding transition at a critical pressure difference across the membrane.
- The membrane-cortex adhesion energy depends on the equilibrium stretching of the linkers, and hence on cortical tension.
- The critical suction pressure for membrane-cortex detachment also depends on cortical tension, thus providing a way to estimate it from micropipette aspiration experiments.
- Our model including membrane undulations allows probing membrane-cortex adhesion from fluctuations of adhered cell membranes.

▷ Fluctuation spectroscopy experiments on adhered membranes of nucleated cells, for different values of the pressure on the membrane.

▷ Model the effects of active membrane fluctuations and their interplay with membrane-cortex adhesion.

In Chapter 3, we employed the membrane-cortex adhesion model proposed in Chapter 2 to study the nucleation of blebs. First, we considered the growth or decay of a local membrane detachment, and predicted the critical radius for bleb nucleation. Second, we performed stochastic simulations of our model to study the kinetics of bleb nucleation. From this study, we conclude:

- Membrane peeling from the cortex, namely the process whereby adjacent membrane-cortex bonds sequentially break, is the mechanism that governs bleb nucleation.
- As a consequence, instead of being controlled by the energy of bleb formation as in the classical nucleation picture, bleb nucleation is entirely controlled by the binding kinetics of membrane-cortex linkers. Thus, bleb nucleation requires a kinetic description that goes beyond the possibilities of the classical nucleation approach.
- The critical radius for bleb nucleation through membrane peeling is estimated to be typically smaller than the one predicted by classical nucleation theory, implying a much shorter time scale of bleb nucleation.
- The probability distribution of bleb nucleation times is dominated by a single time scale that decreases with the pressure difference across the membrane.

▷ Experiments that induce controlled bleb nucleation to identify the critical radius and its dependence on pressure and/or membrane tension.

▷ Study the heterogeneous nucleation of blebs, for instance considering the effect of the curvature of the cell interface, or nonhomogeneous distributions of membrane-cortex bonds.

▷ Study bleb growth by extending the analysis of the model to the nonlinear regime.

▷ Study membrane fluctuations via the stochastic simulation method developed to study the kinetics of bleb nucleation.

Altogether, a global conclusion of Part I is:

⋆ Accounting for the force-dependent kinetics of linker proteins is important to capture essential mechanical aspects of membrane-cortex adhesion and detachments.

Part II focused on the dynamics of active polar gels. Specifically, in Chapter 4, we derived the constitutive equations of an active polar gel from a mesoscopic model for the dynamics of crosslinker molecules. The main conclusions are:

- By explicitly obtaining the transport coefficients in terms of molecular parameters, our derivation provides an explicit connection between the mesoscopic and macroscopic levels of description of active gels.
- In particular, the derivation shows how the binding kinetics of the crosslinkers induce the fluidization of the otherwise elastic material, and how breaking detailed balance for the crosslinker kinetics gives rise to active stresses.
- All transport coefficients feature instrinsic active contributions due to nonequilibrium linker kinetics. For example, in the cell cortex, these active contributions could yield a decrease of viscosity with activity — a phenomenon that we call *active thinning*. This effect could explain experimental results on the rheology of the cell cortex, and potentially of other biological systems such as actomyosin gels, the mitotic spindle, and the nucleolus.

▷ Generalize the model to include nonuniform strain and orientation fields, with the corresponding gradients in the fraction of bound linkers.

▷ Compute fluctuation spectra in active gels from our mesoscopic model to identify equilibrium and nonequilibrium contributions.

▷ Experiments that probe the dependence of transport coefficient on activity.

In general, the results of this part underscore the following conclusion:

⋆ An approach based on coarse-graining microscopic or mesoscopic descriptions of active gels can provide insights that go beyond the physics contained in the phenomenological hydrodynamic theory.

Finally, Part III focuses on tissues, addressing mechanical aspects of collective cell migration. Chapter 5 proposes a particle-based description of cell colonies to study how different tissue organizations arise from cell-cell interactions. The model intends to capture generic cellular behaviours, such as cellular self-propulsion, adhesion, and most importantly, contact inhibition of locomotion (CIL). Combining large-scale simulations, which were performed by collaborators, with simple analytical calculations, we draw the following conclusions:

- Due to the chosen cell-cell interactions, the model recapitulates a number of organizations and collective dynamics of cell colonies that are observed in different existing types of tissue. Examples include gas-like states, regular distributions of cells, dynamic cell clusters, gel-like networks, collectively migrating monolayers, and 3D aggregates.
- CIL yields an effective repulsive force between cells, which hinders the formation of cohesive tissues.
- In continuous cell monolayers, CIL gives rise to self-organized collective motion, ensures tensile intercellular stresses, and opposes cell extrusion, thereby hindering monolayer dewetting.

- CIL plays a prominent role in determining the emergent structures and collective dynamics of cell colonies.

▷ Study epithelial spreading employing this model.

▷ Include cell proliferation in the model to study the interplay between cell migration and proliferation through mechanical forces.

▷ Derive a continuum version of the particle-based model, identifying the connection between the cell-cell interaction parameters and those of hydrodynamic theories.

Chapters 6 and 7 focus on the spreading of epithelial cell monolayers, which is studied using a continuum model based on the theory of active polar gels. In particular, Chapter 6 addresses the wetting transition between spreading and retracting monolayers. Combining traction-force measurements, which were performed by collaborators, with theory, we arrive at the following conclusions:

- Contractility induces a nonmonotonic flow profile that may lead to cell accumulation close to the monolayer edge. These flows might favour cell extrusion and the formation of three-dimensional cell rims observed in some experiments.
- The spreading parameter of a cell monolayer increases with its size. Hence, a critical size exists for the tissue wetting transition, as opposed to what occurs in classical wetting. This critical size for monolayer spreading naturally arises from the competition between contact and bulk active forces — traction forces and contractile stresses, respectively — that defines the wetting transition.
- The wetting properties of a tissue emerge from active cellular forces, evidencing the active nature of the wetting transition in tissues.
- E-cadherin regulates active cellular forces in the monolayer through myosin phosphorylation, and thereby controls tissue wetting.
- Traction forces increase with the concentration of extracellular-matrix ligand.

▷ Investigate the putative relation between nonmonotonic flow fields and cell extrusion.

▷ Study the dynamics of the contact angle during the tissue wetting and dewetting processes.

▷ Study the active wetting transition induced by substrate rigidity.

▷ Investigate the molecular mechanism whereby E-cadherin leads to myosin phosphorylation.

In Chapter 7 we study the morphological stability of the monolayer front. Again, from a combined theoretical and experimental analysis, we draw the following conclusions:

- Cellular traction forces produce a long-wavelength instability of the monolayer front, which could account for the formation of multicellular finger-like protrusions observed in spreading epithelial monolayers.
- Despite their role in the developed fingers, leader cells are not required to trigger the fingering instability. Similarly, couplings of cell motility to curvature or to external signaling fields are not required.
- The characteristic wavelength of the interfacial undulations is determined by the screening of long-range viscous stresses in the tissue.
- The predicted fingering instability explains the symmetry breaking of tissue shape during monolayer dewetting.
- Monolayer viscosity, inferred from the dynamics of monolayer dewetting, increases with the expression of E-cadherin, suggesting that it is mainly due to intercellular adhesion.
- The effective noise intensity of tissue shape fluctuations increases with tissue size, suggesting that such fluctuations have an active origin.

▷ Experiments that test specific predictions, for example probing the role of traction forces or the hydrodynamic screening length in epithelial fingering.

▷ Study finger growth by extending the analysis of the model to the nonlinear regime.

In all, a broader common conclusion of Chapters 6 and 7 is:

⋆ The large-scale, long-time dynamics of epithelial spreading can be described by the hydrodynamics of active polar viscous fluids.

⋆ In particular, taking into account the fluid nature of cell monolayers, with the corresponding long-range viscous coupling, is essential to capture some collective behaviours such as tissue wetting or hydrodynamic instabilities.

In general, Part III emphasizes the following conclusion:

⋆ Physical models based on an active soft matter approach, either implemented in particle-based or continuum descriptions, can yield insights into mechanical aspects of collective behaviour of cell colonies and tissues.

Therefore, in my opinion, building such models, as well as designing experiments aimed at testing their predictions and assess their assumptions, may contribute substantially to advance our understanding of collective cell migration.

Globally, this thesis illustrates how insights into mechanical aspects of diverse biological processes in the context of cells and tissues can be gained by developing theoretical models based on the physics of soft active matter. Thus, it encourages to extend this approach to further biological contexts, with the aim of gaining a physical understanding of specific biological phenomena and, thereby, perhaps ultimately devise general physical principles of biological self-organization.

Resum en català

Aquesta tesi estudia aspectes mecànics d'alguns processos biològics en cèl·lules i teixits, que aborda desenvolupant models teòrics basats en la física de la matèria tova. La tesi s'estructura en tres parts que se centren en sistemes biològics diferents.

A la Part I s'estudia l'adhesió entre la membrana plasmàtica i el còrtex d'actina de les cèl·lules eucariotes, que són dos dels seus principals elements estructurals. Controlar l'adhesió entre aquests dos elements és crucial per a diversos processos cel·lulars, com ara la citoquinesi o la motilitat. Normalment, la membrana i el còrtex es mantenen adherits per mitjà d'un gran nombre de proteïnes específiques que els connecten. Ara bé, en algunes situacions, la membrana es desenganxa del còrtex i s'infla per efecte de la pressió intracel·lular, formant una protrusió amb forma de casquet esfèric anomenada butllofa cel·lular. Les butllofes cel·lulars apareixen en diversos contextos, però una de les seves utilitats principals és com a protrusions per a la motilitat cel·lular de tipus ameboide.

Al Capítol 2 es proposa un model continu que acobla la mecànica i la hidrodinàmica de la membrana amb la cinètica d'enllaçament de les proteïnes que connecten la membrana i el còrtex, que depèn de la força a la qual estan sotmesos. Primer es considera una membrana plana, i es prediu el valor crític de la diferència de pressió que causa el desenganxament de la membrana. També es calcula l'energia d'adhesió entre la membrana i el còrtex. Tant la pressió crítica com l'energia d'adhesió depenen de la tensió cortical generada pels motors moleculars de miosina que hi ha al còrtex. En base a aquestes prediccions, es discuteixen experiments de succió amb micropipeta que provoquen el desenganxament de la membrana. Analitzant dades experimentals publicades, utilitzem el model per estimar la tensió cortical de les cèl·lules de *Dictyostelium discoideum*. En segon lloc, s'estén el model per incloure undulacions de la membrana, tenint en compte les interaccions hidrodinàmiques mediades pel fluid de l'entorn. En el límit en què la cinètica dels connectors és un procés molt més ràpid que el moviment de la membrana, es prediuen les correlacions espaciotemporals de les undulacions d'una membrana adherida. Finalment, se suggereix com es podrien utilitzar aquestes prediccions per inferir propietats de l'adhesió membrana-còrtex per mitjà d'experiments d'espectroscopia de fluctuacions de la membrana.

Al Capítol 3, s'empra el model d'adhesió proposat al Capítol 2 per estudiar la nucleació de butllofes cel·lulars. El model mostra que la nucleació de butllofes cel·lulars està governada pel pelat de la membrana, és a dir, el procés de propagació de fractura pel qual els enllaços adjacents entre la membrana i el còrtex es trenquen seqüencialment. Per mitjà d'aquest mecanisme, el creixement o la reducció d'una

regió de membrana desenganxada està completament determinat per la cinètica d'enllaçament de les proteïnes connectores. Així doncs, la nucleació d'una butllofa cel·lular no està determinada pel cost energètic del desenganxament i inflament de la membrana com s'espera en la teoria clàssica de la nucleació. Així, concloem que la teoria clàssica de la nucleació no captura la física del procés de pelat de la membrana i, per tant, no descriu completament la nucleació de butllofes cel·lulars. Considerant el mecanisme de pelat, prediem el radi crític per la nucleació de butllofes cel·lulars, així com la corresponent barrera energètica efectiva. A més, estimem que aquestes quantitats són típicament més petites que les predites per la teoria clàssica de la nucleació, de manera que s'espera que la nucleació de butllofes sigui més ràpida que el predit clàssicament. Després, fem simulacions numèriques d'una membrana adherida fluctuant per obtenir la distribució de probabilitat del temps de nucleació. Trobem que aquesta distribució està dominada per una única escala de temps que disminueix amb la diferència de pressió a la qual està sotmesa la membrana.

En conjunt, els estudis de la Part I ens permeten concloure que tenir en compte la cinètica d'enllaçament de les proteïnes que connecten la membrana i el còrtex és important per capturar aspectes mecànics essencials de l'adhesió entre aquestes dos elements estructurals bàsics de la cèl·lula.

La Part II se centra en la dinàmica dels gels polars actius. Els gels actius són materials tous, sovint xarxes polimèriques entrellaçades reversiblement, que estan mantingudes fora de l'equilibri termodinàmic per mitjà de processos interns que transdueixen energia contínuament. A més, els constituents d'aquests materials sovint són anisòtrops, i fins i tot polars, de manera que poden formar fases amb ordre orientacional, com ara cristalls líquids. L'exemple paradigmàtic de gel polar actiu és el citosquelet cel·lular, que està compost d'una xarxa dinàmica de filaments polimèrics polars. De fet, la dinàmica col·lectiva de diversos sistemes biològics, com ara el còrtex d'actina, el fus mitòtic, i teixits epitelials, s'ha descrit per mitjà de la teoria hidrodinàmica dels gels polars actius. Les equacions constitutives dels gels polars actius es van derivar inicialment en el marc de la termodinàmica irreversible, de manera que contenen un conjunt de coeficients de transport fenomenològics. Així doncs, la relació entre els coeficients de transport que descriuen el comportament macroscòpic dels gels actius i les propietats dels seus constituents microscòpics és essencialment desconeguda.

En el Capítol 4, deduïm les equacions constitutives d'un gel polar actiu a partir d'un model mesoscòpic de la dinàmica de les molècules que entrellacen els elements polars del sistema. D'aquesta manera, establim una connexió entre propietats moleculars i el comportament macroscòpic dels gels polars actius. Específicament, obtenim explícitament els coeficients de transport en funció de paràmetres moleculars. En particular, això mostra com la cinètica de les molècules entrellaçadores indueix la fluidització del material, que altrament seria elàstic. De forma similar, la violació de la condició de balanç detallat per la cinètica molecular dóna lloc a esforços actius. A més, obtenim que tots els coeficients de transport tenen una contribució activa provinent del trencament de balanç detallat en la cinètica molecular. En particular, pel còrtex cel·lular, aquesta contribució podria produir una disminu-

ció de la viscositat amb l'activitat — un fenomen que anomenem *fluidització activa* (en anglès, "*active thinning*"), i que podria explicar alguns resultats experimentals sobre la reologia del còrtex.

Finalment, la Part III està dedicada a les colònies cel·lulars i els teixits, centrant-se en la migració col·lectiva de cèl·lules i en la morfologia dels teixits. En molts contextos biològics, les cèl·lules migren com a part d'un grup, fins i tot en el si d'un teixit. Per migrar, les cèl·lules s'han de polaritzar i exercir forces tant sobre l'entorn com entre elles, anomenades forces de tracció i intercel·lulars, respectivament. En la migració col·lectiva, les interaccions entre cèl·lules donen lloc a diversos fenòmens dinàmics emergents en els teixits, com ara la mateixa coordinació de la migració cel·lular, la formació de fluxos vorticals, protrusions multicel·lulars al front del teixit, la propagació d'ones mecàniques, etc. Els diversos capítols d'aquesta part de la tesi es dediquen a estudiar fenòmens col·lectius d'aquesta mena.

En primer lloc, el Capítol 5 proposa una descripció basada en partícules per estudiar com les diferents organitzacions de cèl·lules en teixits emergeixen de les interaccions entre cèl·lules. El model pretén capturar comportaments cel·lulars genèrics, com ara la migració cel·lular, l'adhesió amb altres cèl·lules i amb el substrat, i la possibilitat de solapament de cèl·lules. A més, es modelitza l'anomenada inhibició de la motilitat per contacte (CIL, de l'anglès "contact inhibition of locomotion"), que fa repolaritzar la migració cel·lular en direcció oposada als contactes entre cèl·lules, per mitjà d'un parell de força en la direcció de migració. Amb el model, es mostra com la CIL dóna una força repulsiva efectiva entre cèl·lules, amb la qual prediem transicions entre teixits cohesionats, no cohesionats, i tridimensionals. A més, en simulacions del model fetes per col·laboradors, identifiquem diverses estructures i dinàmiques col·lectives observades habitualment en diferents tipus de teixits. Alguns exemples són estats de tipus gas, distribucions regulars de cèl·lules, cúmuls dinàmics, xarxes tipus gel, monocapes cel·lulars que migren col·lectivament, i agregats tridimensionals. Llavors, discutim resultats experimentals publicats des de la perspectiva dels nostres resultats, cosa que ens permet associar diferents tipus de teixits amb els diferents estats predits pel model. En general, concloem que, a baixa adhesió intercel·lular, la CIL dificulta la formació de teixits cohesionats. Ara bé, quan l'adhesió intercel·lular és prou forta per formar monocapes cel·lulars contínues, la CIL dóna lloc a moviment col·lectiu auto-organitzat, garanteix esforços tènsils a la monocapa, i s'oposa a l'extrusió de cèl·lules, dificultant així el col·lapse de la monocapa cap a un agregat tridimensional.

En segon lloc, els Capítols 6 and 7 se centren en l'escampament de monocapes epitelials sobre substrats sintètics, en un dels experiments model per estudiar la migració cel·lular col·lectiva. A les escales de temps en què es produeix el procés d'escampament, el teixit és essencialment fluid, i s'escampa gràcies a les forces de tracció exercides per les cèl·lules de la vora del teixit, que es polaritzen. En base a aquestes observacions, el procés d'escampament s'aborda mitjançant un model continu basat en la teoria dels gels polars actius. En aquests estudis, es combina la teoria amb experiments de microscòpia de forces de tracció realitzats per col·laboradors.

El Capítol 6 es concentra en la transició de mullat en teixits epitelials, que

separa l'escampament d'una monocapa cel·lular de la seva retracció cap a un agregat tridimensional de cèl·lules — que seria l'equivalent d'una gota de fluid. En els experiments, es prepara una monocapa epitelial confinada en una regió del substrat, i en la qual s'indueix un augment de l'expressió de la proteïna E-caderina, responsable de l'adhesió intercel·lular. Aquest augment produeix un increment de les forces cel·lulars a la monocapa, que desemboca en la seva retracció cap a un agregat de tipus gota. El model prediu perfils de força de tracció i de tensió a la monocapa que s'ajusten bé a les mesures experimentals, fet que permet extreure l'evolució temporal d'alguns paràmetres del model. A més, el model també prediu un perfil de flux a la monocapa que, en ser no monòton, tendeix a acumular cèl·lules a la vora de la monocapa. Aquesta acumulació podria fomentar l'extrusió de cèl·lules i la formació de cinturons tridimensionals a la vora de monocapes epitelials tal com s'observa en alguns experiments.

A partir del perfil de flux, s'obté el paràmetre d'escampament de la monocapa, el canvi de signe del qual indica la transició de mullat. El model prediu que el paràmetre d'escampament depèn de la mida del teixit, cosa que implica que hi ha una mida crítica per la transició de mullat. Les monocapes més grans que aquesta mida crítica, que depèn dels paràmetres del model, mullaran el substrat, mentre que les monocapes més petites formaran agregats. L'existència d'un radi crític per la transició de mullat en teixits no té contrapartida en la transició clàssica de mullat, i sorgeix del fet que la transició es deu a una competició entre forces cel·lulars actives de contacte i de volum — les forces de tracció i la contractilitat del teixit, respectivament. Per posar a prova aquestes prediccions, es realitzen experiments amb monocapes confinades en regions de diferent mida. Els experiments mostren que les illes més grans tarden més a començar el procés de retracció, d'acord amb la predicció del model. La retracció també tarda més a començar en substrats amb menor concentració de col·lagen, una proteïna de la matriu extracel·lular, ja que les forces cel·lulars són menors. En conjunt, els resultats d'aquest capítol mostren com les propietats de mullat dels teixits epitelials provenen de les forces actives exercides per les cèl·lules, evidenciant que la transició de mullat té una naturalesa activa, amb característiques fonamentalment diferents de la seva equivalent clàssica.

Al Capítol 7 estudiem l'estabilitat morfològica del front d'una monocapa en escampament. El model prediu que les forces de tracció causen una inestabilitat de gran longitud d'ona del front de la monocapa, mentre que la contractilitat del teixit té un efecte estabilitzador. Les traccions indueixen fluxos viscosos de llarg abast en el teixit, que són responsables que el mode més inestable tingui una longitud d'ona finita, donada per la menor entre l'amplada del teixit i la longitud d'apantallament hidrodinàmic a partir de la qual les forces de fricció esmorteeixen la propagació d'esforços viscosos. Per tant, la inestabilitat predita pel model pot explicar la formació de protrusions multicel·lulars en forma de dits observades durant l'escampament de monocapes epitelials. Així, concloem que la presència de cèl·lules líder, tal com s'ha suggerit en base a observacions experimentals, no és necessària per a la inestabilitat del front, per bé que aquestes tinguin un paper en la dinàmica col·lectiva dels dits de teixit que es desenvolupen subsegüentment. De forma similar, acoblaments de la motilitat cel·lular amb la curvatura de la interfase

o amb camps externs com ara senyalitzadors bioquímics, com s'ha suggerit en base a models teòrics, tampoc són essencials per a la inestabilitat, que pot tenir un origen purament hidrodinàmic.

Finalment, la mencionada inestabilitat morfològica permet explicar el trencament de simetria de la forma del teixit observada durant la retracció de les monocapes epitelials en els experiments dels nostres col·laboradors. Ajustant les prediccions de l'anàlisi d'estabilitat lineal del model a les dades experimentals, inferim la viscositat de la monocapa, que augmenta amb la concentració d'E-caderina, suggerint que aquesta propietat del teixit es deu principalment a l'adhesió intercel·lular. Ajustant el factor d'estructura, també inferim la intensitat del soroll de les fluctuacions de la forma de la monocapa, que augmenta amb la mida del teixit, suggerint que es deu a les forces de tracció i que, per tant, té un origen actiu.

List of Figures

List of Tables

Bibliography

[Abercrombie 1979] M. Abercrombie. *Contact inhibition and malignancy*. Nature **281**, 259 (1979)

[Abercrombie 1958] M. Abercrombie and E. Ambrose. *Interference microscope studies of cell contacts in tissue culture*. Exp. Cell Res. **15**, 332 (1958)

[Abercrombie 1954] M. Abercrombie and J. E. M. Heaysman. *Observations on the social behaviour of cells in tissue culture: II. "Monolayering" of fibroblasts*. Exp. Cell Res. **6**, 293 (1954)

[Ahmed 2015] W. W. Ahmed and T. Betz. *Dynamic cross-links tune the solid-fluid behavior of living cells*. Proc. Natl. Acad. Sci. **112**, 6527 (2015)

[Alberts 2008] B. Alberts, A. Johnson, J. Lewis, M. Raff, K. Roberts, and P. Walter. *Molecular Biology of the Cell* (Garland Science, 2008)

[Alert 2016a] R. Alert and J. Casademunt. *Bleb Nucleation through Membrane Peeling*. Phys. Rev. Lett. **116**, 068101 (2016a)

[Alert 2015] R. Alert, J. Casademunt, J. Brugués, and P. Sens. *Model for Probing Membrane-Cortex Adhesion by Micropipette Aspiration and Fluctuation Spectroscopy*. Biophys. J. **108**, 1878 (2015)

[Alert 2014] R. Alert, J. Casademunt, and P. Tierno. *Landscape-Inversion Phase Transition in Dipolar Colloids: Tuning the Structure and Dynamics of 2D Crystals*. Phys. Rev. Lett. **113**, 198301 (2014)

[Alert 2016b] R. Alert, P. Tierno, and J. Casademunt. *Formation of metastable phases by spinodal decomposition*. Nat. Commun. **7**, 13067 (2016b)

[Ananthakrishnan 2007] R. Ananthakrishnan and A. Ehrlicher. *The Forces Behind Cell Movement*. Int. J. Biol. Sci. **3**, 303 (2007)

[Anon 2012] E. Anon, X. Serra-Picamal, P. Hersen, N. C. Gauthier, M. P. Sheetz, X. Trepat, and B. Ladoux. *Cell crawling mediates collective cell migration to close undamaged epithelial gaps*. Proc. Natl. Acad. Sci. U. S. A. **109**, 10891 (2012)

[Balian 2007] R. Balian. *From Microphysics to Macrophysics. Methods and Applications of Statistical Physics. Volume II* (Springer, 2007)

[Banerjee 2011] S. Banerjee and M. C. Marchetti. *Instabilities and oscillations in isotropic active gels*. Soft Matter **7**, 463 (2011)

[Banerjee 2012] S. Banerjee and M. C. Marchetti. *Contractile Stresses in Cohesive Cell Layers on Finite-Thickness Substrates*. Phys. Rev. Lett. **109**, 108101 (2012)

[Barton 2017] D. L. Barton, S. Henkes, C. J. Weijer, and R. Sknepnek. *Active Vertex Model for cell-resolution description of epithelial tissue mechanics*. PLOS Comput. Biol. **13**, e1005569 (2017)

[Basan 2013] M. Basan, J. Elgeti, E. Hannezo, W.-J. Rappel, and H. Levine. *Alignment of cellular motility forces with tissue flow as a mechanism for efficient wound healing*. Proc. Natl. Acad. Sci. U. S. A. **110**, 2452 (2013)

[Basan 2011] M. Basan, J.-F. Joanny, J. Prost, and T. Risler. *Undulation Instability of Epithelial Tissues*. Phys. Rev. Lett. **106**, 158101 (2011)

[Baskaran 2009] A. Baskaran and M. C. Marchetti. *Statistical mechanics and hydrodynamics of bacterial suspensions*. Proc. Natl. Acad. Sci. U. S. A. **106**, 15567 (2009)

[Bazellières 2015] E. Bazellières, V. Conte, A. Elosegui-Artola, X. Serra-Picamal, M. Bintanel-Morcillo, P. Roca-Cusachs, J. J. Muñoz, M. Sales-Pardo, R. Guimerà, and X. Trepat. *Control of cell-cell forces and collective cell dynamics by the intercellular adhesome*. Nat. Cell Biol. **17**, 409 (2015)

[Beaune 2014] G. Beaune, T. V. Stirbat, N. Khalifat, O. Cochet-Escartin, S. Garcia, V. V. Gurchenkov, M. P. Murrell, S. Dufour, D. Cuvelier, and F. Brochard-Wyart. *How cells flow in the spreading of cellular aggregates*. Proc. Natl. Acad. Sci. U. S. A. **111**, 8055 (2014)

[Behrndt 2012] M. Behrndt, G. Salbreux, P. Campinho, R. Hauschild, F. Oswald, J. Roensch, S. W. Grill, and C.-P. Heisenberg. *Forces Driving Epithelial Spreading in Zebrafish Gastrulation*. Science **338**, 257 (2012)

[Bell 1978] G. Bell. *Models for the Specific Adhesion of Cells to Cells*. Science **200**, 618 (1978)

[Belmonte 2008] J. M. Belmonte, G. L. Thomas, L. G. Brunnet, R. M. C. de Almeida, and H. Chaté. *Self-Propelled Particle Model for Cell-Sorting Phenomena*. Phys. Rev. Lett. **100**, 248702 (2008)

[Ben Amar 2016] M. Ben Amar and C. Bianca. *Onset of nonlinearity in a stochastic model for auto-chemotactic advancing epithelia*. Sci. Rep. **6**, 33849 (2016)

[Ben Amar 2001] M. Ben Amar and L. J. Cummings. *Fingering instabilities in driven thin nematic films*. Phys. Fluids **13**, 1160 (2001)

[Ben-Isaac 2011] E. Ben-Isaac, Y. Park, G. Popescu, F. L. H. Brown, N. S. Gov, and Y. Shokef. *Effective Temperature of Red-Blood-Cell Membrane Fluctuations*. Phys. Rev. Lett. **106**, 238103 (2011)

[Beran 1968] M. J. Beran. *Statistical Continuum Theories* (John Wiley & Sons, 1968)

[Bergert 2012] M. Bergert, S. D. Chandradoss, R. A. Desai, and E. Paluch. *Cell mechanics control rapid transitions between blebs and lamellipodia during migration*. Proc. Natl. Acad. Sci. U. S. A. **109**, 14434 (2012)

[Bergert 2015] M. Bergert, A. Erzberger, R. A. Desai, I. M. Aspalter, A. C. Oates, G. Charras, G. Salbreux, and E. K. Paluch. *Force transmission during adhesion-independent migration*. Nat. Cell Biol. **17**, 524 (2015)

[Betz 2009] T. Betz, M. Lenz, J.-F. Joanny, and C. Sykes. *ATP-dependent mechanics of red blood cells*. Proc. Natl. Acad. Sci. U. S. A. **106**, 15320 (2009)

[Betz 2012] T. Betz and C. Sykes. *Time resolved membrane fluctuation spectroscopy*. Soft Matter **8**, 5317 (2012)

[Bihr 2012] T. Bihr, U. Seifert, and A.-S. Smith. *Nucleation of Ligand-Receptor Domains in Membrane Adhesion*. Phys. Rev. Lett. **109**, 258101 (2012)

[Blanch-Mercader 2017a] C. Blanch-Mercader and J. Casademunt. *Hydrodynamic instabilities, waves and turbulence in spreading epithelia*. Soft Matter page Advance Article (2017a)

[Blanch-Mercader 2017b] C. Blanch-Mercader, R. Vincent, E. Bazellières, X. Serra-Picamal, X. Trepat, and J. Casademunt. *Effective viscosity and dynamics of spreading epithelia: a solvable model*. Soft Matter **13**, 1235 (2017b)

[Blanchoin 2014] L. Blanchoin, R. Boujemaa-Paterski, C. Sykes, and J. Plastino. *Actin dynamics, architecture, and mechanics in cell motility*. Physiol. Rev. **94**, 235 (2014)

[Blaser 2006] H. Blaser, M. Reichman-Fried, I. Castanon, K. Dumstrei, F. L. Marlow, K. Kawakami, L. Solnica-Krezel, and C.-P. Heisenberg. *Migration of Zebrafish Primordial Germ Cells: A Role for Myosin Contraction and Cytoplasmic Flow*. Dev. Cell **11**, 613 (2006)

[Boal 2002] D. Boal. *Mechanics of the Cell* (Cambridge University Press, 2002)

[Bonn 2001] D. Bonn and D. Ross. *Wetting transitions*. Reports Prog. Phys. **64**, 1085 (2001)

[Borghi 2012] N. Borghi, M. Sorokina, O. G. Shcherbakova, W. I. Weis, B. L. Pruitt, W. J. Nelson, and A. R. Dunn. *E-cadherin is under constitutive actomyosin-generated tension that is increased at cell-cell contacts upon externally applied stretch*. Proc. Natl. Acad. Sci. U. S. A. **109**, 12568 (2012)

[Bovellan 2014] M. Bovellan, Y. Romeo, M. Biro, A. Boden, P. Chugh, A. Yonis, M. Vaghela, M. Fritzsche, D. Moulding, R. Thorogate, A. Jégou, A. J. Thrasher, G. Romet-Lemonne, P. P. Roux, E. K. Paluch, and G. Charras. *Cellular control of cortical actin nucleation*. Curr. Biol. **24**, 1628 (2014)

[Brangwynne 2011] C. P. Brangwynne, T. J. Mitchison, and A. A. Hyman. *Active liquid-like behavior of nucleoli determines their size and shape in Xenopus laevis oocytes*. Proc. Natl. Acad. Sci. U. S. A. **108**, 4334 (2011)

[Bray 1994] A. Bray. *Theory of phase-ordering kinetics*. Adv. Phys. **43**, 357 (1994)

[Bray 2001] D. Bray. *Cell Movements: From Molecules to Motility* (Garland Science, 2001)

[Brochard 1975] F. Brochard and J.-F. Lennon. *Frequency spectrum of the flicker phenomenon in erythrocytes*. J. Phys. **36**, 1035 (1975)

[Broedersz 2014] C. P. Broedersz and F. C. MacKintosh. *Modeling semiflexible polymer networks*. Rev. Mod. Phys. **86**, 995 (2014)

[Brown 2008] F. L. H. Brown. *Elastic Modeling of Biomembranes and Lipid Bilayers*. Annu. Rev. Phys. Chem. **59**, 685 (2008)

[Brugués 2014a] A. Brugués, E. Anon, V. Conte, J. H. Veldhuis, M. Gupta, J. Colombelli, J. J. Muñoz, G. W. Brodland, B. Ladoux, and X. Trepat. *Forces driving epithelial wound healing*. Nat. Phys. **10**, 683 (2014a)

[Brugués 2008] J. Brugués. *Studies of dynamical phenomena in soft-matter and physical biology*. Ph.D. thesis, Universitat de Barcelona (2008)

[Brugués 2010] J. Brugués, B. Maugis, J. Casademunt, P. Nassoy, F. Amblard, and P. Sens. *Dynamical organization of the cytoskeletal cortex probed by micropipette aspiration*. Proc. Natl. Acad. Sci. U. S. A. **107**, 15415 (2010)

[Brugués 2014b] J. Brugués and D. Needleman. *Physical basis of spindle self-organization*. Proc. Natl. Acad. Sci. **111**, 18496 (2014b)

[Bruinsma 2014] R. Bruinsma, A. Y. Grosberg, Y. Rabin, and A. Zidovska. *Chromatin Hydrodynamics*. Biophys. J. **106**, 1871 (2014)

[Caicedo-Carvajal 2010] C. E. Caicedo-Carvajal, T. Shinbrot, and R. A. Foty. *Alpha5beta1 Integrin-Fibronectin Interactions Specify Liquid to Solid Phase Transition of 3D Cellular Aggregates*. PLoS One **5**, e11830 (2010)

[Callan-Jones 2008] A. Callan-Jones, J.-F. Joanny, and J. Prost. *Viscous-Fingering-Like Instability of Cell Fragments*. Phys. Rev. Lett. **100**, 258106 (2008)

[Callan-Jones 2011] A. C. Callan-Jones and F. Jülicher. *Hydrodynamics of active permeating gels*. New J. Phys. **13**, 093027 (2011)

[Camley 2017] B. Camley and W.-J. Rappel. *Physical models of collective cell motility: from cell to tissue*. J. Phys. D. Appl. Phys. **50**, 113002 (2017)

[Camley 2016] B. A. Camley, J. Zimmermann, H. Levine, and W.-J. Rappel. *Emergent Collective Chemotaxis without Single-Cell Gradient Sensing*. Phys. Rev. Lett. **116**, 098101 (2016)

[Campillo 2012] C. Campillo, J. Jerber, C. Fisch, M. Simoes-Betbeder, P. Dupuis-Williams, P. Nassoy, and C. Sykes. *Mechanics of membrane-cytoskeleton attachment in Paramecium*. New J. Phys. **14**, 125016 (2012)

[Campinho 2013] P. Campinho, M. Behrndt, J. Ranft, T. Risler, N. Minc, and C.-P. Heisenberg. *Tension-oriented cell divisions limit anisotropic tissue tension in epithelial spreading during zebrafish epiboly*. Nat. Cell Biol. **15**, 1405 (2013)

[Carmona-Fontaine 2008] C. Carmona-Fontaine, H. K. Matthews, S. Kuriyama, M. Moreno, G. A. Dunn, M. Parsons, C. D. Stern, and R. Mayor. *Contact inhibition of locomotion in vivo controls neural crest directional migration*. Nature **456**, 957 (2008)

[Chaikin 1995] P. M. Chaikin and T. C. Lubensky. *Principles of condensed matter physics* (Cambridge University Press, 1995)

[Chan 2015] C. J. Chan, A. E. Ekpenyong, S. Golfier, W. Li, K. J. Chalut, O. Otto, J. Elgeti, J. Guck, and F. Lautenschläger. *Myosin II Activity Softens Cells in Suspension*. Biophys. J. **108**, 1856 (2015)

[Charras 2008a] G. T. Charras. *A short history of blebbing*. J. Microsc. **231**, 466 (2008a)

[Charras 2008b] G. T. Charras, M. Coughlin, T. J. Mitchison, and L. Mahadevan. *Life and Times of a Cellular Bleb*. Biophys. J. **94**, 1836 (2008b)

[Charras 2006] G. T. Charras, C.-K. Hu, M. Coughlin, and T. J. Mitchison. *Reassembly of contractile actin cortex in cell blebs*. J. Cell Biol. **175**, 477 (2006)

[Charras 2009] G. T. Charras, T. J. Mitchison, and L. Mahadevan. *Animal cell hydraulics*. J. Cell Sci. **122**, 3233 (2009)

[Charras 2008c] G. T. Charras and E. Paluch. *Blebs lead the way: how to migrate without lamellipodia*. Nat. Rev. Mol. Cell Biol. **9**, 730 (2008c)

[Charras 2005] G. T. Charras, J. C. Yarrow, M. A. Horton, L. Mahadevan, and T. J. Mitchison. *Non-equilibration of hydrostatic pressure in blebbing cells*. Nature **435**, 365 (2005)

[Cheung 2016] K. J. Cheung and A. J. Ewald. *A collective route to metastasis: Seeding by tumor cell clusters*. Science **352**, 167 (2016)

[Chu 2017] F.-Y. Chu, S. C. Haley, and A. Zidovska. *On the origin of shape fluctuations of the cell nucleus*. Proc. Natl. Acad. Sci. U. S. A. **114**, 10338 (2017)

[Chugh 2017] P. Chugh, A. G. Clark, M. B. Smith, D. A. Cassani, K. Dierkes, A. Ragab, P. P. Roux, G. Charras, G. Salbreux, and E. K. Paluch. *Actin cortex architecture regulates cell surface tension*. Nat. Cell Biol. **19**, 689 (2017)

[Clark 2013] A. G. Clark, K. Dierkes, and E. K. Paluch. *Monitoring Actin Cortex Thickness in Live Cells*. Biophys. J. **105**, 570 (2013)

[Clausen 2017] M. P. Clausen, H. Colin-York, F. Schneider, C. Eggeling, and M. Fritzsche. *Dissecting the actin cortex density and membrane-cortex distance in living cells by super-resolution microscopy*. J. Phys. D. Appl. Phys. **50**, 064002 (2017)

[Coburn 2016] L. Coburn, H. Lopez, B. J. Caldwell, E. Moussa, C. Yap, R. Priya, A. Noppe, A. P. Roberts, V. Lobaskin, A. S. Yap, Z. Neufeld, and G. A. Gomez. *Contact inhibition of locomotion and mechanical cross-talk between cell-cell and cell-substrate adhesion determine the pattern of junctional tension in epithelial cell aggregates*. Mol. Biol. Cell **27**, 3436 (2016)

[Cochet-Escartin 2014] O. Cochet-Escartin, J. Ranft, P. Silberzan, and P. Marcq. *Border Forces and Friction Control Epithelial Closure Dynamics*. Biophys. J. **106**, 65 (2014)

[Coffey 2004] W. T. Coffey, Y. P. Kalmykov, and J. T. Waldron. *The Langevin equation. With applications to stochastic problems in physics, chemistry and electrical engineering* (World Scientific, 2004), 2nd ed.

[Coleman 2001] M. L. Coleman, E. A. Sahai, M. Yeo, M. Bosch, A. Dewar, and M. F. Olson. *Membrane blebbing during apoptosis results from caspase-mediated activation of ROCK I*. Nat. Cell Biol. **3**, 339 (2001)

[Collier 2017] S. Collier, P. Paschke, R. R. Kay, and T. Bretschneider. *Image based modeling of bleb site selection*. Sci. Rep. **7**, 6692 (2017)

[Collins 2015] C. Collins and W. J. Nelson. *Running with neighbors: coordinating cell migration and cell-cell adhesion*. Curr. Opin. Cell Biol. **36**, 62 (2015)

[Curie 1894] P. Curie. *Sur la symétrie dans les phénomènes physiques, symétrie d'un champ électrique et d'un champ magnétique*. J. Phys. Theor. Appl. **3**, 393 (1894)

[Dai 1999a] J. Dai and M. P. Sheetz. *Membrane Tether Formation from Blebbing Cells*. Biophys. J. **77**, 3363 (1999a)

[Dai 1999b] J. Dai, H. P. Ting-Beall, R. M. Hochmuth, M. P. Sheetz, and M. A. Titus. *Myosin I Contributes to the Generation of Resting Cortical Tension*. Biophys. J. **77**, 1168 (1999b)

[Davis 2012] J. R. Davis, C.-Y. Huang, J. Zanet, S. Harrison, E. Rosten, S. Cox, D. Y. Soong, G. A. Dunn, and B. M. Stramer. *Emergence of embryonic pattern through contact inhibition of locomotion*. Development **139**, 4555 (2012)

[Davis 2015] J. R. Davis, A. Luchici, F. Mosis, J. Thackery, J. A. Salazar, Y. Mao, G. A. Dunn, T. Betz, M. Miodownik, and B. M. Stramer. *Inter-cellular forces orchestrate contact inhibition of locomotion*. Cell **161**, 361 (2015)

[de Gennes 2003] P.-G. de Gennes, F. Brochard-Wyart, and D. Quéré. *Capillarity and Wetting Phenomena. Drops, Bubbles, Pearls, Waves* (Springer, 2003)

[de Gennes 1993] P.-G. de Gennes and J. Prost. *The Physics of Liquid Crystals* (Oxford University Press, 1993), 2nd ed.

[de Gennes 1982] P. G. de Gennes and C. Taupin. *Microemulsions and the flexibility of oil/water interfaces*. J. Phys. Chem. **86**, 2294 (1982)

[de Groot 1984] S. R. de Groot and P. Mazur. *Non-Equilibrium Thermodynamics* (Dover, 1984)

[Deforet 2014] M. Deforet, V. Hakim, H. Yevick, G. Duclos, and P. Silberzan. *Emergence of collective modes and tri-dimensional structures from epithelial confinement*. Nat. Commun. **5**, 3747 (2014)

[Dembo 1988] M. Dembo, D. C. Torney, K. Saxman, and D. Hammer. *The Reaction-Limited Kinetics of Membrane-to-Surface Adhesion and Detachment*. Proc. R. Soc. B Biol. Sci. **234**, 55 (1988)

[Desai 2009] R. A. Desai, L. Gao, S. Raghavan, W. F. Liu, and C. S. Chen. *Cell polarity triggered by cell-cell adhesion via E-cadherin*. J. Cell Sci. **122**, 905 (2009)

[Desai 2013] R. A. Desai, S. B. Gopal, S. Chen, and C. S. Chen. *Contact inhibition of locomotion probabilities drive solitary versus collective cell migration*. J. R. Soc. Interface **10**, 20130717 (2013)

[Diz-Muñoz 2013] A. Diz-Muñoz, D. A. Fletcher, and O. D. Weiner. *Use the force: membrane tension as an organizer of cell shape and motility*. Trends Cell Biol. **23**, 47 (2013)

[Diz-Muñoz 2010] A. Diz-Muñoz, M. Krieg, M. Bergert, I. Ibarlucea-Benitez, D. J. Muller, E. Paluch, and C.-P. Heisenberg. *Control of Directed Cell Migration In Vivo by Membrane-to-Cortex Attachment*. PLoS Biol. **8**, e1000544 (2010)

[Diz-Muñoz 2016] A. Diz-Muñoz, P. Romanczuk, W. Yu, M. Bergert, K. Ivanovitch, G. Salbreux, C.-P. Heisenberg, and E. K. Paluch. *Steering cell migration by alternating blebs and actin-rich protrusions*. BMC Biol. **14**, 74 (2016)

[Doi 1986] M. Doi and S. F. Edwards. *The Theory of Polymer Dynamics* (Oxford University Press, 1986)

[Doostmohammadi 2015] A. Doostmohammadi, S. P. Thampi, T. B. Saw, C. T. Lim, B. Ladoux, and J. M. Yeomans. *Cell division: a source of active stress in cellular monolayers*. Soft Matter **11**, 7328 (2015)

[Douezan 2012a] S. Douezan and F. Brochard-Wyart. *Dewetting of cellular monolayers*. Eur. Phys. J. E **35**, 34 (2012a)

[Douezan 2012b] S. Douezan and F. Brochard-Wyart. *Spreading dynamics of cellular aggregates confined to adhesive bands*. Eur. Phys. J. E **35**, 116 (2012b)

[Douezan 2012c] S. Douezan, J. Dumond, and F. Brochard-Wyart. *Wetting transitions of cellular aggregates induced by substrate rigidity*. Soft Matter **8**, 4578 (2012c)

[Douezan 2011] S. Douezan, K. Guevorkian, R. Naouar, S. Dufour, D. Cuvelier, and F. Brochard-Wyart. *Spreading dynamics and wetting transition of cellular aggregates*. Proc. Natl. Acad. Sci. U. S. A. **108**, 7315 (2011)

[Duclos 2017] G. Duclos, C. Erlenkämper, J.-F. Joanny, and P. Silberzan. *Topological defects in confined populations of spindle-shaped cells*. Nat. Phys. **13**, 58 (2017)

[Duclos 2014] G. Duclos, S. Garcia, H. G. Yevick, and P. Silberzan. *Perfect nematic order in confined monolayers of spindle-shaped cells*. Soft Matter **10**, 2346 (2014)

[DuFort 2011] C. C. DuFort, M. J. Paszek, and V. M. Weaver. *Balancing forces: architectural control of mechanotransduction*. Nat. Rev. Mol. Cell Biol. **12**, 308 (2011)

[Dufour 2013] S. Dufour, R.-M. Mège, and J. P. Thiery. *alpha-catenin, vinculin, and F-actin in strengthening E-cadherin cell-cell adhesions and mechanosensing*. Cell Adhes. Migr. **7**, 345 (2013)

[Edwards 2016] A. M. J. Edwards, R. Ledesma-Aguilar, M. I. Newton, C. V. Brown, and G. McHale. *Not spreading in reverse: The dewetting of a liquid film into a single drop*. Sci. Adv. **2** (2016)

[Ehrlicher 2015] A. J. Ehrlicher, R. Krishnan, M. Guo, C. M. Bidan, D. A. Weitz, and M. R. Pollak. *Alpha-actinin binding kinetics modulate cellular dynamics and force generation*. Proc. Natl. Acad. Sci. U. S. A. **112**, 6619 (2015)

[Eisenhoffer 2012] G. T. Eisenhoffer, P. D. Loftus, M. Yoshigi, H. Otsuna, C.-B. Chien, P. A. Morcos, and J. Rosenblatt. *Crowding induces live cell extrusion to maintain homeostatic cell numbers in epithelia*. Nature **484**, 546 (2012)

[Eisenhoffer 2013] G. T. Eisenhoffer and J. Rosenblatt. *Bringing balance by force: live cell extrusion controls epithelial cell numbers*. Trends Cell Biol. **23**, 185 (2013)

[El Alaoui Faris 2009] M. El Alaoui Faris, D. Lacoste, J. Pécréaux, J.-F. Joanny, J. Prost, and P. Bassereau. *Membrane Tension Lowering Induced by Protein Activity*. Phys. Rev. Lett. **102**, 038102 (2009)

[Engl 2014] W. Engl, B. Arasi, L. L. Yap, J. P. Thiery, and V. Viasnoff. *Actin dynamics modulate mechanosensitive immobilization of E-cadherin at adherens junctions*. Nat. Cell Biol. **16**, 587 (2014)

[Erdmann 2004a] T. Erdmann and U. S. Schwarz. *Stability of Adhesion Clusters under Constant Force*. Phys. Rev. Lett. **92**, 108102 (2004a)

[Erdmann 2004b] T. Erdmann and U. S. Schwarz. *Stochastic dynamics of adhesion clusters under shared constant force and with rebinding*. J. Chem. Phys. **121**, 8997 (2004b)

[Etournay 2015] R. Etournay, M. Popović, M. Merkel, A. Nandi, C. Blasse, B. Aigouy, H. Brandl, G. Myers, G. Salbreux, F. Jülicher, and S. Eaton. *Interplay of cell dynamics and epithelial tension during morphogenesis of the Drosophila pupal wing*. eLife **4**, e07090 (2015)

[Evans 2001] E. Evans. *Probing the Relation Between Force–Lifetime–and Chemistry in Single Molecular Bonds*. Annu. Rev. Biophys. Biomol. Struct. **30**, 105 (2001)

[Evans 1985] E. A. Evans. *Detailed Mechanics of Membrane-Membrane Adhesion and Separation. I. Continuum of Molecular Cross-Bridges*. Biophys. J. **48**, 175 (1985)

[Evans 2007] E. A. Evans and D. A. Calderwood. *Forces and Bond Dynamics in Cell Adhesion*. Science **316**, 1148 (2007)

[Fackler 2008] O. T. Fackler and R. Grosse. *Cell motility through plasma membrane blebbing*. J. Cell Biol. **181**, 879 (2008)

[Fily 2014] Y. Fily, S. Henkes, and M. C. Marchetti. *Freezing and phase separation of self-propelled disks*. Soft Matter **10**, 2132 (2014)

[Fily 2012] Y. Fily and M. C. Marchetti. *Athermal Phase Separation of Self-Propelled Particles with No Alignment*. Phys. Rev. Lett. **108**, 235702 (2012)

[Fischer-Friedrich 2016] E. Fischer-Friedrich, Y. Toyoda, C. J. Cattin, D. J. Müller, A. A. Hyman, and F. Jülicher. *Rheology of the Active Cell Cortex in Mitosis*. Biophys. J. **111**, 589 (2016)

[Forgacs 1998] G. Forgacs, R. A. Foty, Y. Shafrir, and M. S. Steinberg. *Viscoelastic Properties of Living Embryonic Tissues: a Quantitative Study*. Biophys. J. **74**, 2227 (1998)

[Forster 1990] D. Forster. *Hydrodynamic Fluctuations, Broken Symmetry, and Correlation Functions* (Addison-Wesley, 1990)

[Foty 1994] R. A. Foty, G. Forgacs, C. M. Pfleger, and M. S. Steinberg. *Liquid Properties of Embryonic Tissues: Measurement of Interfacial Tensions*. Phys. Rev. Lett. **72**, 2298 (1994)

[Fournier 2004] J.-B. Fournier, D. Lacoste, and E. Raphaël. *Fluctuation Spectrum of Fluid Membranes Coupled to an Elastic Meshwork: Jump of the Effective Surface Tension at the Mesh Size*. Phys. Rev. Lett. **92**, 018102 (2004)

[Fournier 2010] M. F. Fournier, R. Sauser, D. Ambrosi, J.-J. Meister, and A. B. Verkhovsky. *Force transmission in migrating cells*. J. Cell Biol. **188**, 287 (2010)

[Friedl 2009] P. Friedl and D. Gilmour. *Collective cell migration in morphogenesis, regeneration and cancer*. Nat. Rev. Mol. Cell Biol. **10**, 445 (2009)

[Friedl 2012] P. Friedl, J. Locker, E. Sahai, and J. E. Segall. *Classifying collective cancer cell invasion*. Nat. Cell Biol. **14**, 777 (2012)

[Friedl 2003] P. Friedl and K. Wolf. *Tumour-cell invasion and migration: diversity and escape mechanisms*. Nat. Rev. Cancer **3**, 362 (2003)

[Fritzsche 2014] M. Fritzsche, R. Thorogate, and G. Charras. *Quantitative Analysis of Ezrin Turnover Dynamics in the Actin Cortex*. Biophys. J. **106**, 343 (2014)

[Gachelin 2013] J. Gachelin, G. Miño, H. Berthet, A. Lindner, A. Rousselet, and É. Clément. *Non-Newtonian Viscosity of Escherichia coli Suspensions*. Phys. Rev. Lett. **110**, 268103 (2013)

[Garcia 2015] S. Garcia, E. Hannezo, J. Elgeti, J.-F. Joanny, P. Silberzan, and N. S. Gov. *Physics of active jamming during collective cellular motion in a monolayer*. Proc. Natl. Acad. Sci. U. S. A. **112**, 15314 (2015)

[García-Ojalvo 1999] J. García-Ojalvo and J. M. Sancho. *Noise in Spatially Extended Systems* (Springer, 1999)

[García-Ojalvo 1992] J. García-Ojalvo, J. M. Sancho, and L. Ramírez-Piscina. *Generation of spatiotemporal colored noise*. Phys. Rev. A **46**, 4670 (1992)

[Gardel 2008] M. L. Gardel, B. Sabass, L. Ji, G. Danuser, U. S. Schwarz, and C. M. Waterman. *Traction stress in focal adhesions correlates biphasically with actin retrograde flow speed*. J. Cell Biol. **183**, 999 (2008)

[Garrivier 2002] D. Garrivier, E. Décavé, Y. Bréchet, F. Bruckert, and B. Fourcade. *Peeling model for cell detachment*. Eur. Phys. J. E **8**, 79 (2002)

[George 2017] M. George, F. Bullo, and O. Campàs. *Connecting individual to collective cell migration*. Sci. Rep. **7**, 9720 (2017)

[Ghibaudo 2008] M. Ghibaudo, A. Saez, L. Trichet, A. Xayaphoummine, J. Browaeys, P. Silberzan, A. Buguin, and B. Ladoux. *Traction forces and rigidity sensing regulate cell functions*. Soft Matter **4**, 1836 (2008)

[Gillespie 1980] D. T. Gillespie. *Approximating the master equation by Fokker-Planck-type equations for single-variable chemical systems*. J. Chem. Phys. **72**, 5363 (1980)

[Gillespie 2000] D. T. Gillespie. *The chemical Langevin equation*. J. Chem. Phys. **113**, 297 (2000)

[Gillespie 2002] D. T. Gillespie. *The Chemical Langevin and Fokker-Planck Equations for the Reversible Isomerization Reaction*. J. Phys. Chem. A **106**, 5063 (2002)

[Giomi 2010] L. Giomi, T. B. Liverpool, and M. C. Marchetti. *Sheared active fluids: Thickening, thinning, and vanishing viscosity*. Phys. Rev. E **81**, 051908 (2010)

[Giverso 2016] C. Giverso and P. Ciarletta. *On the morphological stability of multicellular tumour spheroids growing in porous media*. Eur. Phys. J. E **39**, 92 (2016)

[Goetz 1999] R. Goetz, G. Gompper, and R. Lipowsky. *Mobility and Elasticity of Self-Assembled Membranes*. Phys. Rev. Lett. **82**, 221 (1999)

[Gomez 2011] G. A. Gomez, R. W. McLachlan, and A. S. Yap. *Productive tension: force-sensing and homeostasis of cell-cell junctions*. Trends Cell Biol. **21**, 499 (2011)

[Gonzalez-Rodriguez 2012] D. Gonzalez-Rodriguez, K. Guevorkian, S. Douezan, and F. Brochard-Wyart. *Soft matter models of developing tissues and tumors*. Science **338**, 910 (2012)

[Gov 2004a] N. Gov and S. Safran. *Pinning of fluid membranes by periodic harmonic potentials*. Phys. Rev. E **69**, 011101 (2004a)

[Gov 2004b] N. Gov, A. Zilman, and S. Safran. *Hydrodynamics of confined membranes*. Phys. Rev. E **70**, 011104 (2004b)

[Gov 2004c] N. S. Gov. *Membrane Undulations Driven by Force Fluctuations of Active Proteins*. Phys. Rev. Lett. **93**, 268104 (2004c)

[Gov 2003] N. S. Gov, A. G. Zilman, and S. A. Safran. *Cytoskeleton Confinement and Tension of Red Blood Cell Membranes*. Phys. Rev. Lett. **90**, 228101 (2003)

[Gruler 1999] H. Gruler, U. Dewald, and M. Eberhardt. *Nematic liquid crystals formed by living amoeboid cells*. Eur. Phys. J. B **11**, 187 (1999)

[Guevorkian 2010] K. Guevorkian, M.-J. Colbert, M. Durth, S. Dufour, and F. Brochard-Wyart. *Aspiration of Biological Viscoelastic Drops*. Phys. Rev. Lett. **104**, 218101 (2010)

[Guillot 2013] C. Guillot and T. Lecuit. *Mechanics of Epithelial Tissue Homeostasis and Morphogenesis*. Science **340**, 1185 (2013)

[Guo 2006] W.-h. Guo, M. T. Frey, N. A. Burnham, and Y.-l. Wang. *Substrate Rigidity Regulates the Formation and Maintenance of Tissues*. Biophys. J. **90**, 2213 (2006)

[Gupta 2015] M. Gupta, B. R. Sarangi, J. Deschamps, Y. Nematbakhsh, A. Callan-Jones, F. Margadant, R.-M. Mège, C. T. Lim, R. Voituriez, and B. Ladoux. *Adaptive rheology and ordering of cell cytoskeleton govern matrix rigidity sensing*. Nat. Commun. **6**, 7525 (2015)

[Guyon 2001] E. Guyon, J.-P. Hulin, L. Petit, and C. D. Mitescu. *Physical Hydrodynamics* (Oxford University Press, 2001)

[Hakim 2017] V. Hakim and P. Silberzan. *Collective cell migration: a physics perspective*. Reports Prog. Phys. **80**, 076601 (2017)

[Hameed 2012] F. M. Hameed, M. Rao, and G. V. Shivashankar. *Dynamics of Passive and Active Particles in the Cell Nucleus*. PLoS One **7**, e45843 (2012)

[Harris 2014] A. R. Harris, A. Daeden, and G. T. Charras. *Formation of adherens junctions leads to the emergence of a tissue-level tension in epithelial monolayers*. J. Cell Sci. **127**, 2507 (2014)

[Hatwalne 2004] Y. Hatwalne, S. Ramaswamy, M. Rao, and R. Simha. *Rheology of Active-Particle Suspensions*. Phys. Rev. Lett. **92**, 118101 (2004)

[Hawkins 2014] R. J. Hawkins and T. B. Liverpool. *Stress Reorganization and Response in Active Solids*. Phys. Rev. Lett. **113**, 028102 (2014)

[Helfer 2001] E. Helfer, S. Harlepp, L. Bourdieu, J. Robert, F. MacKintosh, and D. Chatenay. *Viscoelastic properties of actin-coated membranes*. Phys. Rev. E **63**, 021904 (2001)

[Helfrich 1990] W. Helfrich. *Elasticity and thermal undulations of fluid films of amphiphiles*. In *Liquids at Interfaces*, edited by J. Charvolin, J.-F. Joanny, and J. Zinn-Justin, chap. 4 (North-Holland, 1990)

[Hemingway 2015] E. J. Hemingway, A. Maitra, S. Banerjee, M. C. Marchetti, S. Ramaswamy, S. M. Fielding, and M. E. Cates. *Active Viscoelastic Matter: From Bacterial Drag Reduction to Turbulent Solids*. Phys. Rev. Lett. **114**, 098302 (2015)

[Henkes 2011] S. Henkes, Y. Fily, and M. C. Marchetti. *Active jamming: Self-propelled soft particles at high density*. Phys. Rev. E **84**, 040301 (2011)

[Hirst 2017] L. S. Hirst and G. Charras. *Biological physics: Liquid crystals in living tissue*. Nature **544**, 164 (2017)

[Hoffman 2015] B. D. Hoffman and A. S. Yap. *Towards a Dynamic Understanding of Cadherin-Based Mechanobiology*. Trends Cell Biol. **25**, 803 (2015)

[Howard 2001] J. Howard. *Mechanics of Motor Proteins and the Cytoskeleton* (Sinauer Associates, 2001)

[Humphrey 2002] D. Humphrey, C. Duggan, D. Saha, D. Smith, and J. Käs. *Active fluidization of polymer networks through molecular motors*. Nature **416**, 413 (2002)

[Ibo 2016] M. Ibo, V. Srivastava, D. N. Robinson, and Z. R. Gagnon. *Cell Blebbing in Confined Microfluidic Environments*. PLoS One **11**, e0163866 (2016)

[Jacobs 2013] C. R. Jacobs, H. Huang, and R. Y. Kwon. *Introduction to Cell Mechanics and Mechanobiology* (Garland Science, 2013)

[Joanny 2013] J.-F. Joanny, K. Kruse, J. Prost, and S. Ramaswamy. *The actin cortex as an active wetting layer*. Eur. Phys. J. E **36**, 9866 (2013)

[Joanny 2009] J.-F. Joanny and J. Prost. *Active gels as a description of the actin-myosin cytoskeleton*. HFSP J. **3**, 94 (2009)

[Joanny 2011] J.-F. Joanny and J. Prost. *Contructing Tools for the Description of Cell Dynamics*. In *Biological Physics. Poincaré Seminar 2009*, vol. 60 of *Progress in Mathematical Physics*, edited by B. Duplantier and V. Rivasseau. Institut Henry Poincaré (Birkhäuser, 2011)

[Joanny 2012] J.-F. Joanny and S. Ramaswamy. *A drop of active matter*. J. Fluid Mech. **705**, 46 (2012)

[Jones 2002] R. A. L. Jones. *Soft Condensed Matter* (Oxford University Press, 2002)

[Jülicher 2011] F. Jülicher. *Active fluids and gels*. In *New Trends in the Physics and Mechanics of Biological Systems*, edited by M. Ben Amar, A. Goriely, M. M. Müller, and L. Cugliandolo, chap. 4 (Oxford University Press, 2011)

[Jülicher 1997] F. Jülicher, A. Ajdari, and J. Prost. *Modeling molecular motors*. Rev. Mod. Phys. **69**, 1269 (1997)

[Jülicher 2007] F. Jülicher, K. Kruse, J. Prost, and J.-F. Joanny. *Active behavior of the Cytoskeleton*. Phys. Rep. **449**, 3 (2007)

[Jülicher 2009] F. Jülicher and J. Prost. *Generic theory of colloidal transport*. Eur. Phys. J. E **29**, 27 (2009)

[Kadir 2011] S. Kadir, J. W. Astin, L. Tahtamouni, P. Martin, and C. D. Nobes. *Microtubule remodelling is required for the front-rear polarity switch during contact inhibition of locomotion*. J. Cell Sci. **124**, 2642 (2011)

[Kaliman 2014] S. Kaliman, C. Jayachandran, F. Rehfeldt, and A.-S. Smith. *Novel Growth Regime of MDCK II Model Tissues on Soft Substrates*. Biophys. J. **106**, L25 (2014)

[Kametani 2007] Y. Kametani and M. Takeichi. *Basal-to-apical cadherin flow at cell junctions*. Nat. Cell Biol. **9**, 92 (2007)

[Kawaguchi 2017] K. Kawaguchi, R. Kageyama, and M. Sano. *Topological defects control collective dynamics in neural progenitor cell cultures*. Nature **545**, 327 (2017)

[Kemkemer 2000] R. Kemkemer, D. Kling, D. Kaufmann, and H. Gruler. *Elastic properties of nematoid arrangements formed by amoeboid cells*. Eur. Phys. J. E **1**, 215 (2000)

[Khajah 2016] M. A. Khajah and Y. A. Luqmani. *Involvement of Membrane Blebbing in Immunological Disorders and Cancer*. Med. Princ. Pract. **25**, 18 (2016)

[Khalil 2010] A. A. Khalil and P. Friedl. *Determinants of leader cells in collective cell migration*. Integr. Biol. **2**, 568 (2010)

[Khalilgharibi 2016] N. Khalilgharibi, J. Fouchard, P. Recho, G. Charras, and A. Kabla. *The dynamic mechanical properties of cellularised aggregates*. Curr. Opin. Cell Biol. **42**, 113 (2016)

[Klarlund 2012] J. K. Klarlund. *Dual modes of motility at the leading edge of migrating epithelial cell sheets*. Proc. Natl. Acad. Sci. U. S. A. **109**, 15799 (2012)

[Köpf 2013] M. H. Köpf and L. M. Pismen. *A continuum model of epithelial spreading*. Soft Matter **9**, 3727 (2013)

[Kruse 2004] K. Kruse, J. Joanny, F. Jülicher, J. Prost, and K. Sekimoto. *Asters, Vortices, and Rotating Spirals in Active Gels of Polar Filaments*. Phys. Rev. Lett. **92**, 078101 (2004)

[Kruse 2005] K. Kruse, J. F. Joanny, F. Jülicher, J. Prost, and K. Sekimoto. *Generic theory of active polar gels: a paradigm for cytoskeletal dynamics*. Eur. Phys. J. E **16**, 5 (2005)

[Ladoux 2010] B. Ladoux, E. Anon, M. Lambert, A. Rabodzey, P. Hersen, A. Buguin, P. Silberzan, and R.-M. Mège. *Strength Dependence of Cadherin-Mediated Adhesions*. Biophys. J. **98**, 534 (2010)

[Ladoux 2016] B. Ladoux, R.-M. Mège, and X. Trepat. *Front-Rear Polarization by Mechanical Cues: From Single Cells to Tissues*. Trends Cell Biol. **26**, 420 (2016)

[Lämmermann 2009] T. Lämmermann and M. Sixt. *Mechanical modes of 'amoeboid' cell migration*. Curr. Opin. Cell Biol. **21**, 636 (2009)

[Langridge 2006] P. D. Langridge and R. R. Kay. *Blebbing of Dictyostelium cells in response to chemoattractant*. Exp. Cell Res. **312**, 2009 (2006)

[Le Bellac 2004] M. Le Bellac, F. Mortessagne, and G. G. Batrouni. *Equilibrium and Non-Equilibrium Statistical Thermodynamics* (Cambridge University Press, 2004)

[Le Goff 2002] L. Le Goff, F. Amblard, and E. M. Furst. *Motor-Driven Dynamics in Actin-Myosin Networks*. Phys. Rev. Lett. **88**, 018101 (2002)

[Leckband 2011] D. E. Leckband, Q. le Duc, N. Wang, and J. de Rooij. *Mechanotransduction at cadherin-mediated adhesions*. Curr. Opin. Cell Biol. **23**, 523 (2011)

[Lecuit 2015] T. Lecuit and A. S. Yap. *E-cadherin junctions as active mechanical integrators in tissue dynamics*. Nat. Cell Biol. **17**, 533 (2015)

[Lee 2011a] P. Lee and C. Wolgemuth. *Advent of complex flows in epithelial tissues*. Phys. Rev. E **83**, 061920 (2011a)

[Lee 2011b] P. Lee and C. W. Wolgemuth. *Crawling Cells Can Close Wounds without Purse Strings or Signaling*. PLoS Comput. Biol. **7**, e1002007 (2011b)

[Lee 2016] P. Lee and C. W. Wolgemuth. *Physical Mechanisms of Cancer in the Transition to Metastasis*. Biophys. J. **111**, 256 (2016)

[Lee 2017] R. M. Lee, H. Yue, W.-J. Rappel, and W. Losert. *Inferring single-cell behaviour from large-scale epithelial sheet migration patterns*. J. R. Soc. Interface **14**, 20170147 (2017)

[Lelidis 2013] I. Lelidis and J.-F. Joanny. *Interaction of focal adhesions mediated by the substrate elasticity*. Soft Matter **9**, 11120 (2013)

[Levin 1991] S. Levin and R. Korenstein. *Membrane fluctuations in erythrocytes are linked to MgATP-dependent dynamic assembly of the membrane skeleton*. Biophys. J. **60**, 733 (1991)

[Levis 2014] D. Levis and L. Berthier. *Clustering and heterogeneous dynamics in a kinetic Monte Carlo model of self-propelled hard disks*. Phys. Rev. E **89**, 062301 (2014)

[Lieber 2015] A. D. Lieber, Y. Schweitzer, M. M. Kozlov, and K. Keren. *Front-to-Rear Membrane Tension Gradient in Rapidly Moving Cells*. Biophys. J. **108**, 1599 (2015)

[Lim 2012a] F. Y. Lim, K.-H. Chiam, and L. Mahadevan. *The size, shape, and dynamics of cellular blebs*. Europhys. Lett. **100**, 28004 (2012a)

[Lim 2012b] J. Lim and J. P. Thiery. *Epithelial-mesenchymal transitions: insights from development*. Development **139**, 3471 (2012b)

[Lin 2004] L. C.-L. Lin and F. L. H. Brown. *Brownian Dynamics in Fourier Space: Membrane Simulations over Long Length and Time Scales*. Phys. Rev. Lett. **93**, 256001 (2004)

[Liu 2015] Y.-J. Liu, M. Le Berre, F. Lautenschlaeger, P. Maiuri, A. Callan-Jones, M. Heuzé, T. Takaki, R. Voituriez, and M. Piel. *Confinement and Low Adhesion Induce Fast Amoeboid Migration of Slow Mesenchymal Cells*. Cell **160**, 659 (2015)

[Liu 2010] Z. Liu, J. L. Tan, D. M. Cohen, M. T. Yang, N. J. Sniadecki, S. A. Ruiz, C. M. Nelson, and C. S. Chen. *Mechanical tugging force regulates the size of cell-cell junctions*. Proc. Natl. Acad. Sci. U. S. A. **107**, 9944 (2010)

[Liverpool 2006] T. Liverpool and M. Marchetti. *Rheology of Active Filament Solutions*. Phys. Rev. Lett. **97**, 268101 (2006)

[Liverpool 2009] T. B. Liverpool, M. C. Marchetti, J.-F. Joanny, and J. Prost. *Mechanical response of active gels*. Europhys. Lett. **85**, 18007 (2009)

[Lodish 2016] H. Lodish, A. Berk, C. A. Kaiser, M. Krieger, A. Bretscher, H. Ploegh, A. Amon, and K. C. Martin. *Molecular Cell Biology* (W. H. Freeman and Company, 2016)

[Loiseau 2016] E. Loiseau, J. A. M. Schneider, F. C. Keber, C. Pelzl, G. Massiera, G. Salbreux, and A. R. Bausch. *Shape remodeling and blebbing of active cytoskeletal vesicles*. Sci. Adv. **2**, e1500465 (2016)

[López 2015] H. M. López, J. Gachelin, C. Douarche, H. Auradou, and E. Clément. *Turning Bacteria Suspensions into Superfluids*. Phys. Rev. Lett. **115**, 028301 (2015)

[Lubensky 2002] T. C. Lubensky, R. Mukhopadhyay, L. Radzihovsky, and X. Xing. *Symmetries and elasticity of nematic gels*. Phys. Rev. E **66**, 011702 (2002)

[Manakova 2016] K. Manakova, H. Yan, J. Lowengrub, and J. Allard. *Cell Surface Mechanochemistry and the Determinants of Bleb Formation, Healing, and Travel Velocity*. Biophys. J. **110**, 1636 (2016)

[Manneville 1999] J.-B. Manneville, P. Bassereau, D. Lévy, and J. Prost. *Activity of Transmembrane Proteins Induces Magnification of Shape Fluctuations of Lipid Membranes*. Phys. Rev. Lett. **82**, 4356 (1999)

[Manneville 2001] J.-B. Manneville, P. Bassereau, S. Ramaswamy, and J. Prost. *Active membrane fluctuations studied by micropipet aspiration*. Phys. Rev. E **64**, 021908 (2001)

[Marchetti 2013] M. C. Marchetti, J. F. Joanny, S. Ramaswamy, T. B. Liverpool, J. Prost, M. Rao, and R. A. Simha. *Hydrodynamics of soft active matter*. Rev. Mod. Phys. **85**, 1143 (2013)

[Marcq 2011] P. Marcq, N. Yoshinaga, and J. Prost. *Rigidity Sensing Explained by Active Matter Theory*. Biophys. J. **101**, L33 (2011)

[Marinari 2012] E. Marinari, A. Mehonic, S. Curran, J. Gale, T. Duke, and B. Baum. *Live-cell delamination counterbalances epithelial growth to limit tissue overcrowding*. Nature **484**, 542 (2012)

[Mark 2010] S. Mark, R. Shlomovitz, N. S. Gov, M. Poujade, E. Grasland-Mongrain, and P. Silberzan. *Physical Model of the Dynamic Instability in an Expanding Cell Culture*. Biophys. J. **98**, 361 (2010)

[Marmottant 2009] P. Marmottant, A. Mgharbel, J. Käfer, B. Audren, J.-P. Rieu, J.-C. Vial, B. van der Sanden, A. F. M. Marée, F. Graner, and H. Delanoë-Ayari. *The role of fluctuations and stress on the effective viscosity of cell aggregates*. Proc. Natl. Acad. Sci. U. S. A. **106**, 17271 (2009)

[Maruthamuthu 2014] V. Maruthamuthu and M. L. Gardel. *Protrusive Activity Guides Changes in Cell-Cell Tension during Epithelial Cell Scattering*. Biophys. J. **107**, 555 (2014)

[Maruthamuthu 2011] V. Maruthamuthu, B. Sabass, U. S. Schwarz, and M. L. Gardel. *Cell-ECM traction force modulates endogenous tension at cell-cell contacts*. Proc. Natl. Acad. Sci. U. S. A. **108**, 4708 (2011)

[Matoz-Fernandez 2017] D. A. Matoz-Fernandez, K. Martens, R. Sknepnek, J. L. Barrat, and S. Henkes. *Cell division and death inhibit glassy behaviour of confluent tissues*. Soft Matter **13**, 3205 (2017)

[Maugis 2010] B. Maugis, J. Brugués, P. Nassoy, N. Guillen, P. Sens, and F. Amblard. *Dynamic instability of the intracellular pressure drives bleb-based motility*. J. Cell Sci. **123**, 3884 (2010)

[Mayor 2010] R. Mayor and C. Carmona-Fontaine. *Keeping in touch with contact inhibition of locomotion*. Trends Cell Biol. **20**, 319 (2010)

[Mayor 2016] R. Mayor and S. Etienne-Manneville. *The front and rear of collective cell migration*. Nat. Rev. Mol. Cell Biol. **17**, 97 (2016)

[Mazenko 2006] G. F. Mazenko. *Nonequilibrium Statistical Mechanics* (John Wiley & Sons, 2006)

[Méhes 2014] E. Méhes and T. Vicsek. *Collective motion of cells: from experiments to models*. Integr. Biol. (Camb). **6**, 831 (2014)

[Melo 1989] F. Melo, J. F. Joanny, and S. Fauve. *Fingering Instability of Spinning Drops*. Phys. Rev. Lett. **63**, 1958 (1989)

[Merath 2006] R.-J. Merath and U. Seifert. *Nonmonotonic fluctuation spectra of membranes pinned or tethered discretely to a substrate*. Phys. Rev. E **73**, 010401 (2006)

[Merkel 2000] R. Merkel, R. Simson, D. A. Simson, M. Hohenadl, A. Boulbitch, E. Wallraff, and E. Sackmann. *A Micromechanic Study of Cell Polarity and Plasma Membrane Cell Body Coupling in Dictyostelium*. Biophys. J. **79**, 707 (2000)

[Mertz 2012] A. F. Mertz, S. Banerjee, Y. Che, G. K. German, Y. Xu, C. Hyland, M. C. Marchetti, V. Horsley, and E. R. Dufresne. *Scaling of Traction Forces with the Size of Cohesive Cell Colonies*. Phys. Rev. Lett. **108**, 198101 (2012)

[Mertz 2013] A. F. Mertz, Y. Che, S. Banerjee, J. M. Goldstein, K. A. Rosowski, S. F. Revilla, C. M. Niessen, M. C. Marchetti, E. R. Dufresne, and V. Horsley. *Cadherin-based intercellular adhesions organize epithelial cell-matrix traction forces*. Proc. Natl. Acad. Sci. U. S. A. **110**, 842 (2013)

[Mierke 2015] C. T. Mierke. *Physical view on migration modes*. Cell Adh. Migr. **9**, 367 (2015)

[Mills 1998] J. C. Mills, N. L. Stone, J. Erhardt, and R. N. Pittman. *Apoptotic Membrane Blebbing Is Regulated by Myosin Light Chain Phosphorylation*. J. Cell Biol. **140**, 627 (1998)

[Mladek 2006] B. M. Mladek, D. Gottwald, G. Kahl, M. Neumann, and C. N. Likos. *Formation of Polymorphic Cluster Phases for a Class of Models of Purely Repulsive Soft Spheres*. Phys. Rev. Lett. **96**, 045701 (2006)

[Moeendarbary 2013] E. Moeendarbary, L. Valon, M. Fritzsche, A. R. Harris, D. A. Moulding, A. J. Thrasher, E. Stride, L. Mahadevan, and G. T. Charras. *The cytoplasm of living cells behaves as a poroelastic material*. Nat. Mater. **12**, 253 (2013)

[Mones 2015] E. Mones, A. Czirók, and T. Vicsek. *Anomalous segregation dynamics of self-propelled particles*. New J. Phys. **17**, 063013 (2015)

[Monzel 2015] C. Monzel, D. Schmidt, C. Kleusch, D. Kirchenbüchler, U. Seifert, A.-S. Smith, K. Sengupta, and R. Merkel. *Measuring fast stochastic displacements of bio-membranes with dynamic optical displacement spectroscopy*. Nat. Commun. **6**, 8162 (2015)

[Monzel 2016] C. Monzel and K. Sengupta. *Measuring shape fluctuations in biological membranes*. J. Phys. D. Appl. Phys. **49**, 243002 (2016)

[Moreno 2007] A. J. Moreno and C. N. Likos. *Diffusion and Relaxation Dynamics in Cluster Crystals*. Phys. Rev. Lett. **99**, 107801 (2007)

[Morita 2017] H. Morita, S. Grigolon, M. Bock, S. G. Krens, G. Salbreux, and C.-P. Heisenberg. *The Physical Basis of Coordinated Tissue Spreading in Zebrafish Gastrulation*. Dev. Cell **40**, 354 (2017)

[Nambiar 2009] R. Nambiar, R. E. McConnell, and M. J. Tyska. *Control of cell membrane tension by myosin-I*. Proc. Natl. Acad. Sci. U. S. A. **106**, 11972 (2009)

[Needleman 2015] D. Needleman. *The Material Basis of Life*. Trends Cell Biol. **25**, 713 (2015)

[Needleman 2017] D. Needleman and Z. Dogic. *Active matter at the interface between materials science and cell biology*. Nat. Rev. Mater. **2**, 17048 (2017)

[Nesbitt 2017] D. Nesbitt, G. Pruessner, and C. F. Lee. *Edge instability in incompressible planar active fluids*. arXiv:1706.03584v1 (2017)

[Nier 2016] V. Nier, S. Jain, C. T. Lim, S. Ishihara, B. Ladoux, and P. Marcq. *Inference of Internal Stress in a Cell Monolayer*. Biophys. J. **110**, 1625 (2016)

[Nieto 2013] M. A. Nieto. *Epithelial Plasticity: A Common Theme in Embryonic and Cancer Cells*. Science **342**, 1234850 (2013)

[Nieto 2016] M. A. Nieto, R. Y.-J. Huang, R. A. Jackson, and J. P. Thiery. *EMT: 2016*. Cell **166**, 21 (2016)

[Norman 2011] L. Norman, K. Sengupta, and H. Aranda-Espinoza. *Blebbing dynamics during endothelial cell spreading*. Eur. J. Cell Biol. **90**, 37 (2011)

[Norman 2010] L. L. Norman, J. Brugués, K. Sengupta, P. Sens, and H. Aranda-Espinoza. *Cell Blebbing and Membrane Area Homeostasis in Spreading and Retracting Cells*. Biophys. J. **99**, 1726 (2010)

[Notbohm 2016] J. Notbohm, S. Banerjee, K. J. Utuje, B. Gweon, H. Jang, Y. Park, J. Shin, J. P. Butler, J. J. Fredberg, and M. C. Marchetti. *Cellular Contraction and Polarization Drive Collective Cellular Motion*. Biophys. J. **110**, 2729 (2016)

[Omelchenko 2003] T. Omelchenko, J. M. Vasiliev, I. M. Gelfand, H. H. Feder, and E. M. Bonder. *Rho-dependent formation of epithelial "leader" cells during wound healing*. Proc. Natl. Acad. Sci. U. S. A. **100**, 10788 (2003)

[Oriola 2017] D. Oriola, R. Alert, and J. Casademunt. *Fluidization and Active Thinning by Molecular Kinetics in Active Gels*. Phys. Rev. Lett. **118**, 088002 (2017)

[Ouaknin 2009] G. Y. Ouaknin and P. Z. Bar-Yoseph. *Stochastic Collective Movement of Cells and Fingering Morphology: No Maverick Cells*. Biophys. J. **97**, 1811 (2009)

[Paluch 2006] E. Paluch, C. Sykes, J. Prost, and M. Bornens. *Dynamic modes of the cortical actomyosin gel during cell locomotion and division*. Trends Cell Biol. **16**, 5 (2006)

[Paluch 2016] E. K. Paluch, I. M. Aspalter, and M. Sixt. *Focal Adhesion-Independent Cell Migration*. Annu. Rev. Cell Dev. Biol. **32**, 469 (2016)

[Paluch 2013] E. K. Paluch and E. Raz. *The role and regulation of blebs in cell migration*. Curr. Opin. Cell Biol. **25**, 582 (2013)

[Park 2010] Y. Park, C. a. Best, T. Auth, N. S. Gov, S. a. Safran, G. Popescu, S. Suresh, and M. S. Feld. *Metabolic remodeling of the human red blood cell membrane*. Proc. Natl. Acad. Sci. U. S. A. **107**, 1289 (2010)

[Petitjean 2010] L. Petitjean, M. Reffay, E. Grasland-Mongrain, M. Poujade, B. Ladoux, A. Buguin, and P. Silberzan. *Velocity Fields in a Collectively Migrating Epithelium*. Biophys. J. **98**, 1790 (2010)

[Peukes 2014] J. Peukes and T. Betz. *Direct Measurement of the Cortical Tension during the Growth of Membrane Blebs*. Biophys. J. **107**, 1810 (2014)

[Pham 2011] K. Pham, H. B. Frieboes, V. Cristini, and J. Lowengrub. *Predictions of tumour morphological stability and evaluation against experimental observations*. J. R. Soc. Interface **8**, 16 (2011)

[Phillips 2012] R. Phillips, J. Kondev, J. Theriot, and H. G. Garcia. *Physical Biology of the Cell* (Garland Science, 2012)

[Plutoni 2016] C. Plutoni, E. Bazellieres, M. Le Borgne-Rochet, F. Comunale, A. Brugués, M. Séveno, D. Planchon, S. Thuault, N. Morin, S. Bodin, X. Trepat, and C. Gauthier-Rouvière. *P-cadherin promotes collective cell migration via a Cdc42-mediated increase in mechanical forces*. J. Cell Biol. **212**, 199 (2016)

[Popescu 2006] G. Popescu, T. Ikeda, K. Goda, C. Best-Popescu, M. Laposata, S. Manley, R. Dasari, K. Badizadegan, and M. Feld. *Optical Measurement of Cell Membrane Tension*. Phys. Rev. Lett. **97**, 218101 (2006)

[Popović 2017] M. Popović, A. Nandi, M. Merkel, R. Etournay, S. Eaton, F. Jülicher, and G. Salbreux. *Active dynamics of tissue shear flow*. New J. Phys. **19**, 033006 (2017)

[Poujade 2007] M. Poujade, E. Grasland-Mongrain, A. Hertzog, J. Jouanneau, P. Chavrier, B. Ladoux, A. Buguin, and P. Silberzan. *Collective migration of an epithelial monolayer in response to a model wound*. Proc. Natl. Acad. Sci. U. S. A. **104**, 15988 (2007)

[Prost 1996] J. Prost and R. Bruinsma. *Shape fluctuations of active membranes*. Europhys. Lett. **33**, 321 (1996)

[Prost 2015] J. Prost, F. Jülicher, and J.-F. Joanny. *Active gel physics*. Nat. Phys. **11**, 111 (2015)

[Prost 1998] J. Prost, J.-B. Manneville, and R. Bruinsma. *Fluctuation-magnification of non-equilibrium membranes near a wall*. Eur. Phys. J. B **1**, 465 (1998)

[Rafaï 2010] S. Rafaï, L. Jibuti, and P. Peyla. *Effective Viscosity of Microswimmer Suspensions*. Phys. Rev. Lett. **104**, 098102 (2010)

[Rakshit 2014] S. Rakshit and S. Sivasankar. *Biomechanics of cell adhesion: how force regulates the lifetime of adhesive bonds at the single molecule level*. Phys. Chem. Chem. Phys. **16**, 2211 (2014)

[Ramaswamy 2010] S. Ramaswamy. *The Mechanics and Statistics of Active Matter*. Annu. Rev. Condens. Matter Phys. **1**, 323 (2010)

[Ranft 2010] J. Ranft, M. Basan, J. Elgeti, J.-F. Joanny, J. Prost, and F. Jülicher. *Fluidization of tissues by cell division and apoptosis*. Proc. Natl. Acad. Sci. U. S. A. **107**, 20863 (2010)

[Ranft 2012] J. Ranft, J. Prost, F. Jülicher, and J.-F. Joanny. *Tissue dynamics with permeation*. Eur. Phys. J. E **35**, 46 (2012)

[Ravasio 2015] A. Ravasio, A. P. Le, T. B. Saw, V. Tarle, H. T. Ong, C. Bertocchi, R.-M. Mège, C. T. Lim, N. S. Gov, and B. Ladoux. *Regulation of epithelial cell organization by tuning cell-substrate adhesion*. Integr. Biol. **7**, 1228 (2015)

[Recho 2016] P. Recho, J. Ranft, and P. Marcq. *One-dimensional collective migration of a proliferating cell monolayer*. Soft Matter **12**, 2381 (2016)

[Redner 2013a] G. S. Redner, A. Baskaran, and M. F. Hagan. *Reentrant phase behavior in active colloids with attraction*. Phys. Rev. E **88**, 012305 (2013a)

[Redner 2013b] G. S. Redner, M. F. Hagan, and A. Baskaran. *Structure and Dynamics of a Phase-Separating Active Colloidal Fluid*. Phys. Rev. Lett. **110**, 055701 (2013b)

[Reffay 2014] M. Reffay, M. C. Parrini, O. Cochet-Escartin, B. Ladoux, A. Buguin, S. Coscoy, F. Amblard, J. Camonis, and P. Silberzan. *Interplay of RhoA and mechanical forces in collective cell migration driven by leader cells*. Nat. Cell Biol. **16**, 217 (2014)

[Reffay 2011] M. Reffay, L. Petitjean, S. Coscoy, E. Grasland-Mongrain, F. Amblard, A. Buguin, and P. Silberzan. *Orientation and Polarity in Collectively Migrating Cell Structures: Statics and Dynamics*. Biophys. J. **100**, 2566 (2011)

[Reichl 1998] L. E. Reichl. *A Modern Course in Statistical Physics* (John Wiley & Sons, 1998), 2nd ed.

[Rentsch 2000] P. S. Rentsch and H. Keller. *Suction pressure can induce uncoupling of the plasma membrane from cortical actin*. Eur. J. Cell Biol. **79**, 975 (2000)

[Revenu 2009] C. Revenu and D. Gilmour. *EMT 2.0: shaping epithelia through collective migration*. Curr. Opin. Genet. Dev. **19**, 338 (2009)

[Risken 1989] H. Risken. *The Fokker-Planck Equation. Methods of Solution and Applications* (Springer, 1989)

[Risler 2013] T. Risler and M. Basan. *Morphological instabilities of stratified epithelia: a mechanical instability in tumour formation*. New J. Phys. **15**, 065011 (2013)

[Rognoni 2012] L. Rognoni, J. Stigler, B. Pelz, J. Ylänne, and M. Rief. *Dynamic force sensing of filamin revealed in single-molecule experiments*. Proc. Natl. Acad. Sci. U. S. A. **109**, 19679 (2012)

[Rørth 2009] P. Rørth. *Collective Cell Migration*. Annu. Rev. Cell Dev. Biol. **25**, 407 (2009)

[Rørth 2012] P. Rørth. *Fellow travellers: emergent properties of collective cell migration*. EMBO Rep. **13**, 984 (2012)

[Rouven Brückner 2015] B. Rouven Brückner, A. Pietuch, S. Nehls, J. Rother, and A. Janshoff. *Ezrin is a Major Regulator of Membrane Tension in Epithelial Cells*. Sci. Rep. **5**, 14700 (2015)

[Roux 2016] C. Roux, A. Duperray, V. M. Laurent, R. Michel, V. Peschetola, C. Verdier, and J. Étienne. *Prediction of traction forces of motile cells*. Interface Focus **6**, 20160042 (2016)

[Roycroft 2016] A. Roycroft and R. Mayor. *Molecular basis of contact inhibition of locomotion*. Cell. Mol. Life Sci. **73**, 1119 (2016)

[Ruprecht 2015] V. Ruprecht, S. Wieser, A. Callan-Jones, M. Smutny, H. Morita, K. Sako, V. Barone, M. Ritsch-Marte, M. Sixt, R. Voituriez, and C.-P. Heisenberg. *Cortical Contractility Triggers a Stochastic Switch to Fast Amoeboid Cell Motility*. Cell **160**, 673 (2015)

[Ryan 2001] P. L. Ryan, R. A. Foty, J. Kohn, and M. S. Steinberg. *Tissue spreading on implantable substrates is a competitive outcome of cell-cell vs. cell-substratum adhesivity*. Proc. Natl. Acad. Sci. U. S. A. **98**, 4323 (2001)

[Safran 1994] S. A. Safran. *Statistical Thermodynamics of Surfaces, Interfaces, and Membranes* (Addison-Wesley, 1994)

[Sahai 2003] E. Sahai and C. J. Marshall. *Differing modes of tumour cell invasion have distinct requirements for Rho / ROCK signalling and extracellular proteolysis*. Nat. Cell Biol. **5**, 711 (2003)

[Salbreux 2012] G. Salbreux, G. Charras, and E. Paluch. *Actin cortex mechanics and cellular morphogenesis*. Trends Cell Biol. **22**, 536 (2012)

[Salbreux 2009] G. Salbreux, J. Prost, and J. F. Joanny. *Hydrodynamics of Cellular Cortical Flows and the Formation of Contractile Rings*. Phys. Rev. Lett. **103**, 058102 (2009)

[Salm 2012] M. Salm and L. M. Pismen. *Chemical and mechanical signaling in epithelial spreading*. Phys. Biol. **9**, 026009 (2012)

[Sankararaman 2009] S. Sankararaman and S. Ramaswamy. *Instabilities and Waves in Thin Films of Living Fluids*. Phys. Rev. Lett. **102**, 118107 (2009)

[Sarkar 2012] N. Sarkar and A. Basu. *Instabilities and diffusion in a hydrodynamic model of a fluid membrane coupled to a thin active fluid layer*. Eur. Phys. J. E **35**, 115 (2012)

[Sarkar 2013] N. Sarkar and A. Basu. *Generic instabilities in a fluid membrane coupled to a thin layer of ordered active polar fluid*. Eur. Phys. J. E **36**, 86 (2013)

[Sarrió 2009] D. Sarrió, J. Palacios, M. Hergueta-Redondo, G. Gómez-López, A. Cano, and G. Moreno-Bueno. *Functional characterization of E- and P-cadherin in invasive breast cancer cells*. BMC Cancer **9**, 74 (2009)

[Saw 2017] T. B. Saw, A. Doostmohammadi, V. Nier, L. Kocgozlu, S. Thampi, Y. Toyama, P. Marcq, C. T. Lim, J. M. Yeomans, and B. Ladoux. *Topological defects in epithelia govern cell death and extrusion*. Nature **544**, 212 (2017)

[Saw 2014] T. B. Saw, S. Jain, B. Ladoux, and C. T. Lim. *Mechanobiology of collective cell migration*. Cell. Mol. Bioeng. **8**, 3 (2014)

[Scarpa 2016] E. Scarpa and R. Mayor. *Collective cell migration in development*. J. Cell Biol. **212**, 143 (2016)

[Scarpa 2015] E. Scarpa, A. Szabó, A. Bibonne, E. Theveneau, M. Parsons, and R. Mayor. *Cadherin Switch during EMT in Neural Crest Cells Leads to Contact Inhibition of Locomotion via Repolarization of Forces*. Dev. Cell **34**, 421 (2015)

[Schuss 2010] Z. Schuss. *Theory and Applications of Stochastic Processes. An Analytical Approach* (Springer, 2010)

[Schwartz 2008] M. A. Schwartz and D. W. DeSimone. *Cell adhesion receptors in mechanotransduction*. Curr. Opin. Cell Biol. **20**, 551 (2008)

[Schwarz 2013] U. S. Schwarz and S. A. Safran. *Physics of adherent cells*. Rev. Mod. Phys. **85**, 1327 (2013)

[Sedzinski 2011] J. Sedzinski, M. Biro, A. Oswald, J.-Y. Tinevez, G. Salbreux, and E. Paluch. *Polar actomyosin contractility destabilizes the position of the cytokinetic furrow*. Nature **476**, 462 (2011)

[Seifert 1997] U. Seifert. *Configurations of fluid membranes and vesicles*. Adv. Phys. **46**, 13 (1997)

[Sens 2013] P. Sens. *Rigidity sensing by stochastic sliding friction*. Europhys. Lett. **104**, 38003 (2013)

[Sens 2015] P. Sens and J. Plastino. *Membrane tension and cytoskeleton organization in cell motility*. J. Phys. Condens. Matter **27**, 273103 (2015)

[Sepúlveda 2013] N. Sepúlveda, L. Petitjean, O. Cochet, E. Grasland-Mongrain, P. Silberzan, and V. Hakim. *Collective Cell Motion in an Epithelial Sheet Can Be Quantitatively Described by a Stochastic Interacting Particle Model*. PLoS Comput. Biol. **9**, e1002944 (2013)

[Serra-Picamal 2015] X. Serra-Picamal, V. Conte, R. Sunyer, J. J. Muñoz, and X. Trepat. *Mapping forces and kinematics during collective cell migration*. Methods Cell Biol. **125**, 309 (2015)

[Serra-Picamal 2012] X. Serra-Picamal, V. Conte, R. Vincent, E. Añón, D. T. Tambe, E. Bazellieres, J. P. Butler, J. J. Fredberg, and X. Trepat. *Mechanical waves during tissue expansion*. Nat. Phys. **8**, 628 (2012)

[Sheetz 2001] M. P. Sheetz. *Cell control by membrane-cytoskeleton adhesion*. Nat. Rev. Mol. Cell Biol. **2**, 392 (2001)

[Sheetz 2006] M. P. Sheetz, J. E. Sable, and H.-G. Döbereiner. *Continuous Membrane-Cytoskeleton Adhesion Requires Continuous Accommodation to Lipid and Cytoskeleton Dynamics*. Annu. Rev. Biophys. Biomol. Struct. **35**, 417 (2006)

[Shimamoto 2011] Y. Shimamoto, Y. T. Maeda, S. Ishiwata, A. J. Libchaber, and T. M. Kapoor. *Insights into the Micromechanical Properties of the Metaphase Spindle*. Cell **145**, 1062 (2011)

[Simha 2002] R. A. Simha and S. Ramaswamy. *Hydrodynamic Fluctuations and Instabilities in Ordered Suspensions of Self-Propelled Particles*. Phys. Rev. Lett. **89**, 058101 (2002)

[Singh 2002] S. Singh. *Liquid Crystals. Fundamentals* (World Scientific, 2002)

[Sliogeryte 2014] K. Sliogeryte, S. D. Thorpe, D. A. Lee, L. Botto, and M. M. Knight. *Stem cell differentiation increases membrane-actin adhesion regulating cell blebability, migration and mechanics.* Sci. Rep. **4**, 7307 (2014)

[Smeets 2016] B. Smeets, R. Alert, J. Pešek, I. Pagonabarraga, H. Ramon, and R. Vincent. *Emergent structures and dynamics of cell colonies by contact inhibition of locomotion*. Proc. Natl. Acad. Sci. U. S. A. **113**, 14621 (2016)

[Sokolov 2009] A. Sokolov and I. Aranson. *Reduction of Viscosity in Suspension of Swimming Bacteria*. Phys. Rev. Lett. **103**, 148101 (2009)

[Spangler 2011] E. J. Spangler, C. W. Harvey, J. D. Revalee, P. B. S. Kumar, and M. Laradji. *Computer simulation of cytoskeleton-induced blebbing in lipid membranes*. Phys. Rev. E **84**, 051906 (2011)

[Stephen 1974] M. J. Stephen and J. P. Straley. *Physics of liquid crystals*. Rev. Mod. Phys. **46**, 617 (1974)

[Stewart 2004] I. W. Stewart. *The Static and Dynamic Continuum Theory of Liquid Crystals. A Mathematical Introduction* (Taylor & Francis, 2004)

[Stewart 2011] M. P. Stewart, J. Helenius, Y. Toyoda, S. P. Ramanathan, D. J. Muller, and A. A. Hyman. *Hydrostatic pressure and the actomyosin cortex drive mitotic cell rounding*. Nature **469**, 226 (2011)

[Stirbat 2013] T. V. Stirbat, A. Mgharbel, S. Bodennec, K. Ferri, H. C. Mertani, J.-P. Rieu, and H. Delanoë-Ayari. *Fine Tuning of Tissues' Viscosity and Surface Tension through Contractility Suggests a New Role for alpha-Catenin*. PLoS One **8**, e52554 (2013)

[Stramer 2017] B. Stramer and R. Mayor. *Mechanisms and in vivo functions of contact inhibition of locomotion*. Nat. Rev. Mol. Cell Biol. **18**, 43 (2017)

[Strychalski 2013] W. Strychalski and R. D. Guy. *A computational model of bleb formation*. Math. Med. Biol. **30**, 115 (2013)

[Sunyer 2016] R. Sunyer, V. Conte, J. Escribano, A. Elosegui-Artola, A. Labernadie, L. Valon, D. Navajas, J. M. García-Aznar, J. J. Muñoz, P. Roca-Cusachs, and X. Trepat. *Collective cell durotaxis emerges from long-range intercellular force transmission*. Science **353**, 1157 (2016)

[Szabó 2016] A. Szabó and R. Mayor. *Modelling collective cell migration of neural crest*. Curr. Opin. Cell Biol. **42**, 22 (2016)

[Szabó 2006] B. Szabó, G. Szöllösi, B. Gönci, Z. Jurányi, D. Selmeczi, and T. Vicsek. *Phase transition in the collective migration of tissue cells: Experiment and model*. Phys. Rev. E **74**, 061908 (2006)

[Taloni 2015] A. Taloni, E. Kardash, O. U. Salman, L. Truskinovsky, S. Zapperi, and C. A. M. La Porta. *Volume Changes During Active Shape Fluctuations in Cells*. Phys. Rev. Lett. **114**, 208101 (2015)

[Tambe 2011] D. T. Tambe, C. Corey Hardin, T. E. Angelini, K. Rajendran, C. Y. Park, X. Serra-Picamal, E. H. Zhou, M. H. Zaman, J. P. Butler, D. A. Weitz, J. J. Fredberg, and X. Trepat. *Collective cell guidance by cooperative intercellular forces*. Nat. Mater. **10**, 469 (2011)

[Tambe 2013] D. T. Tambe, U. Croutelle, X. Trepat, C. Y. Park, J. H. Kim, E. Millet, J. P. Butler, and J. J. Fredberg. *Monolayer Stress Microscopy: Limitations, Artifacts, and Accuracy of Recovered Intercellular Stresses*. PLoS One **8**, e55172 (2013)

[Tanaka 1992] F. Tanaka and S. F. Edwards. *Viscoelastic Properties of Physically Cross-Linked Networks. Transient Network Theory*. Macromolecules **25**, 1516 (1992)

[Tanimoto 2014] H. Tanimoto and M. Sano. *A Simple Force-Motion Relation for Migrating Cells Revealed by Multipole Analysis of Traction Stress*. Biophys. J. **106**, 16 (2014)

[Tarle 2015] V. Tarle, A. Ravasio, V. Hakim, and N. Gov. *Modeling the finger instability in an expanding cell monolayer*. Integr. Biol. **7**, 1218 (2015)

[Theveneau 2013] E. Theveneau and R. Mayor. *Collective cell migration of epithelial and mesenchymal cells*. Cell. Mol. Life Sci. **70**, 3481 (2013)

[Thiery 2009] J. P. Thiery, H. Acloque, R. Y. J. Huang, and M. A. Nieto. *Epithelial-Mesenchymal Transitions in Development and Disease*. Cell **139**, 871 (2009)

[Tinevez 2009] J.-Y. Tinevez, U. Schulze, G. Salbreux, J. Roensch, J.-F. Joanny, and E. Paluch. *Role of cortical tension in bleb growth*. Proc. Natl. Acad. Sci. U. S. A. **106**, 18581 (2009)

[Tozluoğlu 2013] M. Tozluoğlu, A. L. Tournier, R. P. Jenkins, S. Hooper, P. A. Bates, and E. Sahai. *Matrix geometry determines optimal cancer cell migration strategy and modulates response to interventions*. Nat. Cell Biol. **15**, 751 (2013)

[Trepat 2011] X. Trepat and J. J. Fredberg. *Plithotaxis and emergent dynamics in collective cellular migration*. Trends Cell Biol. **21**, 638 (2011)

[Trepat 2009] X. Trepat, M. R. Wasserman, T. E. Angelini, E. Millet, D. A. Weitz, J. P. Butler, and J. J. Fredberg. *Physical forces during collective cell migration*. Nat. Phys. **5**, 426 (2009)

[Troian 1989] S. M. Troian, E. Herbolzheimer, S. A. Safran, and J. F. Joanny. *Fingering Instabilities of Driven Spreading Films*. Europhys. Lett. **10**, 25 (1989)

[Tsujioka 2012] M. Tsujioka, S. Yumura, K. Inouye, H. Patel, M. Ueda, and S. Yonemura. *Talin couples the actomyosin cortex to the plasma membrane during rear retraction and cytokinesis*. Proc. Natl. Acad. Sci. U. S. A. **109**, 12992 (2012)

[Tsukita 1999] S. Tsukita and S. Yonemura. *Cortical Actin Organization: Lessons from ERM (Ezrin/Radixin/Moesin) Proteins*. J. Biol. Chem. **274**, 34507 (1999)

[Turlier 2016] H. Turlier, D. A. Fedosov, B. Audoly, T. Auth, N. S. Gov, C. Sykes, J.-F. Joanny, G. Gompper, and T. Betz. *Equilibrium physics breakdown reveals the active nature of red blood cell flickering*. Nat. Phys. **12**, 513 (2016)

[Tyson 2014] R. A. Tyson, E. Zatulovskiy, R. R. Kay, and T. Bretschneider. *How blebs and pseudopods cooperate during chemotaxis*. Proc. Natl. Acad. Sci. **111**, 11703 (2014)

[Valon 2017] L. Valon, A. Marín-Llauradó, T. Wyatt, G. Charras, and X. Trepat. *Optogenetic control of cellular forces and mechanotransduction*. Nat. Commun. **8**, 14396 (2017)

[Vedula 2013] S. R. K. Vedula, A. Ravasio, C. T. Lim, and B. Ladoux. *Collective cell migration: a mechanistic perspective*. Physiology **28**, 370 (2013)

[Villar-Cerviño 2013] V. Villar-Cerviño, M. Molano-Mazón, T. Catchpole, M. Valdeolmillos, M. Henkemeyer, L. M. Martínez, V. Borrell, and O. Marín. *Contact Repulsion Controls the Dispersion and Final Distribution of Cajal-Retzius Cells*. Neuron **77**, 457 (2013)

[Vincent 2015] R. Vincent, E. Bazellières, C. Pérez-González, M. Uroz, X. Serra-Picamal, and X. Trepat. *Active Tensile Modulus of an Epithelial Monolayer*. Phys. Rev. Lett. **115**, 248103 (2015)

[Vink 2013] R. L. C. Vink and T. Speck. *Application of classical nucleation theory to the formation of adhesion domains*. Soft Matter **9**, 11197 (2013)

[Voituriez 2005] R. Voituriez, J. F. Joanny, and J. Prost. *Spontaneous flow transition in active polar gels*. Europhys. Lett. **70**, 404 (2005)

[Walcott 2010] S. Walcott and S. X. Sun. *A mechanical model of actin stress fiber formation and substrate elasticity sensing in adherent cells*. Proc. Natl. Acad. Sci. U. S. A. **107**, 7757 (2010)

[Weber 2012] G. F. Weber, M. A. Bjerke, and D. W. DeSimone. *A mechanoresponsive cadherin-keratin complex directs polarized protrusive behavior and collective cell migration*. Dev. Cell **22**, 104 (2012)

[Weijer 2009] C. J. Weijer. *Collective cell migration in development*. J. Cell Sci. **122**, 3215 (2009)

[Weikl 2009] T. R. Weikl, M. Asfaw, H. Krobath, B. Różycki, and R. Lipowsky. *Adhesion of membranes via receptor–ligand complexes: Domain formation, binding cooperativity, and active processes*. Soft Matter **5**, 3213 (2009)

[Welch 2015] M. D. Welch. *Cell Migration, Freshly Squeezed*. Cell **160**, 581 (2015)

[Wolfenson 2011] H. Wolfenson, A. Bershadsky, Y. I. Henis, and B. Geiger. *Actomyosin-generated tension controls the molecular kinetics of focal adhesions*. J. Cell Sci. **124**, 1425 (2011)

[Woods 2014] M. L. Woods, C. Carmona-Fontaine, C. P. Barnes, I. D. Couzin, R. Mayor, and K. M. Page. *Directional Collective Cell Migration Emerges as a Property of Cell Interactions*. PLoS One **9**, e104969 (2014)

[Woolley 2015] T. E. Woolley, E. A. Gaffney, J. M. Oliver, S. L. Waters, R. E. Baker, and A. Goriely. *Global contraction or local growth, bleb shape depends on more than just cell structure*. J. Theor. Biol. **380**, 83 (2015)

[Wottawah 2005] F. Wottawah, S. Schinkinger, B. Lincoln, R. Ananthakrishnan, M. Romeyke, J. Guck, and J. Käs. *Optical Rheology of Biological Cells*. Phys. Rev. Lett. **94**, 098103 (2005)

[Wyatt 2016] T. Wyatt, B. Baum, and G. Charras. *A question of time: tissue adaptation to mechanical forces*. Curr. Opin. Cell Biol. **38**, 68 (2016)

[Yabunaka 2017a] S. Yabunaka and P. Marcq. *Cell growth, division, and death in cohesive tissues: A thermodynamic approach*. Phys. Rev. E **96**, 022406 (2017a)

[Yabunaka 2017b] S. Yabunaka and P. Marcq. *Emergence of epithelial cell density waves*. Soft Matter page Advance Article (2017b)

[Yoshida 2006] K. Yoshida and T. Soldati. *Dissection of amoeboid movement into two mechanically distinct modes*. J. Cell Sci. **119**, 3833 (2006)

[Young 2010] J. Young and S. Mitran. *A numerical model of cellular blebbing: a volume-conserving, fluid-structure interaction model of the entire cell*. J. Biomech. **43**, 210 (2010)

[Zatulovskiy 2014] E. Zatulovskiy, R. Tyson, T. Bretschneider, and R. R. Kay. *Bleb-driven chemotaxis of Dictyostelium cells*. J. Cell Biol. **204**, 1027 (2014)

[Zhang 2008] C.-Z. Zhang and Z.-G. Wang. *Nucleation of membrane adhesions*. Phys. Rev. E **77**, 021906 (2008)

[Zidovska 2006] A. Zidovska and E. Sackmann. *Brownian Motion of Nucleated Cell Envelopes Impedes Adhesion*. Phys. Rev. Lett. **96**, 048103 (2006)

[Zidovska 2013] A. Zidovska, D. A. Weitz, and T. J. Mitchison. *Micron-scale coherence in interphase chromatin dynamics*. Proc. Natl. Acad. Sci. U. S. A. **110**, 15555 (2013)

[Zimmermann 2014a] J. Zimmermann, M. Basan, and H. Levine. *An instability at the edge of a tissue of collectively migrating cells can lead to finger formation during wound healing*. Eur. Phys. J. Spec. Top. **223**, 1259 (2014a)

[Zimmermann 2016] J. Zimmermann, B. A. Camley, W.-J. Rappel, and H. Levine. *Contact inhibition of locomotion determines cell-cell and cell-substrate forces in tissues*. Proc. Natl. Acad. Sci. U. S. A. **113**, 2660 (2016)

[Zimmermann 2014b] J. Zimmermann, R. L. Hayes, M. Basan, J. N. Onuchic, W.-J. Rappel, and H. Levine. *Intercellular Stress Reconstitution from Traction Force Data*. Biophys. J. **107**, 548 (2014b)